ORSAY

N° D'ORDRE:

UNIVERSITE DE PARIS-SUD
U.F.R. SCIENTIFIQUE D'ORSAY

THESE

présentée pour obtenir

Le GRADE de DOCTEUR EN SCIENCES

DE L'UNIVERSITE PARIS XI ORSAY

PAR

Mingzhen TIAN

HOLOGRAPHIE SPECTRO-TEMPORELLE DANS UN MATERIAU AMORPHE ORGANIQUE

Soutenue le 12 décembre 1997 devant la Commission d'examen

MM.

Daniel BLOCH, Rapporteur

Henri DUBOST

Jean-Louis LE GOUËT

Stefan KRÖLL

Michel ORRIT, Rapporteur

Kelvin WAGNER

SPECTRAL-TEMPORAL HOLOGRAPHY IN AN ORGANIC AMORPHOUS MATERIAL

献给我理解孩子的父母

献给我理解父母的孩子

MERCI

Je remercie Madame Catherine Bréchignac et Monsieur Christian Colliex de m'avoir accueilli au Laboratoire. Je tiens à leur exprimer ma profonde gratitude pour les aides qu'ils m'ont accordées.

Je me dois aussi de remercier les services internationaux du CNRS d'une part, de l'Académie des Sciences de mon pays d'autre part, ainsi que l'Association Franco-Chinoise pour la Recherche Scientifique et Technique pour leurs soutiens financiers, sans lesquels cette thèse n'aurait pu être possible.

Je remercie vivement mon directeur de thèse, Jean-Louis Le Gouët qui m'a donné la chance pendant ces trois années de participer à l'aventure de son équipe dans le domaine fantastique du 'hole burning' spectral et du stockage optique. Il a dirigé mon travail avec beaucoup de patience, de responsabilité et en s'évertuant à me faire partager son esprit de rigueur scientifique. Le capital qu'il m'a apporté me bénéficiera pour toute ma carrière future. Je lui suis reconnaissante pour n'avoir pas ménagé ses efforts afin de faciliter les conditions de mon séjour en France. Qu'il veuille bien trouver ici l'expression chaleureuse de mes plus vifs remerciements.

Messieurs Daniel Bloch et Michel Orrit ont accepté la lourde tâche de lire en détail et de rédiger un rapport sur mon mémoire de thèse. Je leur exprime toute ma gratitude pour le temps qu'ils ont ainsi consacré à apprécier mon travail à la lumière de leur grande expérience.

Je remercie Messieurs Henri Dubost, Stefan Kröll et Kelvin Wagner pour l'intérêt qu'ils ont manifesté à mon travail en acceptant de faire partie du Jury.

Pendant mes études, j'ai eu la chance d'avoir rencontré Jean-Pierre Galaup. Son comportement chaleureux et empreint de bonne humeur ont égayé mon séjour et mon travail. Je garderai longtemps le souvenir de bons moments de discussion sur tous les thèmes qu'ils touchent à la science ou à la vie, et qui m'ont aidé à améliorer mon français (et son chinois?). Merci Jean-Pierre pour ton amitié que je souhaite durable.

Je remercie Ivan Lorgeré pour son amitié, sa disponibilité constante. Je garderai de lui le souvenir de son activité étourdissante. Merci aussi pour son invitation à un voyage sur l'océan. Oublierai-je jamais ce jour de tempête où j'ai pu apprécier son sang-froid de capitaine au long-cours? Je lui souhaite 'bon vent' pour la continuation de son activité de chercheur.

J'ai partagé ces trois ans de thèse avec François Grelet. Je veux ici lui faire part de ma gratitude pour m'avoir fait bénéficier de ses connaissances et de son travail en optique et sur les modulateurs spatiaux de lumière. Je lui dis 'merci et bonne chance' dans la voie qu'il a choisie où l'excitation des papilles gustatives revêt la plus haute importance.

Au cours de la première année de mon travail, la compétence de Margus Rätsep m'ont beaucoup aidé. Qu'il en soit ici remercié.

Merci aussi à Donatella Pavolini dont j'ai beaucoup apprécié la gentillesse.

Alain Richard et Michèle Hoffman ont toujours été disponibles pour m'aider à résoudre les petits et grands problèmes informatiques. Merci à tous les deux.

Je ne saurai oublier tous les collègues du Laboratoire, personnels techniques et administratifs qui ont toujours contribué efficacement à la solution des diverses tracasseries qui émaillent la vie d'une étudiante chinoise en France. Je les remercie des marques de sympathie qu'ils m'ont témoignées.

ABSTRACT

We propose a new spectral holography method for storing data in a persistent spectral hole burning (PSHB) material. In these materials, information is recorded as a spectral shape imprinted on the profile of an optical absorption band. In this way, a fourth dimension, the temporal frequency one, is added to the three dimension volume occupied by conventional spatial holograms. We propose, and experimentally demonstrate, an original approach for addressing data within the spectral domain. It relies on spectral interference over the storage window which spans a several THz interval. A broad bandwidth chaotic source delivers a light beam that is split into a reference and an object arms. Data to be stored are encoded as spatial modulation of the object beam. Each address is characterized by a frequency dependent phase factor that is conveyed by the reference beam and that is recorded in the memory medium together with the information to be stored. For reading out a specific address, one uses a probe pulse that is spectrally shaped by the corresponding phase factor. Although addressing takes place in the spectral domain, time-consuming procedures, such as frequency tuning of the light source or adjustment of the optical delay line, are avoided in data storage or retrieval operations. Therefore, high random access rates are expected. The dissertation is mainly devoted to a careful examination of the material contribution to crosstalk between addresses. In the past, the photochemical tautomerization mechanism that is involved in the hole burning process was mainly investigated with the help of narrow band sources. We extend its description to broadband excitation conditions. We develop a theoretical model that includes the photochemical process, the broadband pulse propagation and the spectral holographic storage. It enables us to disclose the dose condition for eliminating the material contribution to crosstalk. Experimental demonstration of the spectral phase encoded storage confirms our predictions.

KEY WORDS:

Spectral hole burning | Holography | Four-wave mixing
Optical storage | Tautomerization | Intercorrelation
Porphyrin

CONTENTS

INTRODUCTION 5

References 11

CHAPTER 1. SPECTRAL HOLE-BURNING AND TEMPORAL HOLOGRAPHY

1.1 Introduction 17

1.2 Persistent spectral hole-burning and spectrally selective materials 18

1.3 Holography 22

1.31 Spatial holography 22

1.32 Spectrally selective holography 26

1.33 Temporal holography 26

1.4 Binary data storage in spectrally selective materials 29

1.41 Frequency domain optical storage (FDOS) 29

1.42 Time domain optical storage (TDOS) 30

1.43 FDOS and TDOS limitations 32

1.5 Two hybrid approaches 35

1.51 Combining TDOS with FDOS 35

1.52 TDOS with a frequency chirped laser 35

1.6 Conclusion 38

1.7 References 39

CHAPTER 2. SPECTRAL-PHASE-ENCODING OF MEMORY ADDRESSES

2.1 Introduction 41

2.2 Principle of spectral-phase addressing 43

2.21 Addressing with a spectral code 43

2.22 Signal detection by field cross-correlation 46

2.23 Biphase encoding: storage capacity, access time and limitations 48

2.3 Experimental set-up 50

2.31 Laser source and the field-correlator 50

2.32 Spectral shaper 52
2.321 Two-grating device 52
2.322 Liquid crystal spatial light modulator (SLM) 54
2.323 Encoding functions 56
2.33 PSHB material : octaethylporphyrin in polystyrene (OEP/PS) 61
2.4 Experimental results 64
2.41 Test of the encoding and the detection systems 64
2.42 Data storage and retrieval 68
2.43 Discussion 71
2.5 Conclusion 74
2.6 References 75

CHAPTER 3. SPECTRAL HOLOGRAPHY: A PORTABLE MODEL

3.1 Introduction 79
3.2 Coupled-wave theory 81
3.3 Accumulated storage 84
3.4 Diffraction on the engraved grating 90
3.41 Index of refraction and absorption gratings 90
3.42 Signal amplitude 91
3.5 Discussion 93
3.51 Connection with the elementary description 93
3.52 Linear regime and beyond 93
3.53 Crosstalk between addresses 96
3.54 Phase-matching requirement 96
3.6 Conclusion 98
3.7. References 99

CHAPTER 4. PHOTOPHYSICS AND BROADBAND HOLOGRAPHY

4.1 Introduction 101
4.2 Phonon side band, burning efficiency 102
4.21 Absorption spectral structure and burning efficiency 102
4.22 Broad band engraving of a space-and-frequency grating 105
4.23 Diffraction spectrum 106
4.24 Experimental 107

4.25 Discussion 112
4.3 Tautomerization model in OEP doped polymer 114
4.4 Holographic recording and diffraction efficiency. 119
4.41 Writing beams 119
4.42 Formal expression of the diffraction efficiency 119
4.43 Computation of the diffraction efficiency. 120
4.44 Numerical results 122
4.5 Experimental 124
4.51 Experimental setup 124
4.52 Diffraction spectra 126
4.53 Calibration of the dose scale by hole burning 128
4.54 Diffraction efficiency as a function of the exposure dose 130
4.55 Radiative saturation 131
4.6 Conclusion 135
4.7 References 136

CHAPTER 5. PHASE ENCODED SPECTRAL HOLOGRAMS IN OEP

5.1 Introduction 139
5.2 Linear regime 140
5.3 Crosstalk and optimization of the storage conditions. 143
5.31 Data retrieval in the linear regime 143
5.32 Optimized exposure conditions. 144
5.33 Spectrum of the holographic signal in the linear regime 145
5.34 Phase-encoding experimental test 146
5.4 Conclusion 151

CONCLUSION 153

ARTICLES

1. Storage of a spectrally shaped hologram in a frequency selective material 159
2. Spectral phase encoding for data storage and addressing 165
3. Fast random access to frequency selective optical memories 171
4. Time-encoding spatial routing in a photorefractive crystal 175

5. Spectral holograms in the terahertz range..... 179
6. Four-wave hole burning spectroscopy with a broadband laser source..... 187

RESUME.....i

INTRODUCTION

Persistent spectral hole-burning (PSHB) and optical holography are the two cornerstones of the present work. This introduction gives an overview of their historical development.

The first 'spectral hole' was observed in 1948 by N. Bloembergen *et al.* as a dip created in a magnetic resonance absorption line of a solid [1]. The same year, D. Gabor proposed a new concept of imaging, 'holography', originated from electronic microscopic studies [2]. Both emerged at the same time in field areas far from optics, but quite soon, they were introduced, one after another, into the optical domain, and achieved great developments after the discovery of the laser.

In magnetic resonance, the inhomogeneity of the applied magnetic field is responsible for a spread-out of the resonance frequencies of the individual nuclear spins. Then the individual spins at a specific frequency can be selectively saturated under the excitation of a resonant radio-frequency field, creating a depopulation of their ground state and therefore, a dip at the specific frequency in the inhomogeneous distribution of the spin ensemble. With the discovery of the laser, this idea has been applied to the optical domain as so-called saturation spectroscopy of atoms in gas phase. In this case, the inhomogeneity responsible for the distribution of the resonance frequencies of atoms arises from the Doppler effect which assigns a specific frequency at each atom according to its velocity. Despite the prediction in the early 60's of a transient laser spectral hole burning phenomenon in solids [3], the first experimental observation was effected only in 1974 on the R lines of a ruby crystal at cryogenic temperatures by Szabo [4]. Almost at the same time, persistent spectral holes were discovered independently by two groups in dye-molecule-doped Shpol'skii [5] and glassy matrix [6] at liquid helium temperatures. In that case, the inhomogeneity is induced by the differences in local environments around the guest molecules. Since 1974, persistent spectral hole burning (PSHB) has been observed successively in a broad class of materials, including ion-, or molecule- doped inorganic crystals, polymers, glasses, and so on [7]. The permanent character of the changes on the absorption profile makes the experiment quite simple and of large applicability. A hole is burnt in

It can be probed with the same laser by scanning it with an attenuated intensity and monitoring the transmission or the fluorescence. A PSHB experiment eliminates the inhomogeneous broadening. A narrow hole is like a negative imprint of a spectral line and high resolution spectroscopy becomes feasible. PSHB is a powerful tool applied in photophysics, photochemistry and photobiology [8,9]. On the application aspect, its potential for ultra-high density optical data storage was quickly realized. Only one year after his first observation on ruby, Szabo proposed to use transient spectral holes for recording optical data in the frequency-dimension beyond the 3D space [10]. The idea was later extended to long-lived data storage with persistent spectral hole burning by Castro *et al.* in 1978 [11]. To utilize the storage potential in the frequency dimension, one has made ceaseless efforts for both optimizing optical configurations and researching suitable PSHB material systems [12-15]. Materials operating at 77K were developed in 1987 [16], which was followed by the discovery of room temperature PSHB materials in 1990 [17,18]. For raising burning efficiency and diminishing a simultaneous erasing effect, a photon-gated arrangement was proposed by Macfarlane *et al.* [19] and related material systems were developed by the works of several groups [20-26].

The idea of holography was originally proposed by Gabor as a way to increase resolution in electron microscopy. He suggested to record the scattered field when an object was illuminated with electrons and then to reconstruct the image of the object from this record with visible light. He also used light wave both to record and to recall the object image which was the primary form of optical holography. In early times, around 1950, the lack of highly coherent light and an inappropriate co-linear configuration maintained optical holography in its infancy. The advent of the laser stimulated investigations and several technical problems were rapidly solved. A dramatic improvement was achieved by Leith and Upatnieks who proposed the off-axis reference arrangement, which avoided image mixing problems[27-29]. The mixed image components were spatially separated with an off-axis reference beam technique, and the new-developed laser provided a powerful coherent light source. These works marked the birth of optical holography. At the time spanning from 1960's to 70's, the spatial imaging properties of monochromatic holograms were studied with a great variety of configurations. In 1969, a coupled-wave theory [30] was developed by Kogelnik and then used as a classical theory of holography in optically thick media. Holography has also been applied to interferometry [31] and three-dimension display.[32] In 1969, Benton created the rainbow hologram [33] which led to a commercially adopted

display technique, the white-light holographic stereography [34,35]. At the same time, new types of recording materials were discovered such as photorefractive materials which show a high capacity for optical image storage [36]. Since the 80's, specially in the 90's, the high parallelism and capacity of holographic storage in 3-dimension attracted attention. D. Psaltis *et al.* recorded 10 000 pages of 320x320 bits in $LiNbO_3$ with an error ratio of 1/100 000 [37]. Recent results on photorefractive crystals demonstrated a storage density 10 to 100 times higher than conventional optical disks. Furthermore, other kinds of materials are under study, for example, the photopolymer developed by the Du Pont Company showing a read-only storage density 2500 times higher than that of $LiNbO_3$.

A new concept of holography, 'temporal holography' in a resonant medium arose from a transient coherent phenomenon, the 'Photon Echo' (PE), predicted in 1963 [38] and first observed in 1964 [39]. It is a process in which a sequence of two or three coherent pulses acting on a phase memory medium generates a time-delayed coherent radiation, called the echo. Two-pulse or three-pulse PE (also called stimulated PE or SPE) have been widely used for optical spectroscopic studies as a transient spectral grating technique. PE as an example of temporal holography was proposed to be applied to optical memory in 1972 [40]. Temporal holography can be considered as a spectral analogue of spatial holography in that sense that an interference pattern in frequency domain is constructed by two temporally separated coherent pulses and probed by a third one. Recording a spectral grating requires long-lived spectral selective memory media which is just the advantage of PSHB materials.

A spatial holographic readout scheme was proposed to be applied to PSHB systems as a non-destructive detection method of the spectral hole[41]. Little attention was paid to it and it was not experimentally implemented. Spatial holography with tunable cw laser was first applied to PSHB material in 1985 by Wild *et al.* [42]. A strong resonant holographic signal was detected with good signal to noise ratio (SNR) and no background feature. In the latter aspect, holography differs from transmission or fluorescence detection methods. A series of works on the diffractive properties of spectrally selective holograms were published in 1989 and 1990, including comparison between holographic and transmission detection, study of the crosstalk between two spectrally adjacent holograms and the effects from the external electric fields, etc... [43]. At the same time, a new concept of molecular computer based on parallel data processing with spectrally selective holography was proposed [44]. In 1993, a frequency-

and-phase-sweeping technique was applied for increasing the diffraction efficiency and reducing the crosstalk between spectrally selective holograms. Combined with the electric field multiplexing, this approach resulted in the storage of 2000 holograms at one spatial spot in organic amorphous material and an animated film was replayed[45]. Recent result with the same method shows a storage of 6000 images at one spatial position [46]. In these works, image replaying was effectuated by scanning the laser frequency and varying the electric field with a high-voltage supply. Frequency scan over a several THz bandwidth strongly hampers fast data retrieval. In inorganic materials, the storage spectral area spreads over a much narrower interval since the inhomogeneous width usually does not exceed a few GHz. Therefore, high scan rates can be reached in these media. Real-time storage and retrieval of a movie was actually demonstrated by spectrally addressing spatial holograms in a rare earth ion doped crystal [47]. In this experiment, the laser rapidly explores the spectral addresses in a sequential way, as it is scanned over the absorption band. The separation between contiguous addresses does not exceed a few KHz. Thus random access to a specific address needs more time since the final value of the laser frequency has to be precisely controlled.

On the other hand, temporal holography was also applied to PSHB systems. Indeed, the long-lived stimulated photon echo process that underlies temporal holography can be observed in all PSHB materials. Recording a temporal hologram in the frequency dimension provided by PSHB was proposed by T.W. Mossberg in 1982 [48], and experimentally performed using photochemically accumulated photon echo with weak picosecond pulses in a porphyrin-derivative/polymer system by A. Rebane *et al.* in 1983 [49]. Since then, temporal holography for PSHB materials with either collinear or off-axis spatial configurations have been widely studied in both organic and inorganic materials for the applications to data (and image) storage [50-56], processing [57-60] with pulsed coherent laser sources, and short-pulse shaping on the time scale from nanosecond to femtosecond [61-63]. Temporal holography in PSHB systems was also performed with a convenient stochastic laser source [64]. The time-domain data are recorded in the form of their Fourier transform that is engraved in the absorption band of the material. To take full advantage of the storage capacity, one has to engrave and retrieve data at rates that range from 10^9 frames/second in inorganic materials to more than 10^{12} frames/second in organic materials. These rates by far exceed the capability of existing matrix cameras. Real-time detection is feasible on point detectors in the

case of inorganic PSHB memories. As for organic materials, one resorts to optical gating techniques that dramatically slow down access to data.

With the extensive studies in both spectrally selective holography and temporal holography, some modified [65,66] or hybrid [67] approaches have been experimented for optimizing storage density and data transfer rate. 1.6 Kbit-storage was demonstrated with combination of spectrally selective and temporal holography approaches in inorganic crystals in 1991 [67]. In 1992, the swept-carrier approach was proposed [68], with which a 8 Gbits/in^2 areal storage density and a 10Mbit/s transfer rate were achieved.[69-71]. However, these approaches intrinsically imply sequential data retrieval and are not well suited to random access.

In summary, disappointing values of the random access rate were obtained in the experimental demonstrations of optical storage in PSHB memories, especially in organic media. In order to reduce the access time in PSHB organic materials, we develop a modified TDOS approach. A spectrally phase-encoding TDOS method was first proposed in ref[72]. In this approach, the spectral channels of the material are utilized parallely and the data are addressed by the spectral phase codes conveyed by the reference and the probe beams. This idea is experimentally demonstrated in our work. A broadband laser is employed without frequency scanning. The data are retrieved individually at a fixed temporal position.

In chapter 1, the principles of PSHB and holography are presented, as also their application to frequency- and time-domain optical storage. Some essential properties of the storage with several existing approaches are discussed. The interest of achieving a fast random bit access is proposed.

Chapter 2 introduces the spectrally phase-encoding idea for data addressing. This approach is applied to multiple binary data storage on Terahertz spectral scale in a material, octaethylporphyrin-doped polystyrene, by the help of a subpicosecond pulse shaping system and a field cross-correlator. A random access time shorter than 0.1 millisecond can be achieved.

However, the experimental results are spoiled by crosstalk between different addresses, which is critical for storage capacity. Both the optical set up and the storage material may contribute to crosstalk. The optical aspect has been studied in the works of ref [73]. The understanding of the physical mechanism and the optical characters of the material forms the subject of the main part of this thesis.

Chapter 3 is devoted to the theoretical analysis of the storage procedure in an optically thick medium with a simple medium model. Some general features are disclosed.

Based on chapter 3, the spectral characters of the memory material used in our experiment are studied in chapter 4. First, the contributions of the electron-phonon coupling and the PSHB quantum yield to the holographic signal are studied by comparing the theory and the experiment under the small exposure condition. Then, a tautomeric model of light-induced molecular reaction is built to complete the theory in the large exposure regime and is verified by the experiment.

The model is used to analyze the spectrally phase addressed multiple-bit storage in chapter 5. An optimized recording condition is obtained under which the crosstalks can be eliminated. Experiment results consist with our predictions, and the storage quality is limited by the performance of the optical setup.

Finally, the presentation will be ended with a general conclusion.

References

[1] N. Bloembergen, E. M. Purcell, and R. V. Pound, *'Relaxation effects in nuclear magnetic resonance absorption'*, Phys. Rev., **73**, 679 (1948).

[2] D. Gabor, *'A new microscopic principle'*, Nature, **161**, 777 (1948).

[3] A. L. Schawlow, in Advanced in Quantum Electronics, (Proc. 2nd Int. Conf. on Quant. Electr.), J. R. Singer Ed., pp. 50 (Columbia Univ. New York, 1961).

[4] A. Szabo, *'Observation of hole burning and cross-relaxation effects in Ruby'*, Phys. Rev., **B11**, 4512 (1975).

[5] A. A. Gorokhovskii, R. K. Kaarli, and L. A. Rebane, *'Hole burning in the contour of a pure electronic line in a Shpol'skii system'*, JETP Lett., **20**, 216 (1974).

[6] B. M. Kharlamov, R. I. Personov, and L. A. Bykovskaya, *'Stable « gap » in absorption spectra of solid solutions of organic molecules by laser irradiation'*, Opt. Commun., **12**, 191 (1974).

[7] 'Persistent spectral hole burning : Science and applications', W. E. Moerner Ed., (Springer-Verlag, Berlin, Heidelberg, 1988).

[8] S. Völker, *'Hole-burning spectroscopy'*, Annu. Rev. Phys. Chem., **40**, 499 (1989).

[9] R. Jankowiak, J. M. Hayes, and G. J. Small, *'Spectral hole-burning spectroscopy in amorphous molecular solid and proteins'*, Chem. Rev., **93**, 1471 (1993).

[10] A. Szabo, *'Frequency selective optical memory'*, U.S. Patent 3,896,420 (1975).

[11] G. Castro, D. Haarer, R. M. Macfarlane, and H. P. Trommsdorff, *'Frequency selective optical data storage system'*, U.S. Patent, 4,101,976 (1978).

[12] W. E. Moerner and M. D. Levenson, *'Can single-photon processes provide useful materials for frequency-domain optical storage'*, J. Opt. Soc. Am., **B2**, 915 (1985).

[13] N. Murase, K. Horie, M. Terao, and M. Ojima, *'Theoretical study of the recording density limit of photochemical hole-burning memory'*, J. Opt. Soc. Am., **B9**, 998 (1992).

[14] S. Kröll and P. Tdlund, *'Recording density limit of photo-echo optical storage with high-speed writing and reading'*, Appl. Opt., **32**, 7233 (1993).

[15] W. R. babbitt and T. W. Mossberg, *'Quasi-two-dimension time-domain color memories: process limitations and potentials'*, J. Opt. Soc. Am., **B11**, 1948 (1994).

[16] C. Wei, S. Huang, and J. Yu, *'Two-photon hole burning and fluorescence-line-narrowing studies on $BaFCl_{0.5}Br_{0.5}:Sm^{2+}$ at 77K'*, J. Lumin., **43**, 161 (1989).

[17] M. Aizengendler, U. Bogner, I. Dolendo, J. Kikas, and J. Sildos, *'Photon-gated thermoresistant spectral hole-burning in a neutron-irradiated sapphire'*, Chem. Phys. Lett., **183**, 245 (1991).

[18] K. Holliday, C. Wei, M. Croci, and U. P. Wild, *'Spectral hole-burning measurements of optical dephasing between 2-300K in a Sm^{2+} doped substitutionally disordered microcrystals'*, J. Lumin., **53**, 227 (1992).

[19] A. Winnacker, R. M. Shelby, and R. M. Macfarlane, *'Photon-gated hole burning: a new mechanism using two-step photoionization'*, Opt. Lett., **10**, 350 (1985).

[20] H. W. H. Lee, M. Gehrtz, E. E. Marinero, and W. E. Moerner, *'Two-color, photon-gated spectral hole-burning in an organic material'*, Chem. Phys. Lett., **58**, 249 (1986).

[21] W. Lenth, and W. E. Moerner, *'Gated spectral hole-burning for frequency optical recording'*, Opt. Commun., **58**, 249 (1986).

[22] L. Zhang, J. Yu, and S. Huang, *'Fluorescence line narrowing and inhomogeneous broadening of Sm^{2+} in $BaCl_xBr_{1-x}$'*, J. Lumin., **45**, 301 (1990).

[23] M. Iannone, G. W. Scott, D. Brinza, and D. R. Coulter, *'Gated photochemical hole burning in photoadducts of polyacenes'*, J. Chem. Phys., **85**, 4863 (1986).

[24] S. Machida, K. Horie, and T. Yamashita, *'Photon-gated photochemical hole burning by two-color sensitization of a photorefractive polymer via triplet-triplet energy transfer'*, Appl. Phys. Lett., **60**, 286 (1992).

[25] W. P. Ambrose and W. E. Moerner, *'Temperature dependence of photon-gated persistent spectral hole-burning for the meso-tetra-p-tolyl-Zn-tetrabenzoporphyrin/chloroform system in poly(methylmethacrylate)'*, Chem. Phys., **144**, 71 (1990).

[26] B. Luo, M. Tian, W. Li, S. Huang, and J. Yu, *'New persistent photon-gated spectral hole burning systems: metal-tetrabenzoporphyrin derivatives/p-hydroxybenzaldehyde/PMMA'*, J. Lumin., **53**, 247 (1992).

[27] E. N. Leith and J. Upatnieks, *'Reconstructed wave fronts and communication theory'*, J. Opt. Soc. Am., **52**, 1123 (1962).

[28] E. N. Leith and J. Upatnieks, *'Wavefront reconstruction with continuous-tone object'*, J. Opt. Soc. Am., **53**, 1377 (1963).

[29] E. N. Leith and J. Upatnieks, *'Wavefront reconstruction with diffused illumination and three-dimension object'*, J. Opt. Soc. Am., **54**, 1295 (1964).

[30] H. Kogelnik, *'Coupled wave theory for thick hologram grating'*, Bell Syst. Tech. J., **48**, 2909 (1969).

[31] S. Amadesi, F. Grella, and G. Guattari, *'Holographic method for painting diagnostics'*, App. Phys., **13**, 2009 (1974).

[32] J.-M. Fournier, G. Tribillon, and J.-C. Viénot, *'Recording of large size holograms in photographic emulsion : image reconstruction'*, in Three-Dimension Imaging, Proc. of the SPIE, S. A. Benton Ed., **120**, 116 (1977).

[33] S. A. Benton, *'Hologram reconstruction with extended incoherent sources'*, J. Opt. Soc. Am., **59**, 1545 (1969).

[34] S. A. Benton, *'Holographic display-a review'*, Opt. Eng., **14**, 402 (1975).

[35] F. S. Chen, J. T. LaMachia, D. B. Frazer, *'Holographic storage in lithium niobate'*, Appl. Phys. Lett., **13**, 223 (1968).

[36] 'Holographic Recording Materials', H. M. Smith Ed., Topic in Applied Physics, (Springer-Verlag, Berlin, Heidelberg, New York, 1977).

[37] D. Psaltis and F. Mok, *'Holographic memories'*, Scientific American, Nov. 95.

[38] U. Kh. Kopvillem and V. R. Nagibarov, *Luminous echo of paramagnetic crystals'*, Fiz. Metallov. Metallovedenie (USSR), **15**, 313 (1963).

[39] N. A. Kurnit, I. D. Abella, and S. R. Hartmann, *'Observation of a photon-echo'*, Phys. Rev. Lett., **13**, 567 (1964).

[40] S. R. Hartmann, N. R. Kurnit, and I. D. Abella, US Patent, 44,459,682 (15.01.1972).

[41] D. Haarer, R. V. Pole, and S. Völker, *'Non-destructive readout scheme for holographic storage system'*, U.S. Patent 4,103,346 (25.07.1978).

[42] A. Renn, A. J. Meixner, U. P. Wild, and F. A. Burkhalter, *'Holographic detection of photochemical holes'*, Chem. Phys., **93**, 157 (1985).

[43] A. J. Meixner, A. Renn, and U. P. Wild, *'Spectral hole-burning and holography: I. transmission and holographic detection of spectral hole'*, J. Chem. Phys., **91**,

6728 (1989), *'Spectral hole-burning and holography: II. Diffraction properties of two spectrally adjacent holograms'*, J. Chem. Phys., **92**, 2748 (1990), *'Spectral hole-burning and holography: III. Electric field-induced interference of hologram'*, J. Chem. Phys., **93**, 2299 (1990).

[44] U. P. Wild, A. Renn, C. De Caro, and S. Bernet, *'Spectral hole burning and molecular computer'*, Appl. Opt., **29**, 4329 (1990).

[45] B. Kohler, S. Bernet, A. Renn, and U. P. Wild, *'Storage of 2000 holograms in a photochemical hole-burning system'*, Opt. Lett., **18**, 2144 (1993).

[46] E. S. Maniloff, S. B. Altner, F. R. Graf, A. Renn, and U. P. Wild, *'Recording of 6000 holograms by use of spectral hole burning'*, Appl. Opt., **34**, 4140 (1995).

[47] M. Mitsunaga, N. Uesugi, H. Sasaki, and K. Karaki, *'Holographic motion picture by Eu^{3+} : Y_2SiO_5'*, Opt. Lett., **19**, 752 (1994).

[48] T. W. Mossberg, *'Time-domain frequency-selective optical data storage'*, Opt. Lett., **7**, 77 (1982).

[49] A. Rebane, R. Kaarli, P. Saari, A. Anijalg, and K. Timpmann, *'Photochemical time-domain holography of weak picosecond pulses'*, Opt. Commun., **47**, 173 (1983).

[50] P. Saari, R. Kaarli, and A. Rebane, *'Picosecond time- and space- domain holography by chemical hole burning'*, J. Opt. Soc. Am., **B3**, 527 (1986).

[51] S. Saikan, T. Kishida, A. Imaoka, K. Uchikawa, A. Furusawa, and H. Oosawa, *'Optical memory based on heterodyne-detected accumulated photon echoes'*, Opt. Lett., **14**, 841 (1989).

[52] A. Rebane and O. Ollokainen, *'Picosecond time-space holographic interferograms stored by persistent spectral hole burning'*, Opt. Commun., **78**, 327 (1990).

[53] M. Mitsunaga and N. Uesugi, *'248-Bit optical data storage in Eu^{3+} : $YAlO_3$ by accumulated photon echoes'*, Opt. Lett., **15**, 195 (1990).

[54] A. Rebane, S. bernet, A. Renn, and U. P. Wild, *'Holography in frequency selective media: hologram phase and causality'*, Opt. Commun., **86**, 7 (1991).

[55] K. Holliday, M. Croci, E. Vauthey, and U. P. Wild, *'Spectral hole burning and holography in an Y_2SiO_5 : Pr^{3+} crystal'*, Phys. Rev., **B47**, 14741 (1993).

[56] A. Rebane and O. Ollokainen, *'Error-corrective optical recall of digital images by photoburning of persistent spectral holes'*, Opt. Commun., **83**, 246 (1991).

[57] P. Saari, R. Kaarli, and M. Rätsep, *'Temporally multiplexed Fourier holography and pattern recognition of femtosecond-duration image'*, J. Lumin., **56**, 175 (1993).

[58] D. Eric, A. Rebane, and U. P. Wild, *'Spectrally controlled interference of picosecond time- and space-domain holograms'*, Opt. Lett., **20**, 1065 (1995).

[59] R. Kaarli, R. Sarapuu, H. Sonajalg, and P. Saari, *'Interference of accumulated stimulated photon echo and storage of temporal segments in time-and space-domain holography'*, Opt. commun., **86**, 211 (1991).

[60] A. Rebane, J. Aaviksoo, and J. Kuhl, *'Storage and time reversal of femtosecond light signals via persistent spectral hole burning holography'*, Appl. Phys. Lett., **54**, 93 (1989).

[61] M. Mitsunaga, R. Yani, and N. Uesugi, *'Spectrally programmed stimulated photon echo'*, Opt. Lett., **16**, 264 (1991).

[62] H. Schwoerer, D. Eric, and A. Rebane, *'Holography in frequency-selective media: III. Spectral synthesis of arbitrary time-domain pulse shapes'*, J. Opt. Soc. Am., **B12**, 1083 (1995).

[63] H. Schwoerer, D. Eric, A. Rebane, and U. P. Wild, *'Subpicosecond pulse shaping via spectral hole-burning'*, Opt. Commun., **107**,123 (1994).

[64] A. Débarre, J.-C. Keller, J.-L. Le Gouët, P. Tchénio, and J.-P. Galaup, *'Optical information storage in condensed matter with stochastic excitation'*, J. Opt. Soc.Am., **B8**, 2529 (1991).

[65] S. Kröll, L. E. Jusinski, and R. Kachru, *'Frequency-chirped copropagating multiple-bit stimulated echo and retrieval in Pr^{2+} : $YAlO_3$'*, Opt.. Lett., **16**, 517 (1991).

[66] S. B. Altner, S. Bernet, A. Renn, E. S. Maniloff, F.R. Graf, and U. P. Wild, *'Spectral holeburning and holography: VI. Photon echoes from cw spectrally programmed holograms in a Pr^{3+} : Y_2SiO_5 crystal'*, Opt. Commun., **120**, 103 (1995).

[67] M. Mitsunaga, R. Yano, and N. Uesugi, *'Time- and frequency-domain hybrid optical memory: 1.6-Kbit data storage in Eu^{3+} : Y_2SiO_5'*, Opt. Lett., **16**, 1890 (1991).

[68] T. W. Mossberg, *'Swept-carrier time-domain optical memory'*, Opt. Lett., **17**, 535 (1992).

[69] H. Lin, T, Wang, G. A. Wilson, and T. W. Mossberg, *'Experimental demonstration of swept-carrier time-domain optical memory'*, Opt. Lett., **20**, 91 (1995).

[70] T. Wang, H. Lin, and T. W. Mossberg, *'Optical bit-rate conversion and bit-stream time reversal by the use of swept-carrier frequency-selective optical data storage techniques'*, Opt. Lett., **20**, 2033 (1995).

[71] H. Lin, T. Wang, and T. W. Mossberg, *'Demonstration of 8 Gbit/in^2 areal storage density based on swept-carrier frequency-selective optical memory'*, Opt. Lett., **20**, 1658 (1995).

[72] H. Sonajalg, A. Débarre, J.-L. Legouët, I. Lorgeré, and P. Tchénio, *'Phase encoding technique in time-domain holography: theoretical estimation'*, J. Opt. Soc. Am., **B12**, 1448 (1995).

[73] F. Grelet, PhD dissertation, (in French)' *Holographie spectro/temporelle: adressage par codage de phase'*, Université Paris XI Orsay, France (July,1997).

CHAPTER 1

SPECTRAL HOLE-BURNING AND TEMPORAL HOLOGRAPHY

1.1 Introduction

This chapter is devoted to the introduction of holographic storage in spectrally selective materials. We give the basic concepts of spectral hole burning, and of optical storage in frequency dimension in section 1.2. Conventional spatial holography in frequency selective materials and its extension to the temporal frequency domain are presented in section 1.3. The application of these techniques to the addressing of binary data in a frequency selective memory is then discussed in section 1.4. With spatial holography storage, each data is located at a specific position in frequency domain. Conversely, data to be saved as spectral holograms are encoded as short light pulses and their address is represented by their time delay with respect to the reference. These two approaches can be considered as extreme opposite forms of holographic storage. Intermediate methods are described in section 1.5. The characteristic parameters, such as the storage capacity, the data transfer rate, the diffraction efficiency and the random access rate, as well as the technical requirements are compared for the different schemes. Finally, the conclusion in section 1.6 is focused on the fast random access issue.

1.2 Persistent spectral hole-burning and spectrally selective materials

In some solid state materials, where absorbing centers are embedded in a matrix, monochromatic irradiation within an absorption band results in a transmission increase at the excitation frequency, as if a spectral hole were burnt inside the absorption profile. The notions of homogeneous and inhomogeneous width are essential to understand the basics of this hole burning mechanism.

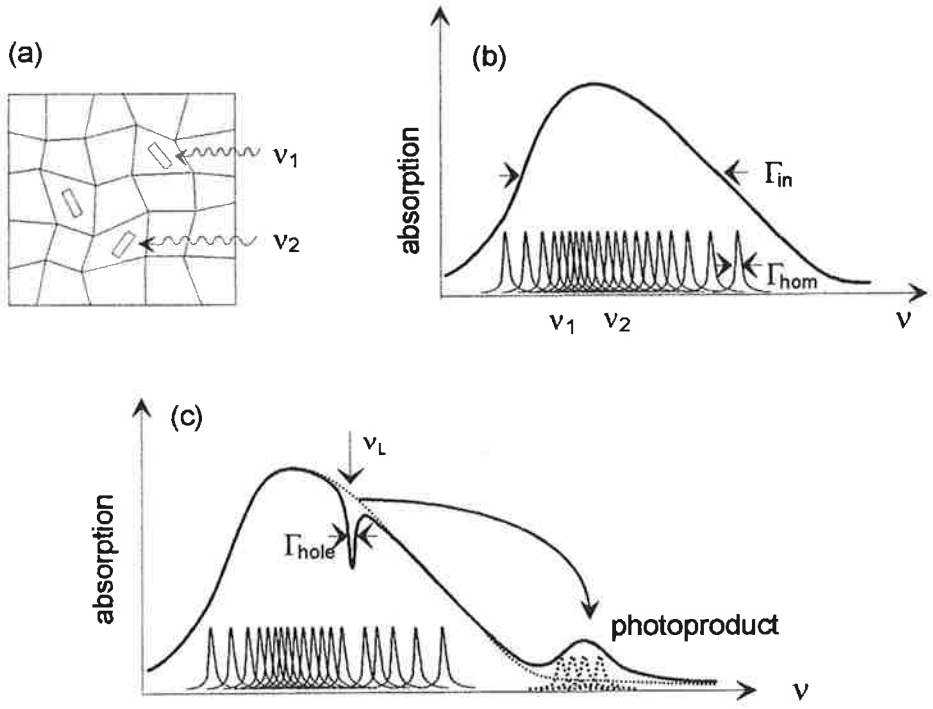

Figure 1.1 *(a), (b) Inhomogeneous broadening. (c) spectral hole burning.*

Let us consider a set of identical absorbers dispersed in a perfect crystal. In this ideal situation, all of them are in sites with identical local environments, and consequently, have the same absorption spectrum with the same resonance frequency and line width. The absorption profile of the ensemble is the same as that of any individual absorbing center. The resulting spectral profile is called a **homogeneous**

line because every absorbing center contributes to it in the same way and cannot be distinguished from each other. Its width Γ_{hom}, called the **homogeneous width**, is determined by the coherence lifetime of the corresponding transition. Actually, a real crystal can not be considered as a perfect lattice structure due to defects such as local strains, impurities, etc... Therefore different absorbers undergo different frequency shifts depending on their local environments. The resulting absorption profile is then inhomogeneously broadened due to the spread-out of the individual resonance frequencies. This **inhomogeneous profile** is what one usually observes by conventional absorption spectroscopy. The **inhomogeneous width**, Γ_{in}, can be much larger than Γ_{hom}. The spectral widths are defined as the full width at half maximum (FWHM), if no other indications are given.

When a laser of line width Γ_L, smaller than Γ_{hom}, illuminates the absorbing system, the specific subset of absorbing centers resonant with the laser line is pumped to the excited state. Consequently, an absorption decrease corresponding to this absorbing subset appears in the absorption profile. It can be detected as long as the excited absorbers have not returned to their initial state. This detection can be done by absorption, fluorescence, or excitation spectra and it can be shown that the measured **hole width** is $\Gamma_{hole} \geq 2\Gamma_{hom}$. The burnt hole survives if selectively excited photoactive centers do not come back to their initial state but reach a long-lived state with a resonance frequency different from that of the laser excited transition. If the long-lived state is only a metastable state (for instance, a triplet state in molecules, an hyperfine sub-level in a rare-earth ion, etc...), we observe only a transient spectral hole. If the final state is a stable one resulting from some photochemical changes of the excited absorbers, then the burnt hole can last infinitely. The association of saturation spectroscopy with photochemistry is known as photochemical hole-burning. Both transient and photochemical hole-burning are powerful tools for the study of doped solids because the lifetime of the hole is no more connected with the lifetime of the initially excited state and can last for microseconds to years. Nowadays this technique is called **'persistent spectral hole burning' (PSHB)**. The interest of 'spectral hole burning' lies in the range, $\Gamma_{in} >> \Gamma_{hom}$, as shown in figure 1.1, which usually occurs at low temperature.

PSHB can occur in many kinds of impurity-doped solid systems. The absorbing centers may be ions, molecules or color centers. The matrix may be crystalline (such

as pure and mixed crystals), or amorphous (such as glasses, polymers, gels). The mechanisms for PSHB are usually classified into photophysical type involving photoinduced local rearrangements of the environment around the guest or guest reorientation, and into photochemical type, such as proton tautomerization for porphyrin and phthalocyanine-derivatives in a variety of matrices, donor-acceptor electron-transfer for organic molecular systems, photoionization and electron trapping for color centers, rare-earth and transition ions, hydrogen bond rearrangement, etc.[1]

At low temperature, for an electronic transition, Γ_{hom} ranges from subkilohertz to hundreds of megahertz. The decay rate Γ_{hom} is expressed as a function of the energy relaxation time T_1 and phase relaxation time T^*_2, by the following equation[3]:

$$\Gamma_{hom} = \frac{1}{\pi T_2} = \frac{1}{2\pi T_1} + \frac{1}{\pi T^*_2}$$

where T_1 is the excited state lifetime. It includes both radiative and non-radiative decays. T^*_2 is related to all the pure dephasing processes which destroy the phase of the initially created coherent state. The homogeneous line is governed by the excited state coherent time T_2 and it is extremely sensitive to microscopic changes, interactions and weak perturbations. By the mean of spectral hole burning, one can extract a narrow homogeneous spectral feature buried in a broad inhomogeneous spectrum and then obtain structural and dynamic information on the system. This underlines the importance of this technique for high resolution spectroscopy of large molecules embedded in amorphous solids[2-4].

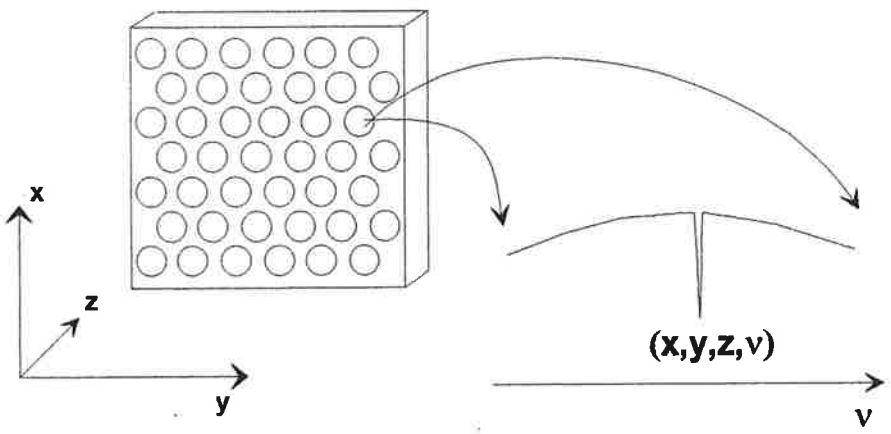

Figure 1.2 Four-dimension optical storage.

Besides its significance for fundamental studies, PSHB opens a way for a new generation of devices for optical storage and processing with high access data rate and capacity. The basic idea is to add the fourth dimension, frequency, to the three usual spatial dimensions. On a broad inhomogeneous band, a binary datum can be stored by burning a hole at one frequency. The existence or absence of a hole represents a bit '1' or '0', respectively. The spectral position of the hole can be regarded as the data coordinate in frequency dimension, i.e. a datum now is addressed by (x,y,z,ν) corresponding to three spatial coordinates (x,y,z) and one frequency coordinate (ν) as shown in figure 1.2. Since each bit occupies a Γ_{hom}-wide spectrum, the upper limit of the additional storage capacity in frequency dimension can be roughly estimated by the ratio $R=\Gamma_{in}/\Gamma_{hom}$ that can reach 10^4 to 10^9 at liquid helium temperature depending on the system. Based on this idea of **spectrally selective storage**, PSHB materials serve the functions of a new class of optical storage media, **spectrally selective materials**.

Two classes of PSHB materials, rare-earth-ion-doped crystalline hosts and dye-molecule-doped polymers have been widely studied for the aim of optical storage and processing according to different requirements on spectral band width and bit transfer rate.

A variety of recording and retrieval methods have also been proposed which may be listed into a classic or a holographic catalogue. In the classic way, a narrow laser line from a tunable monochromatic source is positioned in the 4-dimension volume, and the data are recorded spot by spot as shown in figure 1.2, then retrieved in the same way by detecting the transmission, excitation or fluorescence spectrum. In this fashion, high storage capacity may be achieved, but the recording and retrieving rates are intrinsically limited by spatial and spectral laser positioning. On the other hand, holography is an attractive and rapidly developing part in PSHB applications. Its advantages lie in its spatial and spectral parallelism and high signal-to-background ratio.

In the next paragraphs we introduce the basic concepts of spatial and spectro-temporal holography which are the key techniques used throughout this work.

1.3 Holography

Holography is a well-known method of 3-dimension imaging. Generally, for a given object illuminated by an electromagnetic field, the information on its geometrical structure is carried by the wavefront of the illumination field after being reflected or scattered by it. To reconstruct the image of an object means to recover the form of the wavefront determined by the space- and time- dependent amplitude and relative phase of the field. A photograph records a 3D object by only memorizing the light intensity of the carrier field. Because the information on the phase is lost, the object can be merely recovered as a 2D image. To reconstruct a faithful 'stereoscopic' image of the object, the information on both the amplitude and the phase of the carrier field should be recorded and recovered. Up to now, holography is the unique method to achieve this goal, which utilizes the light coherence. A light beam scattered by the object is called **object beam**. All the information on amplitude and relative phase of the object field is collected in the form of interference fringes with the help of a **reference beam** coherent with the object beam. The interference pattern may be recorded in a memory medium through light induced modifications of some optical properties, such as absorptive or refractive properties. The recorded interference pattern is called a **hologram**. When an appropriate field, the **probe beam** (usually identical to the reference), irradiates the hologram, the diffracted field retrieves the entire information on amplitude and relative phase of the object field so as to reconstruct it. A hologram is usually formed and recorded in spatial dimension, on a 2D photographic plate or in a thick 3D medium. This is the conventional spatial holography that is presented in more details in sections 1.31 and 1.32. One can extend the concept of holography to the temporal frequency domain, as explained in section 1.33, by taking advantage of the coherence properties of the carrier field in the time-domain, and of the spectral selectivity of PSHB materials.

1.31 Spatial holography

To understand the spatial structure of a hologram, we consider a simple case with a plane-wave carrier field. Two beams are split from a monochromatic laser source, one is used as the reference beam, and the other as the object beam after

being scattered by an object. The two beams, the object and the memory medium are configured as in figure 1.3 (a). We write the scalar expression of the field as :

$$E_j(\vec{r},t) = \mathcal{E}_j R_j(\vec{r}) e^{i2\pi\nu_0 t - i\vec{k}_j\cdot\vec{r}}, \quad j= 1,2 \text{ and } 3 \qquad (1.1)$$

where subscript j denotes, respectively, reference, object and probe beams, ν_0, is the common frequency of the fields, and $\vec{k}_j$ the corresponding wave vector. The exponential term takes into account the time- and space- phase of the field. $\mathcal{E}_j$ and $R_j(\vec{r})$ represent the field amplitude and the spatial structure, respectively. For the reference and the probe beam, $R_j(\vec{r})=1$, (j=1,3).

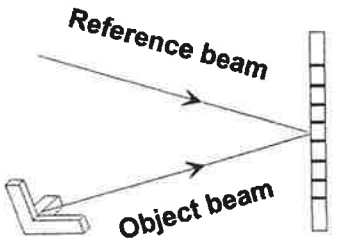

Spatial hologram

(a) Spatial hologram recording

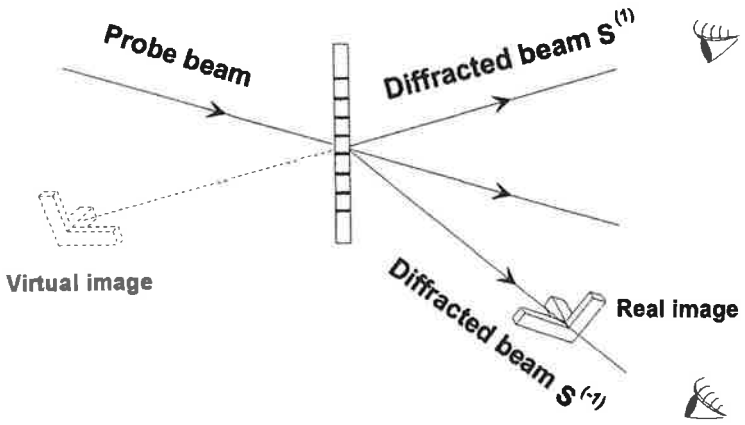

(b) Image reconstruction

Figure 1.3 Spatial holography.

For recording, the memory element is illuminated by the reference and the object beam simultaneously. In an optically thin medium, the local field in the material is the sum of the two incident fields as,

$$E(\vec{r},t) = E_1(\vec{r},t) + E_2(\vec{r},t) \tag{1.2}$$

In a photosensitive material, the interference pattern of the two fields is recorded as a modification of the absorption coefficient and the refractive index. This recording is known as a spatial hologram.

The stored information is retrieved with the help of a probe beam that is directed to the medium along $\vec{k}_1$. The field propagation can be described by a complex absorption coefficient α, the real and imaginary parts of which are linked together by the dispersion relations. This field, which includes the probe and the diffracted modes, is denoted as.

$$S(\vec{r},t) = \tilde{S}(\vec{r},\nu)\, e^{2i\pi\nu t - i\vec{k}_1\bullet\vec{r}} \tag{1.3}$$

The probe field propagation along z-axis is described by the following set of equations:

$$\frac{\partial\tilde{S}(\vec{r},\nu)}{\partial z} = -\frac{\alpha}{2}\tilde{S}(\vec{r},\nu) \tag{1.4}$$

$$\alpha(\nu) = \alpha_r(\nu) + i\alpha_{im}(\nu) \tag{1.5}$$

$$\alpha_{im}(\nu) = \frac{1}{\pi}\int \frac{\alpha_r(\nu')}{\nu'-\nu}\,d\nu' \tag{1.6}$$

Let us restrict the discussion to absorption holograms, which are obtained when the laser is tuned to an absorption band of the recording material. In addition, we only consider the small exposure and small optical density limits.

When illuminated by the combined monochromatic object and reference beams, the absorption coefficient undergoes a variation, $\Delta\alpha_r$, that is proportional to the interference pattern energy distribution:

$$\Delta\alpha_r(\vec{r},\nu) = -\beta\alpha_0\left(\left|\tilde{\mathcal{E}}_1\right|^2 + \left|\tilde{\mathcal{E}}_2 R(\vec{r})\right|^2 + \tilde{\mathcal{E}}_1^{*}\tilde{\mathcal{E}}_2 R(\vec{r}) e^{-i(\vec{k}_2-\vec{k}_1)\bullet\vec{r}} + cc\right) \tag{1.7}$$

Where β, α_0 denote the excitation factor and the initial absorption coefficient, respectively. In this expression, the object spatial distribution $R(\vec{r})$ contributes as the envelope of the interference grating factor $e^{-i(\vec{k}_2-\vec{k}_1)\bullet\vec{r}}$, the spacing of which is denoted as $\Lambda = 2\pi/\left|\vec{k}_2 - \vec{k}_1\right|$.

We assume that the absorption coefficient is a symmetric function of ν around the laser frequency ν_0. Then the Cauchy principal value in equation (1.6) cancels at $\nu=\nu_0$ and the propagation equation reduces to,

$$\frac{\partial \tilde{\mathcal{E}}(\vec{r},\nu_0)}{\partial z} = -\frac{\alpha_0 + \Delta\alpha_r}{2}\tilde{\mathcal{E}}(\vec{r},\nu_0) \qquad (1.8)$$

The modified absorption coefficient reacts on the probe field to generate diffracted emissions in direction $\vec{k}_2$ and $2\vec{k}_1-\vec{k}_2$. The corresponding signal fields after a L-thick sample are, respectively, given by:

$$S^{(1)}(\vec{r},t) = \tfrac{1}{2}\beta\alpha_0 L\tilde{\mathcal{E}}_1^{*}\tilde{\mathcal{E}}_3\tilde{\mathcal{E}}_2 R(\vec{r})e^{2i\pi\nu t - i\vec{k}_2\cdot\vec{r}}$$

$$S^{(-1)}(\vec{r},t) = \tfrac{1}{2}\beta\alpha_0 L\tilde{\mathcal{E}}_1\tilde{\mathcal{E}}_3\tilde{\mathcal{E}}_2^{*}R^{*}(\vec{r})e^{2i\pi\nu t - i(2\vec{k}_1-\vec{k}_2)\cdot\vec{r}} \qquad (1.9)$$

The diffraction efficiency thus includes the two following contributions:

$$\eta^{(1)} = \left|\frac{S^{(1)}(\vec{r},t)}{\tilde{\mathcal{E}}_3}\right|^2 = 1/4[\beta\alpha_0 L\tilde{\mathcal{E}}_1^{*}\tilde{\mathcal{E}}_2 R(\vec{r})]^2 \qquad (1.10)$$

$$\eta^{(-1)} = \left|\frac{S^{(-1)}(\vec{r},t)}{\tilde{\mathcal{E}}_3}\right|^2 = \eta^{(1)} \qquad (1.11)$$

$S^{(1)}(t,\vec{r})$ has the same spatial structure and relative phase factor as the object beam, it can be seen as a faithful copy of the field scattered by the object. $S^{(-1)}(t,\vec{r})$ gives a conjugated field. With the non-collinear scheme shown in figure 1.3, the different components of the output field are spatially separated and can be detected separately. Spatial holography can be applied to optical storage, data and image processing, phase conjugation and so on. Taking data storage as an example, the holographic method allows the storage with spatial parallelism since one 'page' of data can be recorded simultaneously as an hologram. In the volume of a medium, the information can be stored and retrieved 'page' by 'page' in 3D space. Bragg selectivity gives access to the third dimension. In an angle-multiplexed memory, the address of each stored hologram is defined by the value of the reference beam angle of incidence and a datum on the page has an address defined by a pair of x-y coordinates.

1.32 *Spectrally selective holography*

In a PSHB material, optical frequency plays the part of a fourth dimension that is added to the storage volume. At low temperature laser excitation of the chromophores on their homogeneous line gives rise to a Lorentz-shape modification of the absorption coefficient that reads as:

$$\Delta\alpha_r(\vec{r}, \nu) = -\beta\alpha_0 \frac{\Gamma_{hom}^2}{(\nu - \nu_0)^2 + \Gamma_{hom}^2} \left|\tilde{E}(\vec{r}, \nu_0)\right|^2 \qquad (1.12)$$

where ν_0 stands for the frequency of the burning laser and ν for that of the probe beam. According to the dispersion relations, the corresponding modification of the complex absorption coefficient reads as,

$$\Delta\alpha(\vec{r}, \nu) = -\beta\alpha_0 \frac{i\Gamma_{hom}}{(\nu - \nu_0) + i\Gamma_{hom}} \left|\tilde{E}(\vec{r}, \nu_0)\right|^2 \qquad (1.13)$$

Engraving of a spatial hologram at frequency ν_0 , in the configuration depicted by Fig. 1.3, gives rise to the following diffraction efficiency coefficients in directions $\vec{k}_2$ and $2\vec{k}_1 - \vec{k}_2$:

$$\eta^{(\pm)}(\nu) = 1/4 \frac{\Gamma_{hom}^2}{(\nu - \nu_0)^2 + \Gamma_{hom}^2} [\beta\alpha_0 L \tilde{\mathcal{E}}_1^* \tilde{\mathcal{E}}_2 R(\vec{r})]^2 \qquad (1.14)$$

Diffraction efficiency reaches its maximum value at the burning wavelength. It vanishes at a spectral distance much larger than the homogeneous width Γ_{hom}. Therefore, the spatial hologram is located at the well specified position ν_0 within the absorption band.

1.33 *Temporal holography*

A hologram can be formed not only in the spatial dimensions but also in the frequency dimension. Two monochromatic beams may construct a spatial interference pattern with a grating spacing determined by the wave vector difference. Similarly, in frequency-dimension, a spectral interference pattern can be formed by two temporally separated coherent pulses. Let us consider that pulses are substituted to the continuous wave fields that we considered so far. The reference and the probe pulses are represented by the following fields:

$$E_j(t,\vec{r}) = \mathcal{E}_j(t-t_j)e^{2i\pi\nu_0(t-t_j)-i\vec{k}_j\cdot\vec{r}} \quad , j= 1 \text{ and } 3 \qquad (1.15)$$

where ν_0 stands for the central frequency of the pulses which reach the sample at time t_j. The object pulse, that carries the information to be stored as a hologram, is conveniently described as:

$$E_2(t,\vec{r}) = [\mathcal{E}_2(t-t_2)\otimes R(\vec{r},t-t_2)]e^{2i\pi\nu_0(t-t_2)-i\vec{k}_2\cdot\vec{r}} \qquad (1.16)$$

Then the space dependent modification of the absorption coefficient reads as:

$$\Delta\alpha_r(\vec{r},\nu) = -\beta\alpha_0\{\tilde{\mathcal{E}}_1^{\,*}(\nu)\tilde{\mathcal{E}}_2(\nu)\tilde{R}(\vec{r},\nu)]e^{-2i\pi\nu(t_2-t_1)-i(\vec{k}_2-\vec{k}_1)\bullet\vec{r}} + cc\} \qquad (1.17)$$

where $\tilde{\mathcal{E}}_j(\nu) = \int \mathcal{E}_j(t)e^{-2i\pi\nu t}dt$.

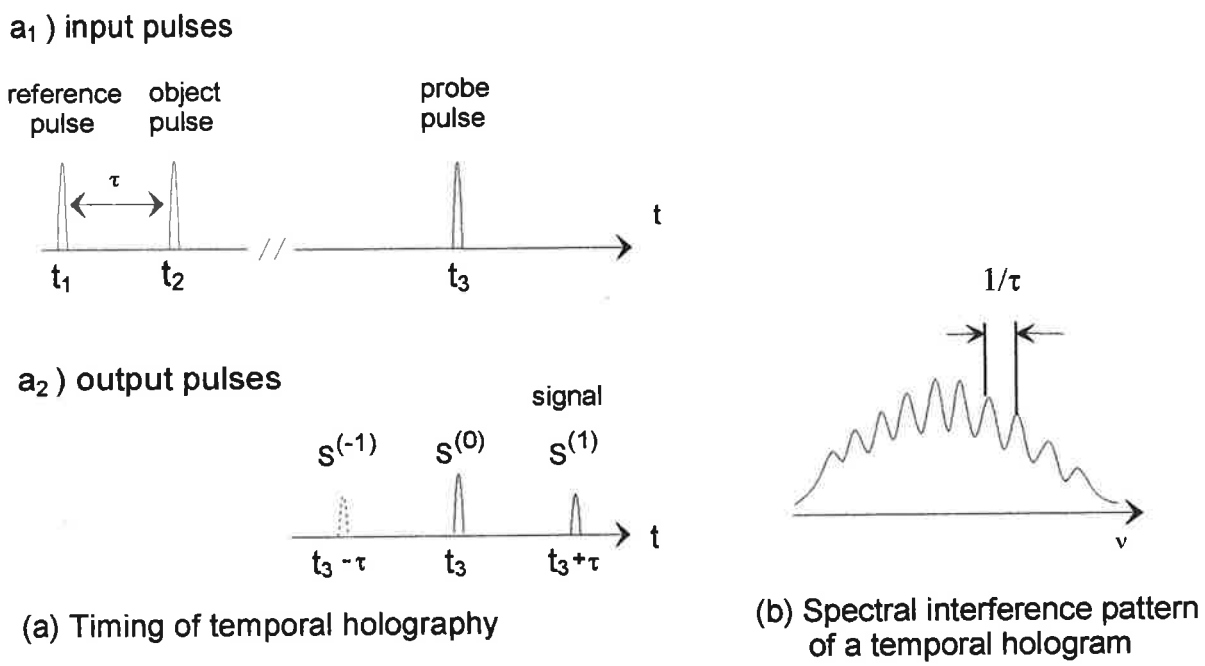

(a) Timing of temporal holography

(b) Spectral interference pattern of a temporal hologram

Figure 1.4 Temporal holography.

It appears that the engraved spatial grating is now combined with a frequency grating, the spacing of which equals $1/(t_2-t_1)$. This frequency structure can be stored as a hologram provided its period exceeds the spectral resolution of the material, which is given by Γ_{hom}. We assume that the spectral width of the pulses, Δ, is much larger than

the modulation period $1/(t_2-t_1)$. In the time-domain this corresponds to an assumption of non-overlapping pulses. This fast modulation imprinted on a slowly varying background results in a simple expression of the modification of the imaginary absorption coefficient for $t_2>t_1$ as,

$$\Delta\alpha_{im}(\nu)=i\beta\alpha_0\{\tilde{\mathcal{E}}_1^*(\nu)\tilde{\mathcal{E}}_2(\nu)\tilde{R}(\vec{r},\nu)e^{-2i\pi\nu(t_2-t_1)-i(\vec{k}_2-\vec{k}_1)\cdot\vec{r}}\text{-cc}\} \qquad (1.18)$$

Combining this expression with the real part of $\Delta\alpha$ given by Eq. (1.17), one obtains:

$$\Delta\alpha=-2\beta\alpha_0\tilde{\mathcal{E}}_1^*(\nu)\tilde{\mathcal{E}}_2(\nu)\tilde{R}(\vec{r},\nu)e^{-2i\pi\nu(t_2-t_1)-i(\vec{k}_2-\vec{k}_1)\cdot\vec{r}} \qquad (1.19)$$

It appears that the $e^{i(\vec{k}_2-\vec{k}_1)\bullet\vec{r}}$ term vanishes, while the $e^{-i(\vec{k}_2-\vec{k}_1)\bullet\vec{r}}$ term is doubled. When a probe pulse $E_3(t,\vec{r})$ is directed to the grating along $\vec{k}_1$, no signal is diffracted in direction $2\vec{k}_1-\vec{k}_2$, while that in direction $\vec{k}_2$ reads as:

$$\tilde{S}^{(1)}(\vec{r},\nu)=\beta\alpha_0L\tilde{\mathcal{E}}_1^*(\nu)\tilde{\mathcal{E}}_2(\nu)\tilde{\mathcal{E}}_3(\nu)\tilde{R}(\vec{r},\nu)e^{-2i\pi\nu(t_2-t_1+t_3)-i\vec{k}_2\cdot\vec{r}} \qquad (1.20)$$

Let us assume that the spectral amplitudes of the pulses can be regarded as constant over the spectral width of the object $\tilde{R}(\vec{r},\nu)$. Then the temporal amplitude of the signal can be expressed as:

$$S^{(1)}(\vec{r},t)=\beta\alpha_0L\tilde{\mathcal{E}}_1^*(\nu_0)\tilde{\mathcal{E}}_2(\nu_0)\tilde{\mathcal{E}}_3(\nu_0)R(\vec{r},t-t_3-(t_2-t_1))e^{2i\pi\nu_0t-i\vec{k}_2\cdot\vec{r}} \qquad (1.21)$$

The recorded spatial and temporal object $R(\vec{r},t-t_2)$ is replayed by the memory. Its delay t_2-t_1 with respect to the probe pulse coincides with that of the object pulse with respect to the reference. The timing diagram of storage and retrieval is depicted in Fig 1.4(a). The spectral profile of the holographic engraving is sketched on Fig. 1.4(b). The diffraction efficiency, which reads as:

$$\eta(\nu)=[\beta\alpha_0L\tilde{\mathcal{E}}_1^*(\nu)\tilde{\mathcal{E}}_2(\nu)\tilde{R}(\vec{r},\nu)]^2 \qquad (1.22)$$

is four times larger than on a frequency selective spatial hologram (see Eq. (1.14)).

1.4 Binary data storage in spectrally selective materials

Frequency-selective holograms as well as spectral holograms in PSHB materials can be applied to optical binary data storage. Based on frequency selective and temporal holographic methods respectively, two basic storage schemes, **frequency-domain optical storage (FDOS)** and **time-domain optical storage (TDOS)**, were proposed. Some combined approaches were also developed. Depending on the storage scheme, data are addressed in different ways. For sake of simplicity, we restrict the discussion to data without spatial structure. A binary '1' is represented by a plane wave object beam (or pulse). It is stored in the medium as a hologram and retrieved as a diffraction signal. The absence of object corresponds to a binary '0'. In addition to the available capacity, two parameters are commonly used to characterize a memory. The random access time represents the time required to recover a specific data located at a given address. The bit rate, ν_d, denotes the rate at which contiguous data can be transferred to or from the memory. The parameters values depend on the addressing method.

1.41 Frequency domain optical storage (FDOS)

In frequency domain optical storage, one bit is stored as a spatial hologram with the help of a tunable monochromatic laser. When the laser spectral width is narrower than Γ_{hom}, the diffraction efficiency is a Lorentz function of the probe frequency, around the recording wavelength with a spectral width ~ Γ_{hom}. Therefore the storage frequency is nothing but the spectral address where the recorded data can be retrieved selectively. Many bits can be addressed at different burning frequencies within the absorption band. The tunable laser has to be scanned over a Γ_{in} range with a Γ_{hom} precision.

Since a PSHB spectrally selective material offers approximately $R=\Gamma_{in}/\Gamma_{hom}$ independent spectral channels on the absorption band, the capacity in spectral dimension is estimated to be R, when the data are stored as spectral holes and are

retrieved by the help of transmission or fluorescence spectra. The maximum capacity in FDOS can be also characterized by R.

However, the situation has to be examined carefully. When a spectral hole is detected by transmission or fluorescence spectroscopy, the signal is associated to the real part of the absorption coefficient. But a holographic signal includes both real and imaginary parts. The latter corresponds to the index of refraction grating contribution. It exhibits a spectral dispersion shape that extends over a spectral range much broader than Γ_{hom}. One hologram may suffer from the background caused by those stored in the neighboring channels. Let us consider a sample where a large number of evenly spaced holograms are stored. Let N be the number of holograms and δ their spacing. The phase between the recording beams is assumed to stay the same all along the recording process. When one reads out the hologram that stands on the very edge of engraved domain, most of the signal does not originate from the interrogated address. The field that is radiated by the N-1 other holograms is about $\Gamma_{hom}\ln(N)/\delta$ times larger than the signal emitted by the readout address. One gets rid of the dramatic cross-talk caused by the index of refraction grating by engraving each data over an interval of a few homogeneous width over which the hologram phase undergoes a 2π shift[5,6]. Another consequence of this phase and frequency scan is that the diffraction efficiency is increased by a factor of four. It reaches its TDOS value (see Eqs.(1.14) and (1.22)).

In a memory where the maximum capacity R is reached, the spectral separation between adjacent data is reduced to about Γ_{hom}. Therefore, a lapse of time of Γ_{hom}^{-1} at least is needed to readout one data without interference with its neighbors. In other words the bit rate ν_d should satisfy $\nu_d \leq \Gamma_{hom}$. The lower limit of the random access time is also Γ_{hom}^{-1} since this is the minimum time required for a laser to jump at any spectral position with resolution Γ_{hom}.

FDOS is a multichannel addressing method. A specific group of active centers located at the relevant address frequency only participates to the storage of one specific data. As a consequence, the diffraction efficiency on one hologram does not depend on the number of the data that are actually stored in the memory.

1.42 *Time domain optical storage (TDOS)*

Temporal holography can be applied to optical storage. One may use the procedure that is presented in section 1.33. Let the object $R(t-t_2)$, that is conveyed in direction $\vec{k}_2$, consist of a train of pulses. When read out by a probe pulse, the memory plate restores the sequence of data pulses, as expressed by Eq.(1.21). Therefore one binary '1' can be represented by a pulse in the train that reaches the PSHB material at time τ after a reference pulse. In the read out session, the corresponding recovered data is emitted at delay τ after the probe. The probe pulse and the signal pulse train have the same timing as the reference and the object pulses. In this approach, the data are addressed on the time-axis. A time-resolved optical gate is needed, in the retrieval stage, to extract a specific signal from the restored data train.

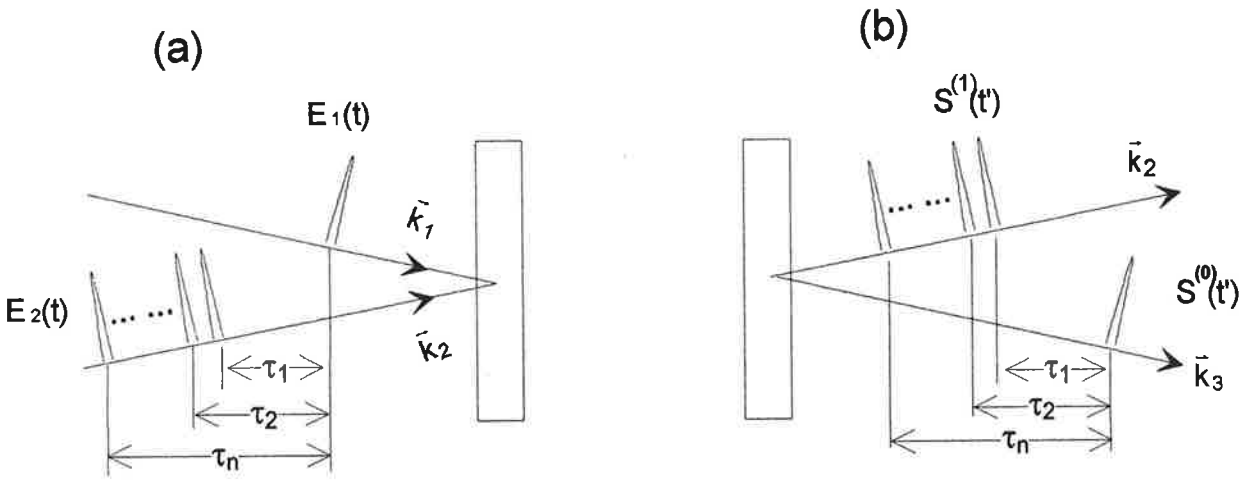

Figure 1.5 Off-axis spatial-temporal holography.
(a): data recording, (b): data retrieval.

The maximal time interval between the reference pulse and an object pulse should be less than the coherent time of the resonant hole burning transition, i.e. $1/\Gamma_{hom}$ sets a limit for the total temporal range for addressing. On the other hand, the temporal (respectively spectral) width of the data pulses cannot be infinitely small

(respectively large). The inhomogeneous width Γ_{in} defines a maximal spectral range. It means that the duration and spacing of the data can not be smaller than $1/\Gamma_{in}$. So the maximal temporal storage capacity is also determined by the material parameter R. If we want to use all the available spectral channels, TDOS should work at bit rate $\nu_d=\Gamma_{in}$, and the signal detector should have a precision $\sim\Gamma_{in}^{-1}$ on a time range $\sim\Gamma_{hom}^{-1}$. To attain a specific datum, one is obliged to retrieve all of the data since they are restored in the shape of a Γ_{hom}^{-1} -long pulse train. Therefore the lower limit of the random access time is Γ_{hom}^{-1} as in the FDOS situation.

When a single datum is recorded in the memory, diffraction efficiency is expected to reach the same maximum value, either in TDOS or in FDOS (provided a phase and frequency are scanned together as mentioned in section 1.41). However the maximum signal amplitude is expected to be R times larger in TDOS than in FDOS, since active centers from the entire absorption band coherently participate to the emission. When R holograms are stacked on the same spectrum in TDOS approach, the active centers are shared between the different stored holograms, and the diffraction efficiency on each hologram is reduced by a factor of R^2. The signal amplitude then attains the same value as in the FDOS method.

1.43 FDOS and TDOS limitations

The common advantage of FDOS and TDOS is based on the use of the frequency-dimension provided by PSHB media. The storage potential determined by the material dependent parameter R is expected in both approaches.

In both cases one finds the same random access time lower limit which equals Γ_{hom}^{-1} . On the contrary, we pointed out that very different bit rates are expected in both methods. More specifically, neither of them gives access to the range comprised bertween Γ_{hom} and Γ_{in} since the bit rate equals Γ_{in} in the TDOS memory, and is smaller than Γ_{hom} in the FDOS one.

In addition to fundamental limitations, one has to consider the requirements on the laser source and the detection technique. FDOS (Figure 1.6(a)) requires a monochromatic laser source with a linewidth narrower than Γ_{hom}, that should be scanned within Γ_{in} interval. In some recently reported investigations, the ratio R is as

high as 10^9. It means that the linewidth and the tuning precision of the laser have to be much smaller than the tuning range. The bit access rate is directly limited by the laser scanning rate, and a fast random access to the data is difficult to achieve. TDOS (Figure 1.6 (b)) can use a convenient stochastic broad band laser. However, a good spectral stability and a relatively strong power are demanded. In the read-out stage, the data are retrieved as a temporal bit train with a bit-spacing $\tau_d=\Gamma_{in}^{-1}$ and total duration Γ_{hom}^{-1}. Thus a fast time gate is required with a temporal width $1/\Gamma_{in}$. For random access to any bit in the data train, a fast random positioning of the time gate should be achieved within the range, $1/\Gamma_{hom}$. This is still a difficulty in present technique for the signal shorter than nanosencond.

Actually, FDOS and TDOS can be considered as two extreme situations of how to combine the holographic method with the use of spectrally selective media. With both approaches, one has met some difficulties to achieve maximum storage capacity with an arbitrary bit rate in the range, $\nu_d<\Gamma_{in}$, and with fast random access. Based on available techniques, some other approaches have been proposed to work with the intermediate situations. Two interesting examples are described in the following paragraph.

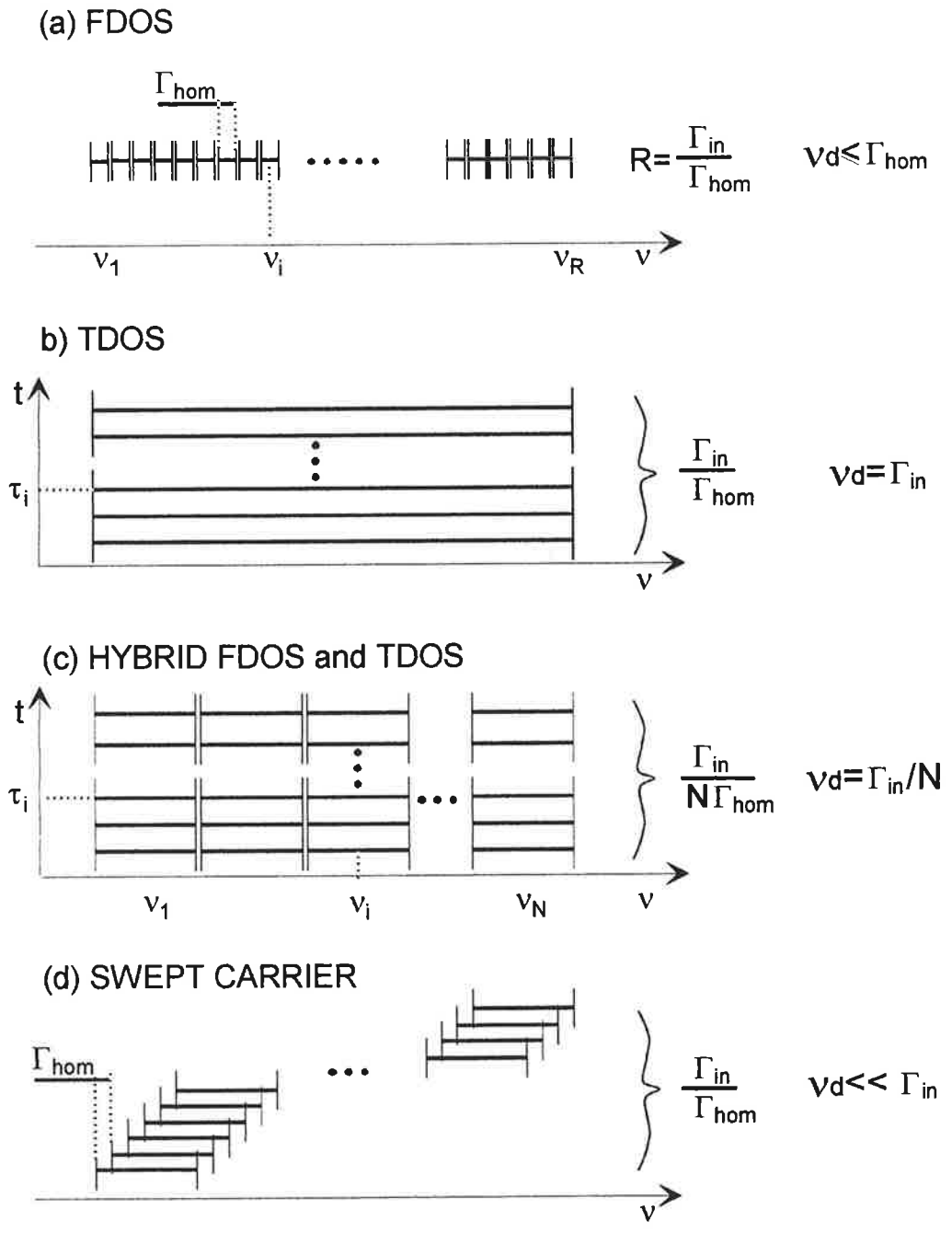

Figure 1.6 *Comparison between FDOS (a), TDOS (b), combined (c) and swept-carrier (d) approaches at maximal storage density.*

1.5 Two hybrid approaches

1.51 Combining TDOS with FDOS

To fulfill storage potential with a variable bit rate, an approach sketched in figure 1.6 (c) was proposed in ref. [7]. For storing R data with a bit rate, $\nu_d << \Gamma_{in}$, the absorption band is divided into $N_d=\Gamma_{in}/\nu_d$ sections, each of them with a spectral width ν_d. A tunable pulsed laser is required. Within each spectral section, the TDOS approach is employed with a ν_d-wide laser tuned to the central frequency of the section. A data train containing R/N_d pulses can be recorded in such a section. Another data series can be stored by repeating the same process except for changing the central frequency. For retrieval, the same laser source is tuned step by step to each section and the recorded data trains can be played back. The advantages of this approach are listed as follows,

i) a broad laser line ν_d, instead of $<\Gamma_{hom}$ as needed for FDOS.

ii) a low precision on frequency tuning, which may be satisfied with several lasers for broad-band media.

iii) a large range of flexibility on bit rates, which means that different data trains can be treated with different bit rates by changing the data section width ν_d.

iv) a possibility to selectively playback a data train by frequency-positioning the probe laser.

With this approach, 1.6 kbits were stored in one spatial location defined by a laser spot[7].

1.52 TDOS with a frequency chirped laser

In ref. [8], swept-carrier time domain optical memory (SCTDOS) was proposed and was experimentally demonstrated in rare-earth-ion-doped crystals[9-11]. This technique keeps the temporal addressing approach, where data are encoded as a train of optical pulses. However, the key feature that it offers is to make the data rate

adjustable over a broad range, without any consequence on the memory capacity. In this way it differs from the basic TDOS method where maximum capacity is only attained at the maximum transfer rate Γ_{in}^{-1}.

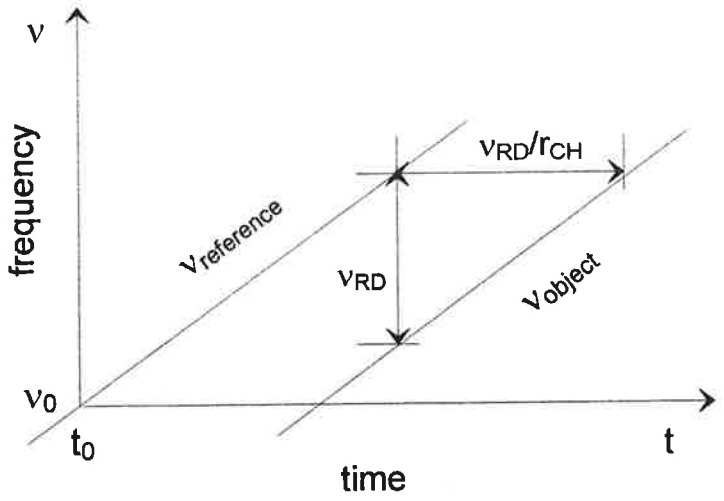

Figure 1.7 Frequency chirping in the swept-carrier approach.

Data are stored and retrieved with the help of the laser beams that are chirped on frequency at rate r_{CH}. The data train is imprinted on the object beam whose frequency is shifted at ν_{RD} from that of the reference beam. In figure 1.7, where the evolution of instantaneous frequency is represented, one notices that the frequency shift ν_{RD} is equivalent to an instantaneous delay ν_{RD}/r_{CH}. Let the instantaneous frequency of the reference be ν_0 at time t_0. A datum with duration τ, that reaches the material at time t_n, engraves a sinusoidal structure with period r_{CH}/ν_{RD} within the absorption profile around the spectral position $\nu_0+r_{CH}(t_n-t_0)-\nu_{RD}$. When read out by a beam that is chirped at the same rate, this engraved region emits a τ-long signal pulse at time $t_p+t_n-t_0$, where t_p represents the time when the readout pulse frequency equals ν_0.

Depending on the relative size of τ^2 and r_{CH}, two situations can be distinguished. When $r_{CH}\tau^2>1$, one calculates that the size of a spectral channel is $r_{CH}\tau$. Let the time separation between adjacent data also equal τ. In other words, let the transfer rate ν_d

be set equal to τ^{-1}. Then, the frequency shift that builds up between two successive data is $r_{CH}\tau$. Thus the spectral storage area is divided into non-overlapping domains and this partition of the available spectral memory is very similar to what occurs in FDOS. When $r_{CH}\tau^2<1$, the size of a spectral channel is τ^{-1}. Since the frequency shift between adjacent data is still $r_{CH}\tau$, the relevant engraved spectral regions tend to overlap as in TDOS.

It may be shown that, in order to preserve the causal character of the engraving sequence, the data duration τ must be larger than ν_{RD}^{-1}. In addition, the spectral modulation period r_{CH}/ν_{RD} has to be larger than the spectral resolution Γ_{hom}. Thus the minimum shift between successive spectral channels is

$$(r_{CH})_{min}(\tau)_{min}=\Gamma_{hom}$$

Combining the width of the channels on the sides of the storage domain with the elementary shifts, one obtains that the spectral width which is needed to accommodate N data is given by: $N\Gamma_{hom}+\tau^{-1}$. This quantity must not exceed the available width Γ_{in}. This condition entails the additional requirement $\tau^{-1}<<\Gamma_{in}$ that must be fulfilled at maximum memory capacity for which $N=\Gamma_{in}/\Gamma_{hom}$. However, half maximum capacity with a transfer rate equal to $\Gamma_{in}/2$ is consistent with the condition $N\Gamma_{hom}+\nu_d\leq\Gamma_{in}$. This is the only limitation on the transfer rate ν_d which can be reduced as much as required.

1.6 Conclusion

By adding a fourth dimension to the storage volume, PSHB materials dramatically increase the potential capacity of optical memories.

Different approaches have been experimented to deal with this enlarged number of addresses. They range from the local storage of each data at a specific spectral position to broad band holographic multiplexing, where each data is spread over the entire available spectral band.

We focused our discussion on the access time issue. Large transfer rates of several hundreds of Gbits/second have been already observed in some experiments in inorganic materials. However there is still a need for fast random access to data. The most promising achievements that combine the frequency addressing and the spectral holography approaches are either sequential in essence (as the swept carrier method) or are limited by the poor precision of fast laser scans over large spectral intervals.

In this Ph.D. dissertation we present the first experimental demonstration of a new data addressing concept that intends to reduce the random access time.

1.7 References

[1] 'Persistent spectral hole burning : Science and applications', W. E. Moerner Ed., (Springer-Verlag, Berlin, Heidelberg, 1988).

[2] A special issue of the Journal of Luminescence devoted to the topic of optical linewidth in glasses, J. Lumin., **36**, 179-329 (1987).

[3] S. Völker, *'High-resolution spectroscopy of organic solids: hole-burning in molecular crystals and amorphous systems at low temperature'*, in Excited Spectroscopy in Solids, XCVI Corso, Soc. Italiana di Fisica (1987).

[4] L. A. Rebane, A. A. Gorokhovskii, and J. V. Kikas, *'Low-temperature spectroscopy of organic molecules in solids by photochemical hole burning'*, Appl. Phys., **B29**, 235-250 (1982).

[5] B. Kohler, S. Bernet, A. Renn, and U. P. Wild, *'Storage of 2000 holograms in a photochemical hole-burning system'*, Opt. Lett., **18**, 2144 (1993).

[6] E. S. Maniloff, S. B. Altner, F. R. Graf, A. Renn, and U. P. Wild, *'Recording of 6000 holograms by use of spectral hole burning'*, Appl. Opt., **34**, 4140 (1995).

[7] M. Mitsunaga, R. Yano, and N. Uesugi, *'Time- and frequency-domain hybrid optical memory: 1.6-Kbit data storage in* Eu^{3+} *:* Y_2SiO_5*'*, Opt. Lett., **16**, 1890 (1991).

[8] T. W. Mossberg, *'Swept-carrier time-domain optical memory'*, Opt. Lett., **17**, 535 (1992).

[9] H. Lin, T, Wang, G. A. Wilson, and T. W. Mossberg, *'Experimental demonstration of swept-carrier time-domain optical memory'*, Opt. Lett., **20**, 91 (1995).

[10] T. Wang, H. Lin, and T. W. Mossberg, *'Optical bit-rate conversion and bit-stream time reversal by the use of swept-carrier frequency-selective optical data storage techniques'*, Opt. Lett., **20**, 2033 (1995).

[11] H. Lin, T. Wang, and T. W. Mossberg, *'Demonstration of 8 Gbit/in*^{2} *areal storage density based on swept-carrier frequency-selective optical memory'*, Opt. Lett., **20**, 1658 (1995).

CHAPTER 2

SPECTRAL-PHASE-ENCODING OF MEMORY ADDRESSES

2.1 Introduction

As discussed in Chapter 1, the minimum expected random access time in a PSHB memory is on the order of Γ_{hom}^{-1}, usually ranging from millisecond to microsecond for inorganic systems, and microsecond to tenths of nanosecond for organic ones. In rare earth ion doped crystals, where the laser has to be scanned over a few hundreds of megahertz, large transfer rates were obtained, but the corresponding random access rate was much lower. The situation is worse in organic systems. In these materials, a FDOS approach requires the frequency scan of a laser over several THz with GHz resolution and a TDOS addressing procedure demands the mechanical displacement of an optical delay-line over several centimeters with a ten micrometer resolution. Even random access to the stored images at video frame rate has not been demonstrated in these systems.

To overcome these difficulties and to improve the random access rate, a new scheme was proposed based on conventional TDOS [1]. In this approach, one records a binary datum by illuminating a PSHB medium successively with a reference and an object pulse with a time interval τ, and an echo signal is retrieved at the same time delay τ after a probe pulse. At this point it is exactly the same as in a classical TDOS experiment, but the reference pulse is no longer short and structureless. The new idea is that the address, for each datum carried by a short object pulse, is encoded as a specific temporal shape of the corresponding reference pulse. The shape of the reference pulse is changed for each datum, but the time interval between the reference and object pulses is set to a fixed value τ. Thus the data as the diffracted signals, recognized by their addresses (temporal shape) emerge at the fixed time interval to the probe pulse. The key point in this approach is to avoid any mechanical motion or laser scanning so as to permit the achievement of fast random data access.

The principle description of spectral-phase-addressing in TDOS was presented in Ref. [1]. In this chapter, we give the first practical demonstration of this idea. In

section 2.2, we survey the principle of the spectral-phase-addressing. Then we detail our experimental configuration in section 2.3. The experimental results are presented in section 2.4. Finally, the chapter is concluded in section 2.5.

2.2 Principle of spectral-phase addressing

2.21 Addressing with a spectral code

The idea of spectral-phase-encoding for TDOS is reminiscent of a method that has been proposed in the frame of angular multiplexing for conventional spatial holography[2-4]. In volume holography, Bragg selectivity is used to disentangle the holograms multiplexed within the third dimension (thickness) of the slab. Each stored hologram is recorded and retrieved at a specific value of the reference beam angle of incidence which represents the hologram address. There are as many reference beam directions as different volume addresses. Instead of shining the reference in one direction at a time, the phase encoding method proposes to keep reference beams present in all directions simultaneously and to have the storage address represented by the set of the relative phases of the combined reference beams. This phase-encoding method is presently applied to the frequency dimension with the help of spectrally selective materials.

The interference pattern engraved by temporal holography on the absorption spectrum of a PSHB material and the temporal amplitude of the diffracted field respectively read as (see section 1.33):

$$\tilde{\mathcal{E}}_1^*(\nu)\tilde{\mathcal{E}}_2(\nu)e^{-2i\pi\nu\tau}$$

$$\mathcal{S}^{(1)}(t) = \int \tilde{\mathcal{E}}_3(\nu)\tilde{\mathcal{E}}_1^*(\nu)\tilde{\mathcal{E}}_2(\nu)e^{2i\pi\nu(t-t_3-\tau)}d\nu \qquad (2.1)$$

Where $\tau=t_2-t_1$, denotes the time interval between reference and object pulses. These expressions remain valid under the following conditions,

i) optically thin medium,

ii) uniform spectral distribution of active molecules over the laser spectrum,

iii) small burning dose, resulting in a small modification of the absorption profile. No radiative saturation of the optical transition.

iv) no temporal overlapping between reference and object fields.

v) spectral modulation period τ^{-1} larger than the material resolution Γ_{hom}.

One usually considers the classical TDOS situation where the temporal profile of the diffracted signal replays the data train, $\mathcal{E}_2(t)$, containing many bits which have

been encoded on its spectral shape, $\tilde{\mathcal{E}}_2(\nu)$, with the help of a short reference/probe pulse.

Now we consider a different configuration. A short object pulse represents a single datum, while the reference/probe pulse is no longer spectrally (or temporally) structureless. Let object, reference and probe beams come from the same pulsed laser source with a spectrum $\tilde{\mathcal{E}}_L(\nu)$. The object pulse carries a binary α_i=1 or 0. The reference and the probe spectra are respectively shaped by the phase factors $f_i(\nu)$ and $f_j(\nu)$. The engraved spectral structure $\left|\tilde{\mathcal{E}}_L(\nu)\right|^2 \alpha_i f_i(\nu)^* e^{-2i\pi\nu\tau}$ carries the information of the binary datum, as well as the spectral shape of the reference pulse. Probed by a pulse with a spectrum $f_j(\nu)\tilde{\mathcal{E}}_L(\nu)$, the temporal profile of the diffracted field reads as,

$$\mathcal{S}_j(t) = \alpha_i \int \left|\tilde{\mathcal{E}}_L(\nu)\right|^2 \tilde{\mathcal{E}}_L(\nu) f_i^*(\nu) f_j(\nu) e^{2i\pi\nu(t-t_3-\tau)} d\nu \qquad (2.2)$$

Under the assumption that the field amplitude is constant and equal to $\tilde{\mathcal{E}}_L(\nu_0)$ over the excitation spectral range , the signal becomes,

$$\mathcal{S}_j(t) = \alpha_i \left|\tilde{\mathcal{E}}_L(\nu_0)\right|^2 \tilde{\mathcal{E}}_L(\nu_0) \int f_i^*(\nu) f_j(\nu) e^{2i\pi\nu(t-t_3-\tau)} d\nu \qquad (2.3)$$

Further, let the two shape factors belong to a family of orthogonal functions $\{f_n(\nu)\}$, in such a way that $\int f_i^*(\nu) f_j(\nu) d\nu = \delta_{ij}$. The signal at a time interval τ after the probe pulse reads as:

$$\mathcal{S}_j(t_3+\tau) = \left|\tilde{\mathcal{E}}_L(\nu_0)\right|^2 \tilde{\mathcal{E}}_L(\nu_0)\, \alpha_i\, \delta_{ij} \qquad (2.4)$$

It replays the stored datum α_i when the probe spectrum has the same structure as the reference and vanishes otherwise. The factor $\left|\tilde{\mathcal{E}}_L(\nu_0)\right|^2 \tilde{\mathcal{E}}_L(\nu_0)$ depends on the laser energy both in recording and retrieving.

To store another datum α_k, we chose a different spectral function $f_k(\nu)$ from the same family to modify the reference pulse spectrum. We keep the same time-delay between reference and object pulses. The grating pattern, $\left|\tilde{\mathcal{E}}_L(\nu)\right|^2 \alpha_k f_k(\nu)^* e^{-2i\pi\nu\tau}$ formed by the second reference-object pair is piled upon the previous pattern within the same spectral region in the medium. For readout, all the function $f_j(\nu)$ of the set

$\{f_n(\nu)\}$ are successively used to shape the probe pulse that illuminates the memory element. The temporal amplitude of the signal that emerges at $t=t_3+\tau$ reads as,

$$S_j(t_3+\tau)=\begin{cases}\left|\tilde{\mathcal{E}}_L(\nu_0)\right|^2\tilde{\mathcal{E}}_L(\nu_0)\,\mathcal{E}_i & j=i\\ \left|\tilde{\mathcal{E}}_L(\nu_0)\right|^2\tilde{\mathcal{E}}_L(\nu_0)\,\mathcal{E}_k & j=k\\ 0 & j\neq i,\ k\end{cases} \qquad (2.5)$$

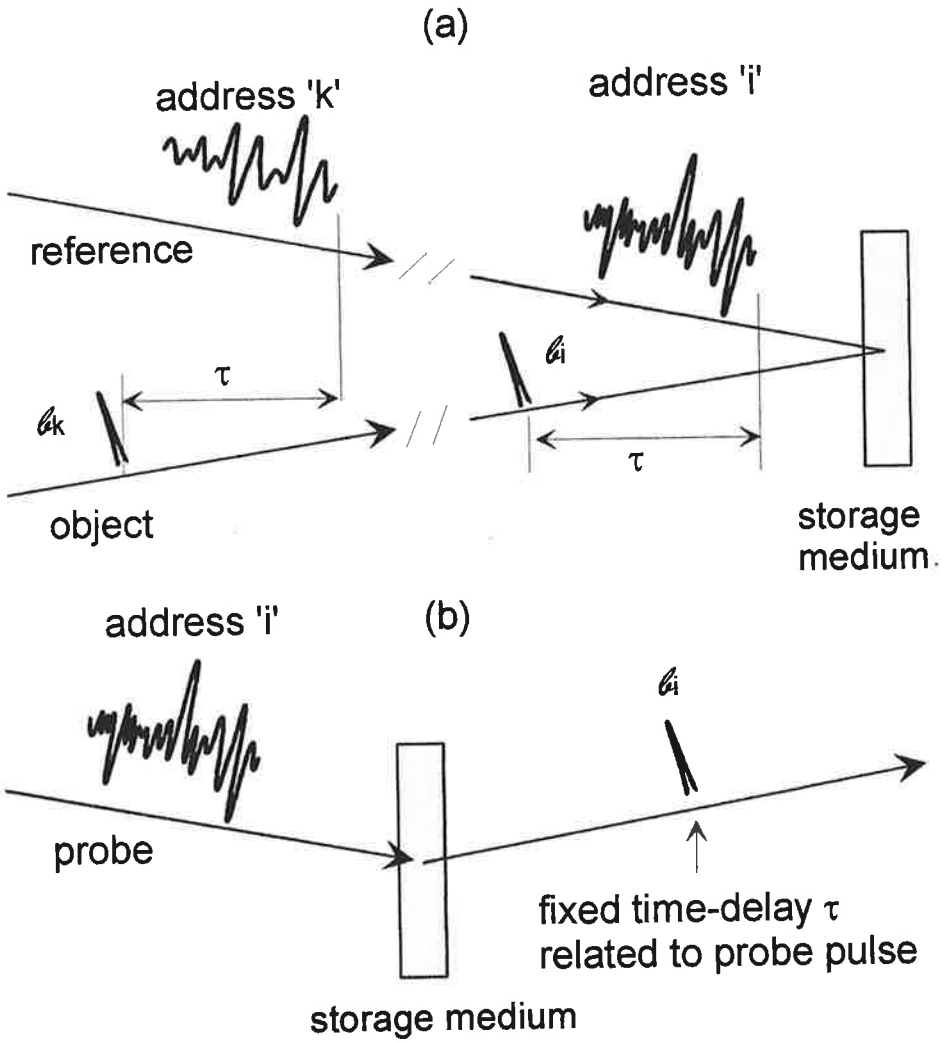

Figure 2.1 Spectrally/temporally addressed storage, (a) recording of two binary data $\mathcal{E}_i$, $\mathcal{E}_k$ represented by short object pulses with the corresponding addresses 'i' and 'k', respectively, in the same 4-D volume. (b) selective retrieval of datum $\mathcal{E}_i$ with address 'i'.

The signal selectively replays the stored data at a fixed detection time τ after the probe pulse, i.e. a datum recorded with a reference code can be uniquely read out when the same code is applied on the probe pulse. If we are able to build N orthogonal spectral functions and to imprint them on the reference beams, we can stack N independent data in the memory. Since the spectral codes are used to identify the data in the engraving and retrieval steps, they can be regarded as the data addresses in the spectral memory.

From expression (2.3), we see that the temporal feature of the signal is characterized by the inverse of the spectral width of the recording range (or the spectral encoding range denoted as Δ). As in classical TDOS, the signal characteristic time equals Γ_{in}^{-1} when the total inhomogeneous band is used for storage. It requires that the signal detection system exhibits subpicosecond time-resolution for organic molecule-doped amorphous materials. This exceeds the capabilities of existing electronic detectors. An interference cross-correlator device is well suited to achieve the needed optical gating.

2.22 *Signal detection by field cross-correlation*

The correlation function G(T) between two fields $\mathcal{S}(t)$ and $\mathcal{E}_g(t)$ is measured as,

$$G(T)=\int \mathcal{E}_g(t-T)\mathcal{S}^*(t)dt/\int\left|\mathcal{E}_g(t)\right|^2 dt$$

$$G(T)=\int \tilde{\mathcal{E}}_g(\nu)\tilde{\mathcal{S}}^*(\nu)e^{-2i\pi\nu T}d\nu/\int\left|\tilde{\mathcal{E}}_g(\nu)\right|^2 d\nu \qquad (2.6)$$

In our experiment, $\mathcal{E}_g(t)$ is called the gating field. It is a beam split from the pulse that is then shaped and used as a probe. By adjusting the optical path lengths we control the time delay T between the gate and the probe. For a signal as in (2.3), the cross-correlation reads as,

$$G_j(T)=\frac{\left|\tilde{\mathcal{E}}_L(\nu_0)\right|^4 \mathcal{A}_i\int f_j^*(\nu)f_i(\nu)e^{-2i\pi\nu(T-\tau)}d\nu}{\int\left|\tilde{\mathcal{E}}_L(\nu_0)\right|^2 d\nu} \qquad (2.7)$$

The T-dependence of G(T) coincides with the t-dependence of the signal field. At a time point $T=\tau$, the correlation function exhibits the orthogonal law of the addresses and the retrieved signal is detected as,

$$G_j(\tau) = g\,\mathcal{E}_i\,\delta_{ij} \qquad (2.8)$$

where the factor g is given by: $g=\left|\tilde{\mathcal{E}}_L(\nu_0)\right|^4 \Big/ \int \left|\tilde{\mathcal{E}}_L(\nu_0)\right|^2 d\nu$. For multiple storage, where the signal amplitude is depicted by Eq.(2.5), the cross-correlation is measured as:

$$G_j(\tau) = \begin{cases} g\,\mathcal{E}_i & j = i \\ g\,\mathcal{E}_k & j = k \\ 0 & j \neq i,\ k \end{cases}$$

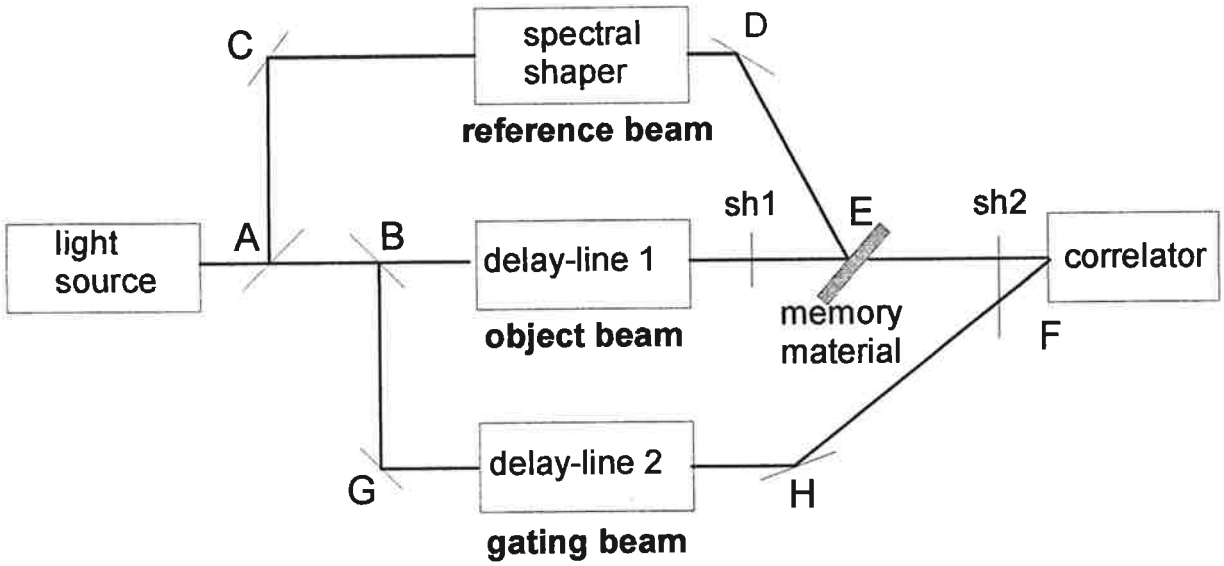

Figure 2.2 Diagram of the complete experimental setup.

Multiple storage and fast random data retrieval based on the ideas of spectral-phase-addressing and cross-correlation detection can be effectuated with the experimental arrangement drawn in figure 2.2. A beam from a laser source is split by two beam-splitters at A and B in three parts, the object, the reference (probe) and the gating beams. The spectral shaper imprints the orthogonal spectral codes on the reference beam. The delay-line 1 (DL1) is adjusted to make the object pulse incident onto the memory material at E with a time-delay τ after the reference pulse. During recording, the shutters 1 and 2 are, respectively, open and closed. The PSHB material acting as a memory element is illuminated by these two pulses successively. A spatial-spectral grating is recorded as a population modification of PSHB molecules in the

memory material. A series of data can be stacked in the same spatial-spectral-volume by changing the corresponding codes. In the retrieval step, the object beam is blocked by shutter 1. The probe beam goes through the same path as the reference, but with a weaker intensity. Shutter 2 is now open and the signal diffracted by the memory element propagates in the same direction as the object beam. The delay-line 2 (DL2) on the gating beam is adjusted to make the optical path BGHF equal to BEF. The field cross-correlation function between the gating and the signal fields is finally detected at F. Thus each stored datum can be randomly accessed by loading an appropriate code on the probe pulse.

2.23 Biphase encoding: storage capacity, access time and limitations

In amorphous materials, the storage interval Δ spans several Terahertz. In this bandwidth range, spectral-phase-encoding is performed with the help of a spatial light modulator (SLM) inserted between two diffraction gratings (see section 2.32). This shaper enables us to control the relative phase of N evenly spaced slices into which the spectral interval Δ is divided. The width of each spectral slice is $\delta=\Delta/N$ and the central frequency of the storage window is denoted by ν_0. In each slice the relative phase can be set equal to 0 or π. A spectral code $f_i(\nu)$ is specified by the sequence of phase shifts that are assigned to the N spectral slices. It can be written as:

$$f_i(\nu)=\frac{1}{\sqrt{\delta}}\sum_{p=1-N/2}^{N/2} b_i^{(p)}\,\mathrm{rect}\left[\frac{\nu-(\nu_0+p\delta-\delta/2)}{\delta}\right] \qquad (2.9)$$

where the rectangle function is defined as $\mathrm{rect}[x]=\begin{cases}1 & |x|\le 1/2\\ 0 & |x|>1/2\end{cases}$, $b_i^{(p)}=\pm\frac{1}{\sqrt{N}}$

corresponds to a relative phase 0 or π, respectively. With the help of N spectral slices, N addresses can be constructed and the orthogonality condition reads as:

$$\int_{\nu_0-\Delta/2}^{\nu_0+\Delta/2} f_i(\nu)f_j(\nu)d\nu=\sum_{p=1-N/2}^{N/2} b_i^{(p)}b_j^{(p)}=\delta_{ij} \quad \text{where } i,j=1\ldots N. \qquad (2.10)$$

In particular, when N equals 2^n (n is a integer), we construct the codes in the form of N orthogonal Hadamard functions, which will be detailed in section 2.32.

The storage capacity in this approach is determined by the number of orthogonal address functions (or the number of the spectral slices). The maximal spectral width available for phase-encoding is restricted by the inhomogeneous width Γ_{in}, and the minimal spectral slice can not be narrower than Γ_{hom}. The maximal number of spectral slices is then determined by the ratio Γ_{in}/Γ_{hom}, which gives the maximal number of orthogonal addresses. So the possible storage capacity for this approach equals that for conventional FDOS and TDOS methods.

The field cross-correlation technique is used to detect the signal at a fixed delay $T=\tau$. Once the delay-line is adjusted to a correct position, it keeps fixed there for detecting the data at any address. Thus this approach does not involve laser scanning (as FDOS) or mechanical motion (as TDOS). It is free from the technical restrictions in those two aspects. The random access time is only determined by the switching time of the encoding system from one address code to another. It takes less than 100μs to enter any specific phase code on a ferroelectric liquid-crystal SLM. This can be regarded as the random access time of the memory.

Since a phase encoding technique is used, there is no energy loss. The light energy that is available to store a single datum does not depend on the number of the addresses in the memory.

With the spectral phase-encoding technique, the selective access to the addresses is guaranteed by the orthogonality between the spectral code structures carried by the reference/probe pulses. In practical storage, the distortion of the code structures should be avoided. Ideal experimental conditions would meet all the prerequisites of expression (2.7). They include optically thin material with narrow homogeneous width, uniform spectral distribution of molecules and laser energy within the recording window, weak burning energy, and temporal separation between the reference and object pulse. Unlike most of the previous conditions, the latter is easy to satisfy. It requires that the delay time τ be set larger than the inverse width δ^{-1} of elementary spectral slices.

2.3 Experimental set-up

2.31 Laser source and the field-correlator

In the above discussion, it is admitted that the duration of the object pulse is not longer than Γ_{in}^{-1}. For an organic PSHB material, it means a time scale of hundreds of femtoseconds. The production of such short pulses requires sophisticated femtosecond lasers. At present time, the use of such kind of lasers does not seem quite pertinent because the quantity that has to be smaller than Γ_{in}^{-1} is not the pulse duration itself but the coherence time of the light. A broad band stochastic light source can also conveniently satisfy the requirement. In our experiment, the light source is a broad band dye laser pumped by the second harmonic of a YAG laser. It delivers 7ns duration pulses at a 15Hz repetition rate; the pulse spectrum is centered at 620nm and spreads over approximately 1.4THz.

The field-correlator has been described in ref[5] and the arrangement used is plotted in figure 2.3. Young's interference fringes between signal and gating beams are formed on a coupled charge device (CCD) linear array that consists of 1000 pixels of the size of 13x39μm and exhibits a dynamic range of 256. The readout time of the CCD array amounts to a few milliseconds. A microcomputer synchronizes the laser shots, the motion of the translation stage in the delay line and the signal detection on the CCD array. Fast Fourier transform of the intensity distribution provides us with the fringe contrast that coincides with the correlation function. For measuring the contrast of the interference pattern, about 20 fringes are formed on the CCD array. Therefore the delay between the edges of the interference pattern is about $20(\lambda/c)$~ 50fs, which represents the temporal resolution of the method. According to theoretical estimations, we find that the narrowest temporal structure Δ^{-1}~800fs is much larger than the temporal resolution offered by the correlator.

The laser coherence time can be measured with the help of the correlator. In the setup represented on figure 2.2, the memory element is removed and the reference arm is blocked. The light intensity is equally shared between the gating and the object beams. The latter plays the role of the signal beam. On figure 2.4 is

displayed the auto-correlation function of the laser source detected with this system, from which the coherence time of the source light is measured to be about 650 fs.

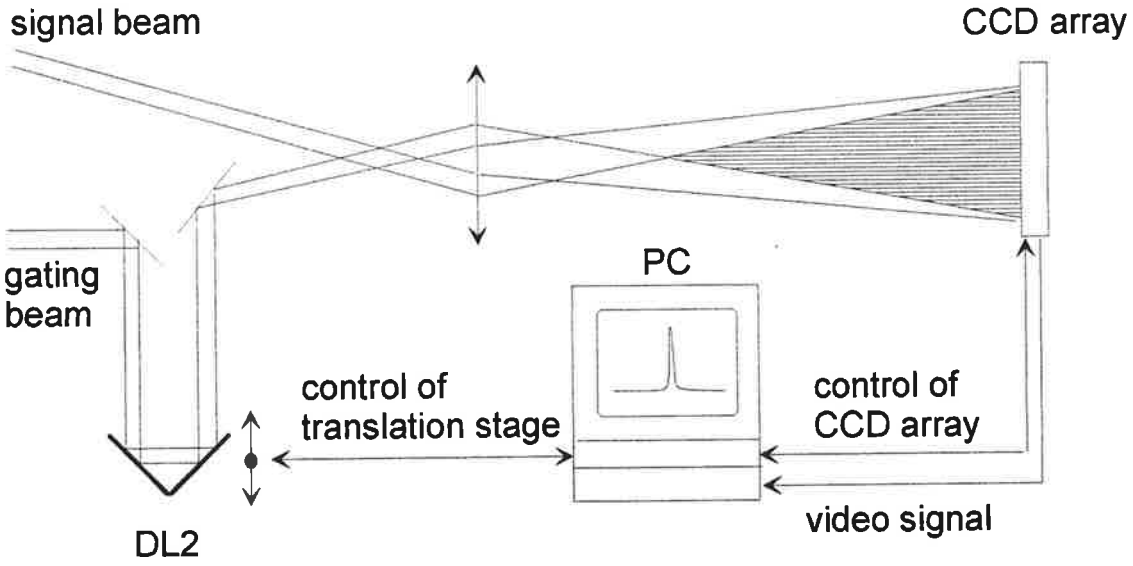

Figure 2.3 The field cross-correlator.

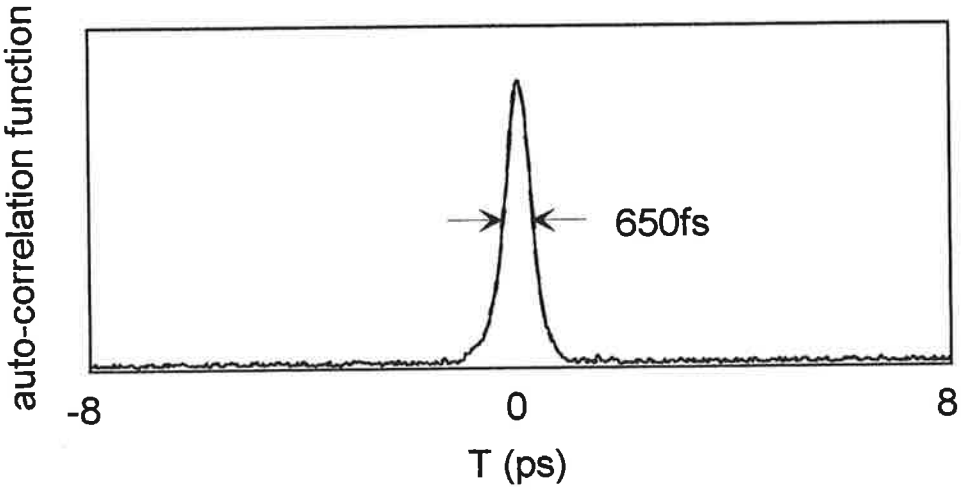

Figure 2.4. Auto-correlation function of the laser source.

2.32 Spectral shaper

Linear spectral filtering has proved to be a powerful tool for temporal shaping of ultrashort light pulses[6-11]. The technique consists in spatially dispersing the frequency components of a short pulse in order to filter its spectral components through phase or amplitude masks. The recombination of the filtered components gives the desired temporal shape. The technique has been used to synthesize femtosecond waveforms in experiments on dark soliton propagation in fibers [8], pulse coding for communication [9], all-optical switching [10] and holographic data processing and image storage [11-16].

For spectral-phase encoding of reference and probe beams for holographic binary data storage, we follow a spectral shaping procedure developed by Wiener [11] and sketched in Figure 2.5. A pair of diffraction gratings works as a light dispersion-recombination device and a series of orthogonal biphase codes are generated by a liquid-crystal SLM inserted between the pair of dispersion gratings.

2.321 Two-grating device

In our spectral shaping apparatus, two identical lenses L1 and L2, with a focal length f=25cm, are set as a telescope with a magnification equal to 1. Two identical diffraction gratings G1 and G2 are respectively placed at its input and output focal plane. An incident beam regarded as a plane wave with a central frequency ν_0 is angularly spread horizontally by dispersion on grating G1. We denote the incident and dispersive angles on G1 by φ and θ, respectively. The diffraction law reads as,

$$\sin(\varphi)+\sin(\theta)=mc/a\nu \qquad (2.11)$$

where m is the diffraction order, c the light velocity, and a is the grating parameter. In our current experiment, G1 is set as m=1, a^{-1}=2400 grooves/mm with maximal diffractive efficiency for an horizontally polarized field. For a pulse with an incident angle φ_0=33° and a central frequency ν_0=c/(620 nm), a dispersion angle θ_0=70° for ν_0 can be calculated from (2.11). When the pulse spectrum ranges within a narrow band with respect to the value of the central frequency, i.e. $\nu-\nu_0<<\nu_0$, the dispersion law for the frequency components can be described as, $\theta-\theta_0=\beta(\nu-\nu_0)$ where the angular dispersion coefficient $\beta=\left.\frac{\partial\theta}{\partial\nu}\right|_{\nu_0}$ =0.009rad/THz. The dispersed light is focused by L1 in

the confocal plane F, where each spatial position x corresponds to a spectral component of the incident beam. The central frequency is adjusted to go through the point x=0, and the frequency-to-space relation thus reads as,

$$x-x_0=\gamma(\nu-\nu_0) \qquad (2.12)$$

where the spatial dispersion coefficient is, $\gamma=\left.\frac{\partial x}{\partial \nu}\right|_{\nu_0} = f\left.\frac{\partial \theta}{\partial \nu}\right|_{\nu_0}$ =2.25mm/THz. The second lens L2 and the grating G2 are symmetric of L1 and G1 with respect to the confocal plane F. The spatial dispersion of the spectral components produced by G1 and L1 is compensated by L2 and G2. The output pulse is identical to the input one without the SLM inside the apparatus. If a relative phase shift is introduced onto each spectral component by the SLM according to a code function, then the output pulse from G2 has a temporal profile corresponding to the spectral-phase code.

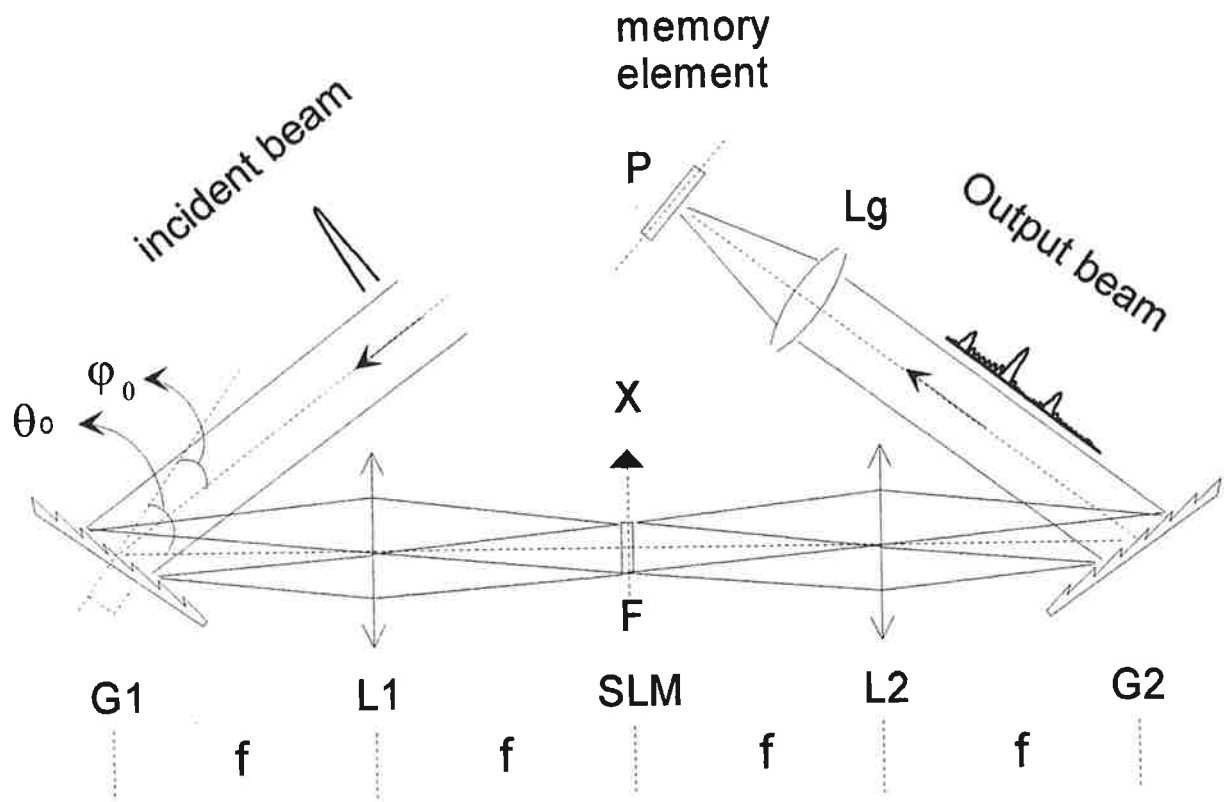

Figure 2.5 Optical configuration of the pulse shaper for spectral-phase encoding.

The spectral resolution of this system depends on the relative sizes of the input beam spot at F and of the SLM pixels. The spectral resolution of the holographic process is improved when the output beam from G2 is focused on the memory element in the plane P with the help of a lens L_g. Indeed, if the planes F and P are optically conjugated through lenses L2 and L_g, this spectral resolution does not depend on the size of the incident beam on G1. It is only affected by the limited diameter of the optics between F and P [16]. Comparing the diameters of the optics and the beam size that results from diffraction through one SLM pixel, one concludes that this effect can be ignored.

2.322 Liquid crystal spatial light modulator (SLM)

The SLM in our light shaper device was built at the Ecole Nationale Supérieure des Télécommunications-Bretagne. A 2μm-thick layer of a smectic C^* liquid crystal is set under a linear array of 128 electrodes as shown in Figure 2.6 (a).

The orientation of the liquid crystal molecules depends on the electric field polarity between the electrodes. As illustrated in Figure 2.6 (b), the smetic cone axis is aligned along the first polarizer direction $\vec{P}_1$, which is set vertically in practice. The molecular director determines the extraordinary index axis n_e which stays 22.5° from $\vec{P}_1$. The crystal thickness ℓ is adjusted in such a way that $|(n_0 - n_e).\ell| = \lambda/2$. The driving electric field $\vec{E}$ is orthogonal to the picture plane. The permanent molecular dipole, which is tangent to the cone and perpendicular to the director, is oriented to the position (1) or (2) respectively, depending on the electric field signs. The second polarizer is set horizontally in direction $\vec{P}_2 \perp \vec{P}_1$. The field emerges from the polarizer $\vec{P}_2$ with a phase shift that depends on the molecular orientation. The switching of the applied electric field polarity results in a π phase shift of the transmitted electromagnetic field. The device transmission is then maximum when the liquid crystal behaves as a half wave plate. The ℓ=2μm matches this requirement in the spectral region of operation. The energy transmission factor is then 0.5. The crystal molecules can be switched from one direction to another in less than 100μs. The SLM was built with a size 40μmx128. When the beam with a central wavelength at 620nm is

dispersed by G1, then focused on the SLM by L1, each pixel of the SLM corresponds to a spectral unit of 17.5GHz and the total spectral window spreads over 2.25THz.

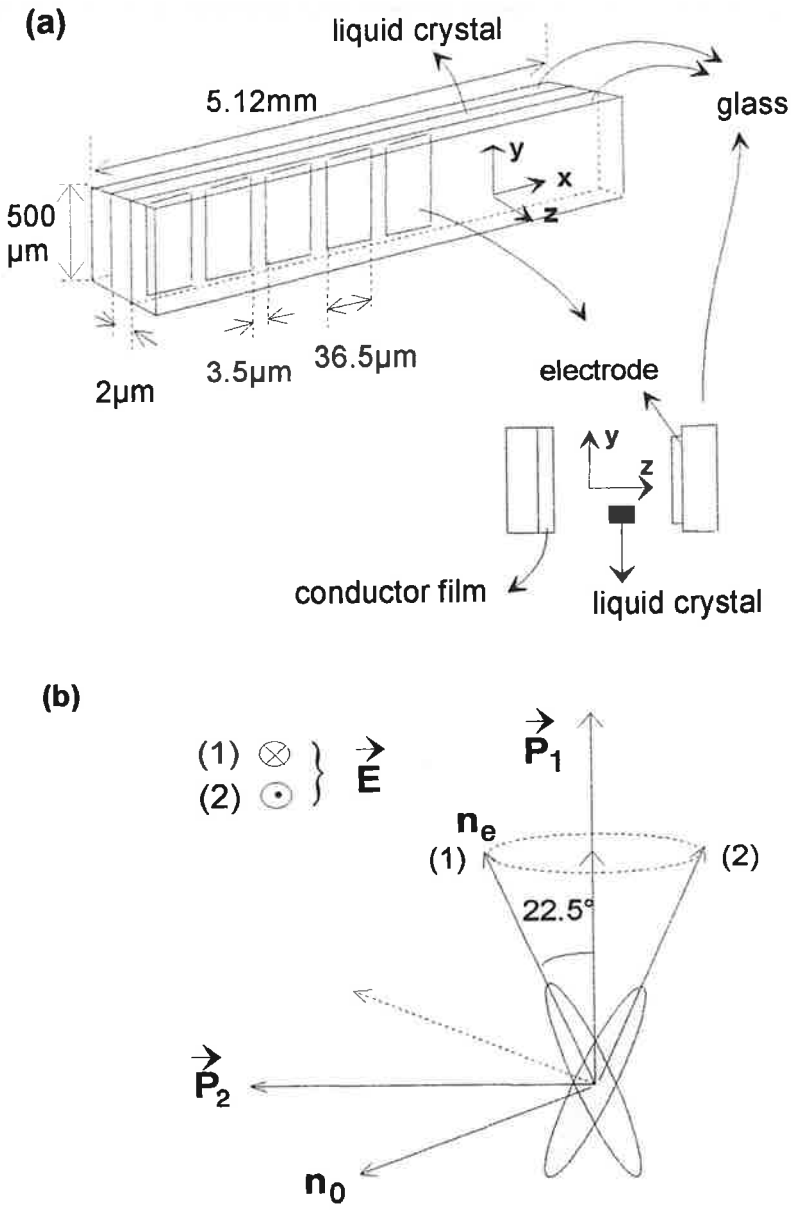

Figure 2.6. *(a) Structure of the SLM.*
(b) Orientation of the smetic C liquid crystal molecule in the presence of an electric field, orthogonal to the figure plane, and birefringence principal axes.*

The diffraction efficiency on the gratings G_1 and G_2 is maximum when the light polarization is oriented in the plane of incidence (that means horizontal polarization in

our setup). Preferred polarization on the gratings has to be made consistent with the SLM action. The horizontally polarized field that emerges from the grating G_1 undergoes a 90° rotation provided by a half wave plate inserted before the liquid crystal cell. This device acts itself as a half wave plate that makes polarization return to horizontal direction. A polarizer inserted before the second grating G_2 selects this polarization component. In the frame of our work, we notice that the SLM is not perfect. Mechanical stresses on the glass windows of the cell induce a small birefringence. We compensate it by inserting a properly oriented quarter wave plate before the SLM.

2.323 Encoding functions

The Hadamard functions are used to generate the biphase codes. A Hadamard matrix is constructed from a 2x2 seed matrix,

$$H_2=\begin{bmatrix}1 & 1\\ 1 & -1\end{bmatrix}$$

with the following recursion method:

$$H_{2^{(n+1)}}=\begin{bmatrix}\left[H_{2^n}\right] & \left[H_{2^n}\right]\\ \left[H_{2^n}\right] & -\left[H_{2^n}\right]\end{bmatrix} \qquad (2.13)$$

The elements obey orthogonality in both rows and columns. We selected the rows to compose the phase code functions.

In our experiment, we actually use only one half of the SLM window because of a narrow laser spectrum, which means that no more than 64 pixels of the SLM are activated. The total width is then Δ=1.1THz. Furthermore, for the sake of simplicity, 32 orthogonal functions are employed as phase codes. So the SLM can be regarded as an array of 32 spectral units, but with a double pixel width δ=35GHz for each unit. The code functions are built and named as that in Figure 2.7. A value '1' of the matrix element corresponds to an electric field between two electrodes charged with a certain voltage level, a value '-1' to the same voltage, but with an opposite sign. In other words, they represent the relative phase shifts '0' or 'π' between the spectral units. The function N°0 with the same phase on all pixels is named the gate function. The function N°16 with the same phase on the first half of the pixels and a π shift on the other half part is called the step function. The product between two functions still

belongs to the same function set. A function multiplied by the gate function equals the function itself (see table 2.1). The square of a function equals the gate function.

The temporal structures of the spectral phase functions can be calculated by Fourier transform. The modules representing the temporal amplitudes of each function are plotted in Figure 2.8. The characteristic of their temporal profile is determined by the width of each peak $1/\Delta$=800fs and the total extension, $1/\delta$=26ps. The temporal structure of a code function can be detected by the mean of the field cross-correlation between two pulses encoded, respectively, by the function itself and by the gate function.

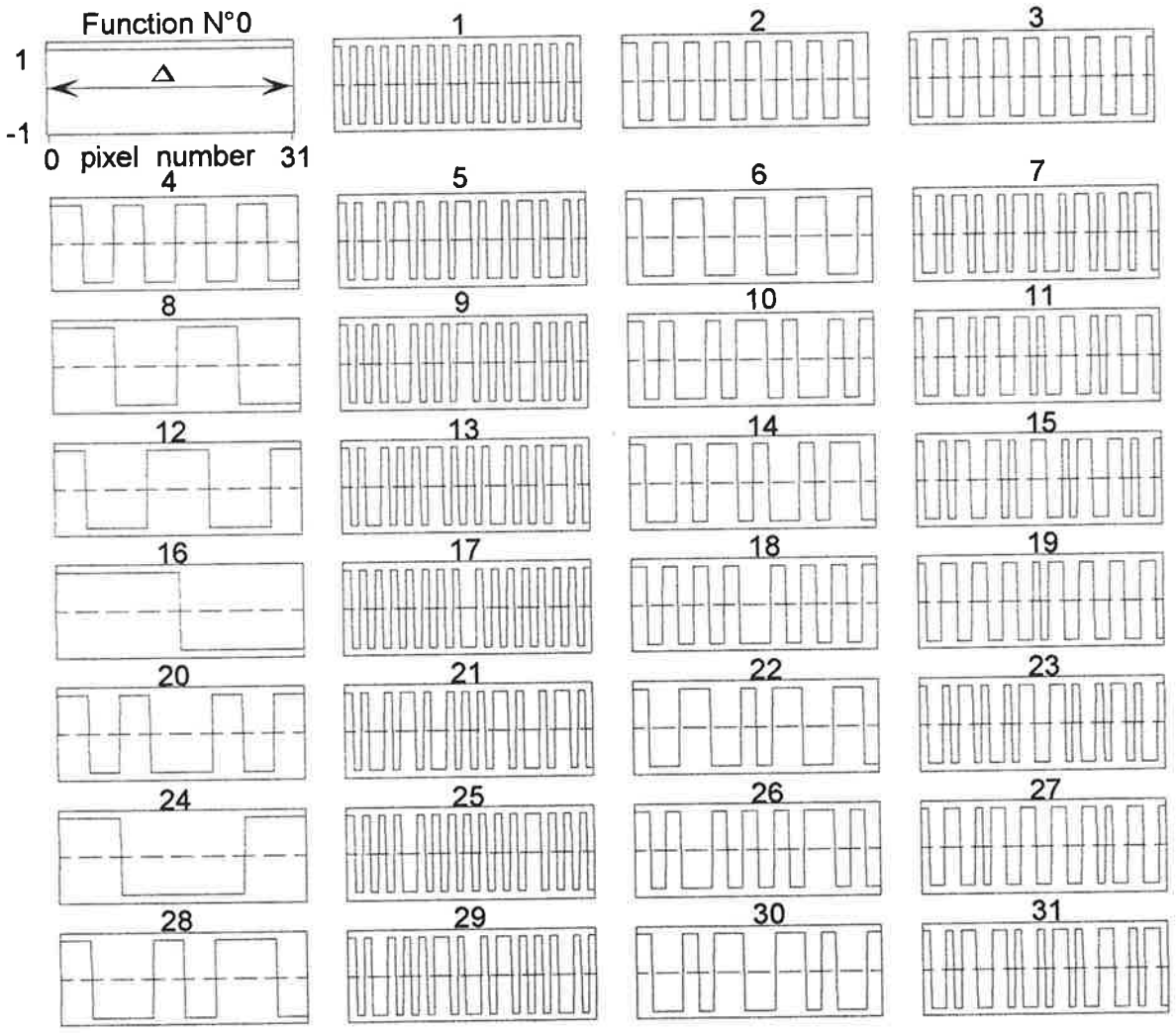

Figure 2.7. The structure of the 32 Hadamard functions (numbered 0~31). The spectral width of each spectral unit is 35GHz and the total window spans 1.1THz.

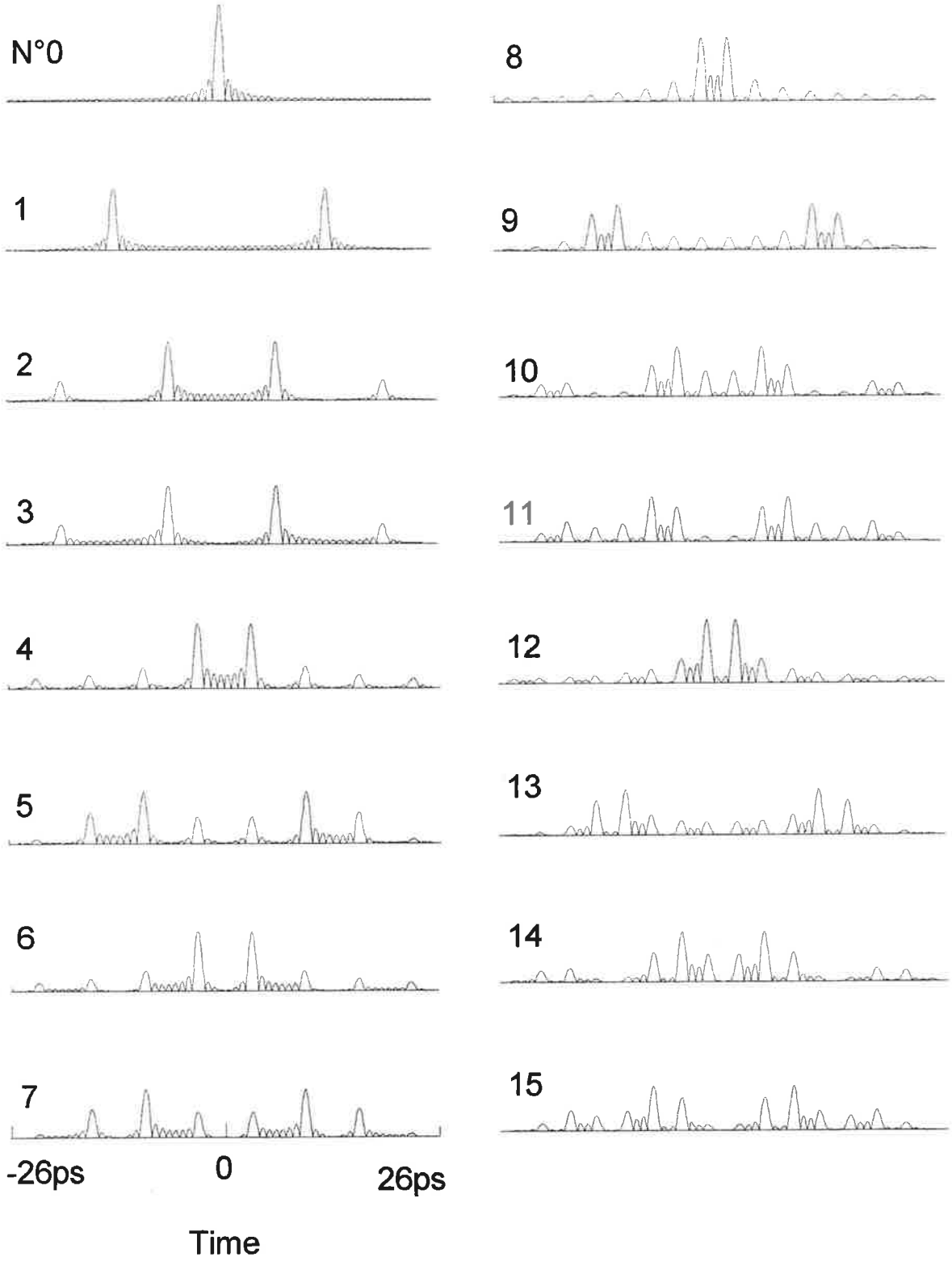
N°0
1
2
3
4
5
6
7
8
9
10
11
12
13
14
15
-26ps
0
26ps
Time

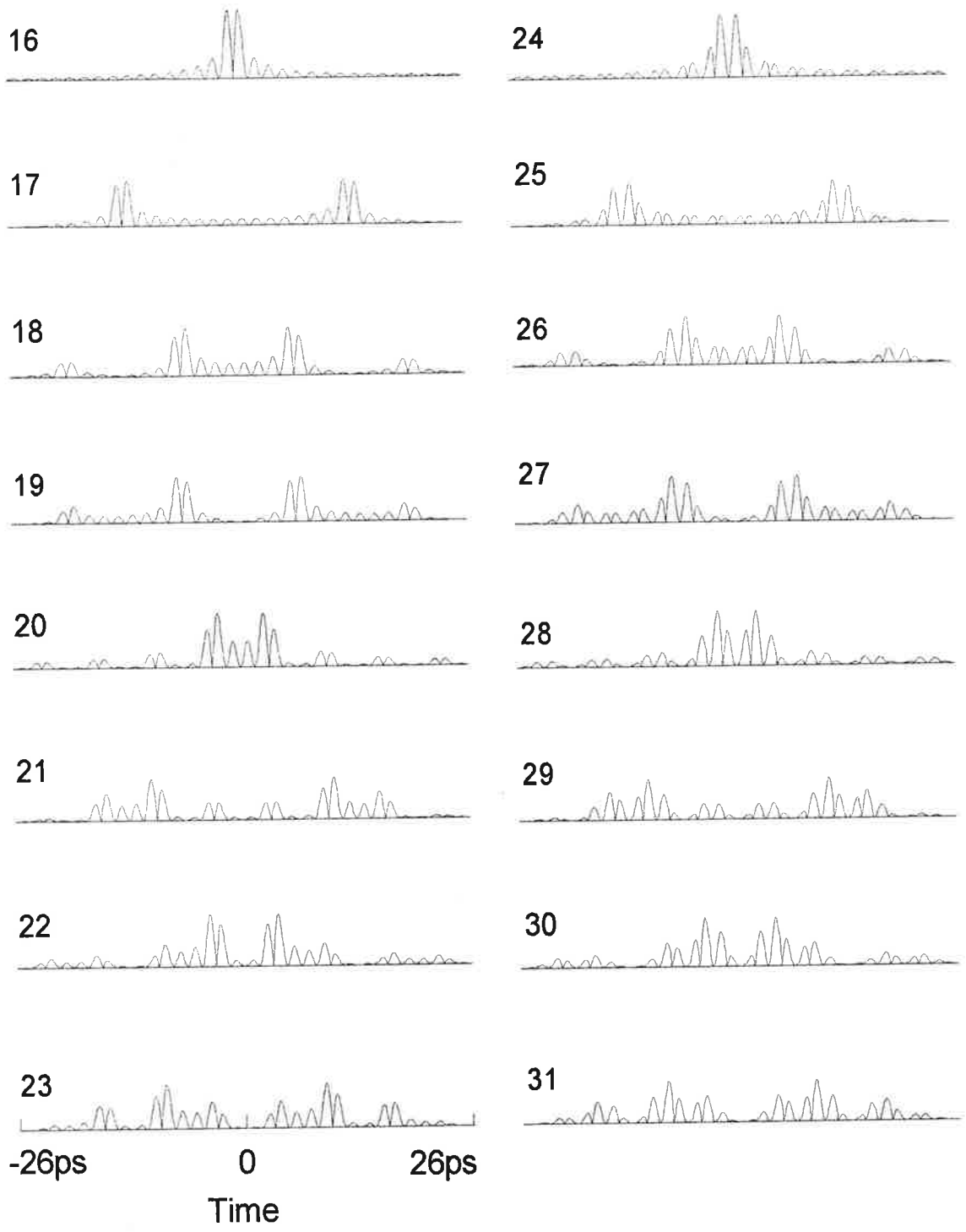

Figure 2.8 *Temporal profiles of spectral-phase codes calculated by Fourier transform corresponding to the 32 Hadamard functions defined within 1.1THz spectral window.*

0	0																															
1	1	0																														
2	2	3	0																													
3	3	2	1	0																												
4	4	5	6	7	0																											
5	5	4	7	6	1	0																										
6	6	7	4	5	2	3	0																									
7	7	6	5	4	3	2	1	0																								
8	8	9	10	11	12	13	14	15	0																							
9	9	8	11	10	13	12	15	14	1	0																						
10	10	11	8	9	14	15	12	13	2	3	0																					
11	11	10	9	8	15	14	13	12	3	2	1	0																				
12	12	13	14	15	8	9	10	11	4	5	6	7	0																			
13	13	12	15	14	9	8	11	10	5	4	7	6	1	0																		
14	14	15	12	13	10	11	8	9	6	7	4	5	2	3	0																	
15	15	14	13	12	11	10	9	8	7	6	5	4	3	2	1	0																
16	16	17	18	19	20	21	22	23	24	25	26	27	28	29	30	31	0															
17	17	16	19	18	21	20	23	22	25	24	27	26	29	28	31	30	1	0														
18	18	19	16	17	22	23	20	21	26	27	24	25	30	31	28	29	2	3	0													
19	19	18	17	16	23	22	21	20	27	27	25	24	31	30	29	28	3	2	1	0												
20	20	21	22	23	16	17	18	19	28	29	30	31	24	25	26	27	4	5	6	7	0											
21	21	20	23	22	17	16	19	18	29	28	31	30	25	24	27	26	5	4	7	6	1	0										
22	22	23	20	21	18	19	16	17	30	31	28	29	26	27	24	25	6	7	4	5	2	3	0									
23	23	22	21	20	19	18	17	16	31	30	29	28	27	26	25	24	7	6	5	4	3	2	1	0								
24	24	25	26	27	28	29	30	31	16	17	18	19	20	21	22	23	8	9	10	11	12	13	14	15	0							
25	25	24	27	26	29	28	31	30	17	16	19	18	21	20	23	22	9	8	11	10	13	12	15	14	1	0						
26	26	27	24	25	30	31	28	29	18	19	16	17	22	23	20	21	10	11	8	9	14	15	12	13	2	3	0					
27	27	26	25	24	31	30	29	28	19	18	17	16	23	22	21	20	11	10	9	8	15	14	13	12	3	2	1	0				
28	28	29	30	31	24	25	26	27	20	21	22	23	16	17	18	19	12	13	14	15	8	9	10	11	4	5	6	7	0			
29	29	28	31	30	25	26	27	28	21	20	23	22	17	18	19	18	13	12	15	14	9	8	11	10	5	4	7	6	1	0		
30	30	31	28	29	26	27	24	25	22	23	20	21	18	19	16	17	14	15	12	13	10	11	8	9	6	7	4	5	2	3	0	
31	31	30	29	28	27	26	25	24	23	22	21	20	19	18	17	16	15	14	13	12	11	10	9	8	7	6	5	4	3	2	1	0
	0	**1**	**2**	**3**	**4**	**5**	**6**	**7**	**8**	**9**	**10**	**11**	**12**	**13**	**14**	**15**	**16**	**17**	**18**	**19**	**20**	**21**	**22**	**23**	**24**	**25**	**26**	**27**	**28**	**29**	**30**	**31**

Table 2.1. The multiplication table between the 32 Hadamard's functions.

2.33 PSHB material : octaethylporphyrin in polystyrene (OEP/PS)

Holographic storage basically requires a medium with high optical quality. Among the PSHB materials, organic dye-molecule-doped polymers and rare-earth-ion-doped crystals, can satisfy the requirement. These two classes of media work on rather different spectral scales with different spectral resolutions. With rare-earth ion/crystal systems, one has made some success using hybrid approaches on the GHz scale at liquid helium temperature. On the other hand, applying PSHB at higher temperature, we should consider a much larger spectral range because the hole width broadens with the temperature according to a $T^{1.3}$ power law in amorphous hosts [23,26]. Dye/polymer systems offer us a material model on a THz scale. Porphyrin-derivatives/polymer systems are a kind of relatively well-studied materials [23]. Some of them have been widely used in holographic FDOS and TDOS for their long-lived spectral holes and easy fabrication with high optical quality and stability [17-22].

In our experiment, we use one of this material family, octaethylporphyrin doped in polystyrene (OEP/PS) as the memory element. Usually, the porphyrin/polymer is made in a simple way, dissolving the dopants and polymer in a solvent, then the mixture solution evaporates naturally at room temperature and finally forms a slab of polymer doped by porphyrin molecules. The structures of the dopant and of the polymer host used are illustrated in Figure 2.9. A 1mm-thick piece of OEP/PS is cooled down to 1.7K in a liquid-helium bath cryostat (from SMC-l'Air Liquide). The processes of data-recording and data-recovery are carried out at this temperature.

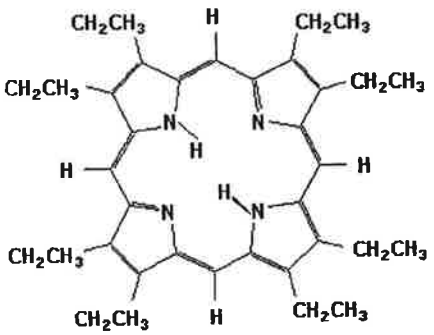

Octaethylporphine

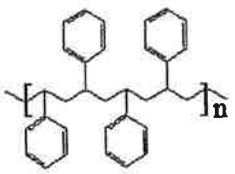

Polystyrene

Figure 2.9. Molecular structure of octaethylporphyrin and polystyrene.

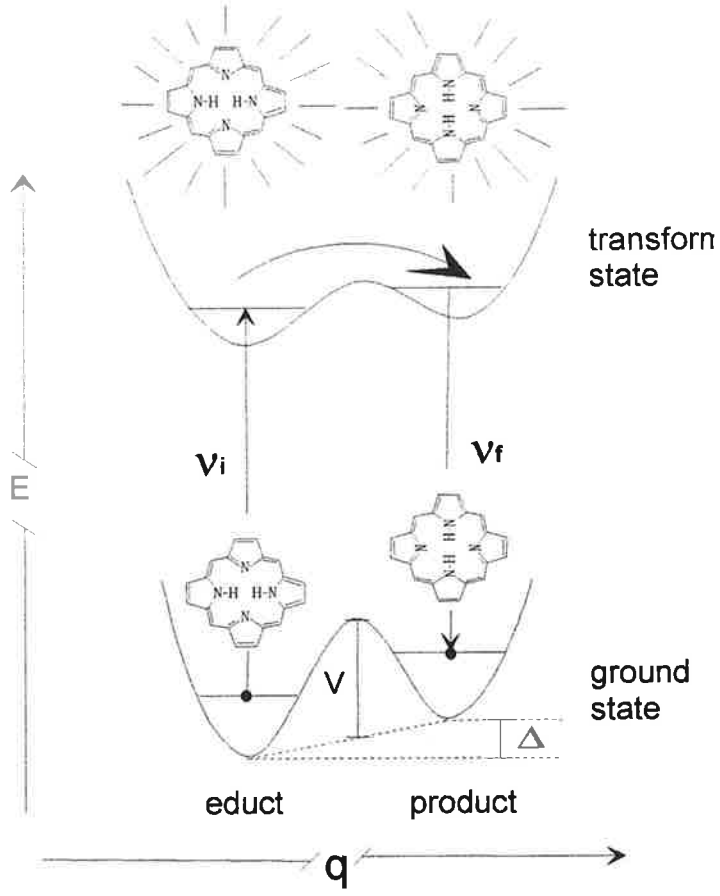

Figure 2.10. Energy diagrams for OEP/PS and the light-induced proton transfer process.

The PSHB mechanism in this sample, as well known for porphyrin/polymer systems, is attributed to the tautomeric photoreaction involving the two inner protons of the porphyrin ring [23,24]. The rotation of the proton pair forms two stable tautomers of porphyrin molecules which absorb at different frequencies in a solid host and can be then distinguished. At room temperature, the proton pair rotates nearly freely between the two positions at a rate of about $6000s^{-1}$ [25]. When the sample is cooled down gradually to liquid helium temperature, the proton transfer is frozen for the ground state, and the molecular distribution between the two tautomers reaches an equilibrium. However, proton transfer can still occur in excited states [24]. A simple diagram of molecular energy levels and light-induced proton transfer is sketched in Figure 2.10. A molecule in one of its tautomeric forms (called educt) is excited from its initial ground state to an excited state, where the proton transfer is active, the molecule transforms into another tautomer (product), and finally relaxes to its stable ground

state. The energy level shift between educt and product results in the difference of resonant frequencies, thus a dip appears on the original absorption band.

The lowest singlet-singlet absorption band (labeled as $Q_x(0\text{-}0)$) of an OEP/PS sample is shown in Figure 2.11. The full width at half maximum of the inhomogeneous line is Γ_{in}~4THz, with a maximal optical density O.D.~1.8 at 618.7nm. The homogeneous width measured at 2K under weak excitation is Γ_{hom}~0.5GHz [23, 26].

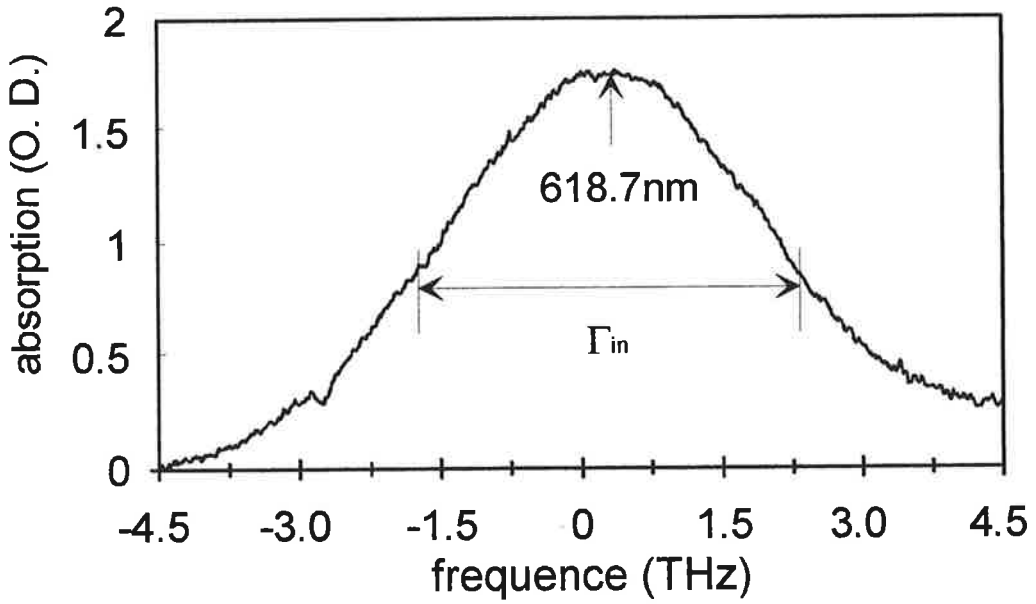

Figure 2.11. The absorption profile of the lowest singlet-singlet electronic transition band of OEP in PS, centered at 618.7nm.

In the actual storage experiment, we use an optically thick sample with an optical density O.D. ~5 at the maximum of the absorption band. The spectral window for recording (Δ=1.1 THz) is several times narrower than Γ_{in}. The width of the elementary spectral slice in the encoding functions (δ=35GHz) is much larger than Γ_{hom}.

2.4 Experimental results

2.41 Test of the encoding and the detection systems

In order to test the encoding and the detection systems, we measure the temporal profiles of the 32-Hadamard functions as follows, with the correlator shown in figure 2.3. The sample is removed and the object path is blocked. The laser beam is split equally into reference and gating beams. The gating beam directly issued from the laser is regarded as a gate function (function 0), while the reference beam passes through the pulse shaper and is encoded by one of the Hadamard function $f_n(\nu)$. The cross-correlation function between the two pulses reads as,

$$G_n(T)=\left|\tilde{\mathcal{E}}_L(\nu_0)\right|^2 \int_{\nu_0-\Delta/2}^{\nu_0+\Delta/2} f_0^{*}(\nu) f_n(\nu) e^{-2i\pi\nu T} d\nu \qquad (2.14)$$

Thus the temporal profile of a given Hadamard function is measured in term of T-dependent cross-correlation by scanning DL2. In figure 2.12, we present the spectral structures of several code functions (figure 2.12(a)), their temporal profiles calculated by Fourier transform (figure 2.12(b)) and those measured in term of cross-correlation (figure 2.12(c)). The good coincidence between the theoretical and experimental profiles verifies that the pulse shaper and correlator combined system works well. All the encoded functions $f_n(\nu)$, with $n \neq 0$, are orthogonal to $f_0(\nu)$. In our experiment it is crucial that this orthogonality property is correctly transferred to the pulse spectra and correctly detected by the correlator. According to Eq. (2.14), the orthogonality of $f_n(\nu)$ and $f_0(\nu)$ is revealed at T=0. This is properly verified on the experimental data of Figure 2.12 (c). Such a good result is based on the correct adjustment of the optics including two-grating system, SLM, and the correlator. Details can be found in the Ph.D dissertation of François Grelet[27].

(a)

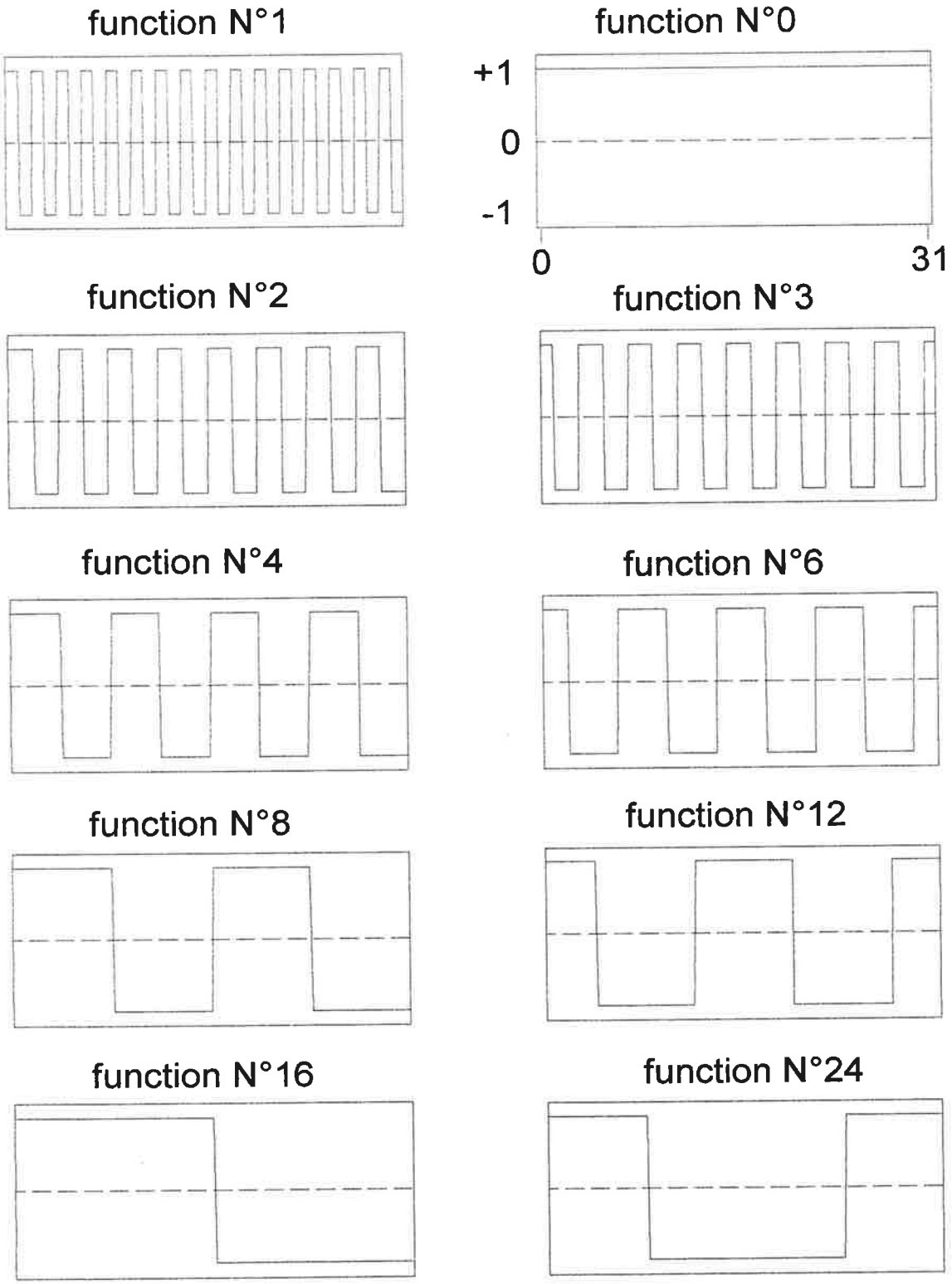

Figure 2.12 (a) Spectral structure of code functions.

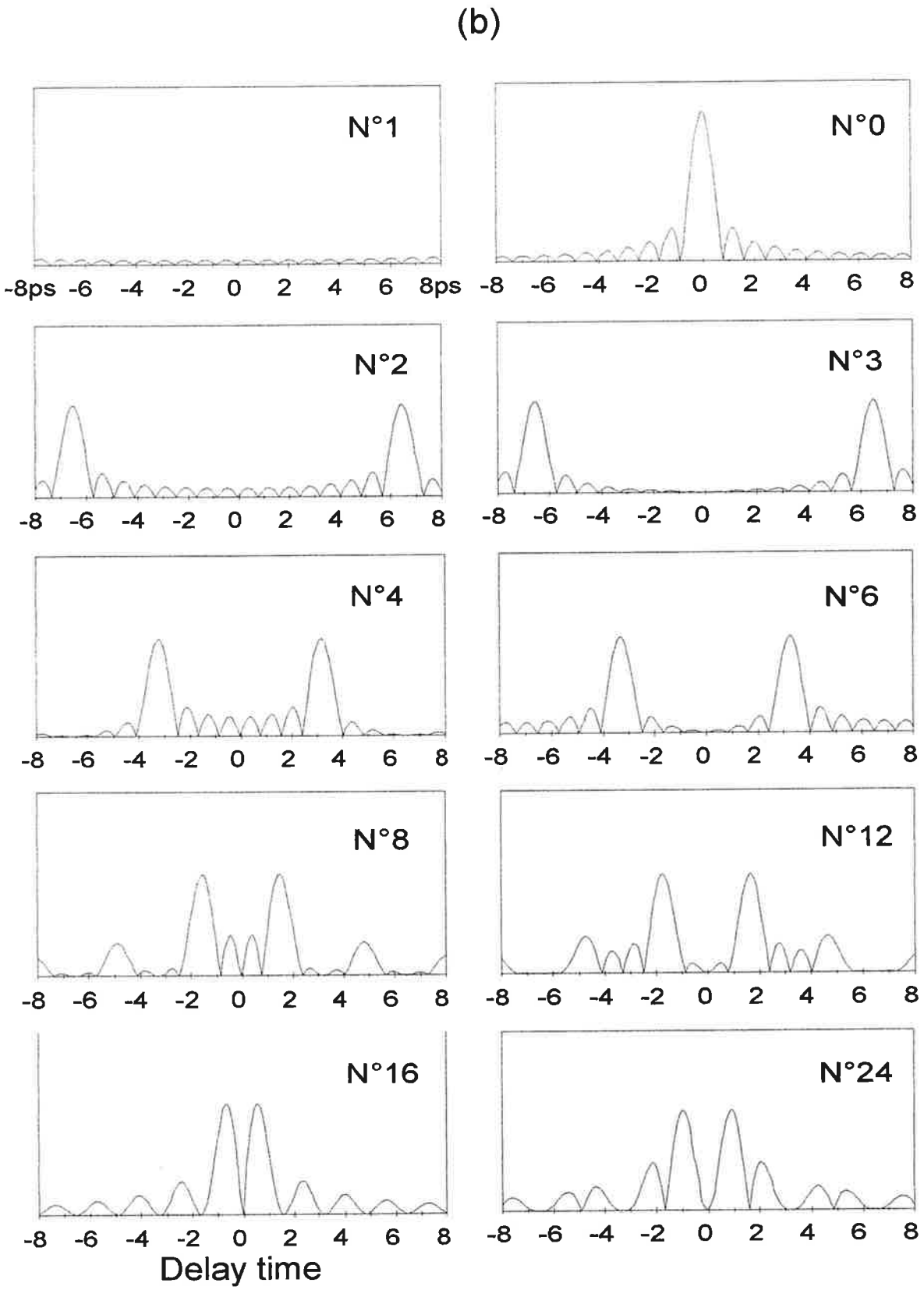

Figure 2.12 (b) Calculated temporal profile of codes.

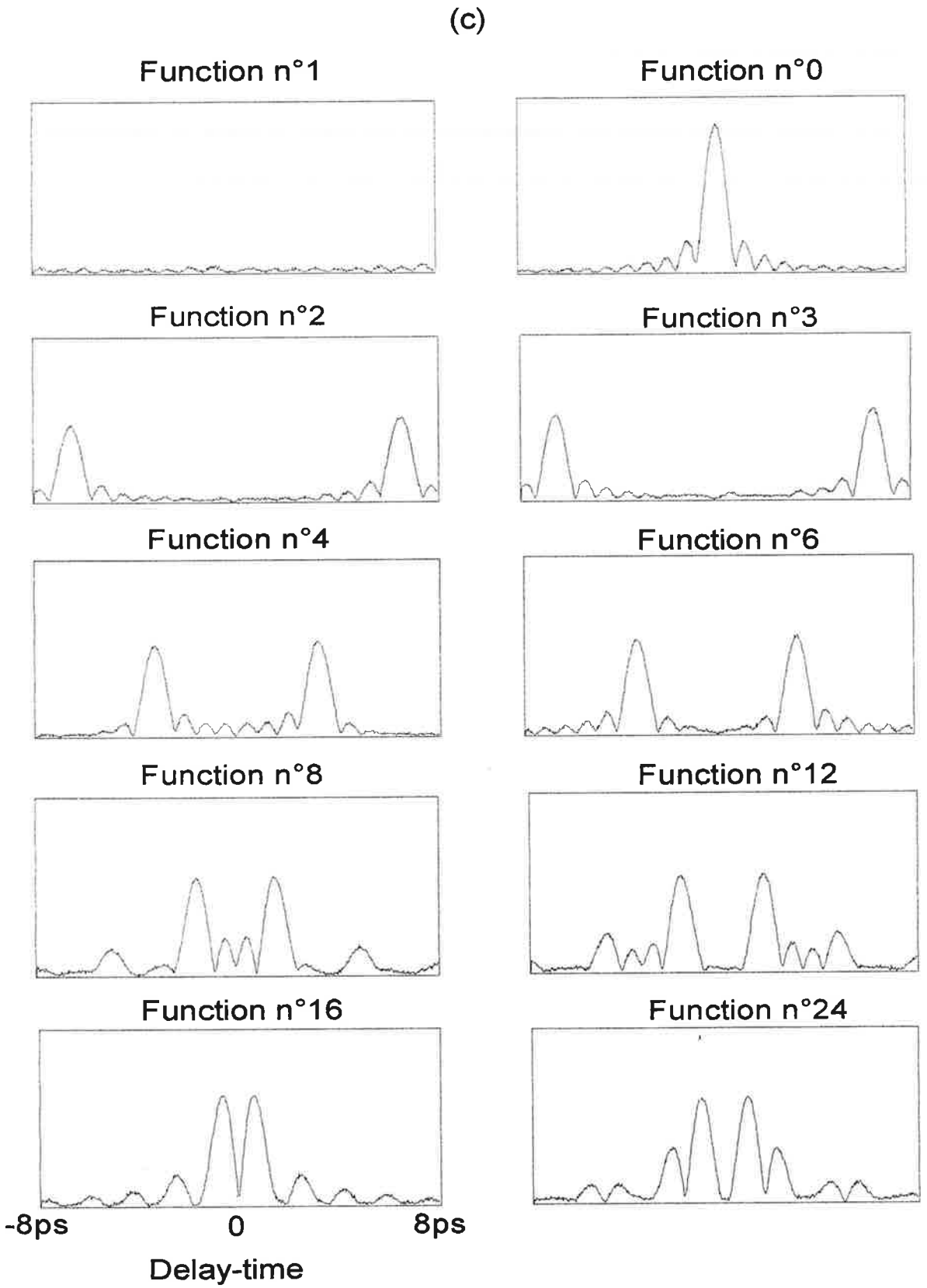

Figure 2.12 (c) Temporal profiles measured by cross-correlation

2.42 Data storage and retrieval

The optical configuration for spectral-phase-encoded storage is presented in Figure 2.13 and 2.14. The SLM is programmed with 32 Hadamard functions as spectral biphase codes. The spectral window is Δ=1.1THz and the pixel width δ=35GHz. The optical delay-lines DL1 and DL2 have a mechanical precision of 1μm/step. The time-delay between the reference and object pulses is set approximately to τ=26ps by adjusting DL1. The DL2 is precisely adjusted to make T=τ where maximal auto-correlation function of code N°0 and minimal cross-correlation function between code N°0 and N°16 can be obtained.

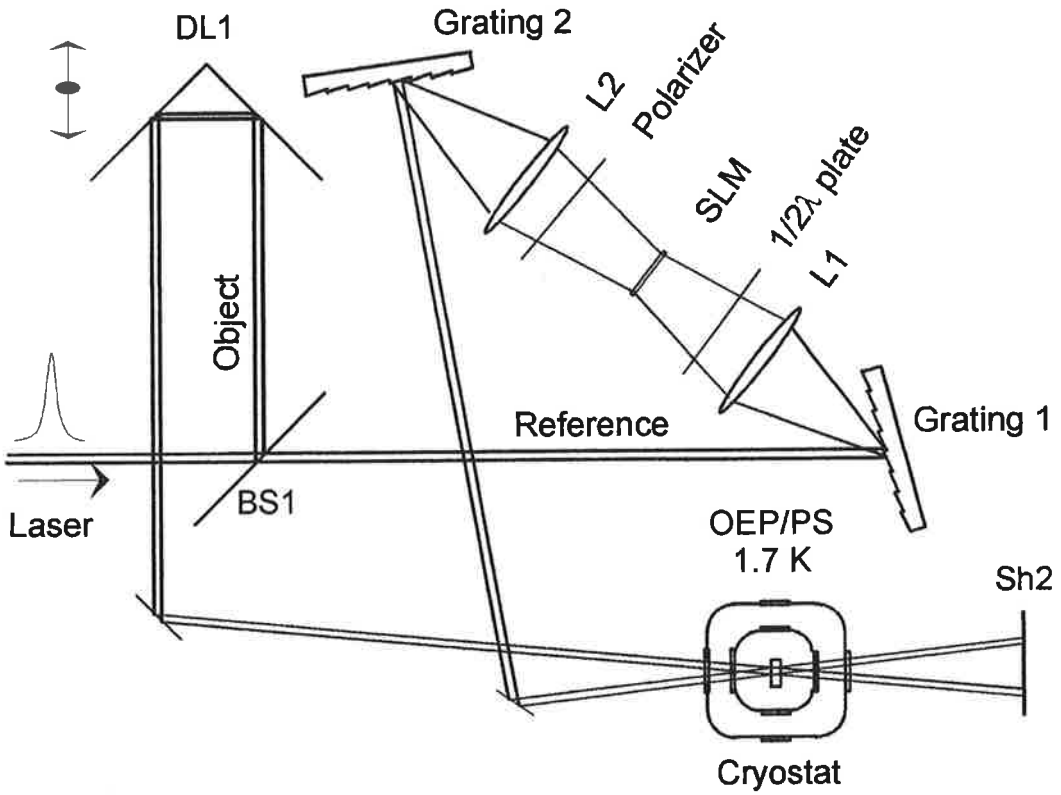

Figure 2.13 *Experimental setup for recording spectrally phase-encoded binary data. BS: Beam Splitter, Sh: Shutter, L: Lens, DL: Delay-line.*

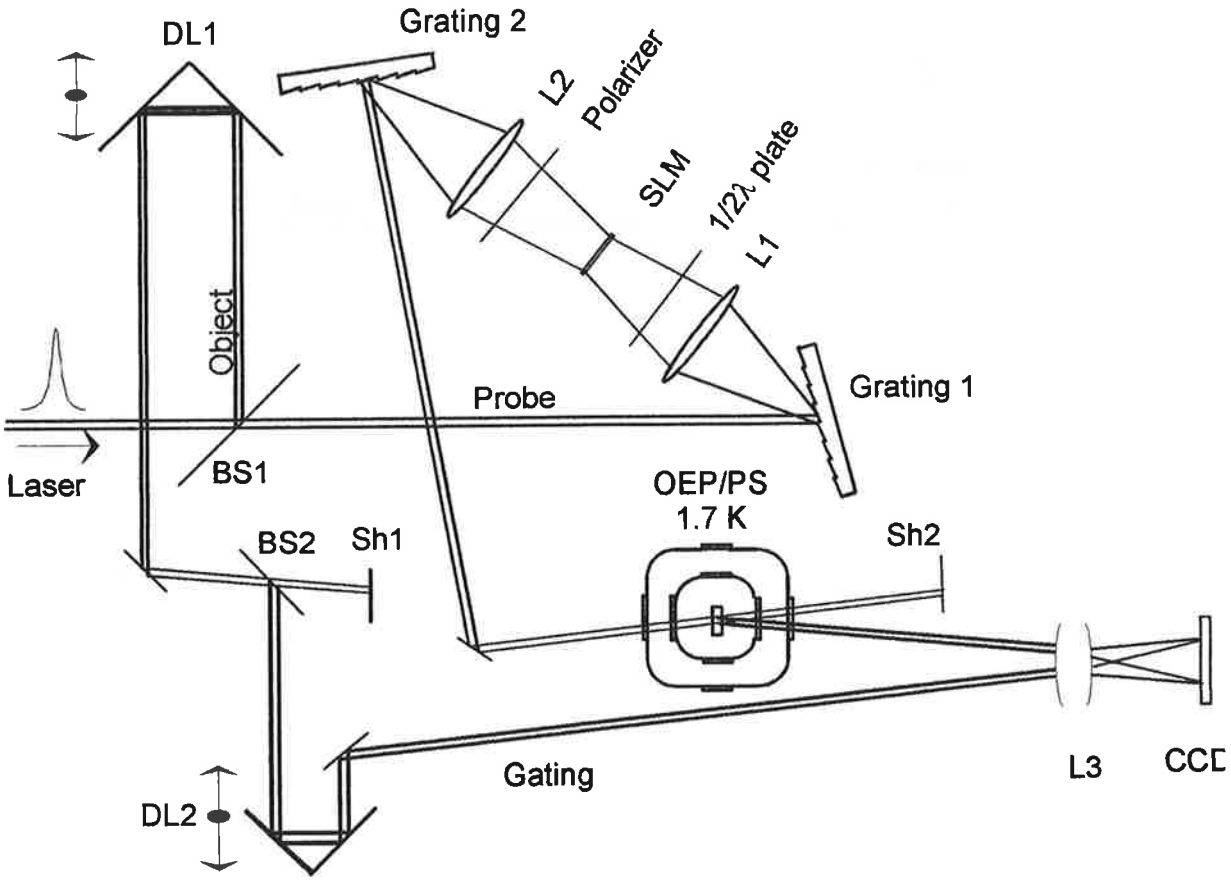

Figure 2.14 Experimental setup for the retrieval of spectral-phases encoded binary data, with the same notations as in Figure 2.13.

We first store a binary '1' with the arrangement shown in Figure 2.13. The SLM is set to the step function. The datum is recorded in the OEP/PS sample by reference and object beams with an areal exposure dose of about 20 $mJ.cm^{-2}$. In recovery step presented in Figure 2.14, the object beam is blocked by Sh1 and the probe beam goes through the same way as that of the reference. The 32 code functions are charged successively to the SLM at the rate of one function every 20 laser shots. In the meanwhile, the correlation function between the gating and diffracted fields is recorded by the CCD array. The experimental data displayed in Figure 2.15 results from the average of the correlation signal amplitude over 20 laser shots at each read-out address. A peak is observed when the readout code coincides with the recording one (N°16). Readout with the 31 other address codes gives rise to a background that defines the binary '0' level.

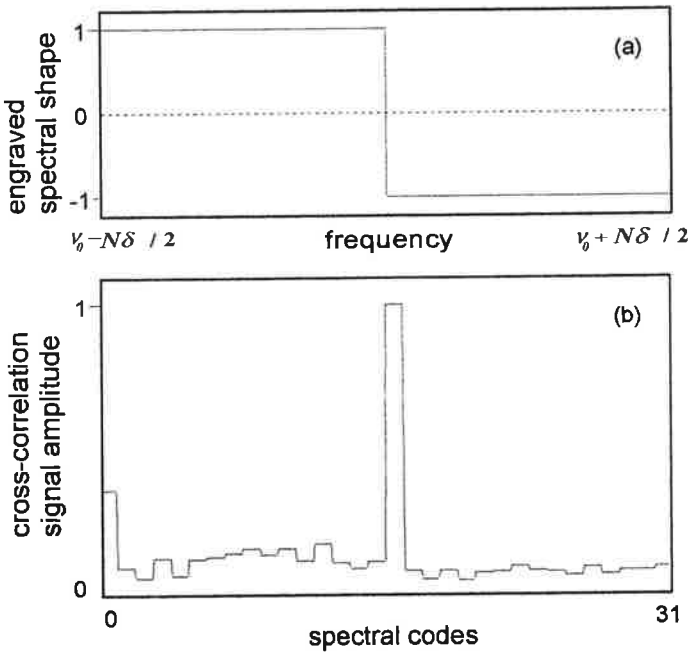

Figure 2.15 *Storage of one bit '1' addressed by the step function (N° 16). (a) The engraved spectral shape modified by the step function. (b) Experimental cross-correlation signal amplitude, measured by succesively applying the 32 address codes.*

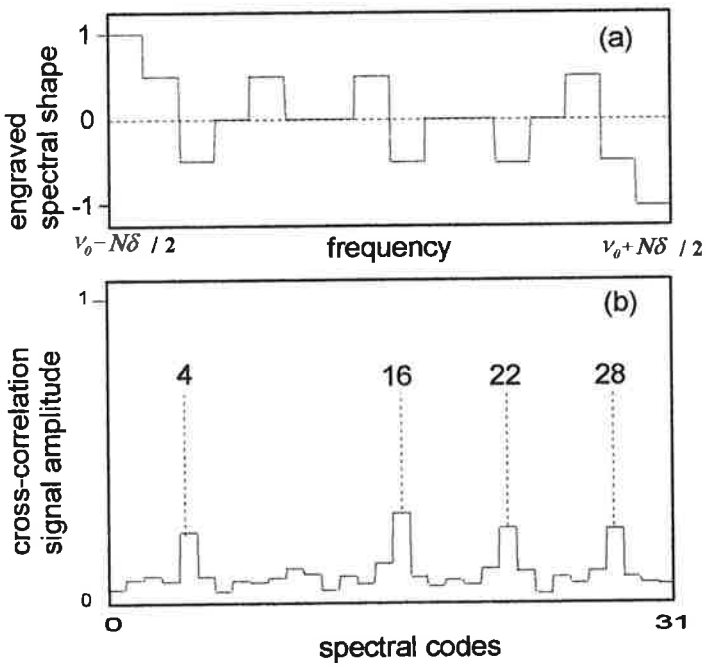

Figure 2.16 *Storage of four bits '1' addressed by the functions N° 4, 16, 22, 28, respectively. Same notations as in Figure 2.15.*

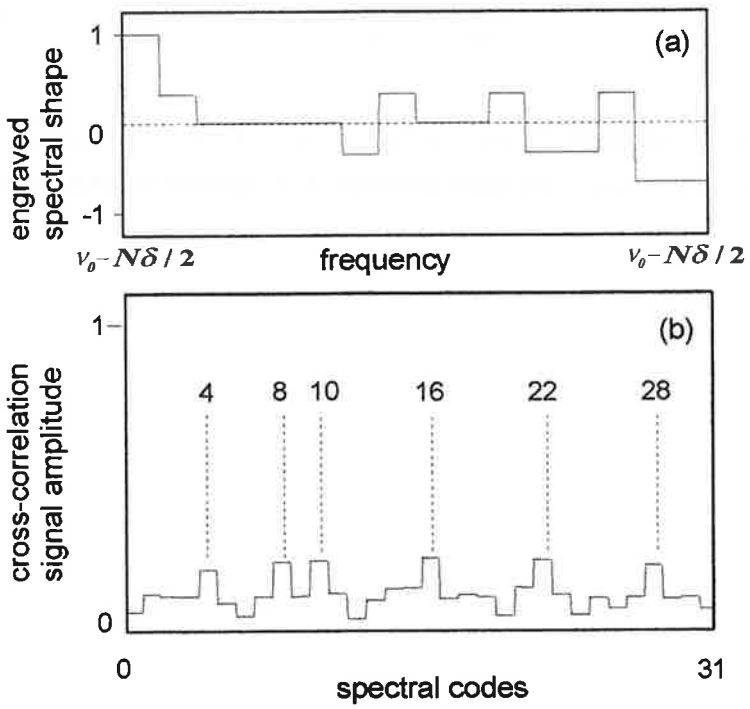

Figure 2.17 Storage of six bits '1' addressed by the functions N° 4, 8, 10, 16, 22, 28, respectively. Same notations as in Figure 2.15.

In storing several data, we meet the problem of spectral hole erasing. When a new hologram is written in the medium, it eliminates the previously recorded one. In order to keep an equilibrium between the diffracted signal from each stored datum, we use a cyclic procedure in recording. During one cycle, the data are successively addressed to the memory. Each datum is exposed for 2 seconds per cycle, and the cycle is repeated 28 times. The read-out signals after the storage of four bits '1' (addressed by the codes N°4, 16, 22, 28) and then six bits '1' (addressed by the codes N°4, 8, 10, 16, 22, 28) are presented, respectively, in Fig 2.16 and 2.17. The incremental recording procedure yields a good balance between the different bits.

2.43 Discussion

In the experiment, distinct data can be observed at their corresponding addresses. But signals are also detected at other empty addresses. The crosstalks between different addresses result from these unexpected signals which are due to the

distortion of the orthogonality between the addresses. Crosstalks form a background as level '0' with respect to level '1'. For a single datum storage, we have an acceptable ratio between the amplitudes of '1' and '0'. But this signal to background ratio decreases rapidly with the number of recorded data. When the total exposure energy is kept at the same value for a M-data storage, the energy devoted to each datum is proportional to M^{-1}. So the stored data signal decreases with M, in the meantime the background of the '0' level coming from crosstalk between different addresses keeps the same level, or even becomes higher. Under this condition, we cannot achieve the expected storage density. In fact, the background at some addresses already reaches 60% of the signal in the case of 6-bit storage. It is necessary to optimize the experimental conditions to attain higher storage density, and this optimization has to be based on a systematic study on the sources of the crosstalk in our present experiment.

Any distortion of the engraved structure, in recording or in retrieval steps, can destroy the orthogonality between the address codes and then generates crosstalks. The encoding device and the cross-correlation detector have been tested in section 2.41. According to this test, their contribution to the cross-talk is expected to be small. Therefore the observed crosstalk in our experiment is likely to result from the violation of the prerequisites of the principle description (section 2.2). They include optically thin material with narrow homogeneous width, uniform spectral distribution of molecules and laser energy within the recording window, weak burning energy, and temporal separation between the reference and object pulse

Only the last condition was surely satisfied in the experiment. The remaining ones were, more or less, disobeyed. The spectral width of the laser source used in experiment was measured to be about 1.4THz, by the help of auto-correlation function. Considered as a Gaussian distribution, the laser intensity undergoes a ~34% variation from the center to the edge of the 1.1THz spectral window. The non-uniformity of the laser spectrum distorts the address structure through recording, probing and signal detection. We realized that we cannot simply broaden the laser spectrum to make it uniform within the SLM window because we need the reference, object and gating bandwidths be similar. When the laser spectrum is much broader than the spectral window of the SLM, the object beam has many spectral components beyond this window, and this affects the structure of recorded holograms. Besides, the gating spectrum is much broader than that of the retrieved signal and this reduces the cross-

correlator sensitivity. A nearly rectangle spectrum of the laser source could be obtained by adding a spectral filter on the laser beam. The consequences of such filtering will be presented in chapter 4.

In our experiment, the poor sensitivity of the detection system caused by the spatial non uniformity of the gating beam intensity on the CCD array forced us to resort to large exposure and large optical density so that we could boost the diffracted signal intensity. It is doubtable that the material works in a perturbation regime. As the engraved spectral shape after a multi-bit storage has a gray-scale structure, it suffers from the distortion caused by the PSHB saturation effect. Furthermore, we used an optically thick sample. The optical density of the sample was measured to be OD~5 at the central absorption. The storage was effectuated in the wing of the absorption band where OD was estimated to be 1~2. The optical thickness of the medium affects the propagation of recording, probing and signal fields, and may result in spectral distortion.

The material model has to be studied also when we consider the complexity of the mechanism of photochemical PSHB and the related microprocesses in OEP/PS sample.

The medium properties and their consequences in the recording/retrieval step will be discussed in the following chapters.

2.5 Conclusion

We have presented a spectral-phase-encoded time-space-domain holographic technique for fast random data access in frequency selective materials. The experimental arrangement was built up for this approach. Single binary bit and multi-bit storage have been practically demonstrated, which can be regarded as a preliminary work of one point-image storage. It should open the way to fast random access retrieval of images in spectral selective materials.

At present time, we meet the problem of the competition between signal intensity and storage density. More efforts are needed to enhance the signal-to-noise ratio to achieve high density storage. Since the analysis in the optical aspect has been presented by ref [27], we will engage our main work in the aspect of material. The next three chapters are devoted to understanding the microprocesses in our medium and researching the optimized storage condition.

2.6 References

[1] H. Sonajalg, A. Débarre, J.-L. Le Gouët, I. Lorgeré, and P. Tchénio, *'Phase-encoding technique in time-domain holography : theoretical estimation'*, J. Opt. Soc. Am., **B12**, 1448 (1995).

[2] Y. Taketomi, J. E. Ford, H. Sasaki, J. Ma, Y. Fainman, and S. H. Lee, *'Incremental recording for photorefractive hologram multiplexing'*, Opt. Lett., **16**, 1774 (1991).

[3] C. Denz, G. Pauliat, G. Roosen, and T. Tschudi, *'Volume hologram multiplexing using a deterministic phase encoding method'*, Opt. Commun., **85**, 171 (1991).

[4] C. Denz, G. Pauliat, G. Roosen, and T. Tschudi, *'Potentialities and limitations of hologram multiplexing by using the phase-encoding technique'*, Appl. Opt., **31**, 5700 (1992).

[5] A. Débarre, J.-C. Keller, J.-L. Le Gouët, A. Richard, and P. Tchénio, *' An amplitude corerlator for broadband laser source charaterization'*, Opt. Commun. **73**, 309 (1989).

[6] R. N. Thurston, J. P. Heritage, A. M. Weiner, and M. J. Tomlinson, *'Analysis of picosecond pulse shape synthesis by spectral masking in a grating pulse compressor'*, IEEE J. Quantum Electron., **22**, 682 (1986).

[7] A. M. Weiner, D. E. Laird, J. S. Patel, and J. R. Wullert, *'Programmable shaping of femtosecond optical pulses by using of 128 liquid crystal phase modulator'*, IEEE J. Quantum Electron., **28**, 908 (1992).

[8] A. M. Weiner, R. N. Thurston, M. J. Tomlinson, J. P. Heritage, D. E. Laird, E. M. Kirshner, and R. J. Hawkins, *'Temporal and spectral self-shifts of dark optical soliton'*, Opt. Lett., **14**, 868 (1989).

[9] A. M. Weiner, J. P. Heritage, and J. A. Salehi, *'Encoding and decoding of femtosecond pulse'*, Opt. Lett., **13**, 300 (1988).

[10] A. M. Weiner, Y. Silberberg, H. Foukhardit, D. E. Laird, M. A. Saifi, M. J. Andrejco, and P. V. Smith, *'Use of femtosecond square pulse to avoid pulse breakup in all-optical switching'*, IEEE J. Quantum Electron., **25**, 2648 (1989).

[11] A. M. Weiner, D. E. Laird, D. H. Reintz, and E. G. Paek, *'Spectral holograph of shaped femtosecond pulse'*, Opt. Lett., **17**, 224 (1992).

[12] W. R. Babbitt and T. W. Mossberg, *'Spectral routing of optical beams through time-domain spatial-spectral filtering '*, Opt. Lett., **20**, 910 (1995).

[13] M. Ratsep, M. Tian, F. Grelet, J.-L. Le Gouët, C. Sigel, and M.-L. Roblin, *'Time-encoded spatial routing in a photorefractive crystal'*, Opt. Lett., **21**, 1292 (1996).

[14] I. Lorgere, M. Ratsep, J.-L. Le Gouët, F. Grelet, M. Tian, A. Debarre, and P. Tchenio, *'Storage of a spectral shaped hologram in a frequency selective material'*, J. Phys. **B**: At. Mol. Phys., **28**, L565 (1995).

[15] M. Ratsep, M. Tian, F. Grelet, J.-L. Le Gouët, *'Fast random access to frequency-selective optical memories'*, Opt. Lett., **21**, 83 (1996).

[16] I. Lorgere, M. Ratsep, J.-L. Le Gouët, F. Grelet, M. Tian, C. Sigel, and M.-L. Roblin, *'Spectral phase encoding for data storage and addressing'*, J. Opt. Soc. Am., **B13**, 2229 (1996).

[17] B. Kohler, S. Berrnet, A. Renn, and U. P. Wild, *'Storage of 2000 holograms in a photochemical hole-burning system'*, Opt. Lett., **18**, 2144 (1993).

[18] E. S. Maniloff, S. B. Altner, S. Berrnet, F. R. Graf, A. Renn, and U. P. Wild, *'Recording of holograms by use of spectral hole burning'*, Appl. Opt., **34**, 4140 (1995).

[19] A. Rebane, R. Kaarli, P. Saari, A. Amjalg, and K. Timpmann, *'Photochemical time-domain holography of weak picosecond pulses'*, Opt. Commun., **47**, 173 (1983).

[20] P. Saari, R. Kaarli, and A. Rebane, *'Picosecond time- and space- domain holography by photochemical hole burning'*, J. Opt. Soc. Am., **B3**, 527 (1986).

[21] A. Rebane, J. Aaviksoo, and J. Kuhl, *'Storage and time reversal of femtosecond light signal via persistent spectral hole burning holography'*, Appl. Phys Lett., **54**, 93 (1989).

[22] D. Erni, A. Rebane, and U. P. Wild, *'Spectral controlled interference of picosecond time- and space- domain holograms'*, Opt. Lett., **20**, 1065 (1995).

[23] 'Persistent Spectral Hole-Burning : Science and Application', W. E. Moerner. Ed., (Springer-Verlag, Berlin, 1988).

[24] S. Volker and R. M. Macfarlane, *'Photochemical hole burning in free-base porphyrin and chlorin in n-alkane matrices'*, IBM J. Res. Develop., **23**, 547 (1979).

[25] M. J. Crossley, M. M. Harding, and S. Sternhell, *' Tautomerism in 2-substituted 5,10,15,20-tetraphenylporphyrins'*, J. Am. Chem. Soc. 108, 3608 (1986).

[26] A special issue of the Journal of Luminescence devoted to the topic of optical linewidth in glasses, J. Lumin., **36**, 179-329 (1987).

[27] F. Grelet, PhD dissertation, (in French)*' Holographie spectro/temporelle: adressage par codage de phase'*, Université Paris XI Orsay, France (July,1997).

CHAPTER 3

SPECTRAL HOLOGRAPHY: A PORTABLE MODEL

3.1 Introduction

The large cross-talk that we observed in the experimental investigation of phase-encoded addresses incites us to clarify our understanding of spectral holography in PSHB materials. Without further investigation we know that uniform spectral distributions of molecules and burning energy over the storage window are required to encode addresses in the way outlined in Chapter 2. From our elementary description of the recording process, we also know that the phase-encoded addresses are orthogonal under small exposure and small optical density conditions. However, according to theoretical investigations [1-4] one expects much larger diffraction efficiency by heavily burning spectral holograms in large optical density samples. Unfortunately, these theoretical predictions do not simply apply to our problem since the burning pulses they consider do not carry any spectral structure. Besides, they assume that burnt molecules disappear from the excitation spectral window, which is not true in octaethylporphine-doped polystyrene. In a previous calculation[5], the spectral phase-encoding structure was included but it was assumed that the burning energy was evenly distributed within the depth of the sample. The validity range of this approximation is restricted to optical densities smaller than unity.

In order to elucidate the influence of the burning dose and of the optical density on the crosstalk between phase-encoded addresses, we have undertaken a two-step investigation. A simple model is first developed. It aims at drawing a few general properties of the signal formation in a large optical density material. This model is exposed in the present chapter. In chapter 4, with these properties in mind, we build a more refined model that includes the tautomerization mechanism of hole burning and we compare theoretical predictions with experimental data.

The model that we develop in chapter 3 relies on the following assumptions:

(i) Accumulated recording is a gradual burning procedure with a large number of weak pulse pairs. Each pulse pair propagates through a medium that has been altered by the previous pairs, but one ignores the feedback of the current pair burning effect on its own propagation.

(ii) A small angle between the reference and object pulses guarantees that a large number of coupled waves are phase-matched for propagation through the sample.

(iii) The time interval between two writing pulses is large enough to avoid overlap.

(iv) The PSHB medium is regarded as an assembly of photosensible grains with a uniform initial spatial distribution. The size of the spectral grains Γ_{hom} is smaller than the period of spectral interference structure τ^{-1}. The photochemical products disappear from the spectral region occupied by the hologram.

After an outline of the coupled-wave theory in section 3.2, we calculate the expression of the stored hologram in section 3.3 and the signal amplitude in section 3.4. In section 3.5, we discuss the signal behavior under different recording energy dose. We end this chapter with a conclusion in section 3.6

3.2 Coupled-wave theory

As depicted in figure. 3.1, a grating is engraved in a PSHB sample by sequences of reference and object pulses that propagate along directions $\vec{k}_1$ and $\vec{k}_2$, respectively, with a small angle θ in x-z plane. Since the field does not take any pattern in the y-direction, this coordinate can be ignored in the present discussion.

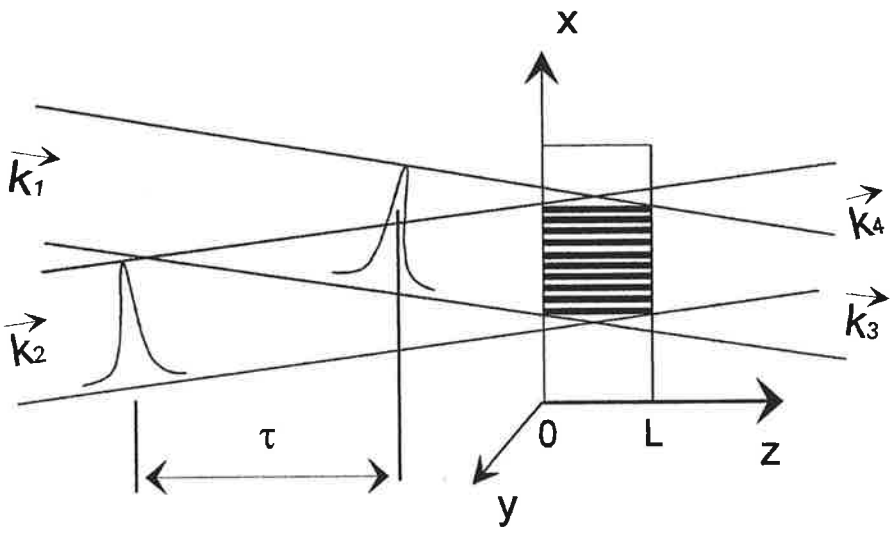

Figure 3.1 *Space-time holography. The reference, object, probe and signal pulses propagate along* $\vec{k}_1$, $\vec{k}_2$, $\vec{k}_3$, *and* $\vec{k}_4$ *respectively.*

According to the dispersion relations[4], the space and frequency dependent relative dielectric permittivity can be expressed as the following function of the absorption coefficient $\alpha(z,x,\nu)$:

$$\varepsilon_r(z,x,\nu)=1-ik_0^{-1}(1+i\hat{H})\alpha(z,x,\nu) \qquad (3.1)$$

where $k_0=\frac{2\pi\nu_0}{c}$, is the wave vector length, ν_0 denotes the central frequency of the propagating field, and the Hilbert operator $\hat{H}$ is defined by:

$$\hat{H}\,[f(\nu)]=\frac{1}{\pi}\int\frac{f(\nu')}{\nu'-\nu}d\nu' \qquad (3.2)$$

The imaginary and the real parts of $\varepsilon_r(z,x,\nu)$ correspond to the absorption and the refraction, respectively. When a population grating is generated in the medium, an absorption grating is formed and it is accompanied by a refraction one. Both of them act on the electric field $E(\vec{r},t)$ in the medium. The spectral components of the field satisfy the wave equation:

$$\Delta\tilde{E}(\vec{r},\nu)+\varepsilon_r(\vec{r},\nu)\,k_0^2\,\tilde{E}(\vec{r},\nu)=0 \qquad (3.3)$$

The spatial population grating engraved by the impinging fields is a x-dependent periodic function. Its period equals $2\pi/K$, where $K=\left|\vec{k}_2-\vec{k}_1\right|$. Thus we can expand $\alpha(x,z,\nu)$ as a Fourier series:

$$\alpha(z,x,\nu)=\sum_p\tilde{\alpha}^{(p)}(z,\nu)\,e^{-ipKx} \qquad (3.4)$$

where:
$$\tilde{\alpha}^{(p)}(z,\nu)=\frac{K}{2\pi}\int_{<\frac{2\pi}{K}>}\alpha(z,x,\nu)e^{ipKx}dx \qquad (3.5)$$

and p numbers the different spatial modes of the grating.

The propagating field is also a periodic function of x and it can be expanded as the following series of spatial modes:

$$\tilde{E}(\vec{r},\nu)=\sum_p\underline{\tilde{E}}^{(p)}(z,\nu)\,e^{-i(\vec{k}_1\cdot\vec{r}+pKx)} \qquad (3.6)$$

where:
$$\underline{\tilde{E}}^{(p)}(z,\nu)=\frac{K}{2\pi}\int_{<2\pi/K>}\tilde{E}(\vec{r},\nu)e^{i(\vec{k}_1\cdot\vec{r}+pKx)}dx \qquad (3.7)$$

Substituting (3.5) and (3.6) into the wave equation (3.3), we obtain the equation of the coupled waves [6]:

$$\frac{\partial}{\partial z}\underline{\tilde{E}}^{(p)}(z,\nu)+\frac{1}{2}(1+i\hat{H})\tilde{\alpha}^{(0)}(z,\nu)\,\underline{\tilde{E}}^{(p)}(z,\nu)-i\frac{(\vec{k}_1+p\vec{K})^2-k_0^2}{2k_0}\underline{\tilde{E}}^{(p)}(z,\nu)=$$

$$-\frac{1}{2}\sum_{q\neq0}[(1+i\hat{H})\tilde{\alpha}^{(q)}(z,\nu)]\,\underline{\tilde{E}}^{(p-q)}(z,\nu) \qquad (3.8)$$

The different contributions to the z-variation of $\underline{\tilde{E}}^{(p)}(z,\nu)$ can be identified as damping, dephasing, and coupling terms. The third component on the left-hand side of the equation accounts for the phase shift that builds up between the propagating field and

the periodic structure that generates it. The phase shift per length unit is $[(\vec{k}_1 + p\vec{K})^2 - {k_0}^2]/2k_0$. In the limit of a small angle θ between $\vec{k}_1$ and $\vec{k}_2$, the phase shift accumulated through the sample thickness L reduces to $\pi p(p-1)\frac{L}{\lambda}\theta^2$. The waves p=0 and p=1 undergo no phase shift.

The coupled-wave equation is used to describe the propagation of the engraving fields and the diffraction of the probe pulse.

3.3 Accumulated storage

A set of M holograms is stored in the PSHB sample. Each hologram is defined by a pair of reference and object pulses. A pulse-pair impinges on the medium after the molecules excited by the previous pulses return to the stable state, and before the accumulated engraving disappears. In our case, the minimal and the maximal time intervals between two adjacent pairs are determined, respectively, by the life time of the triplet state (~10ms) and by the life time of the hole (several hours). One pair of pulses is insufficient to store a detectable hologram. The stability of the spectral holes in this time range allows one to repeat a large number of the same pulse pairs for storing a single hologram. The spatial-spectral interference pattern constructed by each pulse pair is accumulated in the material by the successive modifications of the molecular population by the PSHB reactions. As a consequence, the diffracted holographic signal is enhanced. The accumulation proceeds until the PSHB process is saturated.

We assume N pairs are needed for storing one hologram. For M-hologram storage, the sample is illuminated by M×N pairs successively. In order to average undesired laser-induced erasure, it is preferable to engrave M holograms with a train of M different pairs, each pair corresponding to one hologram, and to repeat this M-pair sequence N times.

We denote the energy spectrum of the mth pulse-pair as, W(0, x, ν,m). It can be written as:

$$W(0, x, \nu, m)=W_0(\nu)[1+f_m(\nu)\cdot\cos(Kx+2\pi\nu\tau)] \qquad (3.9)$$

where the energy spectrum of the laser source, $W_0(\nu)$, is evenly shared between the reference and the object arms. The time interval of the two pulses is denoted by τ. The spectral function encoded on the reference pulse is represented by the shape factor $f_m(\nu)$. In Eq.(3.9), the cosine function describes the space-frequency interference pattern that is built by the fields. Its period is $2\pi/K$ in the x-direction and $1/\tau$ in the frequency dimension. The energy with a spatial and spectral distribution of the interference pattern burns a population grating of PSHB molecules in both the spatial and the spectral dimensions.

For each spectral component, the spatial grating is recorded in the medium as a conventional hologram. However, the spatial and spectral grating are always linked to each other in the spectrally selective medium. The space and frequency independent contribution on the right hand side of Eq.(3.9) only bleaches the molecular population.

In an optically thick sample, the burning energy decays in the z-direction because of absorption.The frequency-and-space energy distribution of the mth pulse pair in the excitation pulse train is denoted as,

$$W(z,x,\nu,m)= |\tilde{E}(z,x,\nu,m)|^2 \tag{3.10}$$

where $\tilde{E}(z,x,\nu,m)$ is the amplitude of the field in the sample. The sinusoidal structure of the interference term in (3.9) may be deformed when the incident energy propagates through an optically thick medium.

The burning effect is depicted by a simple exponential decay law that will be refined in Chapter 4. According to this simple model, the persistent holes burnt by m pairs of pulses affect the molecular distribution and the absorption coefficient in the following way:

$$n(z,x,\nu,m)= n_0(\nu)\prod_{m'=1}^{m} e^{-\beta(\nu)W(z,x,\nu,m')} = n_0(\nu)e^{-\beta(\nu)\sum_{m'=1}^{m}W(z,x,\nu,m')} \tag{3.11}$$

$$\alpha(z,x,\nu,m)=\alpha_0(\nu)e^{-\beta(\nu)\sum_{m'=1}^{m}W(z,x,\nu,m')} \tag{3.12}$$

where, $n_0(\nu)$ and $\alpha_0(\nu)$, respectively, denote the initial values of the molecular distribution and of the absorption coefficient. $\beta(\nu)$, a factor representing the hole burning efficiency. As they propagate through the sample, the burning fields are diffracted on the grating that they are building. The multiple components in which they divide themselves obey the coupled-wave Eq.(3.8). In the following we assume that the phase-matching condition:

$$p(p-1)\frac{L}{\lambda}\theta^2 << 1 \tag{3.13}$$

is satisfied by the most significant waves. We shall check the validity of this assumption in section 3.54. Then Eq.(3.8) reduces to:

$$\frac{\partial\underline{\tilde{E}}(z,x,\nu,m)}{\partial z}+\frac{1}{2}(1+i\hat{H})\alpha(z,x,\nu,m-1)\ \underline{\tilde{E}}(z,x,\nu,m)=0 \tag{3.14}$$

where:

$$\underline{\tilde{E}}(z,x,\nu,m) = \tilde{E}(z,x,\nu,m)e^{i\vec{k}_1\cdot\vec{r}} \tag{3.15}$$

We consider that each individual pulse pair is weak enough in writing. The mth pair propagates through a medium that has been modified by the m-1 previous ones. Derived from Eqs (3.10) and (3.14), the energy density propagation equation reads as:

$$\frac{\partial}{\partial z} W(z,x,\nu,m) + \alpha(z,x,\nu,m-1)W(z,x,\nu,m)=0 \qquad (3.16)$$

The total exposure energy conveyed by the incident pulses is defined as,

$$Y(z,x,\nu)= \sum_{m=1}^{M\times N} W(z,x,\nu,m) \qquad (3.17)$$

Considering $Y(z,x,\nu)$ as a sum of infinitesimal quantities, we integrate Eq. (3.16) over W and finally obtain:

$$\beta(\nu) \frac{\partial}{\partial z} Y(z,x,\nu)=-\alpha_0(\nu)(1-e^{-\beta(\nu)Y(z,x,\nu)}) \qquad (3.18)$$

This equation describes the propagation of the total energy of the pulses in an optically thick medium, and its solution reads as,

$$Y(z,x,\nu)=\beta(\nu)^{-1}\ln\{1+e^{-\alpha_0(\nu)z}[e^{\beta(\nu)\,Y(0,x,\nu)}-1]\} \qquad (3.19)$$

where $Y(0,x,\nu)$ is the total incident energy. Taking the optical thickness into account results in the local energy varying in the z-direction. We plot the z-dependent energy for different incident energy dose denoted by βY_0 in figure 3.2(a). A weak energy dose decays exponentially with the depth from the front side of the sample and is completely absorbed after a certain distance. When the incident dose increases, a portion of it bleaches the sample on its way and makes the rest pass through without absorption so that it can propagate further.

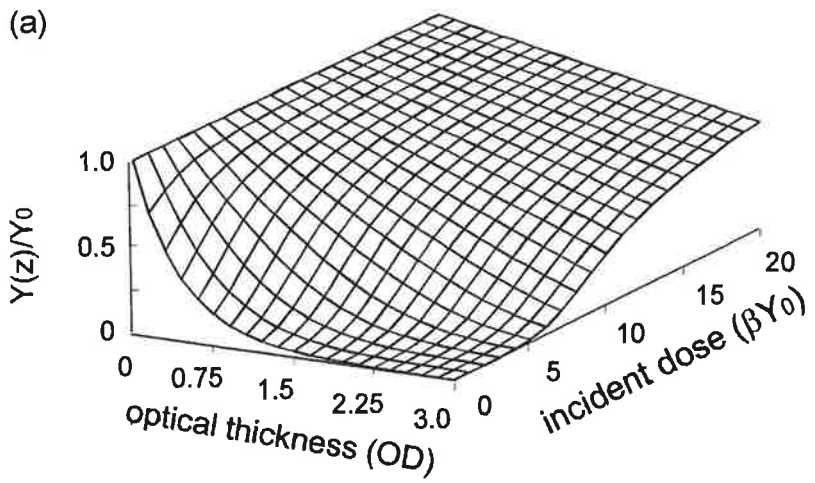

Figure 3.2 (a) Energy propagation in thick sample.

The local absorption coefficient modified by the burning energy can be rewritten as,

$$\alpha(z,x,\nu)=\alpha_0(\nu)e^{-\beta(\nu)Y(z,x,\nu)} \tag{3.20}$$

$$\alpha(z,x,\nu)=\frac{\alpha_0(\nu)}{1+e^{-\alpha_0(\nu)z}[e^{\beta(\nu)Y(0,x,\nu)}-1]} \tag{3.21}$$

Figure 3.2(b) depicts the local absorption coefficient within the sample under different incident dose. The material is burnt firstly on the surface by the small dose, and one can see a steep slope between the burnt and unburnt parts within the material. The bleached area expands with the dose, in the meanwhile the shape of the slope does not change, but its position shifts in the direction of the energy propagation. More precisely, from Eq.(3.21) the position where $\alpha(z,x,\nu)$ is reduced by a factor of two can be expressed as:

$$z_{1/2}=\frac{\beta Y(0,x,\nu)}{\alpha_0(\nu)}+\frac{\ln(1-e^{-\beta Y(0,x,\nu)})}{\alpha_0(\nu)} \tag{3.22}$$

which is a linear function of the dose when $\beta Y(0,x,\nu) >> 1$.

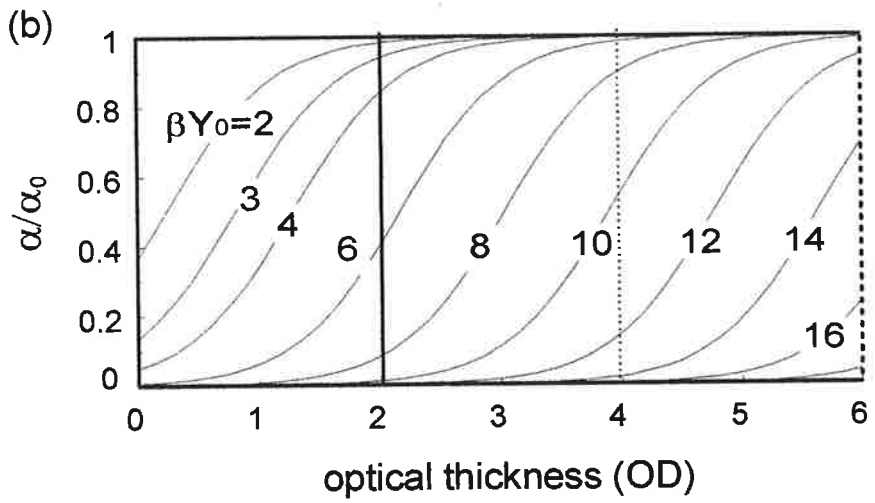

Figure 3.2 *(b) Local absorption coefficient modification in thick sample. The vertical solid, doted and dashed lines, respectively, specify the initial optical densitys equal to 2,4,6 (see figure 3.2c).*

For a L-thick sample, we calculate the optical density: $OD=[\int_0^L \alpha(z)dz]/\ln(10)$. The z-integrated absorption coefficient reads as:

$$A(x,\nu) = \int_0^L \alpha(z,x,\nu)dz = \ln[1+(e^{A_0(\nu)}-1)e^{-\beta Y(0,x,\nu)}] \qquad (3.23)$$

$$= A_0(\nu) - \beta Y(0,x,\nu) + \ln[1+e^{-A_0(\nu)}(e^{\beta Y(0,x,\nu)}-1)] \qquad (3.24)$$

which is expressed as a function of the space and frequency distribution of the total incident energy. The relative reduction of optical densities are plotted as a function of incident dose in figure 3.2(c) for three different values of the initial OD, larger than unity, namely 2, 4 and 6. Each evolution curve exhibits a linear variation over a dose range which by far exceeds the perturbation region $\beta Y(0,x,\nu) << 1$. The size of the linear zone increases with the optical thickness. The energy limit for the linear zone can be estimated from Eq.(3.24). Indeed, if $e^{-A_0(\nu)}(e^{\beta Y(0,x,\nu)}-1) << 1$, the last term in (3.24) can be ignored and the optical density varies linearly with the dose. For an optically thick medium, this condition keeps valid for $\beta Y(0,x,\nu) < A_0(\nu)$, which is consistent with figure 3.2(C).

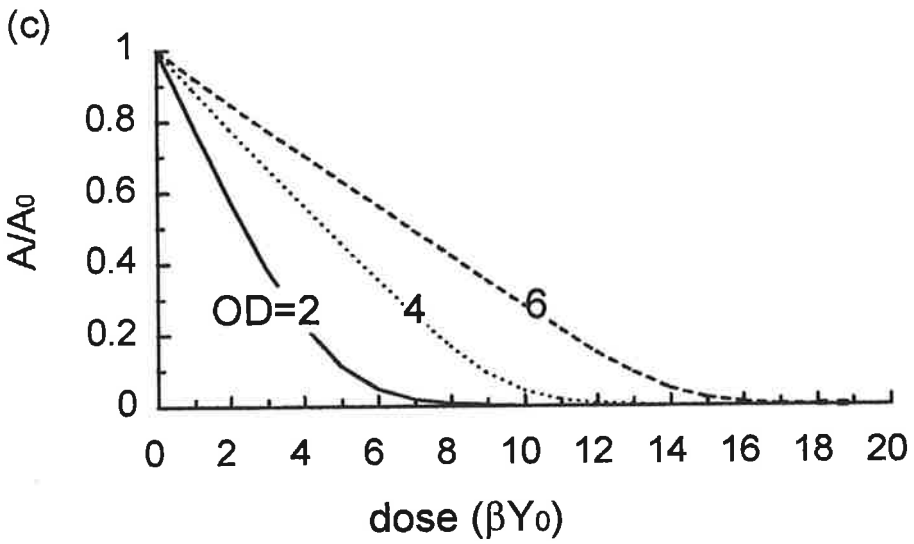

Figure 3.2 *(c) Relative reduction of optical density as a function of incident dose, OD=2, 4, 6 (A_0~ 4.6, 9, 14, respectively).*

This linear behavior is closely connected with the linear character of the hole burning process. As long as the incident dose (βY_0) is less than A_0=OD*ln(10), it is completely absorbed by the medium, so that the depletion of the absorbing molecule population is proportional to the total incident energy. Thus the optical density reduction is linear with the dose. When the dose is as large as ~A_0, it reaches the exit surface, which means that a part of incident energy passes through freely and does not modify the medium. Then the evolution curve of optical density is in the non-linear region. When the energy is strong enough the sample is finally bleached completely.

It should be noticed that the linear regime energy range of the optical density is much broader than that of the local absorption coefficient. Indeed, the region close to the front side of the sample is burnt much earlier than those buried deeply inside the medium. For these early burnt regions, the linear behavior fails in the very energy range where the optical density varies linearly. However, in this energy range, only the first order expansions of the absorption coefficient, at any depth in the sample, contribute to the expression of the optical density. This paradoxical property will prove useful for the calculation of the holographic signal.

3.4 Diffraction on the engraved grating

3.41 Index of refraction and absorption gratings

After the hologram is engraved, a probe field is directed to the sample and a diffracted field is detected. The signal amplitude is calculated with the help of the coupled-wave equation (3.8). It is known that any hologram is twofold. It includes an index of refraction component and an absorption one. This is apparent in Eq.(3.8) where the waves are diffracted on $i\hat{H}\tilde{\alpha}^{(q)}(z,\nu)$ and on $\tilde{\alpha}^{(q)}(z,\nu)$ which respectively represent the index of refraction hologram and its absorption companion.

One may take advantage of the spectral modulation of the engraved holograms to calculate the Hilbert transform of the absorption coefficient and to clarify the connection between the two holographic contributions.

For recording data at M different addresses, one irradiates the memory element with the following total energy:

$$Y(0,x,\nu)=\sum_{m=1}^{M\times N} W(0,x,\nu,m) \tag{3.25}$$

$$Y(0,x,\nu)=Y_0(\nu)\left\{1+\frac{1}{M}\cos(2\pi\nu\tau+Kx)\sum_{m=1}^{M}\ell_m f_m(\nu)\right\} \tag{3.26}$$

From Eq.(3.21) we know that the structure engraved in the PSHB material is not proportional to $Y(0,x,\nu)$. However, the absorption coefficient $\alpha(z,x,\nu)$ can be expressed as a function of $Y(0,x,\nu)$. As such, it depends on x through $\cos(2\pi\nu\tau+Kx)$. Thus the absorption coefficient can be denoted as $\underline{\alpha}(z,\varphi,\nu)$, where $\varphi = 2\pi\nu\tau+Kx$. It results that the Fourier coefficients of $\alpha(z,x,\nu)$ read as:

$$\tilde{\alpha}^{(p)}(z,\nu)=\frac{1}{2\pi}e^{-2i\pi p\nu\tau}\int_0^{2\pi}\underline{\alpha}(z,\varphi,\nu)\cos(p\varphi)d\varphi \tag{3.27}$$

We have assumed that the engraving pulses do not temporally overlap. The temporal extension of the spectrally encoded reference pulse is determined by the inverse of an elementary spectral slice $1/\delta$. The duration of the object pulse is much smaller since it equals the inverse laser bandwidth. Thus the assumption of non overlapping pulses implies that $\tau>1/\delta$. Therefore, the frequency-dependent variations of $\tilde{\alpha}^{(p)}(z,\nu)$ reduce

to the oscillation of the phase factor $e^{-2i\pi p\nu\tau}$ in any interval narrower than δ. As a result, the Hilbert transform of $\tilde{\alpha}^{(p)}(z,\nu)$ can be expressed as:

$$(1+i\hat{H})\tilde{\alpha}^{(p)}(z,\nu)=\begin{cases}2\tilde{\alpha}^{(p)}(z,\nu) & \text{if } p>0\\ 0 & \text{if } p<0\\ \tilde{\alpha}^{(p)}(z,\nu) & \text{if } p=0\end{cases} \qquad (3.28)$$

It appears that the p>0 Fourier coefficients of the index of refraction hologram coincide with those of the absorption one while the p<0 coefficients cancel each other. The coupled-wave equation (3.8) can be rewritten as:

$$\frac{\partial}{\partial z}\tilde{\underline{E}}^{(p)}(z,\nu)+\frac{1}{2}\tilde{\alpha}^{(0)}(z,\nu)\,\tilde{\underline{E}}^{(p)}(z,\nu)-i\frac{(\vec{k}_1+p\vec{K})^2-k_0{}^2}{2k_0}\tilde{\underline{E}}^{(p)}(z,\nu)=$$

$$-\sum_{q>0}\tilde{\alpha}^{(q)}(z,\nu)\,\tilde{\underline{E}}^{(p-q)}(z,\nu) \qquad (3.29)$$

The last term on the right hand side of equation (3.29) shows the coupling effects that generate a field mode. According to Eqs(3.27) and (3.29), the pth order component of the field can be characterized as follows: (i) it is generated only by the lower order modes, which entails that, if the wave p=0 alone is present in the front side of the sample, its propagation is not affected by that of other waves. (ii) it emerges at a time delay $p\tau$ with respect to the probe field, in direction $\vec{k}_p=\vec{k}_1+p(\vec{k}_2-\vec{k}_1)$. (iii) the dephasing effects in a geometrical thick medium may prevent the radiation from the high order modes since the signals emitted at different points within the medium may contribute destructively to the output field. Modes p=0,1 are always phase-matched according to Eq.(3.13).

3.42 Signal amplitude

Let the probe pulse be directed along $\vec{k}_3=\vec{k}_1$. The field diffracted in direction $\vec{k}_2$ is the solution of the following set of coupled-wave equations:

$$\frac{\partial}{\partial z}\tilde{\underline{E}}^{(0)}(z,\nu)+\frac{1}{2}\tilde{\alpha}^{(0)}(z,\nu)\,\tilde{\underline{E}}^{(0)}(z,\nu)=0 \qquad (3.30)$$

$$\frac{\partial}{\partial z}\tilde{\underline{E}}^{(1)}(z,\nu)+\frac{1}{2}\tilde{\alpha}^{(0)}(z,\nu)\,\tilde{\underline{E}}^{(1)}(z,\nu)+\tilde{\alpha}^{(1)}(z,\nu)\,\tilde{\underline{E}}^{(0)}(z,\nu)=0 \qquad (3.31)$$

with the initial conditions:

$$\underline{\tilde{E}}^{(p)}(0,\nu) = 0, \quad \text{if } p \neq 0 \tag{3.32}$$

$$\underline{\tilde{E}}^{(0)}(0,\nu) = \tilde{\mathcal{E}}_L(\nu)\, f_j(\nu). \tag{3.33}$$

The incoming probe pulse spectrum is expressed as the product of the laser spectrum $\tilde{\mathcal{E}}_L(\nu)$ with the encoding function $f_j(\nu)$ which belongs to the family of orthogonal functions already used to encode the reference pulses.

Solving equations (3.30) and (3.31) we obtain:

$$\underline{\tilde{E}}^{(0)}(z,\nu) = \tilde{\mathcal{E}}_L(\nu)\, f_j(\nu).\ e^{-\frac{1}{2}\tilde{A}^{(0)}(\nu)} \tag{3.34}$$

$$\underline{\tilde{E}}^{(1)}(z,\nu) = -\,\tilde{\mathcal{E}}_L(\nu)\, f_j(\nu)\ e^{-\frac{1}{2}\tilde{A}^{(0)}(\nu)}\ \tilde{A}^{(1)}(\nu) \tag{3.35}$$

where:

$$\tilde{A}^{(p)}(\nu) = \frac{K}{2\pi} \int_{<\frac{2\pi}{K}>} A(x,\nu) e^{ipKx} dx \tag{3.36}$$

The z-integrated absorption coefficient $A(x,\nu)$ is defined in Eq.(3.23). Except for the numerical factor ln10, it coincides with the optical density.

Expression of the signal in terms of the first two Fourier coefficients of the optical density only relies on the assumption that $\alpha(z,x,\nu)$ is a function of $\cos(Kx+2\pi\nu\tau)$, and that the ν–dependence described by this cosine is much faster than any other. Thus Eq.(3.35) can be regarded as a general description of a spectral hologram retrieval process in a persistent spectral hole burning material. The hole burning model proposed in section 3.3 only goes into the expression of absorption coefficient. It is used in section 3.5 to discuss the variation of the signal amplitude as a function of the burning dose, and to examine implications on the cross-talk between phase encoded addresses.

3.5 Discussion

3.51 Connection with the elementary description

In Section 2.2 we proposed the principle of phase-encoded addresses within the limits of small optical density ($A_0(\nu)=\alpha_0(\nu)L<<1$) and small burning dose ($\beta Y_0<<1$). In order to connect the present theory with this early description, we expand Eq. (3.35) to lowest order in the optical density and the burning dose, with the help of Eqs. (3.24) and (3.26). It leads to:

$$\underline{\tilde{E}}^{(1)}(z,\nu) = -\,\tilde{\mathcal{E}}_L(\nu)\, f_j(\nu)\, A_0(\nu)\, \beta Y_0(\nu)\, \frac{1}{M}\sum_{m=1}^{M} \mathcal{E}_m f_m^{*}(\nu)\, e^{-2i\pi\nu\tau} \qquad (3.37)$$

The diffracted field is detected through its correlation with a gating field delivered by the laser. The correlation signal reads as:

$$G_j(\tau) = \int d\nu \,|\, \tilde{\mathcal{E}}_L(\nu) \,|^2\, A_0(\nu)\, \beta Y_0(\nu)\, \frac{1}{M}\sum_{m=1}^{M} \mathcal{E}_m f_m^{*}(\nu)\, f_j(\nu) \qquad (3.38)$$

which, as expected, reduces to Eq.(2.10) when the active molecules and the laser intensity are uniformly distributed over the storage spectral window.

In practice, the conditions, $A_0<<1$ and $\beta Y_0<<1$ lead to the difficult detection of the extremely weak signal. We should consider to augment the optical density and the recording energy to get a detectable signal.

3.52 Linear regime and beyond

In section 3.3, we noticed that $A(x,\nu)$ can be expressed as a linear function of the dose in an optically thick medium as long as $\beta Y(0,x,\nu) < A_0(\nu)$. Fortunately the diffracted field amplitude can be expressed as a function of the Fourier coefficients of $A(x,\nu)$. According to Eq.(3.24) the linear approximations of $A(x,\nu)$ and of its first two Fourier coefficients respectively read as:

$$A(x,\nu) = A_0(\nu) - \beta Y(0,x,\nu) \qquad (3.39)$$

$$\tilde{A}^{(0)}(\nu) = A_0(\nu) - \beta(\nu) Y_0(\nu) \qquad (3.40)$$

$$\tilde{A}^{(1)}(\nu) = -1/2\beta(\nu)Y_0(\nu)\ \frac{1}{M}\sum_{m=1}^{M} \ell_m f_m(\nu)\ e^{-2i\pi\nu\tau} \qquad (3.41)$$

According to Eq. (3.26), the maximum value of $\beta Y(0, x, \nu)$ is $2\beta(\nu)Y_0(\nu)$. Therefore, in an optically thick medium, the signal amplitude can be replaced by its linear approximation provided:

$$\beta(\nu)Y_0(\nu) < 1/2A_0(\nu) \qquad (3.42)$$

As an illustration of this feature, we have plotted the exact expression of $\tilde{A}^{(1)}(\nu)$ together with its linear approximation on Fig. 3.3, as functions of the burning dose. The initial optical density is set equal to 1.5 and it is assumed that a single data is stored in the PSHB medium at an address that is represented by a rectangular spectral code: M=1, $\ell_m f_m(\nu) = 1$.

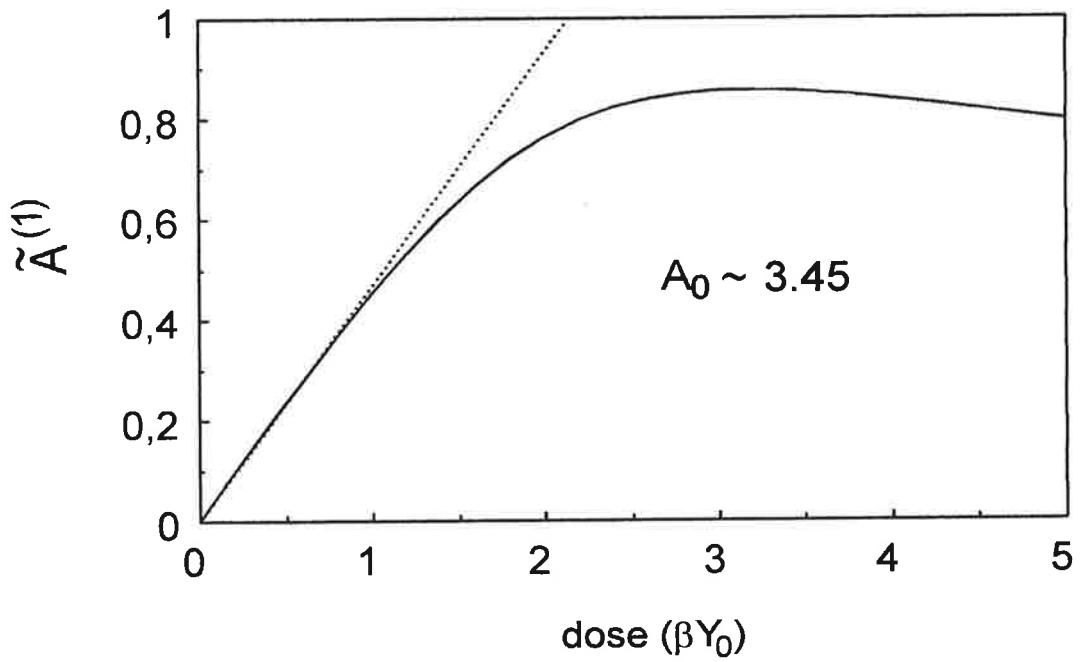

Figure 3.3 *Fourier coefficient $\tilde{A}^{(1)}(\nu)$ as a function of the burning dose. The initial optical density equals 1.5, (i.e. $A_0(\nu) = 3.45$). solid line: exact calculation. dashed line: linear approximation, valid up to $\beta Y_0(\nu) \approx 0.5A_0(\nu) = 1.7$.*

The signal amplitude is plotted on fig 3.4 under the same conditions. It confirms that the linear regime approximation keeps close to the exact calculation as long as $\beta Y_0(\nu) < 0.5A_0(\nu)$. It should be stressed that when $0.5A_0(\nu)>1$, the validity range of the linear regime by far exceeds that of the first order perturbative expansion which is only valid when $\beta Y_0(\nu) << 1$.

When the burning dose $\beta(\nu)Y_0(\nu)$ exceeds $0.5A_0(\nu)$, non linear effects can no longer be ignored. Their contribution entails two consequences. Firstly, the part of the higher order gratings in the engraved structure increases with the energy. They diffract an increasing fraction of the readout pulse and decrease the usable signal generated by the first order grating. Secondly, the recording bleaches the sample and decreases the absorption modulation. As the result of the combined effects, the diffracted signal saturates, then decreases with the energy, as illustrated in Fig.3.4.

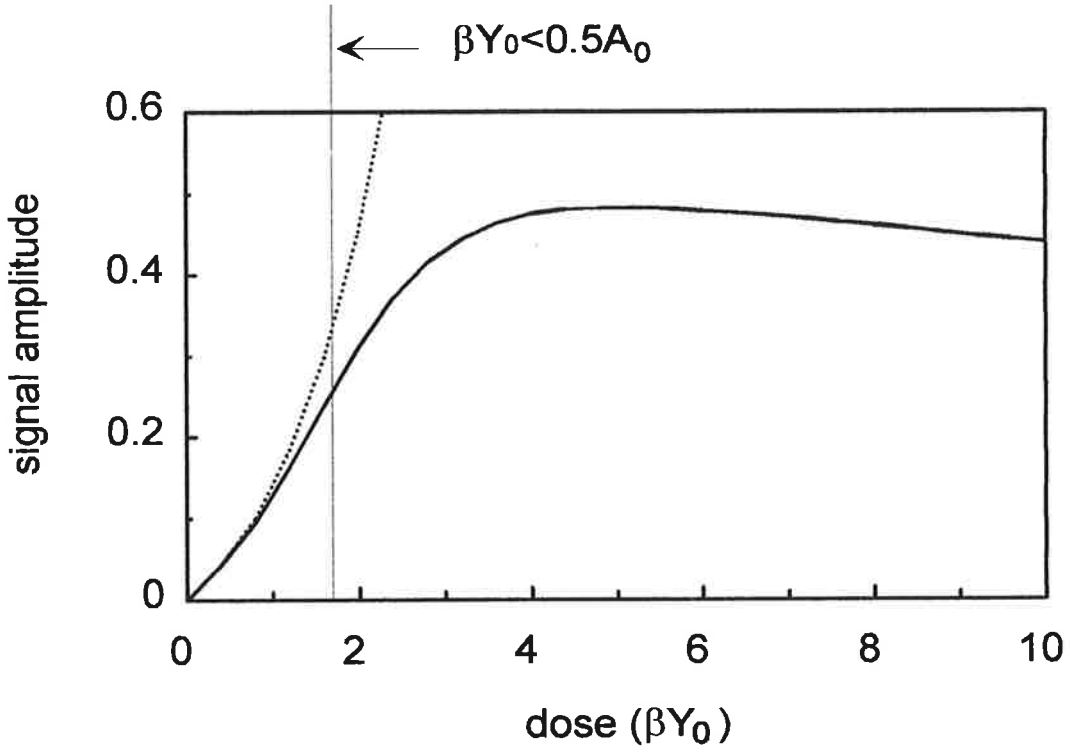

Figure 3.4 *Diffracted field as a function of the burning dose. The initial optical density equals 1.5, (i.e. $A_0(\nu) = 3.45$). Solid line: exact calculation. Dashed line: linear approximation, valid up to $\beta Y_0(\nu) \approx 0.5A_0(\nu) = 1.7$.*

3.53 Crosstalk between addresses

The discussion of crosstalk is restricted to the linear regime. Expressions (3.40) and (3.41) are substituted for $\tilde{A}^{(0)}(\nu)$ and $\tilde{A}^{(1)}(\nu)$ in Eq.(3.35). Thus the correlation signal reads as:

$$G_j(\tau)=\int d\nu F(\nu)\frac{1}{M}\sum_{m=1}^{M}\delta_m f_m^{*}(\nu)f_j(\nu) \qquad (3.43)$$

where:
$$F(\nu) = 0.5\left|\tilde{\mathcal{E}}_L(\nu)\right|^2\beta(\nu)Y_0(\nu)e^{-\frac{1}{2}A_0(\nu)+\frac{1}{2}\beta(\nu)Y_0(\nu)} \qquad (3.44)$$

Therefore the address orthogonality is preserved provided the active molecules and the laser intensity are uniformly distributed over the storage spectral window. It is noteworthy that one is faced with the same orthogonality conditions as in the small optical density, small burning dose limit (Cf. Section 3.51). This feature is connected with the phase-encoding character of the addresses: the 0-order Fourier coefficient of the optical density, which determines the absorption decay of the signal, is not affected by the spectral structure of the filled addresses.

3.54 Phase-matching requirement

The modes that do not satisfy the phase-matching condition expressed by Eq.(3.13) can not propagate through the sample. This condition becomes more and more stringent for higher order waves. During the burning process, the impinging beams are diffracted on the grating that they are building up and they transfer a part of their energy to high order waves. In section 3.3 we assumed that all the generated waves are phase-matched. This assumption is valid if only low order waves significantly contribute to burning. In order to check this hypothesis, we allow a limited number of waves to participate to the hologram engraving, and calculate the signal amplitude. First we assume that a very thick grating is engraved so that only the p=0 and p=1 waves can propagate. Then, an additional p=2 wave is allowed to contribute to energy transmission. Results are plotted on Fig 3.5. together with the curve with no phase-matching restriction. It appears that, in the dose range of interest, very few

waves contribute to burning and that energy propagation is correctly described by Eq.(3.16) provided:

$$\frac{L}{\lambda}\theta^2 << 1 \qquad (3.45)$$

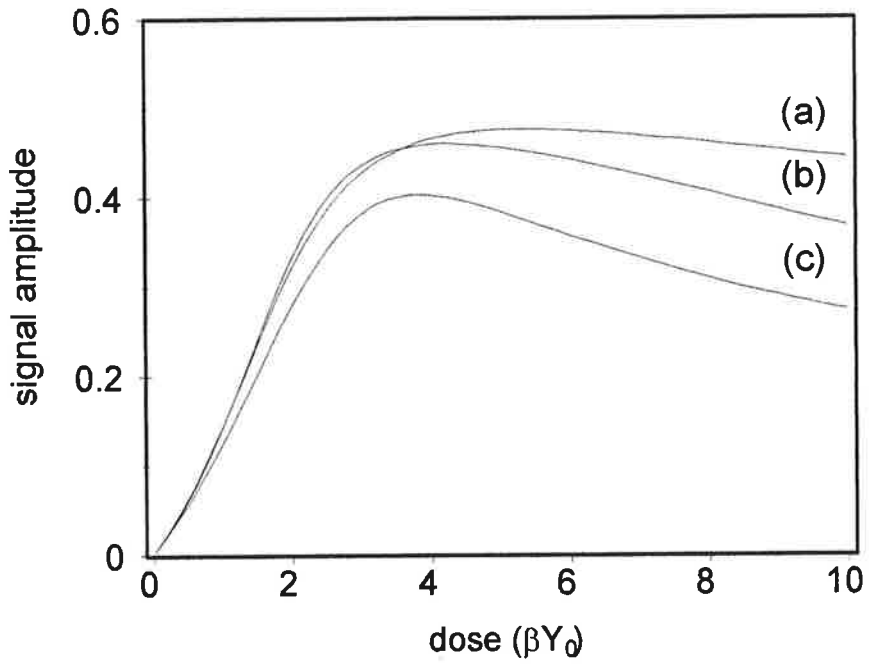

Figure 3.5 *Diffracted field as a function of the burning dose.*
(a) no phase-matching restrictions.
(b) Waves p= 0, 1, 2 can propagate.
(c) Waves p= 0, 1 can propagate.

3.6 Conclusion

Relying on a simple hole burning model, we have brought a few features to light. We have shown that, under quite general conditions, the retrieved data can be expressed as a function of the first two Fourier coefficient of the optical density. We have disclosed a linear regime that results from the linear character of the hole burning process and that ranges a broad burning dose domain in optically thick samples. We have checked that, when a very few spatial waves satisfy the phase-matching conditions, the burning energy propagation is not affected by Bragg selectivity in the dose range of interest. Finally, the conditions required to eliminate cross-talk between the memory addresses appear to be the same in the linear regime as in the small optical density, small burning dose, limit. In Chapter 4 we take advantage of these results to build a more sophisticated model.

3.7. References

[1] P. Saari, R. Kaarli, and A. Rebane, *'Picosecond time- and space- domain holography by photochemical hole burning'*, J. Opt. Soc. Am., **B3**, 527 (1986).

[2] R. Sarapuu, and R. Kaarli, *'Nonlinearity of the recording process of time and space domain holograms in highly selective photochromic media'*, Proc. Est. Acad. Sci. Phys. Math., **36**, 299 (1987).

[3] R. Sarapuu, *'Theoretical problems of space and time domain holography in photochromic media with spectral and polarization selectivity'*, Ph.D. dissertation, Institute of Physics, Estonian Academy of Sciences, Tartu, Estonia, (1989).

[4] H. Sonajalg and P. Saari, *'Diffraction efficiency in space- and time- domain holography'*, J. Opt. Soc. Am., **B11**, 372 (1994).

[5] H. Sonajalg, A. Débarre, J.-L. Le Gouët, I. Lorgeré, and P. Tchénio, *'Phase-encoding technique in time-domain holography : theoretical estimation'*, J. Opt. Soc. Am., **B12**, 1448 (1995).

[6] H. Kogelnik, *'Coupled wave theory for thick hologram gratings'*, Bell. Syst. Tech. J., **48**, 2909 (1969).

CHAPTER 4

PHOTOPHYSICS AND BROADBAND HOLOGRAPHY

4.1 Introduction

Our investigations on spectral phase encoding also open new experimental ways for approaching the hole burning process. Additional informations are added to our knowledge of this mechanism. It implies that its theoretical description has to be consistent, not only with the standard burning of a spectral hole in the absorption profile by a monochromatic laser, but also with hole burning by broad band sources and with diffraction on a hologram engraved over a broad spectral window.

In order to complement the hole burning model we have to clarify the electron-phonon coupling which affects the homogeneous line structure, the frequency dependence of the PSHB quantum yield $\beta(\nu)$, and the spectral distribution of the phototransformed molecules.

In addition we have to build a unified analysis of light propagation in a PSHB material that relates the hole depth measured in conventional experiments with the diffraction efficiency on a broad band spectral hologram. The unified theory is derived from the model that we developed in chapter 3. We relax the two following assumptions that underlie this model:

(i) optical absorption does not depend on the relative orientation of light polarization and of molecular optical dipole.

(ii) the absorption spectrum of the photoproducts is situated out of the initial inhomogeneous absorption band.

Section 4.2 is devoted to the electron-phonon coupling and to the frequency dependence of the PSHB quantum yield. The hole burning model is presented in section 4.3. The hologram engraving calculation is outlined in section 4.4. The experimental data are examined in the light of the theoretical achievements in section 4.5. Results are summarized in section 4.6

4.2 Phonon side band, burning efficiency

The hole burning process includes an optical excitation step followed by an engraving mechanism. All the active centers interact with the light in the same way, irrespective of their local environments and of their transition frequencies. On the contrary, the reactive channels which are opened in the upper level of the optical transition may depend on the local environment. The reaction in the excited state is characterized by the burning efficiency. We investigate the frequency dependence of this parameter in the present paragraph by exploring the spectrum of the light diffracted on a PSHB-engraved grating. This hologram is recorded over the entire inhomogeneous width, which emphasizes the frequency variation of the burning rate. Our description of the homogeneous line includes the zero-phonon component and the phonon side-band that describes the matrix excitation through electron-phonon coupling. The experiment is performed in OEP-doped polystyrene. As noticed in section 2.33, burning is caused by a tautomerization process. As a consequence, the burning products may fall within the inhomogeneous band. In order that the observed signal be not affected by the secondary photo excitation of the photoproducts, we perform the experiment under small exposure condition.

4.21 Absorption spectral structure and burning efficiency

The optical properties of dye-doped polymers are determined by both the dopant and the matrix. The absorption spectra are due to electronic transitions, inter- or intra-molecular bond vibrations and also contain guest-host interactions. At low temperature, a dopant molecule can be optically excited on its zero-phonon line (ZPL) coming from the 0-0 pure electronic transition. On account of the inhomogeneity of the host matrix, guest molecules located at different positions exhibit different ZPL transition frequencies. A ZPL frequency-dependent dopant distribution $n_0(\nu)$ can thus be defined as the inhomogeneous distribution function. In a simple model it can be described by a Gaussian function centered at ν_0,

$$n_0(\nu)=C_n e^{-(\frac{\nu-\nu_0}{\Gamma_{in}})^2 4\ln 2} \qquad (4.1)$$

where C_n is a normalization constant. In addition to the ZPL component denoted as $k_{ZPL}(\nu-\nu',\Gamma_0)$, the absorption spectrum of each single set of molecules with the same ZPL resonance frequency ν' includes a blue-shifted broad phonon side band $k_{PSB}(\nu-\nu',\Gamma_p)$, which is caused by electron-phonon interaction. The resulted absorption spectrum reads as:

$$k(\nu-\nu') = k_{ZPL}(\nu-\nu', \Gamma_0) + k_{PSB}(\nu-\nu', \Gamma_p) \tag{4.2}$$

At low temperature, the line shape of the ZPL can be described by a Lorentzian function:

$$k_{ZPL}(\nu, \Gamma_0) = \alpha_{DW}\cdot\frac{1}{\pi}\cdot\frac{\Gamma_0}{\nu^2+\Gamma_0^2} \tag{4.3}$$

where Γ_0 =1/2 Γ_{hom} is the HWHM of the ZPL, and α_{DW}, the Debye-Waller factor. To simplify the mathematical description of the PSB, three assumptions, harmonic potential, low temperature and linear electron-phonon coupling were introduced in ref.[1], which are also satisfied in the cases we are interested in. Then, the PSB line shape can be expressed as:

$$k_{PSB}(\nu, \Gamma_p) = (1-\alpha_{DW})\cdot\frac{\nu}{\Gamma_p^2}\cdot e^{-\frac{\nu}{\Gamma_p}} \tag{4.4}$$

where Γ_p equals the half Stoke's shift, which is usually two or three orders of magnitude larger than Γ_{hom} in porphyrin-derivatives/polymer system. The relative intensity of the ZPL and PSB of the homogeneous line depends upon the linear electron-phonon coupling strength which is measured by the Debye-Waller factor α_{DW} defined as the relative integration area of the ZPL to the total homogeneous spectral area including the ZPL and PSB. When the coupling is weak (or strong), α_{DW} is close to unity (or zero).

The profile of the whole absorption spectrum $\alpha(\nu)$ can be described as the convolution of $n_0(\nu)$ with $k(\nu)$, i.e.:

$$\alpha(\nu) = \alpha_0\, n_0(\nu) \otimes k(\nu) \tag{4.5}$$

where α_0 denotes the initial maximal absorption coefficient, $n_0(\nu)$ is normalized such that $\alpha_0(\nu)=\alpha_0$, at the maximal absorption. These spectral structures are schematically depicted in figure 4.1.

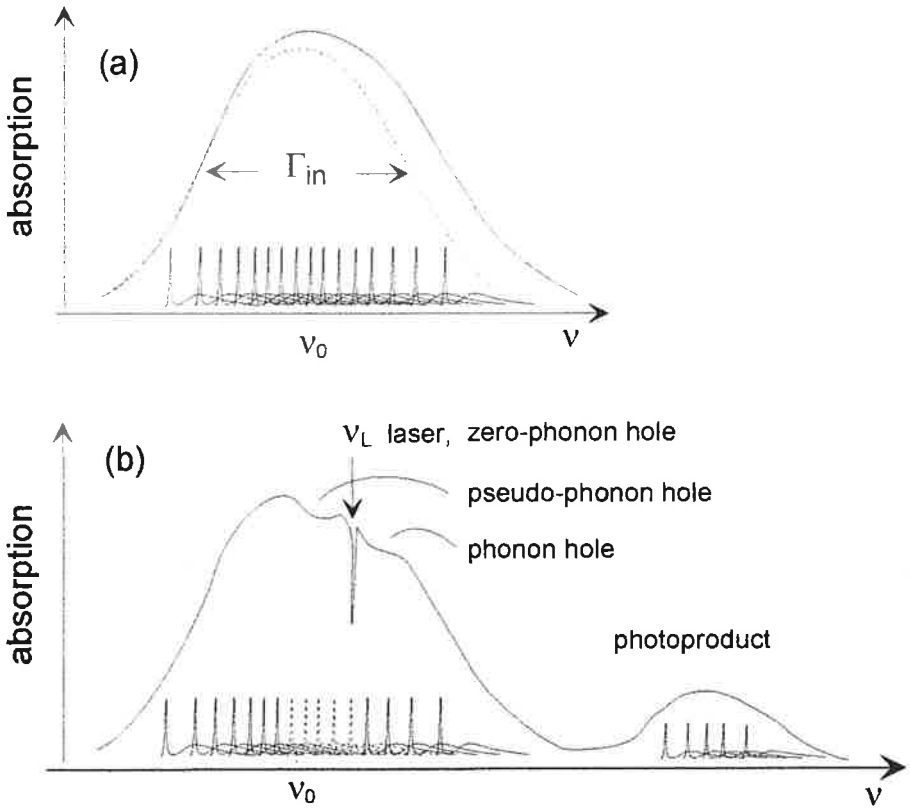

Figure 4.1 (a) Underlying structure of the absorption profile. (b) Hole burnt by a weak monochromatic laser.

Based on this feature, we consider the spectral hole profile which may be rather complicated and strongly depends on laser line width, exposure intensity and time. First, we assume a monochromatic laser line $\delta(\nu-\nu_L)$ as the burning light. In addition to the molecules which have their ZPL's exactly in resonance with the laser frequency at ν_L, the off-resonance molecules which are located on the red side of ν_L and whose PSB's overlap the laser line are burnt through their phonon side bands. When the energy is weak enough, hole burning is in the linear regime, the resulted depletion of the molecular distribution is proportional to the burning energy Y_0, the homogenous line shape $k(\nu_L-\nu)$ and the burning efficiency $\beta(\nu)$ as,

$$n(\nu)=n_0(\nu)[1-\beta(\nu)Y_0\, k(\nu_L-\nu)] \qquad (4.6)$$

The disappearance of the molecules undergoing PSHB through their ZPL's form a sharp ZPL hole and a relatively broad blue-shifted phonon side hole, while the

molecules burnt through their PSB's give rise to a red-shifted pseudo-phonon hole as shown in figure 4.1 (b).

In an optically thick sample, the propagation of the incident light field through the absorbing sample reduces the burning intensity. We restrict our discussion to the weak energy region where the sample is not bleached in the burning process. At a depth z from the surface of the sample, the modified distribution function reads as:

$$n_0(\nu)[1-\beta(\nu)Y_0\, e^{-\alpha_0(\nu_L)z}\, k(\nu_L-\nu)] \qquad (4.7)$$

4.22 Broad band engraving of a space-and-frequency grating

Instead of a Dirac peak, let the incident energy have a spatially and spectrally structured spectrum described by,

$$Y(0,x,\nu)=Y_0(\nu)(1+1/2e^{2i\pi\nu\tau+iK.x}+c.c.) \qquad (4.8)$$

where $Y_0(\nu)$ stands for the spectral energy dose delivered by a broad band source $I_L(\nu)$, and $K=|\vec{k}_1-\vec{k}_2|$. Then, the modified molecular distribution and absorption coefficient can be expressed, respectively as:

$$n(z,x,\nu)=n_0(\nu).\left[1-\beta(\nu).Y(z,x,\nu)\otimes k(-\nu)\right] \qquad (4.9)$$

$$\alpha(z,x,\nu)=\alpha_0\, n(z,x,\nu)\otimes k(\nu)$$

In the frequency domain, the grating period equals the inverse of the time separation between the recording pulses. However, the period cannot be arbitrary small. It cannot be smaller than the width of $k(-\nu)$, which can be regarded as the grain size of a frequency domain photographic plate and which limits the resolution of the plate. As a matter of fact, the grain structure includes two components with very different sizes. In dye-doped polymers at low temperature, Γ_{in} is several times larger than Γ_p , and Γ_p is two or three orders of magnitude larger than Γ_{hom}. In the regime $\Gamma_{in}>\tau^{-1}>\Gamma_p$, both kinds of grains contribute to the grating structure. If $\Gamma_p >>\tau^{-1}$, the PSB component, with its Γ_p wide grain, no longer contributes to the grating. The zero phonon line contribution survives alone, as long as $\Gamma_{hom}\tau<1$.

In our storage approach, the time interval τ is adjusted in such a way that, $\Gamma_{hom}<<\tau^{-1}<<\Gamma_p$. Since the only surviving component in $k(-\nu)$ is much narrower than $\alpha(\nu)$ and $Y_0(\nu)$, the engraved structure can be simplified as:

$$n(z,x,\nu)-n_0(\nu)\propto -n_0(\nu)Y_0(\nu)\beta(\nu).e^{-\alpha_0(\nu)z}(e^{-2i\pi\nu\tau+iK.x}+c.c.) \qquad (4.10)$$

$$\alpha(z,x,\nu)-\alpha_0(\nu)\propto -n_0(\nu)Y_0(\nu)\beta(\nu).e^{-\alpha_0(\nu)z}(e^{-2i\pi\nu\tau+iK.x}+c.c.) \qquad (4.11)$$

Then the zero- and first- order Fourier components of the z-integrated absorption coefficient read as,

$$\tilde{A}^{(0)}(z,\nu)=\alpha_0(\nu)L=A_0(\nu)$$

$$\tilde{A}^{(1)}(z,\nu)\propto n_0(\nu)\beta(\nu)\,Y_0(\nu)\,(1-e^{-A_0(\nu)})/A_0(\nu) \qquad (4.12)$$

4.23 Diffraction spectrum

We use the same broad laser as a probe beam. According to expression (3.35), the diffraction spectrum has the profile as,

$$\tilde{\mathcal{S}}(\nu)\propto\frac{n_0(\nu)}{A_0(\nu)}\,(1-e^{-A_0(\nu)})e^{-1/2A_0(\nu)}\;\beta(\nu)Y_0(\nu)\;\tilde{\mathcal{E}}_L(\nu) \qquad (4.13)$$

Where $\tilde{\mathcal{E}}_L(\nu)$ denotes the laser spectrum. Here the PSB components do not participate to the signal emission. It can be explained by the principle of the SPE process. When the probe field excites the optical dipoles either through their ZPL's or through their PSB's, an interval τ elapses between the excitation of the dipoles and the moment when their relative phase shifts cancel and they emit a coherent signal. Since τ is adjusted in such a way that $\Gamma_p\tau >> 1$, the PSB dipoles decay before the emission time. So in summary, PSB's participate neither to the grating etching nor to the signal emission. The signal is radiated only from zero phonon lines. The existence of PSB's affects the signal spectrum in term of absorption.

According to expression (4.13), the contributions of molecular distribution, PSB components, and quantum efficiency can be studied experimentally. The signal intensity can be expressed as,

$$\left|\tilde{\mathcal{S}}(\nu)\right|^2\propto\left\{\frac{n_0(\nu)}{A_0(\nu)}\right\}^2(1-e^{-A_0(\nu)})^2\;e^{-A_0(\nu)}\;[\beta(\nu)]^2\;I_L^3(\nu) \qquad (4.14)$$

where $I_L(\nu)=\left|\tilde{\mathcal{E}}_L(\nu)\right|^2$.

In this expression, the quantities $A_0(\nu)$, $I_L(\nu)$ and $|\tilde{S}(\nu)|^2$ can be accessed directly by standard spectroscopy techniques. α_{DW}, Γ_p, and Γ_0 may be referred to some literature [1-5]. With these parameters, we may get $n_0(\nu)$ and $\beta(\nu)$ by simulating absorption, signal spectra and comparing them with experimental results.

4.24 Experimental

The experiment relies on the spectral analysis of SPE. This can be achieved in a conventional way by probing the engraved grating with a broad band pulse and by directing the signal to a spectrometer, at the expense of important energy losses. In addition, a high sensitivity detector array is required in order to simultaneously analyze all the radiated signal and to avoid the damage to the stored grating with an excessive exposure of the readout field. We prefer to analyze the signal spectrum by probing the engraved grating with the help of a narrow band tunable laser. Then all the radiated energy is directly detected on a photomultiplier, and the signal spectrum is obtained by scanning the laser frequency.

A scheme of the set-up is plotted in Fig. 4.2. The laser source is a Nd:YAG (with second harmonic generation) pumped dye-laser, delivering wide band chaotic pulses with 10 ns-duration at 15 Hz repetition rate. The spectrum of the source is centered at 620 nm and covers a 9 THz bandwidth approximately. The laser beam is split into reference and object beams with equal intensities. On the reference arm, pulses go through the spectral shaping device. This device is the same as described in chapter 2 and figure 2.5, except that an adjustable slit replaces the SLM in the focal plane. In the recording stage (figure. 4.2 a), the slit is opened to let all the spectral components of the laser source pass through so that the reference beam holds the same broad band spectrum as the object pulse. In the readout stage (figure 4.2 b), the slit is adjusted to be as narrow as possible. In our experiment, a minimum slit width of 0.16 mm corresponds to a spectral width 80 GHz. A tunable probe beam is prepared by scanning the slit in the focal plane with the additional benefit that the probe pulse propagates exactly along the same direction as the reference pulse, so that the phase matching condition is automatically satisfied. The diffracted signal is detected in the direction of the object beam by a PM (RTC XP101, with S20R

photocathode). The time separation between the object and the reference pulses is set to 20 ps throughout the experiment.

The tunable beam is also used to obtain the absorption spectrum of the sample. When the object beam is blocked, the reference beam through the narrow spectral slit, is directed to the sample with an attenuated intensity. The transmitted light is detected on the same PM in the direction of reference beam. We detected also the laser spectral profile in the same way after removing the sample.

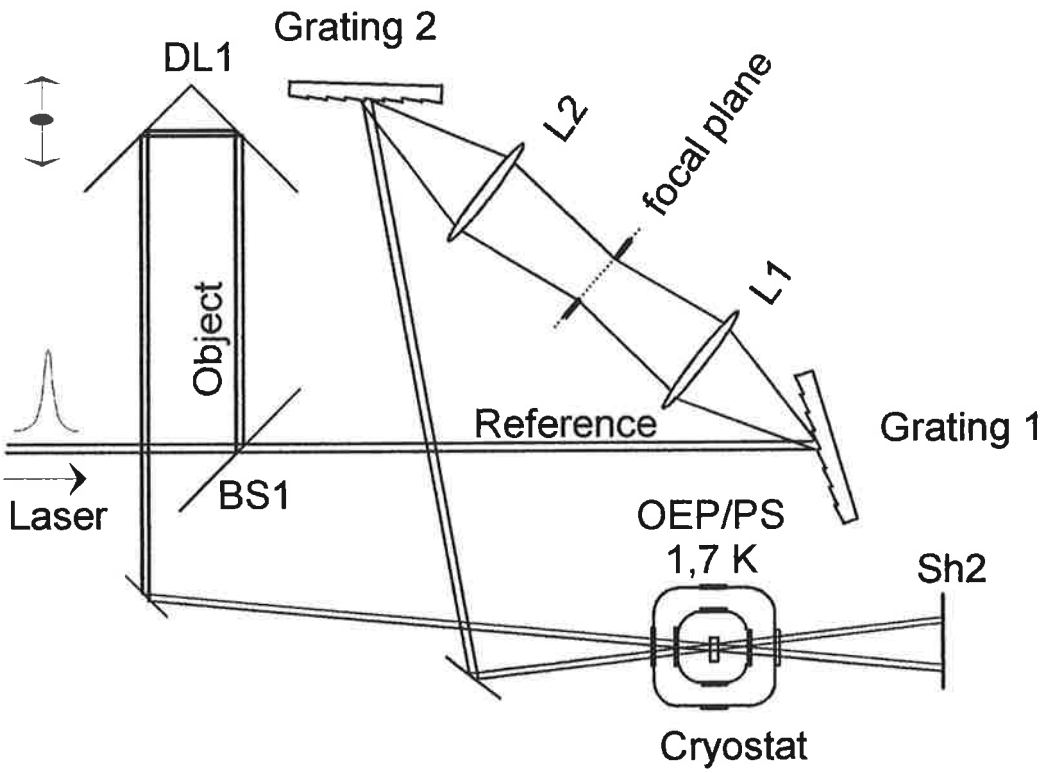

(a)

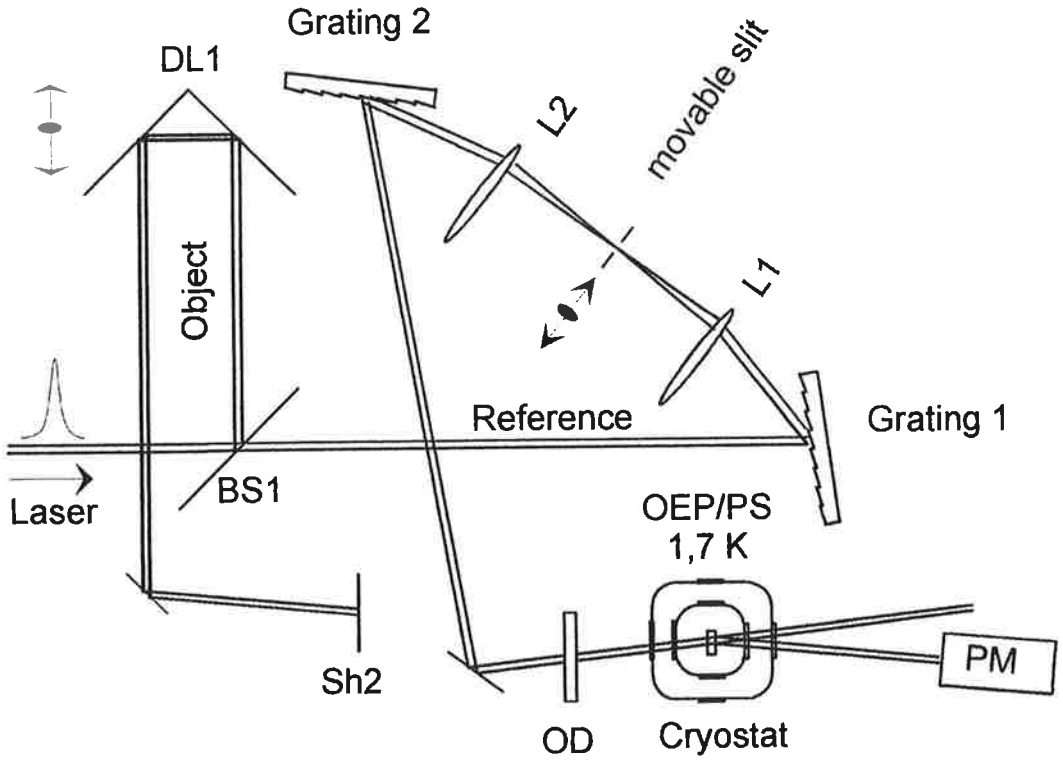

(b)

Figure 4.2 (a) Experimental setup for broad band recording. DL1 adds a 6mm delay on the object path with respect to the reference. (b) Analysis of the signal spectrum, with the help of a movable slit.

The sample is an 0.5mm-thick OEP/PS slab with initial optical density OD~2 and the concentration ~ 6×10^{-3} mol/l. Firstly, we analyze the ZPL and PSB components on the absorption spectrum as shown in figure 4.3. The absorption profile does not depend on the value of Γ_{hom} as long as $\Gamma_{hom} << \Gamma_p, \Gamma_{in}$. On the contrary, the parameters Γ_p, Γ_{in}, α_{DW} affect the absorption profile in such an intricate way that one cannot derive their values from the analysis of this single spectrum. Fortunately, the parameters Γ_p and α_{DW} have been measured by means of time-resolved PE and temperature cycling hole burning for the same porphyrin-derivative/polymer system [1-4], according to which we can fix Γ_p=0.45THz, α_{DW}=0.9 for our situation. Figure 4.3(c) gives a simulated absorption with Γ_{in}=4THz which coincides with the experimental profile (a). The slight deviation on the blue side is assigned to the effect of high energy vibrational modes which are not taken into

account in our model. The curve (b) in the same figure gives an absorption spectrum of the sample after being irradiated by the reference and object beams with a very weak exposure dose. The rather slight modification of the absorption spectrum shows that the PSHB memory element works in the perturbation regime.

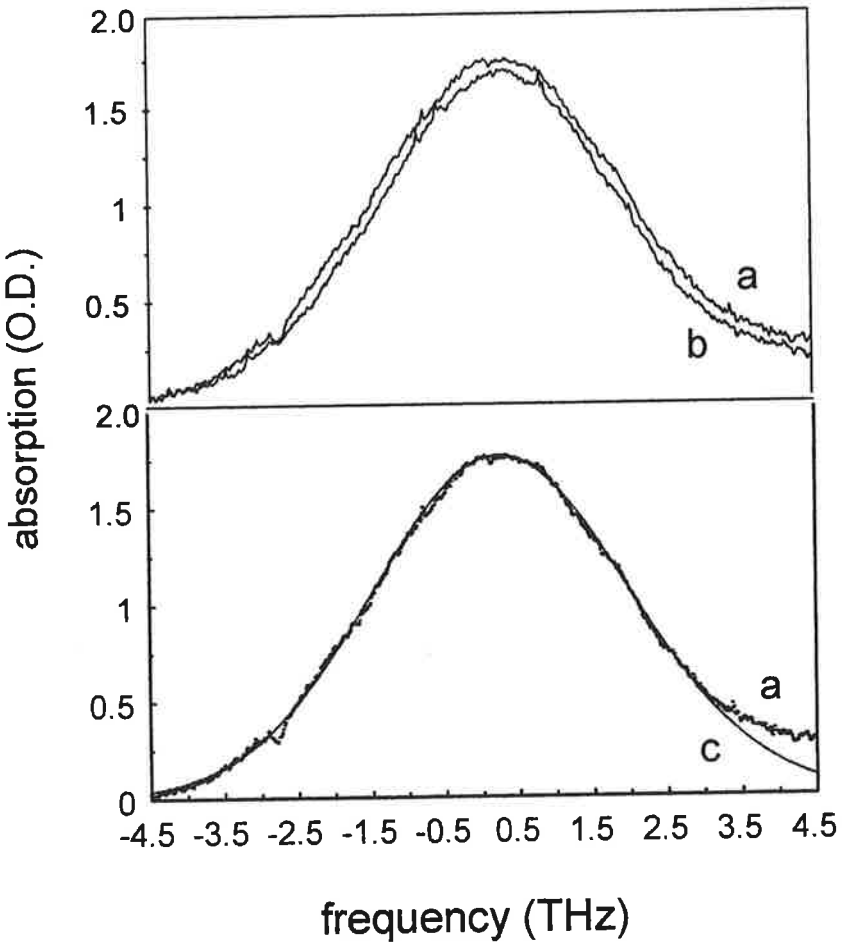

Figure 4.3 Absorption before (a), after (b) recording, and simulated one (c). The fitting parameter values are: α_{DW} = 0.9, Γ_p = 0.45 THz, Γ_{in}=4THz.

Then we turn to $\beta(\nu)$. At the present time, there is a little information on the value and the wavelength dependence of this quantity. If the quantum efficiency is assumed to be uniform over the inhomogeneous width, figure 4.4(b) gives the simulated signal spectrum with the following relevant parameters values obtained in last paragraph,

$$\alpha_{DW} = 0.9,\ \Gamma_p = 0.45\ \text{THz},\ \Gamma_{in} = 4\ \text{THz}$$

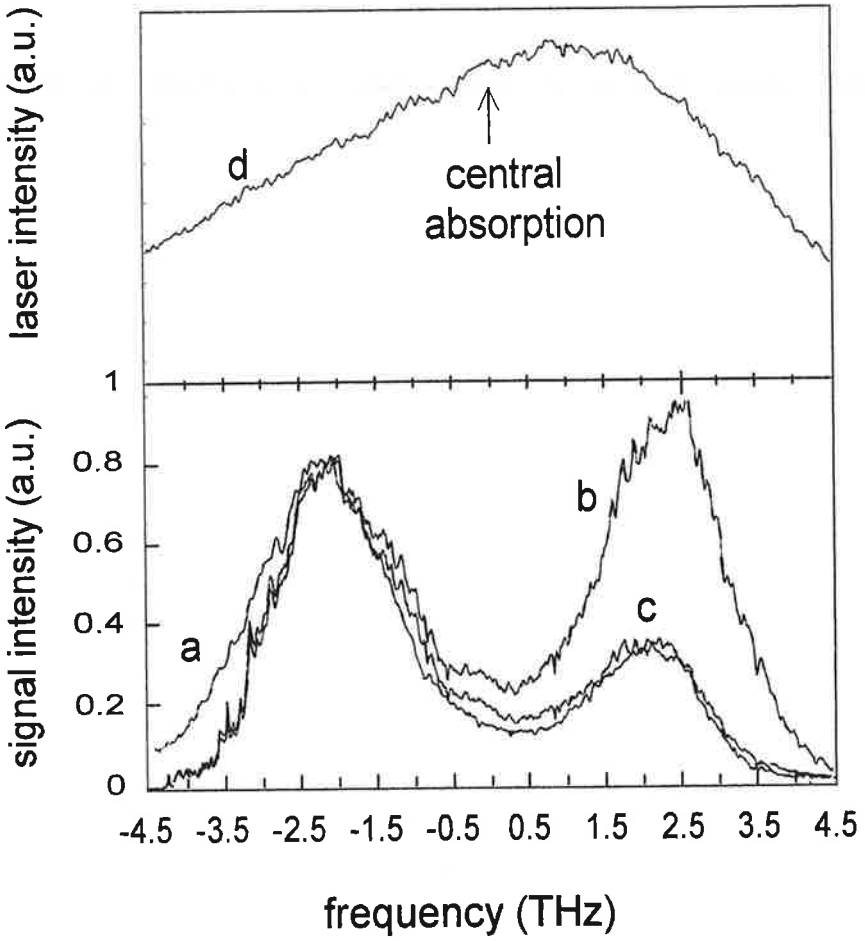

Figure 4.4 *(a) Experimental spectrum of signal intensity.*
(b) Simulation of signal with the fitting parameters of figure 4.3(c) and uniform $\beta(\nu)$.
(c) Simulation of signal with the fitting parameters of figure 4.3(c) and $\beta(\nu)=\beta_0.[1-0.112(\nu-\nu_0)]$.
(d) Laser intensity spectrum $I_L(\nu)$.

which shows a large discrepancy with the experimental curve 4.3(a). So the assumption of a constant hole-burning efficiency over the entire inhomogeneous width appears as non-realistic and on the contrary, we have to consider its wavelength dependence. In order to eliminate the discordance, the simplest hypothesis is to assume a linear dependence of $\beta(\nu)$ on the wavelength. The best fit of the theory to the experimental data is drawn in figure 4.3(c) and corresponds to the following relation,

$$\beta(\nu) = \beta_0.[1-0.112(\nu-\nu_0)] \qquad (4.15)$$

where β_0 is a proportionality factor and ν is in THz.

Horie *et al.* [6] reported that the quantum efficiency decreases by about one order of magnitude from the red side to the blue side of the inhomogeneous absorption band. These measurements were made point by point for several systems like tetraphenylporphyrin (TPP) or sulfonated TPP in PMMA and poly(vinyl)alcohol (PVA) at 20 K. The covered range was about 490 cm^{-1} (20 nm). For methylene blue in PVA at 4K, a one order of magnitude decrease was also observed for a covered range of 1000cm^{-1} (50 nm). From our experiment, we obtain a reasonable understanding of our data only if we introduce a continuous variation of the excitation factor $\beta(\nu)$ over the whole inhomogeneous band. The slope of the variation of $\beta(\nu)$ versus the wavelength is obtained and we observe that $\beta(\nu)$ changes by only a factor of 2 over 180-200 cm^{-1} in OEP/PS. Our result agrees with the general observation fact that PSHB is less efficient on the blue edge than on the red edge of the inhomogeneous band. A possible reason is that off-resonance excitation processes through phonon side bands and energy-transfer which both contribute to the diminution of the probability for a photochemical event in the molecules excited at resonance have a higher rate at higher energies.

4.25 Discussion

We have investigated the diffraction spectrum affected by the homogeneous line structures and quantum efficiency. This study gives a general view over the signal spectrum on the scale of the whole inhomogeneous band under weak recording. More importantly, we proposed a novel method, by adopting a spectral approach for describing a time-resolved coherent transient process, to study electron-phonon coupling and frequency dependence of relative quantum efficiency of photochemical reaction in a low temperature dye-doped amorphous material. Based on these parameters, we can estimate the situation of our realistic material. Firstly, we noticed that the factor $n_0(\nu)/A(\nu)$ for our sample is close to unity because of the weak electron-phonon coupling. So the effect of PSB on the temporal holographic signal is of little importance under the condition of large time interval between reference and object pulses. Furthermore, The slow frequency variation of the

burning rate should be neglected in our spectral storage experiment (chapter 2) since the encoding window spans a 1.1THz interval which is much narrower than 4THz-wide absorption band. With these two approximations, the consideration of a more complicated model of spectral redistribution can be facilitated and effectuated.

4.3 Tautomerization model in OEP doped polymer

The PSHB mechanism for free-base porphyrin-derivative doped solids is usually well understood as a light-induced tautomerization reaction at low temperature. The displacement between the resonant spectra of the two tautomers depends on both dopant molecules and matrix. Distinct hole burning product spectra, called antiholes, have been experimentally observed for porphyrin-doped crystalline matrices in which the tautomers have well-separated absorption peaks because the spectral separation is larger than the inhomogeneous broadening. In those observations, one also noticed that a narrow hole always corresponds to a relatively broadened antihole and the inverse tautomeric process from the product to the educt can occur provided one irradiates at the product resonant frequency. Comparatively, the measurement of antihole structures for a symmetric molecule in amorphous hosts is rather difficult since the spectral shifts of the products from the reactants are usually less than the inhomogeneous width. No clear spectral distribution of PSHB products for OEP/PS has been found so far. However, some observations indicate that a widely spread product spectrum exists and overlaps with that of the educt [7,10].

The spectral distribution of photoproducts is a crucial issue since under large burning exposure conditions a molecule may undergo successive photo-tautomerizations if the photoproduct frequency falls within the laser bandwidth.

An OEP molecule may exist in one of two tautomeric forms according to the position of its inner protons. The aromatic delocalization path is defined by a 18-annulene system of isolated double bonds on the porphyrin periphery and changes with the different position of the pair of inner proton-nitrogen bonds as shown in figure 4.5. For the light-excited electronic transition on $Q_x(0\text{-}0)$ band, a molecule can be regarded as an oscillator whose optical dipole is directed along the long axis of the electron delocalization path. The optical dipoles corresponding to the two tautomeric forms are oriented perpendicularly to each other in the molecular plane. In other words, when the molecule swings from one form to another, its optical dipole undergoes a 90° rotation in the molecular plane[11,12]. A coordinate system (X,Y,Z) is attached to each molecule in such a way that the Z axis is normal to the molecular plane and the two tautomeric dipoles directions are labeled as X and Y, respectively. In the laboratory frame (ijk), the external electromagnetic field is polarized along the z-

axis unit vector $\vec{e}_k$ (see figure 4.5(b)). The Euler angles of an optical dipole oriented along X and Y are respectively denoted as (ϕ, θ, ψ) and (ϕ, θ, $\psi+\pi/2$). The unit vector $\vec{e}_k$ can be expressed in the molecular frame as:

$$\vec{e}_k = \begin{pmatrix} \sin\theta\sin\psi \\ \sin\theta\cos\psi \\ \cos\theta \end{pmatrix} (\vec{e}_X, \vec{e}_Y, \vec{e}_Z) \qquad (4.15)$$

Considering that the molecules are randomly oriented in the amorphous host, the angles ϕ, θ, ψ range, respectively, in $[0,2\pi]$, $[0,\pi/2]$, $[0,\pi]$.

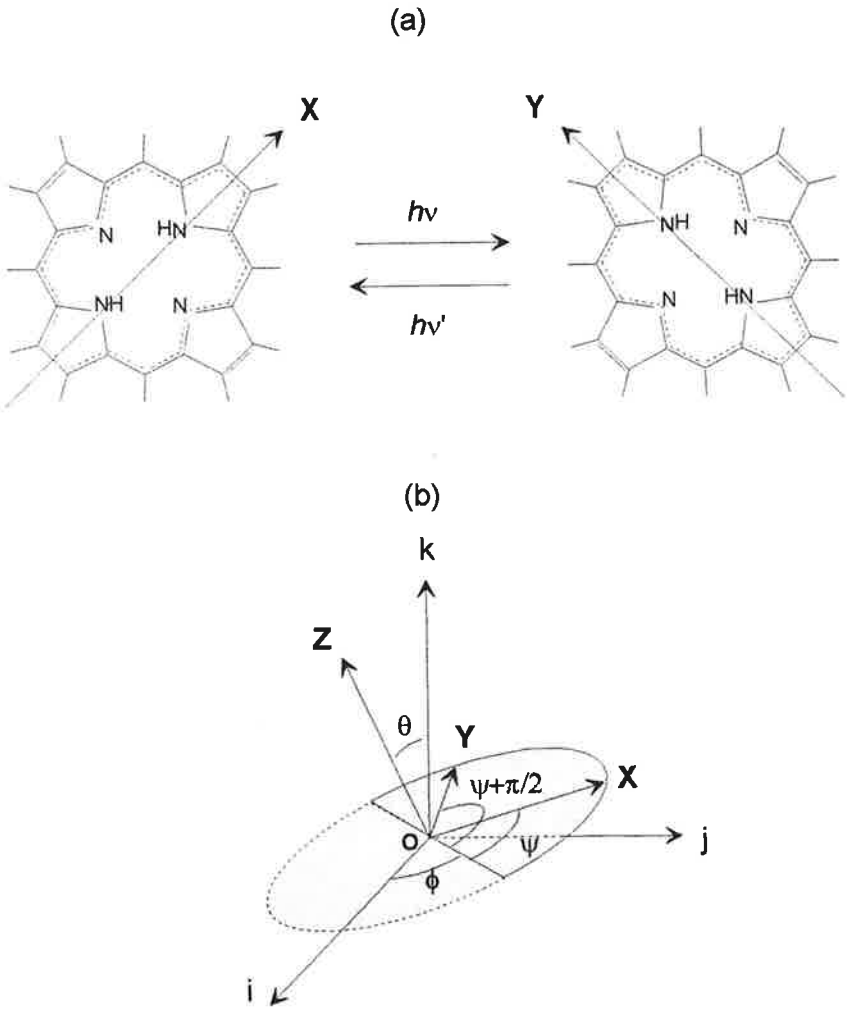

Figure 4.5 (a) Optical dipoles corresponding to two tautomers. (b) Coordinate systems for sitting a molecule: (X,Y,Z)-molecular coordinates, (ijk)-laboratory coordinates. A dipole in X or Y direction is respectively labeled as (ϕ, θ, ψ) or (ϕ, θ, $\psi+\pi/2$).

Now we take the molecular resonant frequency into account. The energy states of the two tautomers are diagrammed in figure 4.6 as two level systems [7] (TLS) consisting of double-well potentials. For an isolated molecule, the double-well potential has a symmetric structure which implies an identical resonant frequency for both forms. But this is not true when the molecule is embedded in an amorphous host. The guest/host interaction which is rather complicated and locally-dependent, usually deforms the potential wells, and results in a splitting of the resonant frequencies of the two tautomers.

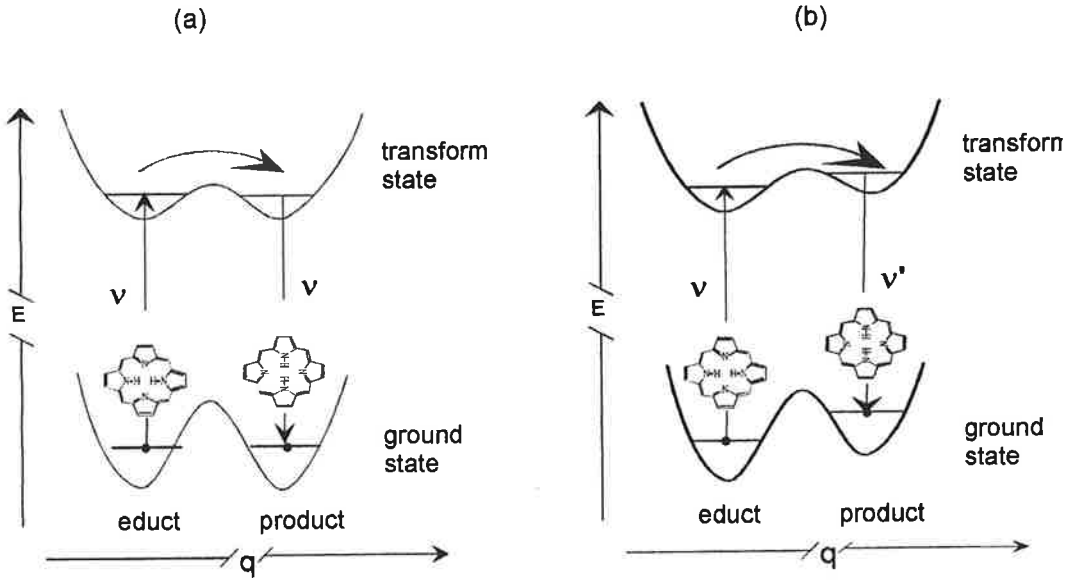

Figure 4.6 Energy levels of an isolated molecule (a), and of a molecule doped in an amorphous matrix (b).

The PSHB model that we propose relies on the two following assumptions:

(1) When a group of molecules is burnt at an initial state (ϕ,θ,ψ,ν), the photo-product dipoles are switched into direction $(\phi,\theta,\psi+\pi/2)$, with various resonant frequencies ν'. For sake of convenience, the directions (ϕ,θ,ψ) and $(\phi,\theta,\psi+\pi/2)$ are denoted, respectively, by Ω and Ω' hereafter.

(2) If a molecule burnt at (Ω,ν) relaxes to its tautomeric form at (Ω',ν'), it comes back to its initial form when it is re-burnt at ν'.

Let $n(\Omega,\vec{r},\nu \mid \nu')$ represent the distribution of molecules at position $\vec{r}$ within the sample, resonant at ν, heading in direction Ω, which can be converted into a tautomeric form heading in direction Ω', resonant at ν'. When the molecular system is

burnt by a light field $\vec{E}(\vec{r}, \nu)$ polarized in direction $\vec{e}_k$, the kinetic equation of the photochemical reaction is written as:

$$\frac{dn(\Omega, \vec{r}, \nu|\nu')}{dt} = -\kappa(\Omega, \vec{r}, \nu)n(\Omega, \vec{r}, \nu|\nu') + \kappa(\Omega', \vec{r}, \nu')n(\Omega', \vec{r}, \nu'|\nu) \quad (4.16)$$

The first term on the right-hand side is the result of a population decrease caused by the molecular transformation from (Ω,ν) to (Ω',ν'), the second term represents the reverse process that increases the population. The transformation rates for the two processes respectively read as:

$$\kappa(\Omega, \vec{r}, \nu)=\sigma\left|\vec{E}(\vec{r}, \nu)\cdot\vec{P}\right|^2 =\beta(\nu)\, I(\vec{r}, \nu)\, \sin^2\theta\, \sin^2\psi, \quad (4.17)$$

$$\kappa(\Omega', \vec{r}, \nu')=\beta(\nu')\, I(\vec{r}, \nu')\, \sin^2\theta\, \cos^2\psi, \quad (4.18)$$

where $\beta(\nu)$ represents the burning efficiency, and $I(\vec{r}, \nu)= \left|\tilde{E}(\vec{r}, \nu)\right|^2$ is the spectral intensity of the burning light. One implicitely assumes that the photochemical process has enough spectral resolution to imprint the spectral profile of the burning light into the photosensitive material. We admit that this resolution is given by the homogeneous width of the transition, Γ_{hom}, which is supposed to be smaller than the narrowest spectral structure in $I(\vec{r}, \nu)$. This description also requires that the optical excitation is not hampered by radiative saturation. More precisely, one assumes that the relative population in triplet state is smaller than unity.

The molecule conservation is written as:

$$n(\Omega, \vec{r}, \nu \mid \nu')+ n(\Omega', \vec{r}, \nu' \mid \nu)= n_0(\nu \mid \nu')+ n_0(\nu' \mid \nu) \quad (4.19)$$

where $n_0(\nu \mid \nu')$ represents the initial distribution of the molecules that swing from ν to ν' when they undergo a tautomerization reaction. This initial distribution is assumed to be isotropic with respect to dipole orientation. Substitution of Eq.(4.19) into Eq.(4.20) leads to the following equation for $n(\Omega, \vec{r}, \nu \mid \nu')$:

$$\frac{dn(\Omega, \vec{r}, \nu|\nu')}{dt} = \kappa(\Omega', \vec{r}, \nu')[n_0(\nu|\nu') + n_0(\nu'|\nu)] - [\kappa(\Omega, \vec{r}, \nu) + \kappa(\Omega', \vec{r}, \nu')]n(\Omega, \vec{r}, \nu|\nu') \quad (4.20)$$

The solution of this equation is then integrated over ν' and one gets the density of molecules heading in direction Ω at frequency ν:

$$n(\Omega, \vec{r}, \nu) = \int n(\Omega, \vec{r}, \nu|\nu')d\nu' \quad (4.21)$$

Angular averaging finally leads to the following expression of the absorption coefficient for a field polarized in direction $\vec{e}_k$:

$$\alpha(\vec{r},\nu)=\alpha_0\langle n(\Omega,\vec{r},\nu)(\vec{e}_X\cdot\vec{e}_k)^2\rangle_\Omega / \left(\langle(\vec{e}_X\cdot\vec{e}_k)^2\rangle_\Omega \int n_0(\nu_0|\nu')d\nu'\right) \qquad (4.22)$$

where, $\vec{e}_X\cdot\vec{e}_k=\sin\theta.\sin\psi$, $\langle(\vec{e}_X\cdot\vec{e}_k)^2\rangle_\Omega=2\pi^2/3$, and α_0 is the initial absorption coefficient at the line center ν_0.

In order to proceed further, one has to specify $n_0(\nu \mid \nu')$. We assume that the tautomeric forms have the same spectral profile and that the molecules which are resonant at frequency ν, with their optical dipole oriented in direction Ω, are evenly redistributed over the entire bandwidth if they undergo a tautomerization reaction, irrespective of their initial frequency ν. Then $n_0(\nu \mid \nu')$ reads as:

$$n_0(\nu \mid \nu')= n_0(\nu)n_0(\nu') \Big/ \int n_0(\nu)d\nu \qquad (4.23)$$

where $n_0(\nu)$ represents the initial molecule density. The latter function is represented by a Gaussian profile,

$$n_0(\nu) = e^{-4\ln 2\left(\frac{\nu-\nu_0}{\Gamma_{in}}\right)^2} \qquad (4.24)$$

where the inhomogeneous width Γ_{in} is taken as the full width at half maximum of this function.

The tautomerization model connects the spectral density of fluence with the spatial and spectral distribution of the absorption coefficient. The equilibrium spectral distribution $n_0(\nu \mid \nu')$ contains the crucial assumptions of the model. It determines the evolution of the system exposed to the burning light. We have to check that the postulated shape of $n_0(\nu \mid \nu')$ is consistent with the measured efficiency of diffraction on a broadband spectral hologram. In order to connect the microscopic model with hologram readout, one has to describe the propagation of light fields through the photosensitive material. This is achieved with the model developed in chapter 3.

4.4 Holographic recording and diffraction efficiency

4.41 Writing beams

We check the tautomerization model in the simple situation where no spectral phase code is imprinted on the engraving beams. On the front side of the sample, the energy distribution in each elementary pulse pair is described as:

$$W(z=0, x, \nu)=W_0 \, \mathrm{rect}\left[\frac{\nu-\nu_L}{\Delta}\right](1+\cos\varphi) \qquad (4.25)$$

where $\mathrm{rect}[x]=\begin{cases}1 & |x| \le 1/2 \\ 0 & |x| \ge 1/2\end{cases}$ and $\varphi= Kx+2\pi\nu\tau$. The width of the excitation spectrum, Δ, is assumed to satisfy the condition,

$$1/\tau << \Delta \qquad (4.26)$$

As energy propagates through the material, its spectral and spatial distribution is modified. Indeed the progressive bleaching affects the sample transmission in a space and frequency dependent way. As in chapter 3, we consider that very few waves contribute to energy propagation through the PSHB plate. Then the phase matching condition reads as:

$$\frac{L}{\lambda}\theta^2 << 1 \qquad (4.27)$$

and the energy transmission can be described by:

$$W(z, x, \nu)= W(0, x, \nu)\, e^{-\int_0^z \alpha(z', x, \nu)dz'} \qquad (4.28)$$

where the absorption coefficient $\alpha(z, x, \nu)$ reflects the etching action of the previous pulse pairs.

4.42 Formal expression of the diffraction efficiency

In order to calculate the engraved structure, one has to solve the coupled equations (4.20-22) and (4.28) with the initial conditions $n(\Omega, \vec{r}, \nu\,|\nu')= n_0(\nu\,|\nu')$ and the boundary value condition given by Eq. (4.25).

In a tentative solution, let us assume the energy remains a function of cosφ as it propagates through the sample. Then, the driving factors $\kappa(\Omega, \vec{r}, \nu)$ and $\kappa(\Omega', \vec{r}, \nu)$ in equation (4.20) are respectively functions of cosφ and cosφ' (where $\varphi'=2\pi\nu'\tau+Kx$). It results that the population $n(\Omega, \vec{r}, \nu)$ is a function of cosφ, except for a slow variation as a function of ν. So the bleaching modified absorption coefficient is also a function of cosφ, which, according to equation (4.28), is consistent with our initial assumption of the cosφ-dependence of the propagating energy. As a consequence, in the Fourier series expansion of $\alpha(\vec{r}, \nu)$:

$$\alpha(\vec{r}, \nu)=\sum_{p}\tilde{\alpha}^{(p)}(z, \nu)e^{-ipKx},$$

the frequency dependence of the coefficient $\tilde{\alpha}^{(p)}(z, \nu)$ is mainly contained in an oscillating factor $e^{2ip\pi\nu\tau}$ (refer to section 3.3). Then, diffraction in direction $\vec{k}_2$ is described by expression (3.35) and the diffraction efficiency on the engraved hologram reads as:

$$\eta(\nu)= \left|\tilde{A}^{(1)}(\nu)\right|^2 e^{-\tilde{A}^{(0)}(\nu)} \qquad (4.29)$$

Within the limits set by Eq.(4.27) this model is valid for arbitrary optical density, dose and excitation bandwidth. However, an analytical solution of the equation set does not seem to be feasible and we have to resort to a numerical calculation.

4.43 Computation of the diffraction efficiency.

We divide a PSHB sample into R identical δz-thick slices. Each one is thin enough so as to satisfy the small optical density condition $\alpha_0\delta z<<1$. A sample with arbitrary optical density may be dealt with this method by changing the total slice number. The burning energy is also divided into small units W_0. During the time separation between two bursts of energy the molecule returns to a stable state. Each elementary dose can be regarded as a perturbation, i.e. $\beta W_0<<1$. A single hologram recording requires the accumulation of a certain number of elementary doses.

The elementary step of the calculation describes the action of one elementary dose within one elementary slice of the PSHB material. The procedure is depicted in

figure 4.7. One starts from an initial value of the molecular distribution $n(\Omega,r\delta z,x,\nu \mid \nu')$ and a boundary value of the elementary dose $W_0((r-1)\delta z,x,\nu)$ on the front side of the elementary slice. The initial value of $n(\Omega,r\delta z,x,\nu \mid \nu')$ is the result of the previous dose transmission and the front side value of $W_0((r-1)\delta z,x,\nu)$ is nothing but the energy distribution on the backside of the precedent slice. The absorption coefficient at $r\delta z$, $\alpha(r\delta z,x,\nu)$, and its z-integrated value up to $r\delta z$, $A(r\delta z,x,\nu)$, are computed from $n(\Omega,r\delta z,x,\nu \mid \nu')$. From the first two Fourier coefficients of $A(r\delta z,x,\nu)$, the diffraction efficiency $\eta(r\delta z, \nu)$ of a $r\delta z$-thick slice is computed with the help of Eq.(4.29). This quantity is saved to data files.

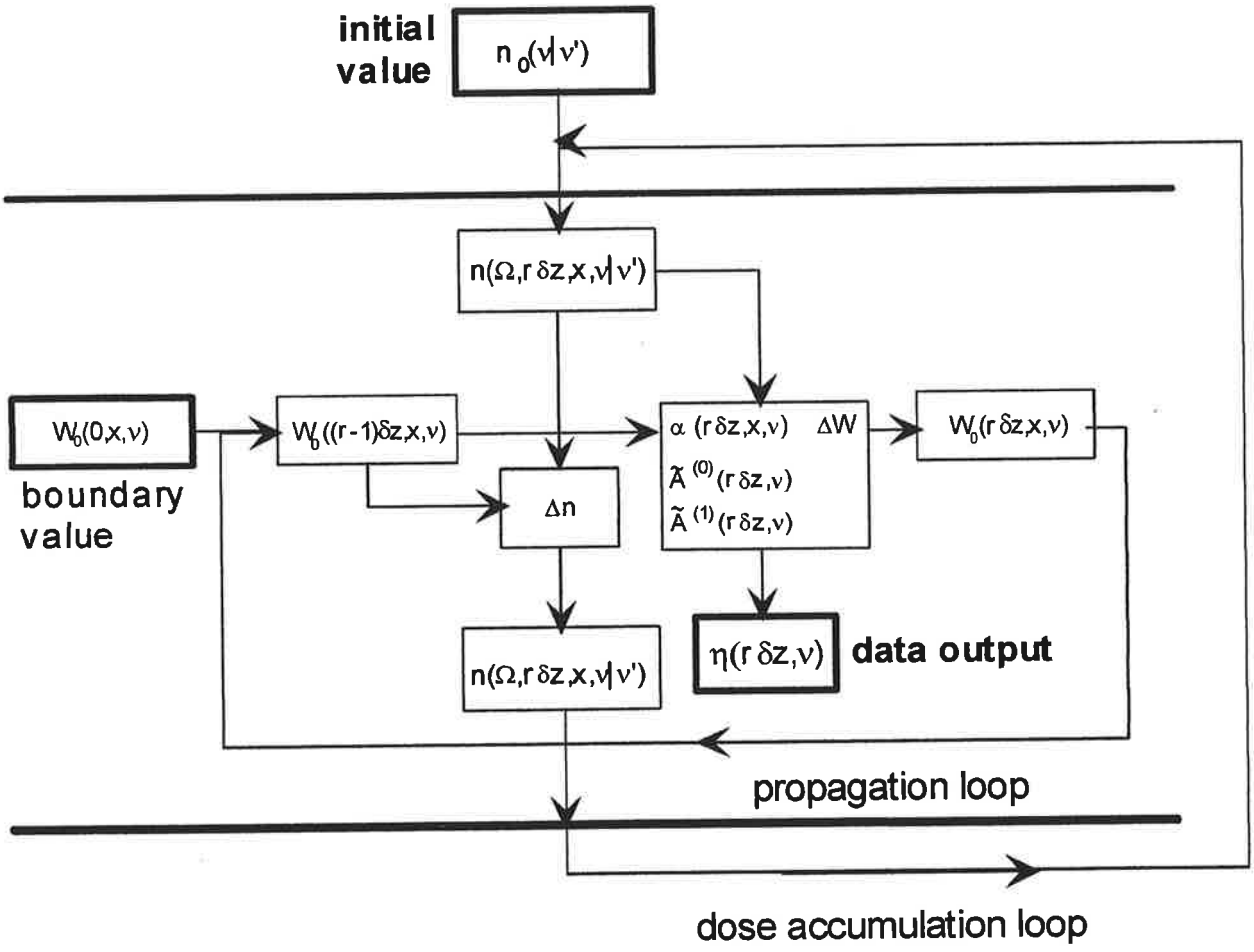

Figure 4.7 Numerical procedure for computing diffraction efficiency. The value of $W_0((p-1)\delta z,x,\nu)$ on the back side of the slice #p-1 is used as the input value of the energy distribution in the front side of slice #p. The output value of $n(\Omega,p\delta z,x,\nu|\nu')$ is used as the input value of the calculation with the next elementary dose.

Then the absorbed energy is calculated as:

$$\Delta W = - W_0((r-1)\delta z,x,\nu)\ \alpha(r\delta z,x,\nu)\ \delta z, \qquad (4.30)$$

and is used to obtain the output energy $W_0(r\delta z,x,\nu)$. One also computes the burning action of $W_0((r-1)\delta z,x,\nu)$. The resulting modification of the molecular distribution reads as:

$$\Delta n = 2\beta(\nu)\ W_0((r-1)\delta z,x,\nu')\ \sin^2\theta\ \cos^2\psi\ n_0(\nu \mid \nu') -$$

$$- \beta(\nu)\ \sin^2\theta[W_0((r-1)\delta z,x,\nu)\ \sin^2\psi + W_0((r-1)\delta z,x,\nu')\ \cos^2\psi]\ n(\Omega,r\delta z,x,\nu \mid \nu') \quad (4.31)$$

The molecular distribution is updated as $n(\Omega,r\delta z,x,\nu \mid \nu')+\Delta n$. The calculation is iterated from the front side of the PSHB plate to the distance $L=R\delta z$. Then an additional elementary dose is directed to the front side of the plate.

4.44 Numerical results

The saved values of $\eta(r\delta z,\nu)$ form a 2-dimensional array. One dimension represents the initial optical density $\alpha_0(\nu)p\delta z$ /ln10 of the sample that gives rise to the signal. The other dimension corresponds to the dose $m\beta W_0$ that has been used to engrave the diffracting hologram. Therefore, for various initial optical densities, and various excitation bandwidths, we can plot the diffraction efficiency as a function of burning dose. Two of these curves are displayed on figure 4.8. The initial optical density is OD=1.5 and the burning bandwidth has been set equal to Δ= 80GHz (curve a), and 1.56THz (curve b).

These two cases are studied as the examples of narrow and broad band storages. The 80GHz-wide recording can be regarded as a case of non-redistribution since $\Delta << \Gamma_{in}$. Except for the molecular orientation dependence of the interaction with the polarized pulses, this situation is correctly described by the simple model of chapter 3. Hologram engraving over a 1.56THz-wide window is a situation similar to that of our preliminary experiment presented in chapter 2. The storage bandwidth is on the order of magnitude of Γ_{in} and the spectral redistribution has to be taken into account.

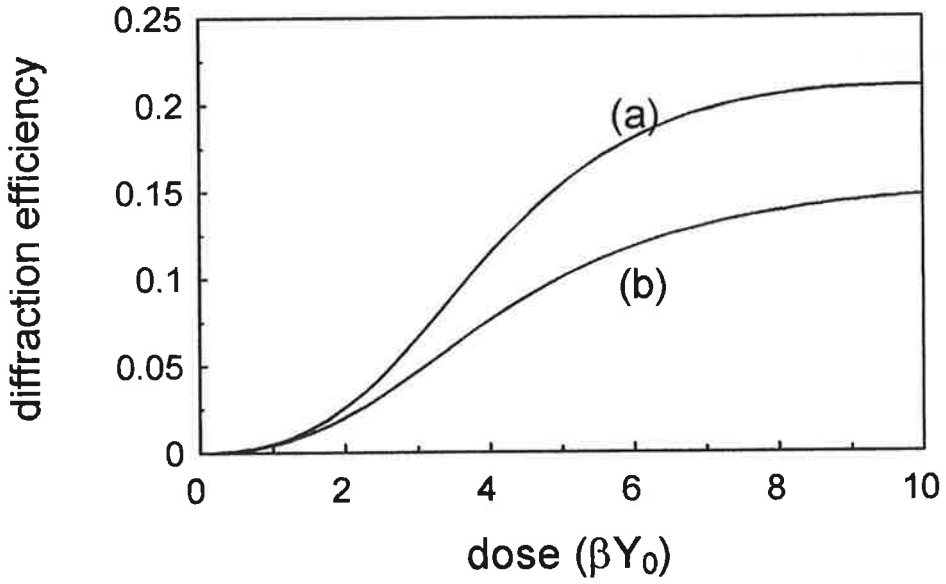

Figure 4.8 Numerical computation of the diffraction efficiency with 80GHz (a) and 1.56THz (b) recording bandwidth.

According to Fig 4.8 the diffraction efficiency does not depend on the burning bandwidth in the small dose region. As the burning energy is increased, the diffraction efficiency grows less rapidly in the broadband recording situation than in the narrow band burning conditions and it saturates at a lower value. In order to get a physical picture of these features, let us consider the class of molecules with resonant transition frequency ν. Broadband excitation of the sample makes some molecules leave the frequency class at ν while some molecules from various frequency classes ν' inside the excitation bandwidth are transfered to ν. Departure from ν results in the etching, inside the molecular distribution, of the spectral structure conveyed by the burning light. This is the hologram that diffracts the probe pulse. On the contrary, molecules that arrive at ν originate from different phase regions in the writing beam interference pattern. The scrambled spectral structure that they build at frequency ν does not contribute to the diffracted signal. Therefore the diffraction efficiency does not depend on the storage bandwidth in the small dose region. As doses are accumulated, the sample is more deeply bleached and the signal is less absorbed. However, the molecules that arrive at ν from ν', in the broadband situation partly compensate for the absorption reduction. At a given spectral density of burning energy, the signal is thus expected to decrease as the storage bandwidth is enlarged.

4.5 Experimental

4.51 Experimental setup

We designed an experiment to check our redistribution model. The same OEP/PS sample as that in section 4.2 was used as memory medium. Its maximal absorption (OD=1.8) is located at 618.7nm.

A setup drawn in figure 4.9 and similar to that used in section 4.2 is employed for hole burning and holographic experiments with an adjustable spectral window. Two differences have to be pointed out. First, a Lyot spectral filter has been inserted in the optical path just after the dye-laser. One equalizes the spectral distribution in the excitation beam by adjusting the orientation of the birefringent plate. Second, the reference and object pulses are both split from the beam that emerges from the spectral shaper device so that they both exhibit the same spectral and spatial distribution.

(a)

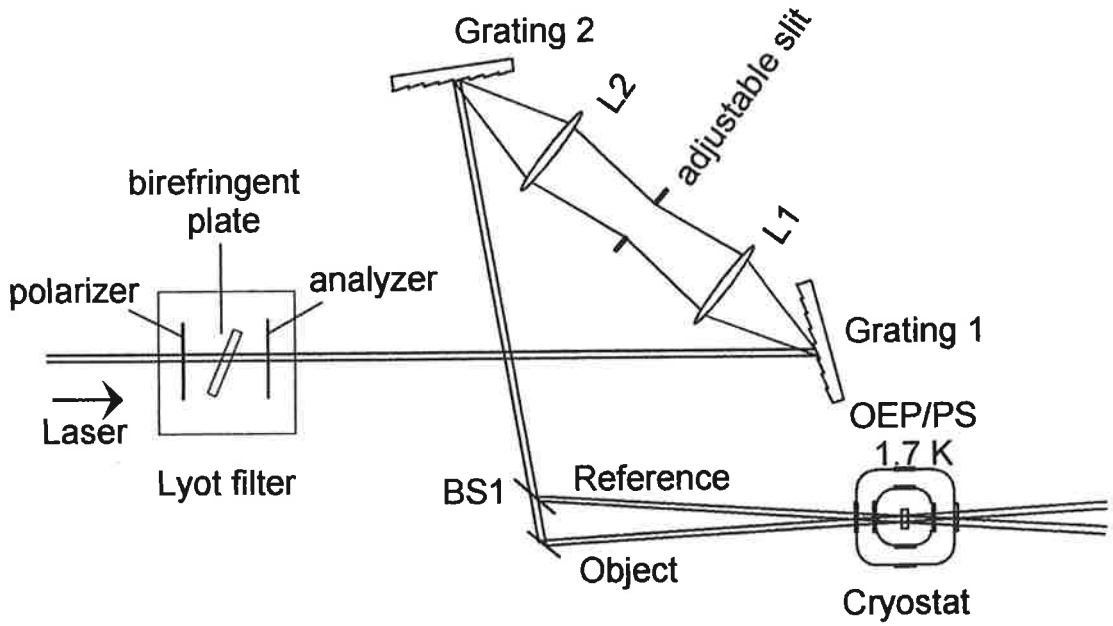

(b)

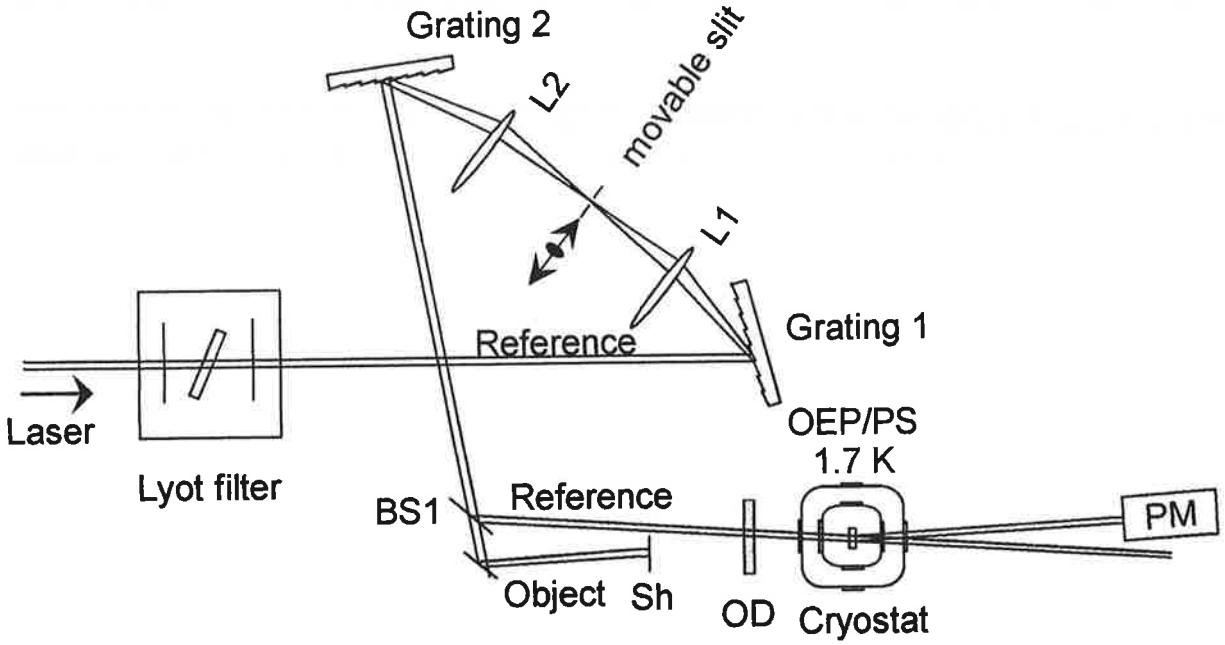

Figure 4.9 *(a) Experimental setup for arbitrary band recording. A 2cm delay is added on the object path with respect to the reference. (b) Setup for signal spectrum analysis.*

The spectral width and the central position of the writing and readout beams are controlled with an adjustable slit (with a precision of 80GHz around 620nm), mounted on a translation stage, that is positioned in the focal plane of the two-gratings spectral shaper. The optical path of the object pulse is 2cm longer than that of the reference one. Therefore a time interval τ~60ps is maintained between the pulses. The angle θ between the two beams is adjusted to be ~0.01rad. In our sample with thickness L=0.5mm, the phase matching condition $\theta^2 L/\lambda << 1$ is satisfied.

For recording a hologram, one sets the slit position to 618.7nm and one adjusts its width to Δ. The shutter before the sample is removed. The engraving processes are accumulated by successive pairs of pulses at a repetition rate of 15Hz. The energy of the pulse-pair w_0 (in Joule) is measured with a pyroelectric Joule meter (Molectron J9LP) placed just before the cryostat where the sample is immersed. The incident energy dose per spectral unit during t seconds is calculated as,

$$Q_{exp} = 15 w_0 t/\Delta \quad \text{(in J/THz)}$$

For probing, one sets the slit to its minimal width (80GHz) and the object beam is blocked. A neutral density filter (usually OD~3) is inserted before the cryostat to attenuate the probe intensity. The diffraction spectra are detected on a photomultiplier in the object direction while the translation stage is scanned. In summary we are able to vary the width of the storage window and the exposure dose, and to spectrally analyze the engraved holograms

4.52 Diffraction spectra

Two series of recordings are achieved. In the first one, the spectral width of the recording window is set equal to 80GHz. It is much smaller than the inhomogeneous width (4THz). In this situation, most of the burnt molecules fall out of the excitation region and can not be switched back to their original frequency by the driving field. The diffracted signal is recorded as a function of the exposure. The same quantity is monitored in the second series of experiments, but the recording window is enlarged to 1.56THz which is close to the size of the spectral encoding window in the storage experiment described in chapter 2.

The narrow and broad band holograms, at a given dose spectral density value, are both recorded on the same sample spot. In this way the comparison of their respective diffraction efficiencies is not spoilt by a possible homogeneity defect of the sample. A narrow band hologram is recorded and detected first. Then it is overwritten by a broadband one. Due to the great difference of bandwidths between two recordings, the broadband hologram is hardly affected by the previously engraved narrow band one. The average pulse-pair energy spectral density is adjusted to 0.86μJ/THz/shot for all recordings. The exposure dose is controlled by the exposure time. 16 holograms are recorded on 8 spots corresponding to the exposure times from 30 seconds to 16 minutes. After each recording, the attenuated reference beam, with its spectral width reduced to 80GHz, is directed to the engraved hologram. The diffracted energy is measured as a function of the probe beam wavelength which is scanned over a 2THz interval. The diffracted signal spectra are plotted in figure 4.10. At each sample spot, a narrow peak on the broad spectrum is the remnant of the narrow recording. The broad spectra are interpolated at this frequency.

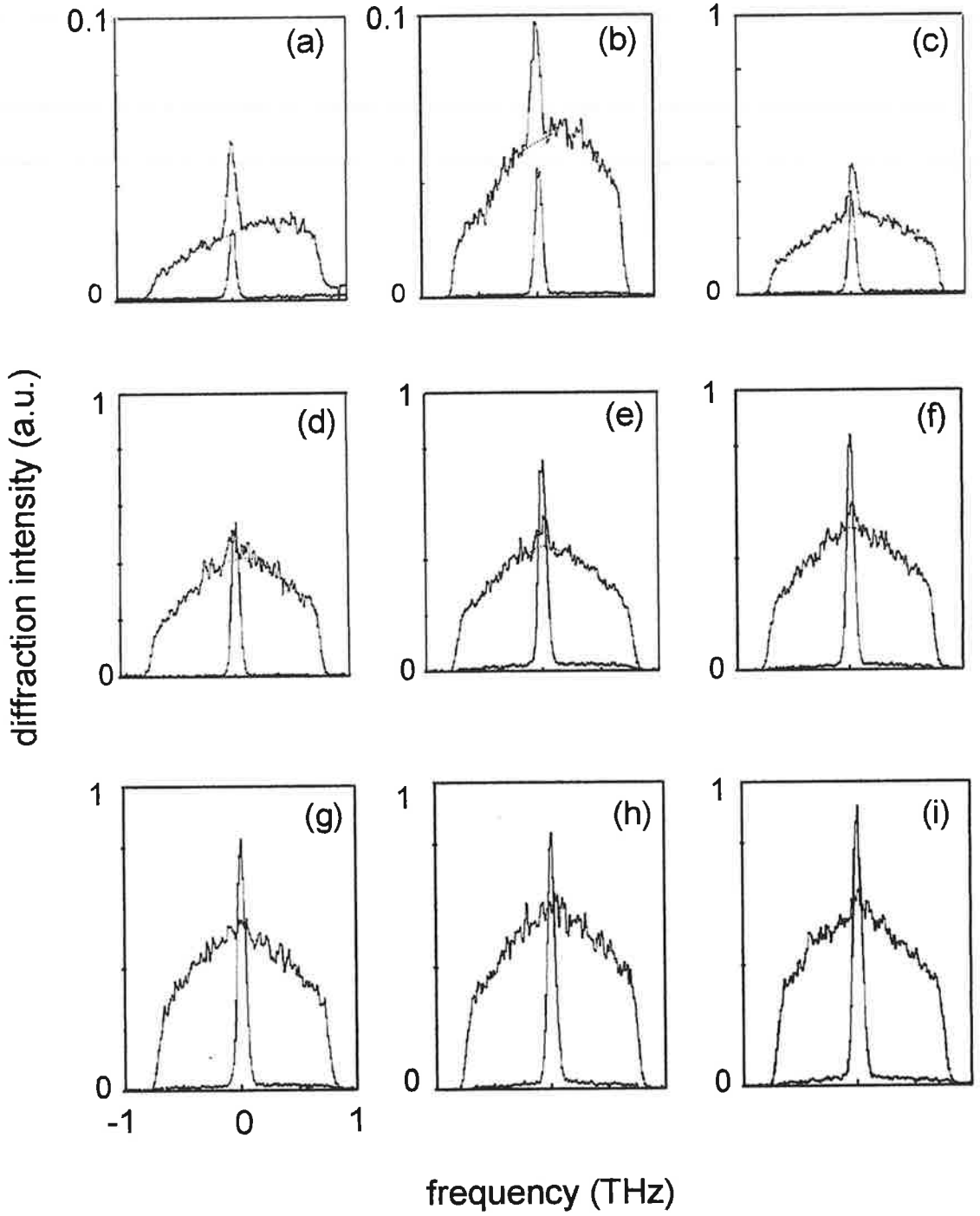

Figure 4.10 Diffracted energy, for narrow and broad band engravings. Exposure spectral density of energy: 0.8(a), 1.6(b), 3.2(c), 4.6(d), 6.2(e), 7.2(f), 8.6(g), 9.9(h), 11.3 mJ/THz(i).

Figure 4.10 shows the common evolution trend of the signal for both recording widths. It increases with the dose at the beginning, then reaches saturation. But,

depending on the storage width, it evolves at different rates and saturates at different levels. For quantitative analysis, the experimental and theoretical evolution curves have to be compared.

The theoretical evolution of the diffraction efficiency in section 4.4 is expressed as a function of the dimensionless parameter βY_0. Comparison with experimental results requires that we find the relationship between this dose parameter and the measured spectral density of energy. This is done with the help of a simple hole burning experiment.

4.53 Calibration of the dose scale by hole burning

According to Eqs.(4.22-24), the z-integrated absorption in the small dose, narrow band limit, reads as:

$$A(\nu)=A_0(\nu)-\frac{3}{5}\,\beta Y_0\,(1-e^{-A_0(\nu)}) \qquad (4.32)$$

which expresses $A(\nu)$ as a linear function of the dose parameter βY_0. In a narrow band hole burning experiment we plot the hole depth vs the burning dose. From the slope of the curve at the origin, with the help of Eq.(4.32), we relate the dose parameter βY_0 to the experimental energy scale.

The hole burning experiment is performed with the setup depicted in figure 4.9 where the reference path is blocked. The object beam alone is used alternatively as the burning beam and as the probe beam with an intensity attenuated by the neutral intensity filter OD=3. The slit is always set to its minimal width. The pulse average energy is adjusted to w_0=0.4μJ/shot corresponding to a spectral intensity 5.1μJ/THz/shot. Before burning, the initial transmission spectrum $T_{before}(\nu)$ of the sample is detected by scanning the probe beam frequency. Then the position of the slit is fixed at 618.7nm and the sample spot is illuminated by the burning beam for 30 seconds. The transmission $T_{after}(\nu)$ is recorded after burning. The frequency dependent modification of the optical density is calculated as:

$$\Delta(OD)=\frac{1}{\ln 10}\log\frac{T_{after}}{T_{before}}$$

The hole depth is given by Δ(OD) at 618.7nm. Then the same spot is exposed to an additional dose and the hole depth is detected again. With this method we get a curve

of dose dependent hole depth as plotted in figure 4.11. The hole depth first increases linearly with the burning energy, then saturates at higher energy. From the slope at the origin, we conclude that:

$$Q_{exp}=1.22\ (\beta Y_0)(mJ/THz) \qquad (4.33)$$

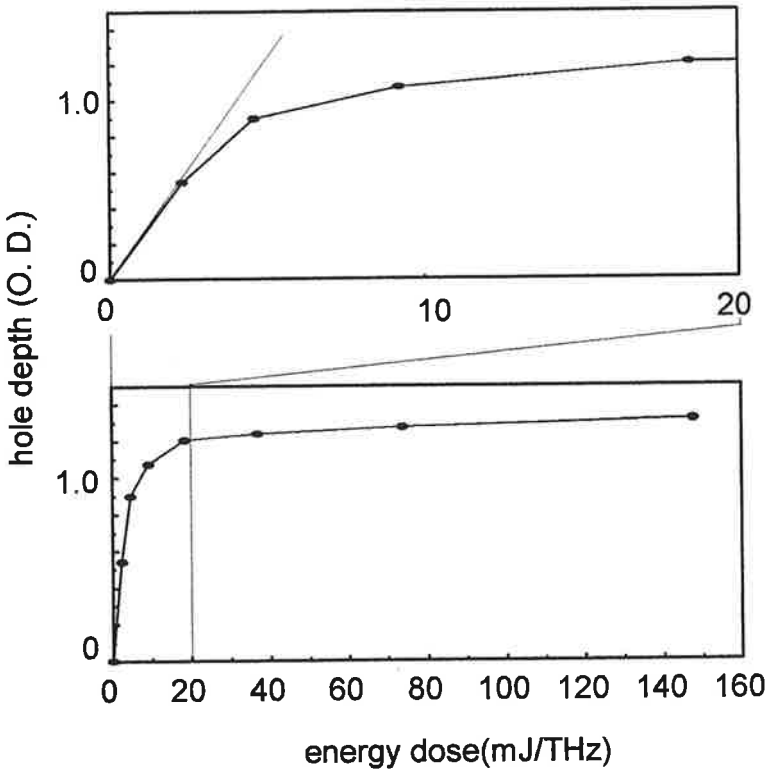

Figure 4.11 Evolution of the hole depth with the dose at 618.7nm, with a 80GHz-wide burning band.

The hole depth maximum does not exceed ~1.5 at the center of the line where the initial optical density is ~1.8. We attribute this incomplete bleaching to the existence of photo-inactive molecules and regard the maximal optical density as OD=1.5 in our calculation.

It should be noticed that the numerical parameter Y_0 actually represents a spatial and spectral density of energy, while the measured quantity Q_{exp} is integrated over the laser spot surface. It does not matter provided the same beam size is used in both the hole- burning and the holography experiment.

4.54 Diffraction efficiency as a function of the exposure dose

The measured diffraction efficiency at 618.7nm is plotted on figure (4.12) as a function of the burning dose. We have also plotted the diffraction efficiency that is measured at 618.7nm at the end of the two-step engraving process and that results from the accumulation of successive narrow band and broadband recordings. The theoretical curves corresponding to the three situations are drawn on the same figure. They are calibrated to the experimental energy scale with the help of Eq.(4.33). Curve (a) is for the narrow band, (b) for the broad band, and the (c) for the mixed one. The precision on the absolute value of the measured diffraction efficiency is rather poor. Therefore the experimental data scale on the vertical axis is adjusted by fitting the narrow band data to the corresponding theoretical curve.

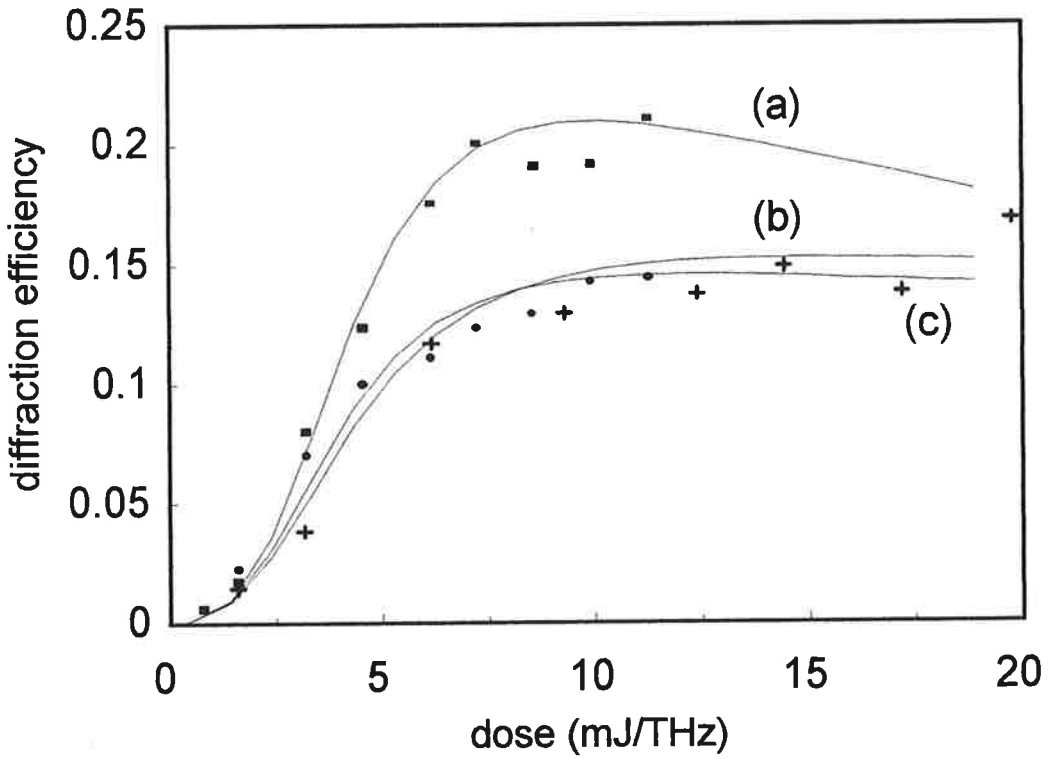

Figure 4.12 *Evolution of the diffraction efficiency with the incident dose. Solid lines: computed curves for 80GHz-wide burning (a), 1.56THz-wide burning (b), and for successive burnings over 80GHz and 1.56THz (c). Square dots, circles and crosses respectively represent the experimental results for 80GHz, 1.56THz and mixed burning conditions.*

From the coincidence between the experimental results and the computed curves, we may conclude that the redistribution model correctly describes the hole burning mechanism in our material. However, the absolute value of the experimental diffraction efficiency is about one order of magnitude smaller than expected from the theory. The origin of this discrepancy is not clear. The energy, the spectral and spatial distribution of the beams were carefully controled. Their superposition on the sample was checked. The mechanical stability of the setup during hologram recording could be called into question but the theoretical profile fits the experimental data over an exposure range that spreads from 30 seconds to 2x16 minutes. Mechanical vibrations should affect the long exposure data more seriously.

4.55 Radiative saturation

Our description of holographic recording relies on the assumption that each elementary pulse pair slightly affects the molecular distribution. According to the hole burning experiment discussed in section 4.53 the relative variation of the optical density produced by a single pulse is indeed about 10^{-3}. This actually represents the photochemical final balance of the excitation process, after the molecules have returned to steady state. It does not reflect the transient modification of the molecular population that is caused by radiative transfer to excited states and that is erased after a few tens of milliseconds. In this section, we check the effect of radiative saturation on the experimental results. Then we elucidate the conditions that avoid a large transient depletion of the ground state.

We measure diffraction efficiency as a function of energy per pulse-pair at a constant energy dose. In the absence of radiative saturation, the diffraction efficiency is independent of the pulse energy. Figure 4.13 represents the variations of the measured diffraction efficiency as a function of the energy per shot, for both narrow and broad band storage. Spectral dose is kept constant at 1.85mJ/THz by adjustment of the exposure time. The normalized values of the two curves are extrapolated to 1 when the pulse energy is zero. The diffraction efficiency decreases with the pulse energy, and the decreasing rate is more rapid for the broad hologram. The recording energy in the experiment of section 4.54, 0.7μJ/THz/shot, is close to the extrapolated point. So the data on Figure 4.12 are not affected by radiative saturation effects.

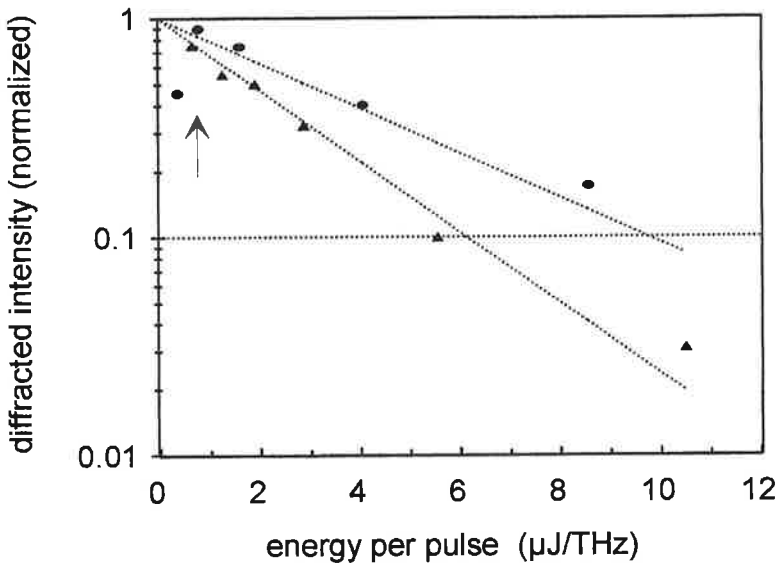

Figure 4.13 Radiative saturation for narrow band (circles), and broad band (triangles) burning conditions. The common extrapolated point represents the situation without radiative saturation. The arrow indicates the condition corresponding to the situation in figure 4.12.

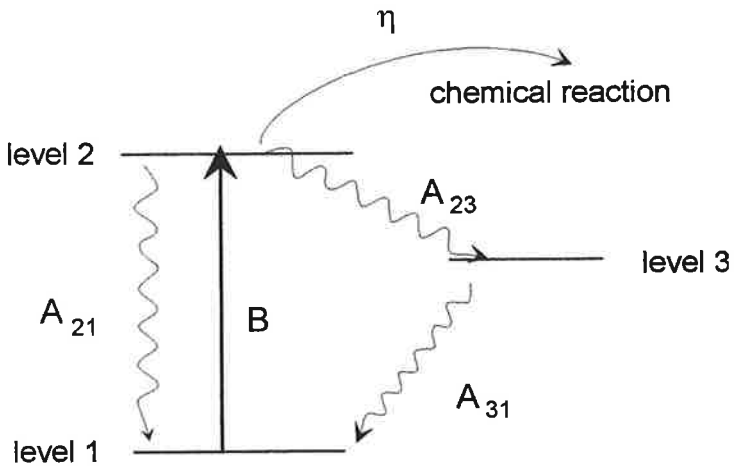

Figure 4.14 Light-induced transition, relaxation and chemical reaction processes in a three-level system.

In order to analyze radiative saturation, we describe OEP molecules as three-level systems. In figure 4.13, level 1 (2) represents the ground (excited) state where the molecular population is denoted as n_1 (n_2). Molecules are excited by a light with spectral intensity $I(\nu)$ from level 1 to level 2 where a part of them undergoes

photochemical hole burning with a quantum efficiency η. The rest relaxes to an intermediate level 3 and finally returns to the ground state. The light-induced transition and the relaxation rates are denoted by Einstein's coefficients, respectively, as B, A_{21}, A_{23}, A_{31}. The dynamic functions of the system are expressed as:

$$\frac{dn_1}{dt} = A_{21}n_2 + \frac{I(\nu)}{c}B(n_2 - n_1) + A_{31}n_3$$

$$\frac{dn_2}{dt} = \frac{I(\nu)}{c}B(n_2 - n_1) - (1+\eta)(A_{21} + A_{23})n_2$$

$$\frac{dn_3}{dt} = A_{23}n_2 - A_{31}n_3 \qquad (4.34)$$

In our system, the process from level 2 to 3 is much faster than the light-induced transition and the relaxation from 2 to 1. Thus level 2 can be regarded as vacant at any time and the absorption of the system depends only on the population of the ground state. Since the lifetime of level 3 is rather long (~ms) compared to the duration of one pulse-pair (~ns), but shorter than the time interval between two pulse-pairs, the ground state population during the pulse-pair reads as,

$$n = n_0 e^{-\frac{B}{c}w_0(\nu)} \qquad (4.35)$$

where n_0 denotes the initial molecular population, and $w_0(\nu)=\int I(\nu)dt$ represents here the energy of one pulse-pair. The subscripts labeling the energy levels are removed since we are only interested in the population variation of the ground state. Within the duration of one pulse-pair, a few excited molecules are transformed by photochemical reaction and disappear permanently, while most of them stay on the intermediate level 3 so that the ground state is bleached exponentially. Just before the arrival of the next pulse-pair, the molecules excited by the last pulse-pair have all relaxed to the ground state. The population then reads as:

$$n = n_0[1 - \eta(1 - e^{-\frac{B}{c}w_0})] \qquad (4.36)$$

And the number of the molecules contributing to engraving is expressed as,

$$\Delta n = n_0 - n = n_0\eta(1 - e^{-\frac{B}{c}w_0})] \qquad (4.37)$$

The excitation by a pulse-pair results in a permanent and a transient bleaching terms among which only the permanent part contributes to recording. The transient one will

cause a radiative saturation of the transition. In our sample, $A_{21}=6x10^{6}s^{-1}$ [9]. The parameter B can be calculated from the relation $B=\frac{\lambda^3}{8\pi h}A_{21}$ where λ is the wave length of the light field, h is the Planck's constant $h=6.62x10^{-34}$Js. Then we have $B/c=28.6x10^{10}m^2Hz/J$.

In order to place our experimental conditions with respect to the saturation regime, we have to estimate the spectral density of one pulse. We illuminate the sample with one beam, insert a lens (with 10cm focal distance) after the sample and get the image (~25mm^2) at 1m after the lens. Thus we know that the spot area on the sample is approximately 0.25mm^2, and the spectral energy density used in our experiment is about 0.35mJ/THz/cm^2/shot. This corresponds to a factor $w_0B/c\sim1$.

In a thin medium, this energy density would cause a noticeable transient saturation effect and make the diffracted signal shrink to 0.4 times the extrapolated value. As a matter of fact, saturation effect is not so severe in the optically thick sample that we use. First, the saturation parameter w_0B/c rapidly drops under unity as the pulse propagates through the absorbing medium. In addition, two saturation features exhibit contradictory effects. Let us consider a thin slice within the sample. Due to the transient depletion of the ground state by the front edge of a saturating pulse, the hologram engraving is reduced. In compensation, the transmitted energy is less absorbed within this slice, which enlarges the engraving dose in the next slice. The balance between these two effects results in total diffraction efficiency decaying slower than the estimation, and makes our experimental conditions acceptable. This is confirmed by numerical simulation.

4.6 Conclusion

The tautomerization hole burning mechanism in the OEP/PS system is a well known process. However, it has been mainly investigated under monochromatic burning conditions. In this chapter we extend investigation to broadband excitation, keeping in mind that we need a model to describe the storage and retrieval of spectral holograms.

Two points are elucidated. First, the tautomerization quantum efficiency weakly depends on the transition frequency. It can be considered as constant over a 1.1THz-width window. Second, we have checked the photoproduct spectral distribution. Random distribution over the absorption band profile is consistent with experimental results.

With these informations, we have built a theory that connects conventional narrow band hole burning with the engraving and retrieval of broadband holograms.

4.7 References

[1] S. Saikan, T. Nakabayashi, Y. Kamematsu, and N. Tato, *'Fourier tranform spectroscopy in dye-doped polymers using the femtosecond accumulated photon echo'*, Phys. Rev., **B38** 7777 (1988).

[2] S. Saikan, A. Imaoka, Y. Kanematsu, and T. Kishida, *'Linear electron-phonon interaction in dye-doped polymers'*, Chem. Phys. Lett., **162** 317 (1989).

[3] S. Saikan, A. Imaoka, Y. Kanematsu, K. Sakoda, K. Kominami, and M. Iwamoto, *'Temperature dependence of Debye-Waller factor in dye-doped polymers'*, Phys. Rev.B, **41** 3185 (1990).

[4] S. Saikan, *'Linear eletron-phonon coupling in dye-polymer system: in search of weakly coupled systems'*, J. Lumin., **53** 147 (1992).

[5] *'Persistent spectral hole burning : Science and applications'*, W. E. Moerner Ed., (Springer-Verlag, Berlin, Heidelberg, 1988).

[6] K. Horie, M. Gehitz, and A. L. Huston, *'Frequency dependence of quantum efficiency for hole formation in photochemical hole-burning for dye-doped polymer systems'*, Chem. Phys. Lett., **195**, 563 (1992).

[7] S. Völker, and R. M. Macfarlane, *'Photochemical hole burning in free-base porphyrin and chlorin in n-alkane matrices'*, IBM J. Res. Develop., **23**, 547 (1979).

[8] B. M. Kharlamov, E. I. Al'shits, and R. I. Personov, *'Hole burning of dips and transformation of band contours of absorption bands of molecules in solution'*, J. Chem. Phys., **72**, 1851 (1980).

[9] S. Volker, J. H. van der Waals,*'Laser-induced photochemical isomerization of free base porphyrin in an n-octane crystal at 4.2K'*, Mol. Phys. **32**, 1703 (1976)

[10] I.-J. Lee, G. J. Small, and J. M. Hayes, *'Photochemical hole burning of porphine in amorphous matrices'*, J. Phys. Chem. **94**, 3376 (1990)

[11] J. G. Radziszewski, J. Waluk, and J. Michl, *'Site-population conserving and sit-population altering photo-orientation of matrix-isolated free-base porphine by double proton transfer: IR dichromism and vibrational symmetry assignments'*, Chem. Phys. **136**, 165 (1989).

[12] J. G. Radziszewski, F. A. Burhalter, and J. Michl, *'Nondestructive photo-orientation by generalized pseudoreorientation: a quantitative treatment'*, J; Am. Chem. Soc. **109**, 61 (1987).

CHAPTER 5

PHASE ENCODED SPECTRAL HOLOGRAMS IN OEP

5.1 Introduction

With the theoretical model that has been tested in chapter 4, we are able to predict the burning energy range that makes minimum crosstalk consistent with maximum signal, in a phase-encoded spectral memory. However the computation in section 4.44 is restricted to the buildup of holograms that do not carry any spectral phase code. We do not extend the computation to the complex structures that one is faced with when the spectral phase codes are imprinted on the reference beam. Instead, we try to extend the notion of linear regime, first discussed in chapter 3, to the present context of tautomerization engraving. Minimum crosstalk energy range is expected to coincide with the linear regime domain. In this dose range it is an easy matter to include the spectral shaping of the reference beam. Predictions regarding crosstalk are checked in a new series of phase-encoded storage experiments.

Section 5.2 is devoted to the discussion of the linear regime. In section 5.3, the optimized burning dose conditions are summarized and they are experimentally tested. The chapter is concluded in section 5.4.

5.2 Linear regime

Within the frame of the simple model in chapter 3, we discussed a linear regime approximation in optically thick medium. We noticed that the optical density modification remains proportional to the incident dose over a burning energy range that by far exceeds the validity domain of a first order expansion. Since the linear character of the hole burning process underlies this approximation, we expect that it can be extended to the more complex model developed in chapter 4. We check that guess in the present section.

In order to calculate the linear regime approximation of the diffraction efficiency, we have to express the molecule density to the lowest order in powers of the burning dose. To the first order, the energy received by the molecules within the sample is given by,

$$Y(z,x,\nu)=Y(0,x,\nu)\,e^{-\alpha_0(\nu)z} \tag{5.1}$$

where the incident energy is given by Eq.(4.25). The kinetic equation (4.22) can be solved as:

$$n(\Omega,z,x,\nu,\nu')=n_0(\nu,\nu')[1-\beta\, Y(0,x,\nu)\,\sin^2\theta\,\sin^2\psi\; e^{-\alpha_0(\nu)z} + \beta\, Y(0,x,\nu')\,\sin^2\theta\,\cos^2\psi\; e^{-\alpha_0(\nu')z}] \tag{5.2}$$

With the help of Eqs (4.23) and (4.24), we obtain the absorption coefficient that is then integrated over the sample's thickness to give the total absorption and its zero- and first- order Fourier components, as:

$$A(x,\nu)=A_0(\nu)-\frac{3}{5}\,\beta Y_0\,(1+\cos\varphi)+\frac{1}{5}A_0(\nu)\beta Y_0\rho(\Delta) \tag{5.3}$$

$$\tilde{A}^{(0)}(\nu)=A_0(\nu)-\frac{3}{5}\,\beta Y_0+\frac{1}{5}A_0(\nu)\,\rho(\Delta)(\beta\, Y_0) \tag{5.4}$$

$$\tilde{A}^{(1)}(\nu)=-\frac{3}{10}\,\beta Y_0 \tag{5.5}$$

where $\rho(\Delta)=\int_{\nu_L-\Delta/2}^{\nu_L+\Delta/2} p_0(\nu')\frac{1-e^{-A_0(\nu')}}{A_0(\nu')}d\nu'$, Δ is the storage spectral width and where

$$p_0(\nu')=\frac{2\sqrt{\ln 2}}{\sqrt{\pi}\Gamma_{in}}\,e^{-(\frac{\nu'-\nu_0}{\Gamma_{in}})^2 4\ln 2}.$$

Finally, substituting Eqs (5.4) and (5.5) for $\tilde{A}^{(0)}(\nu)$ and for $\tilde{A}^{(1)}(\nu)$ respectively in Eq.(4.29), one obtains the expression of the diffraction efficiency.

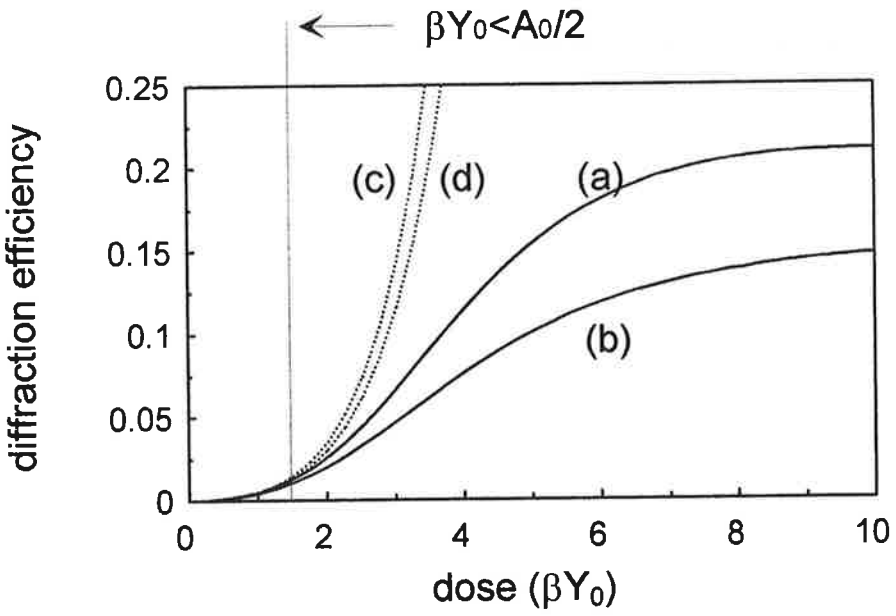

Figure 5.1 Diffraction efficiency. (a) and (b): numerical computation with 80GHz and 1.56THz recording bandwidth, respectively.(c) and (d): corresponding linear regime approximation.

The linear approximation values of $\eta(\nu)$ are displayed on figure 5.1 (curves c and d). Agreement with the numerical computation is satisfactory within the validity range ($\beta Y_0 < A_0(\nu)$) that has been established in chapter 3. The broadband curves do not significantly depart from the narrow band ones over this interval, due to the parameter set we elected for the calculation (OD=1.5, $\Delta < \Gamma_{in}/2$).

As expected, the signal emission term $\tilde{A}^{(1)}(\nu)$ is proportional to the incident dose and is independent of the recording width Δ. The absorption term $\tilde{A}^{(0)}(\nu)$ is also a linear function of the dose, but its slope depends on Δ. In fact, the absorption term represents the hole burning and the erasing processes with the simple rectangle-shaped laser. We rewrite Eq. (5.3) in the form of the hole depth as:

$$A_0(\nu) - \tilde{A}^{(0)}(\nu) = \beta Y_0 \left[3 - A_0(\nu)\rho(\Delta)\right] / 5 \qquad (5.6)$$

The resonant burning part and the redistribution part contribute to the hole depth in opposite ways, and the latter depends on the burning bandwidth. A broad-band

excitation results in a relatively shallow hole since it corresponds to a large redistribution factor $\rho(\Delta)$. Some slopes of the curves of hole depth vs (βY_0) for thick samples (OD>1) with different Δ values are given in table 5.1.

Δ(THz)	slope of the burning term	slope of the erasing term	resulting slope
0	0.6	0	0.6
0.078	0.6	0	0.6.
1.1	0.6	0.05	0.55
1.56	0.6	0.07	0.53
>>4(~∞)	0.6	0.28	0.32

Table 5.1: Slopes of [$A_0(\nu)$- $\tilde{A}^{(0)}(\nu)$] vs (βY_0) for OD>1 with different burning bandwidths.

It appears that the erasing effect is small when Δ is narrower than the inhomogeneous width Γ_{in}. This is valid in the linear regime and it is reflected in the coincidence between the narrow band and the broad band values of the diffraction efficiency in this regime on Fig. 5.1.

Substituting $\beta Y_0 = A_0/2$ into expression (5.6), we obtain that the maximal absorption reduction in linear regime equals ~0.3 A_0. It gives us a practical criterion to identify the upper limit of this regime.

5.3 Crosstalk of phase-encoded addresses

5.31 Data retrieval in the linear regime

The recording/retrieval procedure of a spectral-phase encoded multi-bit storage can be summarized as follows: the holographic structure conveyed by the incident field is expressed as,

$$Y(0,x,\nu)=Y_0(\nu)\left\{1+\frac{1}{M}\sum_{m=1}^{M}\ell_m f_m^{*}(\nu)\cos\varphi\right\} \tag{5.7}$$

where a binary ℓ_m is addressed by a spectral phase function $f_m(\nu)$ belonging to a orthogonal family, M is the number of the restored bits. The diffracted signal spectral amplitude can be described as,

$$\tilde{\mathcal{E}}(\nu)= -\tilde{\mathcal{E}}_L(\nu)\ f_j(\nu).\ \tilde{A}^{(1)}(\nu)\ e^{-1/2\tilde{A}^{(0)}(\nu)} \tag{5.8}$$

where the Fourier components of the z-integrated absorption $A(x,\nu)$ are given by:

$$\tilde{A}^{(p)}(\nu)=\frac{K}{2\pi}\int_{<\frac{2\pi}{K}>}A(x,\nu)e^{-ipKx}dx \tag{5.9}$$

The retrieved signal is measured by the correlation function:

$$G_j(\tau)=\int I_L(\nu)\ f_j(\nu)\ \tilde{A}^{(1)}(\nu)\ e^{-1/2\tilde{A}^{(0)}(\nu)}\ d\nu \tag{5.10}$$

In chapter 3, in the framework of a simple hole burning model, we showed that the holographic structure conveyed by the incident field may be recorded in the material without distortion when exposure the dose βY_0 is less than $\sim 0.5A_0$. The recorded structure $A(x,\nu)$ is a linear function of incident energy $Y(0,x,\nu)$. In section 5.1, we verified that the linear relationship keeps valid with the tautomerization model. According to Eqs (5.2-5.5), the signal absorption and emission terms can be expressed as:

$$\tilde{A}^{(0)}(\nu)=A_0(\nu)-\frac{3}{5}\ \beta Y_0(\nu)+\frac{1}{5}A_0(\nu)\ \rho(\Delta)\ \beta Y_0(\nu) \tag{5.11}$$

$$\tilde{A}^{(1)}(\nu)=-\frac{3}{10}\ \beta Y_0(\nu)\frac{1}{M}\sum_{m=1}^{M}\ell_m f_m^{*}(\nu) \tag{5.12}$$

The absorption term $\tilde{A}^{(0)}(\nu)$ is modified by the bleaching effects accumulated by the storage of all the bits at different addresses. It is determined by the total energy dose, but is independent of the address codes since the spectral codes are modulated on phase, not on amplitude. The emission term $\tilde{A}^{(1)}(\nu)$ has the spectral structure of the holograms, i.e. the data bits and their addresses. Then the retrieved signal reads as:

$$G_j(\tau)= \frac{1}{M}\sum_{m=1}^{M} \ell_m \int_{-\Delta/2}^{\Delta/2} F(\nu) f_j(\nu) f_m^{*}(\nu) d\nu \qquad (5.13)$$

where the non-uniformity of the factor:

$$F(\nu)=I_L(\nu)\beta Y_0(\nu)\, e^{-\frac{1}{2}\{A_0(\nu)-\beta Y_0(\nu)[0.6-0.2\, A_0(\nu)\, \rho(\Delta)]\}} \qquad (5.14)$$

is the main cause of the crosstalk.

If the recording energy is stronger than the limit of linear regime, the effects of higher order terms $[\beta Y(0,x,\nu)]^n$ $(n>1)$ make the engraved structure deviate from the structure originally conveyed by the incident field $Y_0(0,x,\nu)$. In this case, the distortion of the hologram is intrinsic and the resulted crosstalks cannot be avoided by spectral adjustment. For high signal-to-background storage, the high energy situation should be excluded.

5.32. Optimized exposure conditions

In order to work in the linear regime, where no saturation of the photochemical burning process has to be feared, one has to satisfy the condition $\beta Y_0<0.5A_0$. The link between the numerical dose parameter βY_0 and the amount of light energy that is forwarded to the sample is determined with the help of a side hole-burning experiment, as we did in section 4.53. If the size of the laser spot is the same in both hole-burning and holography experiments, it does not need to be precisely measured. One simply gets the burning energy as a function of the dose parameter. In section 4.53 we obtained: $Q_{exp}=1.22\ (\beta Y_0)$(mJ/THz). In our polystyrene plate, with $A_0=1.5$ ln10, the linear regime extends up to an exposure dose of ~2-2.5mJ/THz. Since the spot area is about 0.25mm^2, the upper limit of the linear regime corresponds to a spectral and spatial density of the exposure dose of ~10J/THz/cm^2.

Another condition has to be fulfilled to avoid radiative saturation. In octaethylporphine-doped polystyrene, the spatial and spectral density of energy per shot has to be less than ~0.35mJ/THz/cm^2/shot.

Finally, from the expression of $F(\nu)$ given by Eq. (5.14), one can evaluate the optical density that leads to a maximum signal at the upper energy limit of the linear regime. Substituting $0.5A_0$ for βY_0 , one gets that the signal is maximum when $A_0 \cong 3$, which is OD$\cong$ 1.3.

5.33 Spectrum of the holographic signal in the linear regime

We experimentally check the spectral uniformity of the holographic signal in the linear regime. A single hologram is engraved in the material. Then according to Eq. (5.8), the spectral distribution of the holographic signal intensity reads as:

$$\left|\tilde{S}(\nu)\right|^2 \propto I_L(\nu)[\beta Y_0(\nu)]^2 e^{-A_0(\nu)+\beta Y_0(\nu)[0.6-0.2\,A_0(\nu)\,\rho(\Delta)]} = [F(\nu)]^2 / I_L(\nu) \quad (5.15)$$

where $F(\nu)$ is defined in Eq. (5.14). Provided the molecules and the laser energy are uniformly distributed over the storage window, the signal spectral intensity is expected to be uniform too.

With the method described in section 4.51 and the setup represented on figure 4.9, we engrave a hologram within a 1.1THz spectral window as shown in figure 5.2 . The average pulse energy and the exposure dose are respectively set equal to ~0.5µJ/THz/shot, and ~2.7mJ/THz.

The laser spectrum and the absorption profile are displayed on Figures 5.2 (a) and 5.2 (b, c). They appear to be nearly uniform over the storage window. As expected, the holographic signal spectrum, drawn on Figure 5.2 (d), is also uniform.

This result leads us to conclude that Eq (5.15) correctly describes the spectral distribution of the diffracted signal. The spectral shape factor $F(\nu)$ is uniform under optimized conditions, which guarantees the orthogonality between the different addresses. So we can expect a realistic storage with a high signal-to-background ratio.

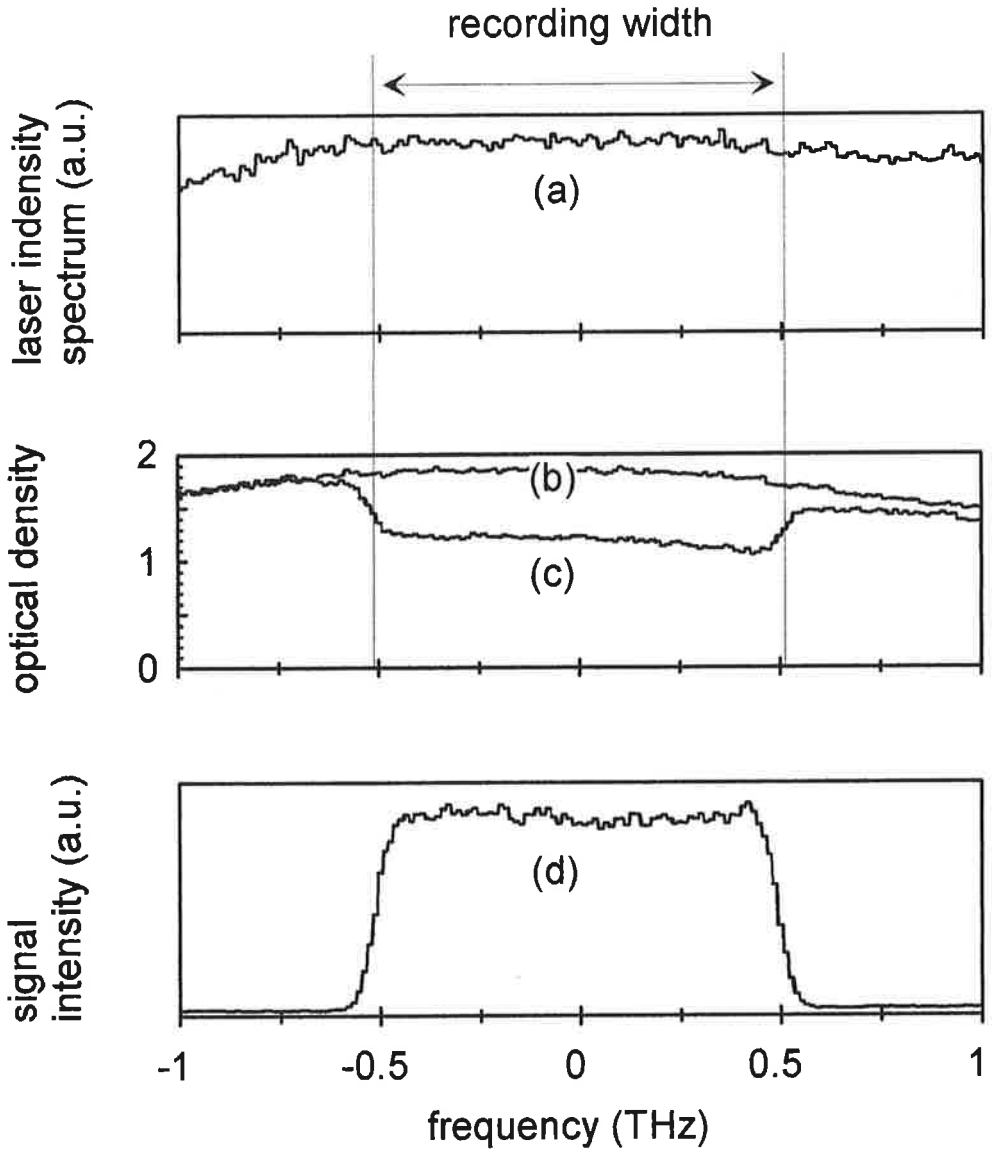

Figure 5.2 *(a) Laser spectrum.*
(b) Optical density of the sample before engraving.
(c) Optical density after engraving within a 1.1THz window, with an average laser energy of 0.7μJ/THz/shot for 6 minutes.
(d) Diffracted energy spectrum.

5.34 Phase-encoding experimental test

With a better understanding of the engraving condition, we return to the storage experiment as described in chapter 2. The same setup as in figure 2.13 and 2.14 is

employed with the exception that a Lyot filter is now used to equalize the laser spectrum. This spectrum is made nearly flat within the 1.1THz-wide SLM window and is about 4THz wide at half maximum intensity. The optics are readjusted in such a way that the beam area on the sample is about 4 times smaller than in section 5.33.

The reference and object beam intensities are balanced so that they evenly contribute to the spatial and spectral energy density on the sample. Dose calibration is effected by monitoring spectral hole depth, as explained in section 4.53. A dose of 0.63mJ/THz is needed to achieve a 0.5 reduction of the optical density, that initially equals1.5. This is consistent with previous data. The holographic storage dose is set equal to this value which represents the linear regime upper limit. The burning window is centered at the top of the absorption band.

A single bit '1' is stored at address #16. The burning dose is provided by a 2 minute pulse sequence, with a repetition rate of 15pulses per second. The average pulse energy on the sample amounts to 0.44μJ/THz/Pulse. The 32 addresses of the memory are successively read out by a conveniently spectrally shaped probe beam. The result is given in figure 5.3 where the stored '1' is retrieved at its address #16. In comparison with our previous result (see figure 2.15b), the crosstalk is remarkably decreased and the signal to maximal crosstalk ratio reaches about 15 instead of 3.

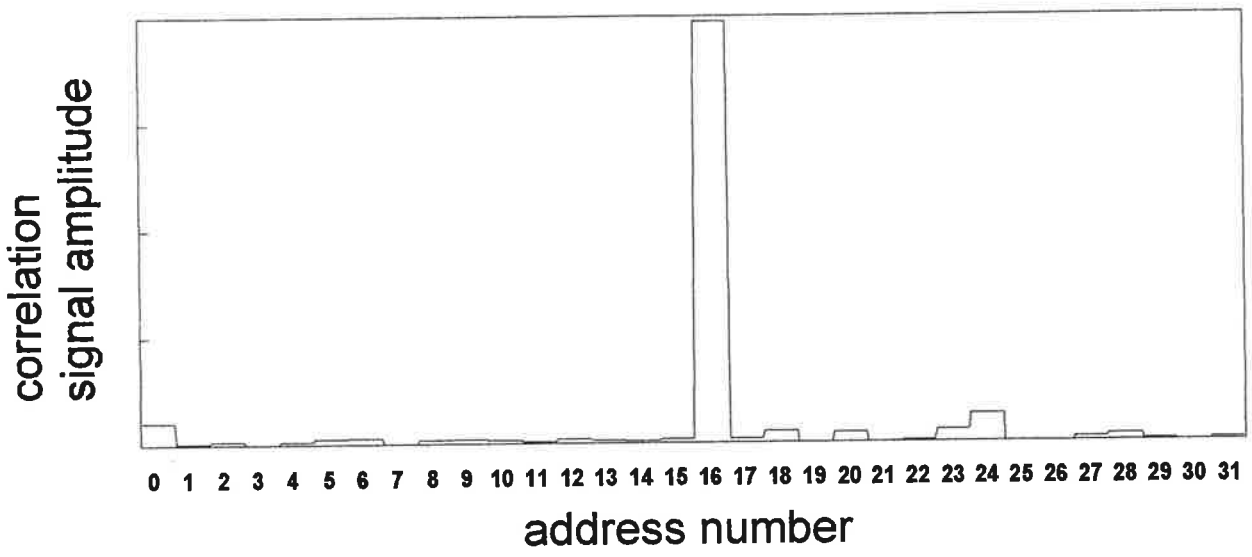

Figure 5.3 Storage at address #16, at the upper limit of the linear regime.

The most important crosstalk occurs at addresses #0 and #24 in figure 5.3. For a single bit '1' storage, the spectral structure of the diffracted field results from the

product of the occupied address spectral shape factor with that imprinted on the read out pulse. As explained in chapter 2, the square of a shape function equals the gate function (#0) and the product between any two different shape functions is another function in the same family. At address #0, the diffracted field spectrum should be given by the product of functions #0 and #16, which coincides with the shape factor #16. In the same way, the emission spectrum at address #24 should be described by function #8, which results from the product of functions #16 and #24 (see the multiplication table 2.1, in chapter 2). One detects the cross-correlation of the diffracted and gating fields at zero time delay. This cross-correlation function is nothing but the frequency-to-time Fourier transform of the emitted field spectral amplitude. At zero delay it coincides with the integral of the spectral amplitude over the frequency-domain storage window. Among the 32 shape factors that label the addresses, functions #8 and #16 exhibit the narrowest Fourier transform structures at zero time delay (see figure 2.8). When the diffracted field is spectrally shaped by these functions, the correlation signal is very sensitive to the source uniformity and to the adjustement of the delay line.

The same crosstalk feature is observed when a bit is stored at other addresses. For instance, figure 5.4 represents the memory readout when a bit '1' is stored at address #12. Then the largest crosstalk is found at address #28. The product of functions #12 and #28 again gives the function #16.

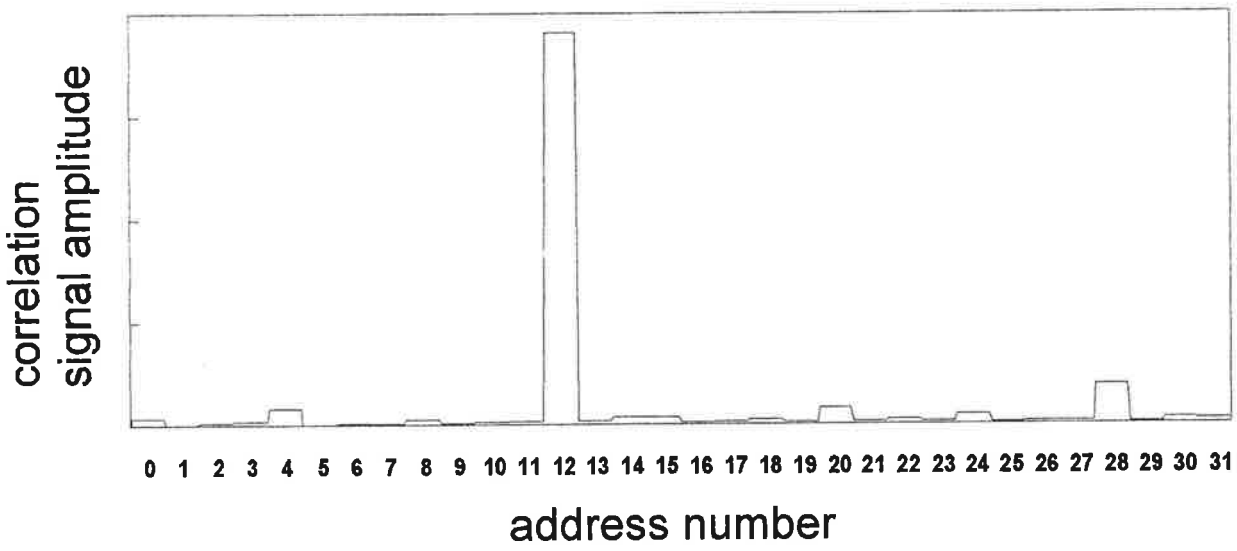

Figure 5.4 Storage at address #12, at the upper limit of the linear regime.

With a '1' bit stored at address #12, and keeping the probe beam shaped by function #28, we record the correlation between the signal and the gating fields as a function of the time delay. The resulting profile is displayed on figure 5.5(a). The amplitude at t=0 corresponds to the crosstalk at address #28. In the same way, one records the time-delay dependence of the correlation signal when readout is effected at address #12 (see figure 5.5(b)). As expected, these profiles are close to the cross-correlation of functions #16 and #0, which are plotted on figure 2.8. The ratio of data '1', retrieved at address #12, to the '0' signal at the empty address #28 is estimated from the ratio of the amplitudes of the two profiles at zero time delay, which is about 17. Surprisingly, this is two times better than the ratio observed on figure 5.4, when all the addresses are successively interrogated at constant delay. This is the more puzzling as the delay has been adjusted by monitoring the variations of the signal represented on figure 5.5(a).

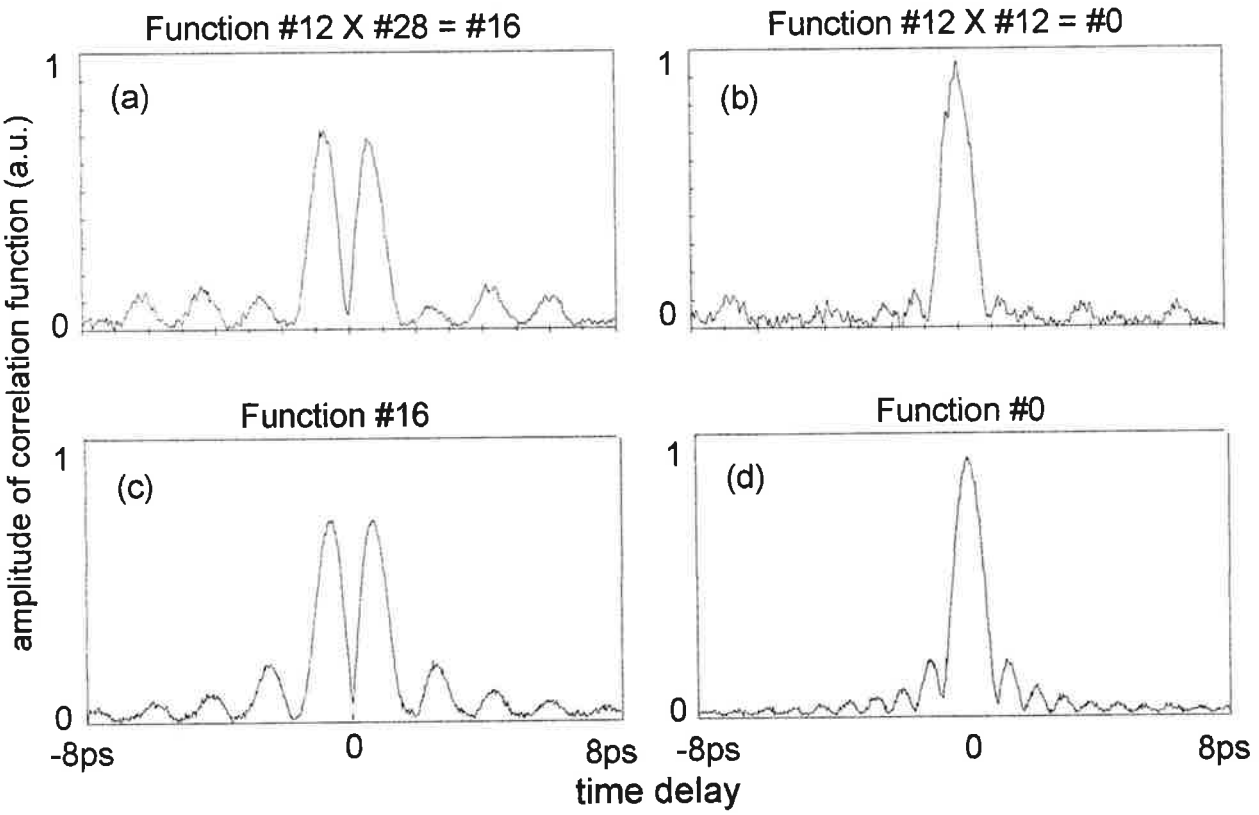

Figure 5.5 *(a) and (b): Correlation between the gate and the sample diffracted field, as a function of the time delay. A '1' bit is stored at address #12. Readout is performed at addresses #28 (a), and #12 (b). (c) and (d): Correlation between the gate and the reference modulated by codes #16 (c), and #0 (d).*

Section 2.41 of chapter 2 reports on the experimental test of the encoding and detection systems. For that purpose, one recorded the correlation of the gate and the reference on which a phase code was imprinted (see figure 2.12(c)). Correlation profiles obtained with function #16 and #0 are plotted on figure 5.5(c) and (d) respectively. They can be compared with the diffracted field correlation data diagramed on figure 5.5 (a) and (b). On figure 5.5(c), the correlation signal at t=0 for function #16 is not zero. Therefore the code structures themselves, the laser spectrum or the detector still have some defects. The ratio of the correlation amplitude at zero delay with code # 0 (figure 5.5(d)) to that obtained with code #16 (figure 5.5(c)) is about 16. This is consistent with the ratio of the occupied and empty memory address signals, as observed in figure 5.5(a) and (b).

Therefore, in the linear regime, the material contribution to the crosstalk seems to be eliminated. The experimental performance is now limited by some part of the setup. Residual distortion is at least partly attributed to the non-uniformity and uncontrollable instability of both spatial and spectral distributions of the laser beam. The SLM interpixel dead zones also result in a crosstalk up to ~5% at some addresses for one bit storage. Finally, the laser spectrum is still much broader than the SLM window. This damages the sensitivity of the correlator.

5.5 Conclusion

Some theoretical and experimental findings can be highlighted. First, within the framework of the theoretical model presented and checked in chapter 4, a linear regime dose condition has been disclosed. A complete description of spectral phase encoded storage is achieved within the limits of this regime, where it is shown that engraving and propagation processes do not damage the orthogonality of the memory addresses.

It is predicted that maximal diffraction efficiency within the linear regime should be attained in a sample with an optical density of about 1.3. This *a posteriori* justifies our investigations on optically thick samples. The linear regime dose condition is easily controled experimentally by limiting the burnt hole depth to about one third of the initial optical density.

Experiments confirm that the material contribution to crosstalk has been dramatically reduced. The residual signal collected in empty addresses probably results from imperfections of the source, the spectral shaper and/or the detection device, which still have to be cured.

CONCLUSION

Aiming at the achievement of fast random access optical data storage in spectrally selective organic materials, we have conducted the first time and space holography experiment with spectral phase encoding of memory addresses. The storage of one bit and the multiplexing of several bits have been effectuated in an octaethylporphyrin doped polystyrene sample. A broad bandwidth (several THz) stochastic source is used to deliver light pulses that are spectrally shaped by a ferroelectric liquid crystal modulator array. We have attained a random access time of about 0.1ms.

In the preliminary experiment, the retrieved data are spoilt by an important crosstalk between the memory addresses. After the optical device has been optimized, as reported on by François Grelet in his PhD dissertation, we concentrate on elucidating the material contribution to crosstalk.

In a first step, using a simple model to describe the spectral hole burning engraving process, we disclose the existence of a « linear regime » where the address orthogonality is preserved. In an optically thick sample, with initial optical density larger than unity, this regime spans a much broader burning dose range than the perturbative expansion.

In an actual material, the hole burning mechanism involves complex features. Optical excitation drives the host matrix vibrations together with the electronic transition of the guest molecule. This electron-phonon coupling damages the spectral selectivity of the burning process. In addition, the persistent burning efficiency may depend on the spectral position within the absorption band. In octaethylporphyrin doped polystyrene, it is known that, at liquid helium temperature, ninety per cent of the optical transition proceeds through the pure, zero-phonon, line. We have experimentally verified that the frequency dependence of the burning process can be neglected over the storage window. In the material under investigation, persistent hole burning results from a photochemical tautomerization transformation of the absorbing molecule. We have included a microscopic model of this process in the coupled-mode equations that describe the propagation of the burning light pulses

through the sample and the engraving of their interference pattern in the shape of a space and frequency hologram. We experimentally test the validity of this realistic theory, varying the burning bandwidth from a small fraction of the absorption bandwidth up to nearly half of it. The computed and experimental results are again consistent with the existence of a linear regime of bleaching and engraving, just as in the case of the simple hole burning model. The optical density can be reduced to its lower order expansion in powers of the burning dose, far away from the perturbative approximation energy region. Within the limits of the linear regime, the holograms should not be distorted by the material and the address orthogonality should be preserved.

Reiterating the phase encoded data storage experiment after elucidation of the material behavior, we observe a dramatic improvement of the crosstalk. The subsisting undesirable signal from the empty addresses probably originates from imperfections of the optical set up, including the light source, the spectral shaper and the detection. Indeed, the spectral shape functions that mainly contribute to the crosstalk already manifested themselves in a similar way when we recorded the cross-correlation profiles of the gating and the shaped reference pulses, in the absence of the memory material.

A superluminescent diode should be prefered to the present Neodymium YAG pumped dye laser source, since a much better spectral and spatial stability should be expected. However, different materials, such as phtalocyanin derivatives should be used instead of porphyrin, in order to match the emission wavelength of existing diodes. With a superluminescent diode the signal detection should be improved too since the main limitation of the correlator sensitivity presently results from the spatial fluctuations of the gating pulse. For better sensitivity, useless energy must not be conveyed to the detector by the gating pulse. Thus the gating pulse band width has to exactly match that of the hologram diffracted field. With the combination of an interference bandpass filter and of a birefringent one it should be possible to shape the needed spectral profile.

The redistribution of burnt molecules over the initial absorption spectrum is generally regarded as a inherent drawback of symmetric porphyrin systems in the context of frequency selective data storage. Asymmetric molecules such as chlorine are prefered. We disagree with this assessment. In our investigations on the symmetric octaethylporphyrin molecules, we did not observe dramatic signal

reduction caused by intraband redistribution, as long as the width of the storage window is kept smaller than half the absorption bandwidth.

Among the unsolved problems met in this work, we have to mention the unexpected low experimentally observed diffraction efficiency on the engraved holograms, irrespective of the storage band width. Neither the finite size of the laser spots nor the wavefront distorsion seem to be enough to account for a discrepancy of more than one order of magnitude with the predictions.

The interest of spectral phase shaped holograms exceeds the field of optical data storage. Applications should be found in an extended domain of optical information processing, including interconnects, computing, pattern recognition. Finally, spectral holography is not confined to low temperature, frequency selective materials. It can be extended to spectrally non-selective materials such as the photorefractive ones. The spectral components of a hologram are then recorded in the form of their frequency-to-time Fourier transform. Indeed, the axial spatial coordinate plays the role of the time in counter-propagating configuration. Spectro/temporal holography in different kinds of media is analyzed in paper 4. As an illustration, we performed an optical routing experiment in a Fe^{3+}: $LiNbO_3$ crystal, a femtosecond sub-coding of the data pulses carrying their address. This work is reported on in paper 5.

ARTICLES

J. Phys. B: At. Mol. Opt. Phys. 28 (1995) L565–L570. Printed in the UK

Storage of a spectrally shaped hologram in a frequency selective material

I Lorgeré†, M Rätsep†‡, J-L Le Gouët†, F Grelet†, M Tian†§, A Débarre† and P Tchénio†

† Laboratoire Aimé Cotton, CNRS II Bât. 505, Campus d'Orsay, 91405 Orsay Cédex, France
‡ Institute of Physics, Estonian Academy of Sciences, EE2400 Tartu, Estonia
§ Changchun Institute of Physics, Chinese Academy of Sciences, People's Republic of China

Received 18 April 1995

Abstract. A spectral holography experiment is performed in a hole-burning material. A shaping device is used to tailor the spectrum of the pulses which engrave the hologram. The resolution of the spectral shaping technique is investigated both theoretically and experimentally.

Linear spectral filtering has proved to be a powerful technique for temporal shaping of ultrashort light pulses [1–7]. The technique consists of spatially dispersing the frequency components of a short pulse in order to filter the components through phase and amplitude masks. Recombination of the filtered components then gives the desired temporal shape. The technique has been used to synthesize femtosecond waveforms according to specifications in experiments involving all-optical switching [6], dark soliton propagation in fibres [4] and pulse coding for communication [5].

Recently Weiner *et al* demonstrated a spectral holography technique which allows the recording and non-linear filtering of temporal waveforms [7]. A hologram is recorded as a spatial interference pattern on a conventional holographic plate placed in the filtering plane of a pulse shaper. Time-reversal, convolution and correlation of femtosecond waveforms have been demonstrated with this technique. Spectral holography can also be performed in a frequency selective recording material through the processes of time-delayed DFWM and spectral hole-burning [8–10]. For recording, the hole-burning material is illuminated by two pulses separated by the time delay T. One is a short pulse that serves as a time-domain reference. The other is the temporally structured object pulse. Thus the spectral interference pattern between the object and the reference pulses is stored as a modification of the inhomogeneously broadened absorption band of the material. The engraved spectral pattern is the spectral hologram. Subsequent excitation of the material by a short reading pulse gives rise to emission of a signal after a delay equal to T. The shape of the emitted signal is that of the recorded object pulse or its time-reversed version depending on the time order of the object and the reference pulses. With a temporally structured reading pulse the emitted signal waveform is the result of the convolution or the correlation of the reading and the object temporal shapes [11]. The development of spectral holography in hole-burning materials is limited by the necessary cryogenic technique. In addition the excitation spectrum must match the absorption band of the material. On the other hand, hole-burning materials make it possible to record and process both spectral and spatial

0953-4075/95/170565+06$19.50

structures which is not the case with the above holographic technique [7]. For this reason hole-burning materials are attractive for high-density image storage and parallel processing [12–15].

Pulse shapers may prove useful in the development of hole-burning memories and processors. A spectral encoding technique using a pulse shaper has recently been proposed for addressing images stored as spectral holograms [16]. The development of such techniques is conditioned by their spectral resolution, that is, by the width of the smallest spectral feature that can be processed in the experiment. The spectral resolution of a pulse shaper was studied both theoretically and experimentally [2]. It was found that this resolution was limited by the size of the diffraction spot produced by the input beam on the filtering plane. This letter shows theoretically that a resolution below this limit can be obtained with a pulse shaper. A spectral holography experiment in a hole-burning material is reported which demonstrates the theoretical conclusions.

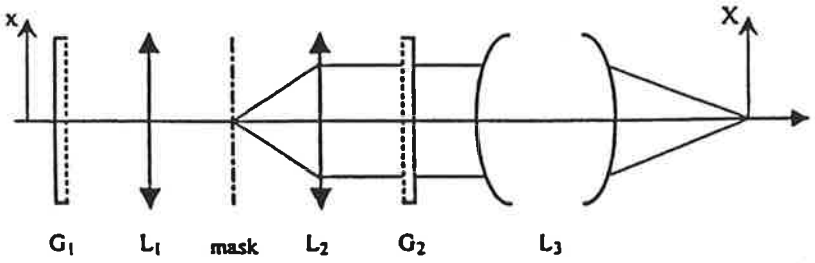

Figure 1. Sketch of the optical system. The grating pair G_1 and G_2 together with the mask and the lenses L_1 and L_2 form the pulse shaper. The lens L_2 together with the optical combination L_3 form an imaging system that conjugates the mask and the X-plane.

Let us consider the optical system sketched in figure 1. It consists of a pulse shaper followed by an optical combination that focuses the beam on a plane (X-plane), where the shaped pulses are observed. The pulse shaper device is that first proposed by Froehly and further developed by Weiner *et al* [1, 7]. It is made of a unit magnification telescope with a pair of gratings placed in its outer focal planes. The spectrum of the input pulse spreads in the plane situated midway between the lenses. Phase and amplitude masks placed in this plane filter the spectral components of the pulse. These components are recombined together by the output lens and grating, symmetric with the input dispersing system. The output lens of the telescope together with the combination L_3 form an imaging system that conjugate the mask and the X-plane. The pulse entering the shaper is described by the spectral amplitude $E_i(x;\omega) = E(\omega)E_i(x)$ of the optical field. The variable ω is the frequency shift with respect to the central frequency Ω_0 of the pulse spectrum. The function $E_i(x)$ gives the beam shape in the grating plane of incidence. The beam shape in the perpendicular direction is not considered since it is not affected by the gratings. The action of the gratings on the above field is described following Martinez [17]. The relevant parameters are the angular dispersion coefficient $\beta = -\partial\theta/\partial\omega$ of the gratings and the coefficient $\alpha = -\partial\theta/\partial\gamma$ which gives the relative variations of the diffraction angle and of the incident angle on the first grating (i.e. the angular magnification of the first grating). Accounting for the gratings, and describing the propagation of the pulse through the optical system with the diffraction theory, one finds that the field $E(X;\omega)$ on the X-plane is expressed as

$$E(X;\omega) = E(\omega)\int du\, m(u)\hat{E}_i\left(\frac{u-\beta f\omega}{\alpha\lambda f}\right)R(u-\beta f\omega+\alpha X/g) \qquad (1)$$

where $\lambda = 2\pi c/\Omega_0$, f is the focal length of the telescope and g is the transverse magnification of the imaging system. The function $\hat{E}_i(\xi) = \int dx\, E_i(x) \exp 2i\pi x\xi$ is the spatial Fourier transform of the input field $E_i(x)$. It describes the diffraction spot produced by the input beam on the mask (for one frequency component). The function $R(u)$ is the impulse response function of the reversed imaging system, accounting for its apertures: it describes the diffraction spot that the imaging system would produce on the mask in response to a point source located on the X-plane (if the light direction of propagation were reversed). The mask is represented by the function $m(u)$. The integral is the effective spectral mask as seen by the point X on the observation plane. It is the convolution of the physical mask with the product of the impulse response and of the input beam diffraction spot. This means that the spectral resolution of the device is determined by the width of the input beam diffraction spot or by that of the impulse response, depending on which is the smallest. The size of the input beam diffraction spot depends mostly upon the transverse coherence length of the beam. In an experimental situation it is rather difficult to achieve a large spatially coherent beam and therefore a small diffraction spot. On the other hand, the impulse response width only depends upon the apertures of the imaging system and can be made very small. As a result the spectral resolution of the system is in practice determined by the impulse response width and is independent of the input beam coherence length. It follows that in order to produce a faithful spectral image of the physical mask in the spectrum $E(X;\omega)$, it is only required that the impulse response width be much smaller than the size d of the smallest mask feature. In our device, the aperture of the imaging system has an $O = 25$ mm diameter and lies in the plane of the telescope output grating. The above condition therefore gives $d \gg \lambda f/O = 6\ \mu$m ($f = 250$ mm). With 1800 grooves/mm gratings giving a 2500 rad nm^{-1} angular dispersion and a typical 5 nm input bandwidth, this allows the synthesis of spectral patterns with several hundred independent features. Under the above condition the field in the X-plane reads as

$$E(X;\omega) = E(\omega)\hat{E}_i(-X/g\lambda f)m(\beta f\omega - \alpha X/g)\,. \tag{2}$$

In this expression the spectral mask depends upon the position in the X-plane. But this dependence is a mere shift in frequency. At every point of the X-plane, the shape of the spectral mask is that of the physical mask whatever the input beam shape. The frequency shift can be understood with geometrical optics considerations. Let us consider the frequency component ω of the pulse. This component is focused on the mask around the point $u = \beta f\omega$. It spreads over an area whose typical size w_0 is the input beam diffraction spot width. The image of this spot on the X-plane spreads over an area of width $w_0 g/\alpha$ centred on the point $X = 0$. The central point of the X-plane is the image of the central point of the spot on the mask. For this point the filtering mask is therefore $m(\beta f\omega)$. But at distance X from the central point one observes the image of the point located at $u = \beta f\omega - \alpha X/g$ on the mask. Hence the point X sees a shifted mask, as indicated by (2).

The above discussion assumes that the mask and the X-plane are perfectly conjugated by the imaging system. In an experimental situation it might not be easy to fulfil this condition. Failure to do so results in enlargement of the impulse response and deterioration of the spectral resolution. Let us consider a default ε (conjugation default) between the position of the mask and the position of the X-plane conjugate. The angular aperture of the beam leaving the mask is λ/d. The image of a point of the sample on the mask therefore spreads over a spot of size $\varepsilon\lambda/d$. For the conjugation default not to spoil the spectral resolution of the system it is necessary that this geometrical spot be much smaller than the size d of the smallest mask feature. This condition demands that the default ε be much smaller than d^2/λ that is $\sim$3.3 mm with $d = 45\ \mu$m. This means that in a practical situation

the conjugation default is the key parameter to achieving a good spectral resolution. If care is not taken in this parameter, one may reach the situation when the width of the impulse response is larger than the input beam diffraction spot, in which case the spectral resolution is determined by the input beam diffraction spot. This may explain the results found by Weiner in his early works on pulse shaping devices [2].

In order to check the validity of the above analysis we have performed a spectral holography experiment in a hole-burning material (octaethylporphine in polystyrene at 1.4 K). This experiment is related to our interest in the storage capabilities of such materials [18, 19, 16]. The experiment is the following. First the spectral structure of an object pulse which has been synthesized with the pulse shaper is recorded as a spectral hologram in the hole-burning material. Then the stored structure is probed by a test pulse which has also been structured by the pulse shaper and the energy of the holographic signal recorded.

The holographic signal is described by the amplitude $E_S(X;\omega)$ of the corresponding field on the sample. This amplitude can be expressed as

$$E_S(X;\omega) = E_1^*(X;\omega)E_2(X;\omega)E_3(X;\omega)\,. \tag{3}$$

In this expression, the field $E_2(X;\omega)$ describes the short unstructured pulse used as a reference for the holographic recording. The field $E_1(X;\omega)$ describes the object pulse whose spectral shape is stored in the sample while the field $E_3(X;\omega)$ is that of the reading pulse used to probe the hologram. The mask used to shape the object pulse is an amplitude mask which consists of ten transparent ~45 μm width slits separated from each other by the periodic distance $p = 400$ μm. The same mask is used for shaping the test pulse except that it is shifted by the distance u_0 with respect to the recording mask. The width of our imaging system impulse response is typically 6 μm. As a consequence it can be neglected at the scale of the mask slits. Therefore, if the sample is perfectly positioned with respect to the mask plane and the spectrum $E(\omega)$ is flat other the mask width, the energy $W(u_0) = \int dX \int d\omega |E_s(X;\omega)|^2$ of the holographic signal, recorded as a function of the mask shift u_0, is proportional to the autoconvolution function of the mask:

$$W(u_0) \propto \int d\omega\, m(\beta f\omega)m(\beta f\omega - u_0)\,. \tag{4}$$

This function consists of $2d$-width triangles spaced by the distance p. The amplitude of the triangles decreases as the shift u_0 increases due to the finite width of the mask. It should be pointed out that (4) relies on the assumption that the sample is not translated in the X-direction between the recording and the reading steps. Translating the sample by the distance X_0 is equivalent to shifting the mask by $\alpha X_0/g$. This is not significant in this particular experiment because the whole convolution function $W(u_0)$ is recorded. But this feature should be considered in experiments such as the one proposed in [16], where the hole-burning material is used to process one specific point of the convolution function of the recording and the reading mask.

We have not tried to measure the spectral resolution limit of our device. Instead, we have measured the cross-talk between the spectral slices cut in the field spectrum by the mask slits. The cross-talk is defined by the ratio $W(u_0 = d)/W(0)$. It is the value of the signal energy in the wings of the triangle relative to the peak energy value. This parameter measures the independence of the spectral slices. It is related to the spectral resolution of the experiment. It approaches zero when the spectral resolution is much better than the spectral width of the mask slits.

Figure 2 shows experimental profiles of the signal energy $W(u_0)$. The first one (figure 2(a)) gives the overall characteristics of the profiles. The irregular variation of the peak amplitudes is probably due to the fact that the spectral bandwidth (FWHM ~ 3 nm)

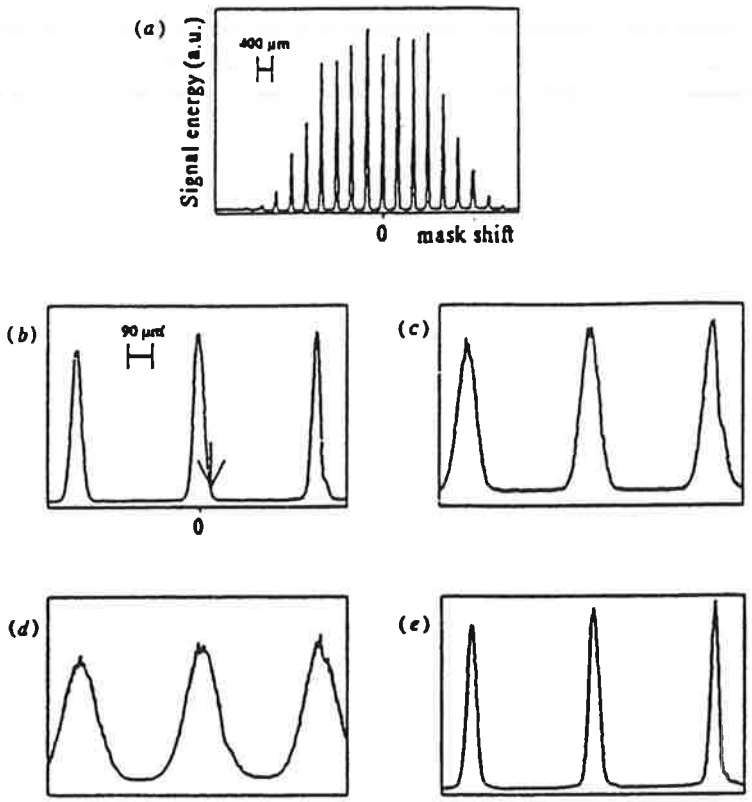

Figure 2. Experimental records of the holographic signal energy as a function of the shift u_0 between the recorded and the testing masks: (*a*) general aspect of the records, (*b*) first three central peaks recorded with optimal conditions (the arrow indicates where the cross-talk is measured), (*c*) with a 5 mm conjugation default, (*d*) with a 5 mm conjugation default and a 2 mm aperture on the input beam and (*e*) with a 2 mm aperture on the input beam but a zero conjugation default.

of the laser is not uniform over the mask width (5.8 nm). Figure 2(*b*) shows the first three central peaks recorded when the conjugation between the mask and the sample plane is optimally adjusted. This corresponds to optimal conditions to achieve good spectral resolution. This profile shows the triangular shape of the peaks. The cross-talk is best measured on the central peak because the others are affected by the irregularity of the mask pattern. The FWHM of this peak is 41 μm which is close to the expected value. The cross-talk value is 3.8%. Figure 2(*c*) shows the influence of the conjugation default. For the recording of this profile, the parameter ε was set to 5 mm. This results in broadening of the peaks and an increase of the cross-talk. The FWHM of the central peak is 69 μm and the cross-talk value measured on this peak is 32%. With such a large conjugation default one would expect a larger cross-talk value. This indicates that the spectral resolution is actually determined by the width of the input beam diffraction spot as confirmed by figure 2(*d*). This profile was recorded with the same conjugation default, but in addition, the input beam was limited by a 2 mm diameter aperture on lens L_1. The result is a considerable increase of the peak width (125 μm) and of the cross-talk, the latter now reaching 70%. For the profile of figure 2(*e*), the same limiting aperture was used but the conjugation was best adjusted. The

FWHM of the peak (38 μm) is now again close to the theoretical value and the cross-talk value is only 3.4%. This shows that the spectral resolution is indeed independent of the input beam size provided that the sample is in the image plane of the mask.

In summary this letter demonstrates that the spectral resolution of a pulse shaper is independent of the input beam size when the shaped pulses are observed in the image plane of the shaping mask. The spectral resolution is then determined by the width of the imaging system impulse response. We have also demonstrated the storage and readout of a spectrally shaped hologram in a frequency selective material. These results are encouraging for the development of pulse shaping techniques in hole-burning memory devices.

References

[1] Froehly C, Colombeau B and Vampouille M 1983 Shaping and analysis of picosecond light pulses ed E Wolf *Progress in Optics XX* (Amsterdam: North-Holland) pp 65–153

[2] Thurston R N, Heritage J P, Weiner A M and Tomlinson W J 1986 Analysis of picosecond pulse shape synthesis by spectral masking in a grating pulse compressor *IEEE J. Quantum Electron.* **22** 682

[3] Weiner A M, Laird D E, Patel J S and Wullert J R 1992 Programmable shaping of femtosecond optical pulses by use of 128 element liquid crystal phase modulator *IEEE J. Quantum Electron.* **28** 908–19

[4] Weiner A M, Thurston R N, Tomlinson W J, Heritage J P, Laird D E, Kirshner E M and Hawkins R J 1989 Temporal and spectral self-shifts of dark optical solitons *Opt. Lett.* **14** 868

[5] Weiner A M, Heritage J P and Salehi J A 1988 Encoding and decoding of femtosecond pulses *Opt. Lett.* **13** 300

[6] Weiner A M, Silberberg Y, Foukhardt H, Laird D E, Saifi M A, Andrejco M J and Smith P V 1989 Use of femtosecond square pulses to avoid pulse breakup in all-optical switching *IEEE J. Quantum Electron.* **25** 2648

[7] Weiner A M, Laird D E, Reitze D H and Paek E G 1992 Spectral holography of shaped femtosecond pulses *Opt. Lett.* **17** 224

[8] Rebane A, Kaarli R and Saari P 1983 Photochemical time-domain holography of weak picosecond pulses *Opt. Commun.* **47** 173

[9] Saari P, Kaarli R and Rebane A 1986 Picosecond time and space domain holography by photochemical hole-burning *J. Opt. Soc. Am.* B **3** 527

[10] Kim M K and Kachru R 1987 Storage and phase conjugation of multiple images using backward-stimulated echoes in Pr^{3+}:LaF_3 *Opt. Commun.* **12** 593–5

[11] Bai Y S, Babitt W R, Carlson N W and Mossberg T W 1984 Real time optical waveform convolver/cross-correlator *Appl. Phys. Lett.* **45** 714–6

[12] Mitsunaga M, Yano R and Uesugi N 1991 Time and frequency domain hybrid optical memory: 1.6 Kbit data storage in Eu^{3+}:Y_2SiO_5 *Opt. Lett.* **16** 1890

[13] Shen X A and Kachru R 1993 Time-domain optical memory for image storage and high speed image processing *Appl. Opt.* **32** 5811

[14] Sasaki H and Karaki K 1994 Hole-burning holography in Eu^{3+}:Y_2SiO_5 *Persistent Spectral Hole-Burning and Related Spectroscopies: Science and Applications* (Optical Society of America) p 384

[15] Kohler B, Bernet S, Renn A and Wild U P 1991 Holographic optical data storage of 2000 images by photochemical hole-burning *Persistent Spectral Hole-Burning: Science and Application* (Optical Society of America) pp 46–9

[16] Sõnajalg H, Débarre A, Le Gouët J-L, Lorgeré I and Tchénio P 1995 Phase encoding technique in time-domain holography: theoretical estimation *J. Opt. Soc. Am.* B accepted

[17] Martinez O E 1986 Grating and prism compressors in the case of finite beam size *J. Opt. Soc. Am.* B **3** 929

[18] Débarre A, Keller J-C, Le Gouët J-L and Tchénio P 1991 Field cross-correlation retrieval of optically stored data *J. Opt. Soc. Am.* B **8** 153–9

[19] Débarre A, Keller J-C, Le Gouët J-L, Tchénio P and Galaup J-P 1991 Optical information storage in condensed matter with stochastic excitation *J. Opt. Soc. Am.* B **12** 2529–36

Spectral phase encoding for data storage and addressing

I. Lorgeré, F. Grelet, M. Ratsep, M. Tian, and J. L. Le Gouët

Laboratoire Aimé Cotton, Bâtiment 505, 91405 Orsay Cedex, France

C. Sigel and M. L. Roblin

Groupe de Physique des Solides, Université Paris VII, Tour 23, 2 Place Jussieu, 75251, Paris Cedex 05, France

Received February 5, 1996; revised manuscript received April 5, 1996

We propose to use a broad-bandwidth laser source for storing and retrieving multiple holograms in a photorefractive material. Each storage address is defined by a specific spectral encoding of the reference beam. The validity of the spectral encoding method is tested in a preliminary experiment. © 1996 Optical Society of America.

1. INTRODUCTION

Holographic materials are well known for their ability to record phase laws, and holograms can act as phase filters. Moreover, many holograms can be recorded in the same sample. These properties have been used for data storage. One problem is to retrieve selectively each piece of recorded information without any cross-talk effect.

Cross-talk effects can be avoided by use of various methods. The most widely used methods take advantage of the Bragg selectivity of thick holograms. Independent addresses can be specified by the angle of incidence of the reference beam[1] or by its temporal frequency.[2,3] In this case, spectrally selective materials can also be used.

A spatial phase-encoding method has also been proposed in which, for recording each datum, a set of reference beams with different angles of incidence simultaneously illuminates the storage material. Each beam is affected by a phase shift. Orthogonal phase sets guarantee the independence of the data addresses.[4,5]

We propose a spectral phase-encoding method. The necessary broad-frequency spectrum is obtained by use of optical pulses of short coherence time (in the picosecond or the femtosecond range). A previous study[6,7] examined this method in the case of spectrally selective materials. Here we consider the case of nonfrequency-selective materials (thick holograms in photorefractive crystals).

2. GENERAL PRINCIPLE OF DATA STORAGE AND ADDRESSING BY A SPECTRAL PHASE LAW

This principle has already been presented in Ref. 6. Let us briefly review it.

The object and the reference optical pulses have the same spectral amplitudes, denoted by $a(\nu)$. On the reference pulse the spectrum has been encoded, and its spectral amplitude becomes $a(\nu)C_i(\nu)$. By holography[8,9] it is possible to realize the spectral filter

$$a(\nu)[a^*(\nu)C^*(\nu)].$$

Several object pulses can be recorded in the same holographic material, acting as a multiple phase filter for the different codes. In the readout step this hologram is illuminated by one of the reference beams, of spectral amplitude $a(\nu)C_j(\nu)$. The spectral amplitude of the reconstructed beam for the ith hologram is given by

$$a_{ri}(\nu) = |a(\nu)|^2 a(\nu)C_i^*(\nu)C_j(\nu),$$

corresponding to a temporal signal

$$S_{ri}(t) = \int a_{ri}(\nu)\exp(j2\pi\nu t)\mathrm{d}\nu.$$

In the considered picosecond or femtosecond range, the temporal signal cannot be directly studied. Instead, we record the field cross correlation of the signal with a time-delayed replica of the object field.[9,10] As a function of the delay τ, the cross-correlation function is expressed as

$$A(\tau) = \int |a(\nu)|^4 C_i^*(\nu)C_j(\nu)\exp(j2\pi\nu\tau)\mathrm{d}\nu.$$

The τ dependence of the cross-correlation function reflects the temporal evolution of $S_{ri}(t)$. Cross correlation works as an optical sampling procedure that is gated by the time-delayed replica of the object field. The time resolution of the technique is given by the coherence time of the light, which coincides with the inverse spectral width of the laser.

Let us assume that the spectral intensity has a constant value, limited by a spectral window of width $\Delta\mu$, over the useful part of the encoding function. At zero delay we obtain

$$A(0) \propto \int C_i^*(\nu)C_j(\nu)\mathrm{d}\nu = \Delta\mu\delta(i-j) \qquad (1)$$

if we assume the encoding functions to be orthogonal. The signal recovered at $\tau = 0$ is well selected: Each recorded hologram can be read only by its own reference

0740-3224/96/1002229-06$10.00

beam. Note that such a method does not impose coherent Fourier-transform pulses because the result depends only on the spectrum intensity.

Practical Realization of the Spectral Phase Encoding

We use a method previously applied by Wiener[11] for pulse shaping (Fig. 1). The laser beam is angularly dispersed by a diffraction grating G1 set in the object focal plane of a lens L1. Because of the finite size of the laser beam, each spectral frequency gives a diffraction pattern $p[X - K(\nu - \nu_0)]$ in the image focal plane of L1, where X is the abscissa in this plane, ν_0 is the central frequency of the spectrum, and K characterizes the spectral dispersion of the grating. In this plane a phase shaper based on a spatial light modulator is inserted to encode the pulse spectrum. The spatial light modulator acts as a spectral aperture of width $\Delta\mu$. This mask is a set of M jointed slits of identical width, which gives rise to a spatial distribution of 0 and π phase shifts (transmission factor of +1 and −1). The ith reference beam is then encoded by a mask

$$\mathcal{M}_i(X) = f(X) * \Sigma \exp j\phi_{pi} \cdot \delta(X - p\Delta X), \qquad (2)$$

where $f(X)$ represents a slit of width equal to ΔX, with ϕ_{pi} being the 0 or π phase shift corresponding to the pth slit in the ith code. The resulting amplitude in the focal plane can be written as

$$\mathcal{M}_i(X)p[X - K(\nu - \nu_0)].$$

If the spectral dispersion is exactly compensated by a second grating, which stays in the image of the first one, for example, in a $4f$ setup (Fig. 1), the equivalent amplitude in the X plane becomes

$$p(X)\mathcal{M}_i[X + K(\nu - \nu_0)].$$

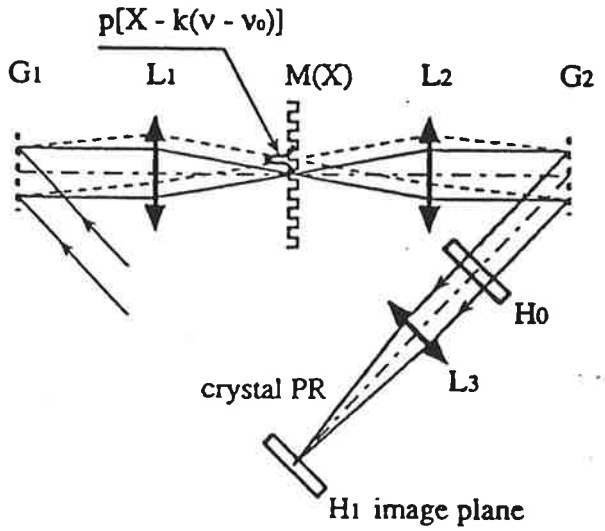

Fig. 1. Experimental setup for spectral encoding. The mask is set in the spectrum angularly dispersed by the grating G1. The angular dispersion is compensated by a second grating G2 in the image of G1.

If the width of $p(X)$ is small compared with that of $f(X)$, the field amplitude can be written as

$$p(X)\mathcal{M}_i[K(\nu - \nu_0)],$$

and the encoding function is $C_i(\nu - \nu_0) = \mathcal{M}_i[K(\nu - \nu_0)]$. It does not depend on the geometrical position of the hologram. In contrast, if the width of $p(X)$ cannot be neglected, the encoding function depends on the position of the plane.

Just behind the second grating, or in any plane in the parallel beam beyond this grating, the encoding function is given by the convolution of the mask function by the diffraction spot on the mask.

In the image of the X plane, the encoding function is well defined by $\mathcal{M}_i$ but varies with X as

$$C_i(\nu - \nu_0, X) = p(X)\mathcal{M}_i[X + K(\nu - \nu_0)].$$

The resolution of this spectral shaping technique as a function of the conjugation default of the mask is fully discussed in Ref. 12.

For such an array of M jointed elements, it has been shown that M orthogonal sets can be generated, satisfying the orthogonality condition as specified by relation (1). Thus the number of independent addresses with which data can be stored is given by M.

Note that each address spans the entire spectral storage domain. The multiplexing character of this approach has to be distinguished from multichannel procedures in which each datum is stored at a specific position in the memory space. What is known as wavelength multiplexing is actually an intrinsically multichannel procedure even if it can be regarded as a spatial multiplexing technique.

In Sections 1 and 2 we have reviewed some general properties. In the following sections we consider the specific case of a photorefractive material.

3. REALIZATION OF A SPECTRAL PHASE FILTER IN A PHOTOREFRACTIVE MATERIAL

A. Recording of Uniform-Contrast Sinusoidal Fringes

Such fringes describe the hologram that is formed by plane waves in monochromatic light. The intensity spatial distribution can be written as

$$I(z) = I_0[1 - m \cos(2\pi/d)z],$$

where z is the coordinate on an axis perpendicular to the fringes; d, the fringe spacing; and m, the contrast of the fringes. The response of a photorefractive material is a spatial variation of the refractive index n, whose amplitude is usually written[13] as

$$\Delta n = \Delta n_M[1 - \exp(-t/\tau)],$$

where t is the exposure time and Δn_M and τ are constant parameters determined by the material and the characteristics of the fringes.

Δn_M, the saturation index, does not depend on I_0 and is equal to $m\Delta N$, where ΔN is a constant of the material.

τ does not depend on m and is proportional to $1/I_0$.

Note that such a law can be understood as a competition between the increase of Δn by the modulated part of

the intensity and an erasing effect related to its constant part, resulting in a saturation value of the refractive-index variation. Note also that, despite saturation, the value of Δn always remains proportional to m, regardless of its value.

B. Interference Fringes between Two Beams with Broad-Spectrum Pulses

Let us consider two counterpropagating beams (Fig. 2). One of them is the object pulse, and the other is the spectrally encoded reference pulse. The holographic material is located in (or near) an image plane of the mask. We assume that inside the crystal the diffraction effects can be neglected. Then the temporal signal on the two beams can be written as

$$E_0(t, X) = p(X)\exp[j2\pi\nu_0(t - z/v)]\int a(\mu) \times \exp[j2\pi\mu(t - z/v)]\mathrm{d}\mu,$$

$$E_R(t, X) = p(X)\exp[j2\pi\nu_0(t + z/v)] \times \int a(\mu)C_i(\mu)\exp[j2\pi\mu(t + z/v)]\mathrm{d}\mu,$$

respectively, where $\mu = \nu - \nu_0$, v is the light velocity inside the material, and $p(X)$ denotes the transversal field variation and does not vary inside the crystal.

As the holographic material has a response time that is long compared with the pulse duration, it is sensitive to the time-integrated intensity of the interference signal. The equivalent interference fringes are given by

$$W(z, X) = p(X)^2\Big\{\int |a(\mu)|^2\mathrm{d}\mu + \int |a(\mu)|^2C_i(\mu)^2\mathrm{d}\mu + \exp -j2\pi\nu_0(2z/v)\int |a(\mu)|^2C_i^*(\mu) \times \exp[-j2\pi\mu(2z/v)]\mathrm{d}\mu + \mathrm{c.c.}\Big\}. \quad (3)$$

The interference term in Eq. (3) can be characterized by a complex visibility function $V(z)$:

$$V(z) = \int |a(\mu)|^2C_i^*(\mu)\exp[-j2\pi\mu(2z/v)]\mathrm{d}\mu = \int E_0(t - 2z/v)E_R^*(t)\mathrm{d}t.$$

The constant part of the exposure is

$$W_0 = \int |a(\mu)|^2\mathrm{d}\mu + \int |a(\mu)|^2|C_i(\mu)|^2\mathrm{d}\mu = \int |E_0(t)|^2\mathrm{d}t + \int |E_R(t)|^2\mathrm{d}t,$$

and the contrast $m(z) = 2V(z)/W_0$.

Note that at any point inside the hologram the buildup occurs during the overlap time, i.e., the short-pulse duration, whereas erasing occurs during the entire duration of pulses. This means that if, for identical pulses, the contrast factor m becomes equal to 1 near $z = 0$, this value can never be reached if one of the pulse is encoded. We shall show in Subsection 3.C that this effect is compensated by the larger extension of the visibility curve and does not affect the diffraction efficiency, which is the same for any encoded readout beam.

C. Reconstructed Signal in the Image Plane $z = 0$

Let us consider a readout beam (identical to one of the reference beams), encoded by $C_j(\mu)$. Note that calculating the reconstructed field for each frequency and coherently adding the corresponding fields is equivalent to directly calculating the temporal reconstructed signal. We used the first method.

If we neglect the depletion and the absorption of the beam, the spectral amplitude field at a position (z, X) inside the crystal, for a specific readout beam j, is

$$a_j(\mu, X, z) = p(X)a(\mu)C_j(\mu, X)\exp j2\pi(\nu_0 + \mu)(z/v).$$

Assuming low efficiency, we can consider the engraved hologram as a collection of contiguous thin gratings of identical thickness dz, each modulated by the term $\exp -j2\pi\nu_0(2z/v)$, with a diffraction efficiency proportional to $V(z)$. According to Kogelnik,[14] the diffraction efficiency of an elementary reflective grating is given by

$$\tanh(\pi\Delta n\,\mathrm{d}z/\lambda) \cong \pi\Delta n\,\mathrm{d}z/\lambda,$$

where Δn is proportional to $m(z)$ and λ is the wavelength inside the crystal. In the case in which the saturation index modulation has been reached,

$$\Delta n(z) = 2\Delta NV(z)/W_0.$$

By adding the contributions of the elementary gratings, we find that in the plane $z = 0$, the frequency spectrum of the reconstructed field spatially limited by $|p(X)|^2p(X)$ is

$$a_r(\mu, X) = (2\pi/\lambda)(\Delta N/W_0)\int a_j(\mu, X, z)V(z) \times \exp[-j2\pi\nu_0(2z/v)] \times \exp[j2\pi(\nu_0 + \mu)(2z/v)]\mathrm{d}z.$$

It becomes

$$a_r(\mu, X) = (2\pi/\lambda)(\Delta N/W_0)(v/2)|a(\mu)|^2 \times a(\mu)C_i^*(\mu, X)C_j(\mu, X) \quad (4)$$

if the length of the crystal can be considered as infinite, that is, much larger than the useful length of $V(z)$.

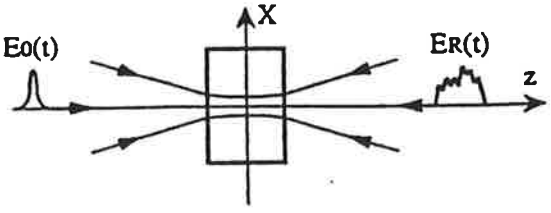

Fig. 2. Hologram recording with two counterpropagating beams near a focus.

We have seen that the spectral code for the image plane depends on the position X in this plane. $C(\mu, X)$ can be replaced by $\mathcal{M}(X + K\mu)$, and the frequency spectrum becomes

$$a_r(\mu, X) = (2\pi/\lambda)(\Delta N/W_0)(v/2)|a(\mu)|^2 a(\mu) \times \mathcal{M}_i^*(X + K\mu)\mathcal{M}_j(X + K\mu).$$

The frequency spectrum of the field cross correlation is

$$|a(\mu, X)|^4 \mathcal{M}_i^*(X + K\mu)\mathcal{M}_j(X + K\mu).$$

Then the field cross correlation $A(0)$ at a zero delay, for a constant value of the spectral density, is

$$A(0) \propto \int p(X)^4 \left[\int \mathcal{M}_i^*(X + K\mu)\mathcal{M}_j(X + K\mu) \mathrm{d}\mu \right] \mathrm{d}X.$$

By substituting $X + K\mu$ with μ', we can see that the integral on μ' does not depend on X, which confirms that the finite dimension of $p(X)$ does not impose any limitation on the spectral resolution in our experiment, provided that the image of the mask is positioned inside the recording material.

4. DISCUSSION

A. Diffraction Efficiency

Let us first consider the energy that is diffracted by an engraved hologram that is read by an encoded field. The diffracted signal S_d is given by

$$S_d = \int |a_r(\mu)|^2 \mathrm{d}\mu = \int |E(t)|^2 \mathrm{d}t.$$

Below we assume that the light-source intensity is uniformly distributed over the spectral bandwidth $\Delta\mu$. By using expression (4) for $a_r(\mu)$, we obtain

$$S_d = (\pi/2\lambda)^2 (v/\Delta\mu)^2 \Delta N^2 W_0/2 \int |C_i^*(\mu)C_j(\mu)|^2 \mathrm{d}\mu/\Delta\mu.$$

If C_i, C_j are constant or pure phase laws, then the integral is equal to $\Delta\mu$, and the signal is the same for any j. The resulting efficiency is written as

$$\eta = (\pi\Delta N/2\lambda)^2 (v/\Delta\mu)^2 = (\pi\Delta NL/\lambda)^2 (v\tau_c/2L)^2 = \eta_{cw}(v\tau_c/2L)^2,$$

where $\tau_c = 1/\Delta\mu$ is the coherence time of the pulse; L, the crystal length; and η_{cw}, the cw diffraction efficiency. One of the major differences between cw and pulsed recording lies in the hologram dimension. It is limited by the crystal length or by the pulse coherence length $v\tau_c$ for cw or pulse recording, respectively. For femtosecond pulses this length becomes much shorter (roughly 10 μm) than L (several millimeters).

Note that, as the crystal length determines the spectral resolution (minimal value for one element of the mask), the ratio of the crystal length to the pulse coherence length is the maximum number M of possible addresses. This recording scheme can be compared with the angular phase-encoding technique.[4,5] In the latter approach the readout beam intensity is shared among M reference beamlets, the field amplitude of which is $\sqrt{M}$ lower than that of the initial beam. M holograms are coherently recorded; the available refractive-index modulation of each of them is $\Delta N/\sqrt{M}$. Each beamlet is diffracted on a single hologram. The resulting M signals combine into a single field that represents the retrieved data. The resulting diffraction efficiency is

$$\eta = [(\pi L/\lambda)(\Delta N/\sqrt{M})(M/\sqrt{M})]^2 = (\pi\Delta NL/\lambda)^2.$$

Thus, for the same number M of addresses, the signal diffraction efficiency in our method is approximately M^2 times lower than in the angular phase-encoding method. This result can be ascribed to the mutual incoherence of hologram recordings at different wavelengths. Although the storage material is simultaneously illuminated by the object and the reference pulses, each spectral component of the object pulse interferes with a single spectral component of the reference. In contrast, in the case of angular phase encoding, the entire object field interferes with any reference beamlet.

Assuming that the saturation value was reached—10^{-3} for $LiNbO_3$—we calculated a theoretical diffraction efficiency (for one recorded hologram) of a few 10^{-2} for a phase mask, 10^{-3} for the amplitude mask that we used, and a spectrum width of 5 nm.

B. Selectivity

We have seen that the orthogonality of the encoding function results in the perfect selectivity of addressing if the engraved spectral filter is exactly proportional to the mask function. The conditions to be fulfilled are

1. uniform spectral distribution of the laser intensity over the encoding mask,
2. positioning of the recording material inside the image plane of the mask, and
3. crystal length much larger than the spatial extension of the visibility curve (approximately the equivalent length of the encoded pulse).

The first condition can be satisfied at the expense of energy loss. In our experiment some nonuniformity remains, and its effect is shown in the experimental data (Section 5). The important point is the finite length of the crystal.

We have seen [Eq. (2)] that the encoding function can be written as

$$f(\mu) * \Sigma(\exp j\phi_{pi})\delta(\mu - p\Delta\mu) = f(\mu) * C_i(\mu).$$

The visibility curve is obtained as a Fourier transform (FT) of this encoding function as

$$V(z) = [\mathrm{FT}f(\mu)][\mathrm{FT}C_i(\mu)] = \mathrm{sinc}(b2z/v)[\mathrm{FT}C_i(\mu)].$$

Because of the finite length of the crystal, which can be written as a rectangle function $R(z)$, the equivalent visibility curve is

$$[R(z)\mathrm{sinc}(b2z/v)][\mathrm{FT}C_i(\mu)],$$

which means that, in the engraved spectral filter, $f(\mu)$ has to be replaced by a convolution with a sinc function of the crystal length. It results in an enlargement of each spec-

tral element, which is a cause of cross talk, as discussed in Section 5. One can avoid this cross talk by increasing the distance between the mask slits.

Note that the role of this sinc function is well known in the case of wavelength multiplexing, where $f(\mu)$ is a δ function and one avoids the cross talk by placing the successive wavelengths in the zeros of the sinc that is centered on one of them.

5. EXPERIMENTAL METHODS

To check this principle of storage and addressing, we performed a preliminary experiment in which we used an amplitude mask instead of a spatial light modulator, with the aim being to check the spectral resolution of the system. The setup can be described as follows.

The laser source was a dye laser pumped by a YAG laser delivering broadband chaotic pulses at 620 nm of 10-ns duration and 5-nm bandwidth at a 15-Hz repetition rate. The coherence time of the pulse is thus $\tau_c = 250$ fs, which corresponds to a coherence length l_c of 80 μm. The laser beam is split into an object pulse, which is sent directly to the sample, and a spectrally shaped reference pulse. The spectral shaping device is identical to the one developed by Weiner *et al.*[11] (see Fig. 1). The shaped spectrum presents a grooved structure with 0.05-nm-wide bright slices every 0.4 nm. The two beams counterpropagate (Fig. 2), and the delay is adjusted so that they interfere at zero delay at the center of the sample, a 6-mm-thick Fe:$LiNbO_3$ crystal. A chaotic pulse can be regarded as a train of elementary uncorrelated components of duration τ_c. After shaping by the 0.05-nm-wide slits of the spectral mask, each 80-μm-long subpulse in the reference beam is expanded into a 7.7-mm-long structure. In the crystal, it shrinks into a 3-mm-long hologram because of the counterpropagating scheme and because of the refractive index of $LiNbO_3$ ($n = 2.5$). Each stored hologram spans the same spatial domain. However, owing to the multiplexing character of the storage, the memory capacity is given by $2nL/l_c \cong 400$. During readout the object beam is blocked, and the spectrally shaped reference pulse is diffracted on the engraved hologram. The diffracted signal energy is collected by a photomultiplier (Subsection 3.C) and is written as

$$S_d \alpha \int |a(\mu)|^6 |C_i(\mu) C_j(\mu)|^2 d\mu.$$

The same mask is used for readout. One varies the readout function $C_j(\mu)$ by scanning the mask position along the X direction in the focal plane of $L1$. Figure 3(a) represents the signal intensity as a function of the spectral distance of the readout mask from its recording position. The irregularities in the variations of the peak intensities most probably arise from the nonuniformity of the spectral intensity over the 5-nm bandwidth. The constant background is ascribed to scattering of the readout beam on the beam splitter through which the diffracted beam is detected.

Figure 3(b) shows the signal intensity for the central peaks as a function of the spectral shift. The triangle width is close to the expected value. The signal intensity at a distance of one slit width from the recording position represents the cross talk. It appears to amount to approximately 3% of the peak signal intensity. This can be explained by the finite length of the crystal. For an infinite-length crystal, the signal intensity is an exact triangular function. The effect of finite crystal length, as was already explained above, is to convolve the slit function $f(\mu)$ by a sinc function, which for an equivalent crystal length of 6 mm × 2.5 mm is 0.025-nm wide. The net

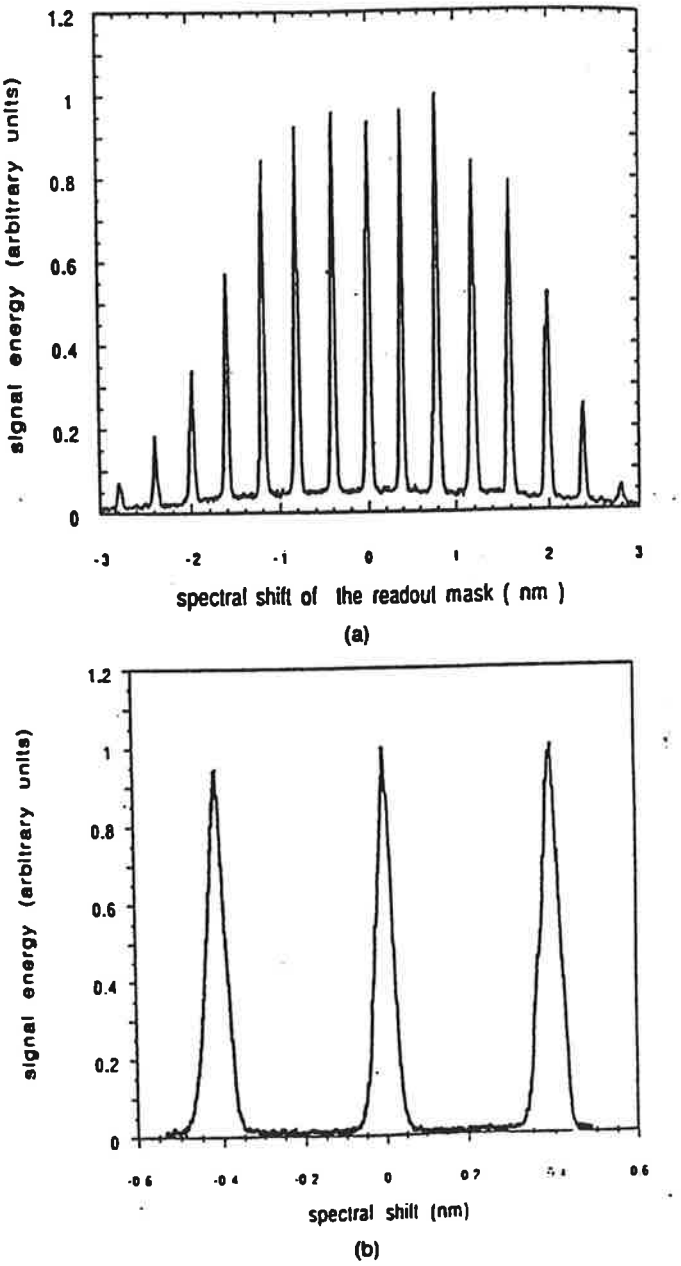

Fig. 3. (a) Hologram readout by a spectrally shaped reference pulse. The hologram was stored by illumination of the sample by an unshaped object pulse counterpropagating with a shaped reference pulse. Spectral shaping is realized by a mask consisting of ten 0.05-nm-wide rectangular slits placed every 0.4 nm. The readout mask is the same, and it can be spectrally shifted with regard to the recording position. Signal energy is detected as a function of the shift. (b) Signal energy as a function of the spectral shift for the three central peaks. Signal intensity at one slit width from the recording position corresponds to the cross-talk level between adjacent slits.

effect is a widening of the slits. In other words, the slits' edges are smoothed because of cutoff of the high-frequency components of the visibility function.

6. SUMMARY

We have experimentally verified a temporal spectrum-shaping technique for addressing data in a photorefractive material. This technique has been previously used in persistent-spectral-hole-burning materials working at low temperature. Formal comparison has been worked out between the explored spectral phase encoding and the angular phase encoding. The scattering efficiency appears to be less affected by the number of the storage addresses in the latter case.

ACKNOWLEDGMENT

I. Lorgeré is grateful to the Société des Amis des Sciences for its financial support.

REFERENCES

1. F. H. Mok, "Angle multiplexed storage of 5000 holograms in lithium niobate," Opt. Lett. 18, 915 (1993).
2. G. A. Rajuljic, V. Levya, and A. Yariv, "Optical data storage by using orthogonal wavelength-multiplexed volume holograms," Opt. Lett. 17, 1471 (1992); A. Yariv, "Interpage and interpixel cross talk in orthogonal (wavelength-multiplexed) holograms," Opt. Lett. 18, 652 (1993).
3. K. Curtis, C. Gu, and D. Psaltis, "Cross talk in wavelength-multiplexed holographic memories," Opt. Lett. 18, 1001 (1993).
4. C. Denz, G. Pauliat, G. Roosen, and T. Tschudi, "Volume hologram multiplexing using a deterministic phase encoding method," Opt. Commun. 85, 171 (1991).
5. Y. Taketomi, J. E. Ford, H. Sasaki, J. Ma, Y. Fainman, and S. H. Lee, "Incremental recording for photorefractive hologram multiplexing," Opt. Lett. 16, 1774 (1994).
6. H. Sonajalg, A. Débarre, J. L. Le Gouët, I. Lorgeré, and P. Tchénio, "Phase-encoding technique in time-domain holography: theoretical estimation," J. Opt. Soc. Am. B 12, 1448 (1995).
7. I. Lorgere, F. Grelet, J. L. Le Gouët, M. Rätsep, and M. Tian, "Phase encoding technique for spectral hole-burning memories," in *Photonics in Computing II*, L. J. Irakliotis, ed. (Society of Photo-Optical Instrumentation Engineers, Bellingham, Wash., 1995), p. 127.
8. Y. T. Mazurenko, "Reconstruction of a nonstationary wavefield by holography in a 3-D medium," Opt. Spektrosk. (USSR) 57, 569 (1984); Appl. Phys. B 50, 101 (1990).
9. C. Joubert, M. L. Roblin, and R. Grousson, "Temporal reversal of picosecond optical pulses by holographic phase conjugation," Appl. Opt. 28, 4604 (1989).
10. A. Débarre, J. C. Keller, J. L. Le Gouët, A. Richard, and P. Tchénio, "An amplitude correlator for broadband laser source characterization," Opt. Commun. 73, 309 (1989).
11. A. M. Weiner, J. P. Heritage, and E. M. Kirschner, "High-resolution femtosecond shaping," J. Opt. Soc. Am. B 5, 1563 (1988).
12. I. Lorgeré, M. Rätsep, J. L. Le Gouët, F. Grelet, M. Tian, A. Débarre, and P. Tchénio, "Storage of a spectrally shaped hologram in a frequency selective material," J. Phys. B 28, L565 (1995).
13. G. C. Valley and M. B. Klein, "Optimal properties of photorefractive materials for optical data processing," Opt. Eng. 22, 704 (1983).
14. H. Kogelnik, "Coupled wave theory for thick hologram grating," Bell Syst. Tech. J. 48, 2909 (1969).

Fast random access to frequency-selective optical memories

M. Rätsep,* M. Tian,† I. Lorgeré, F. Grelet, and J.-L. Le Gouët

Laboratoire Aimé Cotton, Bâtiment 505, 91405, Orsay Cedex, France

Received August 23, 1995

Spectral phase codes are used as storage addresses in a frequency-selective optical memory. Data are engraved over a 1.5-THz-wide spectral interval. With the help of a ferroelectric liquid-crystal modulator it takes less than 100 μs to retrieve any spectrally addressed data. © 1996 Optical Society of America

The persistent spectral hole-burning property is known to add a fourth dimension to the optical data storage volume. One could take full advantage of this large memory capacity and of its optically inherent parallelism in an application such as image storage. Two main classes of persistent spectral hole-burning materials have been investigated. In rare-earth ion-doped crystals, data are stacked within a typically 1-GHz-wide absorption band. With a homogeneous width ν_h in the megahertz range or smaller, these crystals can accommodate more than 1000 spectral addresses within their absorption bands. In dye-molecule-doped amorphous polymers, the absorption bandwidth grows to several terahertz, and the homogeneous width, which determines the spectral extension of elementary stored information, reaches several gigahertz. A few years ago the storage of 2000 images within the absorption band of a chlorin-doped polyvinylbutyral sample was demonstrated.[1] However, the readout rate was dramatically limited by the frequency scan speed of the laser, which had to be tuned over the 1.5-THz-wide spectral domain occupied by the images. Much faster sequential readout of stored images was achieved recently in crystals, for which the absorption bandwidth is smaller.[2] However, the wavelength sweeping rate has not yet been large enough to permit the rapid long-distance spectral jumps that are required for fast random access. In addition, one has to keep in mind the problem of working at the helium temperature. Practical applications probably cannot tolerate this temperature constraint. It is expected that any material working at a higher temperature will exhibit a large homogeneous width and that a larger memory capacity will be kept only at the expense of a larger absorption bandwidth.[3] This should stimulate efforts to develop fast readout techniques in materials in which the inhomogeneous absorption bandwidth ν_i exceeds 1 THz.

We report the experimental demonstration of the addressing procedure that we proposed in a previous theoretical work.[4] It is reminiscent of a recently investigated technique for angular multiplexing in space-domain holography.[5,6] This method should give random access to stored images at video rates in persistent spectral hole-burning materials with an absorption bandwidth of several terahertz. It is derived from the three-pulse photon echo process and can be regarded as a time-and-space holography technique. The memory element is illuminated by the combination of the reference and the object pulses, which propagate along the wave vectors $\mathbf{k}_1$ and $\mathbf{k}_2$, respectively (see Fig. 1), and which are separated in time by the delay τ. The interference pattern engraved at position $\mathbf{r}$ in the material can be expressed as the product $E_1^*(\nu)E_2(\nu)P(\mathbf{r})\exp[i(\mathbf{k}_1 - \mathbf{k}_2)\cdot\mathbf{r} - 2i\pi\nu\tau$ of the corresponding space- and frequency-dependent field amplitudes. The $\mathbf{r}$ dependence of the object field $E_2(\nu)P(\mathbf{r})\exp(-i\mathbf{k}_2\cdot\mathbf{r})$ conveys the two-dimensional spatial image to be stored, and its spectral profile $E_2(\nu)$ is assumed to be a slowly varying function of the frequency ν over the absorption bandwidth. In other words, the duration of the object field is supposed to be smaller than ν_i^{-1} (that is, <200 fs in an amorphous material). Conversely, the reference field is a spatial plane wave, and the characteristic scale of variation of its profile $E_1(\nu)$ is as small as ν_h. Indeed, the ν-dependent shape $E_1(\nu)$ encodes the address of the recorded image. A specific address code corresponds to each stored image. At readout, a probe field $\tilde{E}_3(t - t_3)\exp(-i\mathbf{k}_1\cdot\mathbf{r})$ reaches the memory element at time t_3 and is diffracted by the engraved hologram. Provided that τ is large enough to prevent temporal overlap between the object and the reference pulses, the temporal profile of the radiated signal reads as[7]

$$\tilde{E}_s(\mathbf{r}, t) = P(\mathbf{r})E_2(\nu_0)\int \mathrm{d}\nu E_1^*(\nu)E_3(\nu) \times \exp[2i\pi\nu(t - t_3 - \tau)], \quad (1)$$

where the slow ν variation of $E_2(\nu)$ is ignored and $E_3(\nu)$ stands for the time-to-frequency Fourier transform of $\tilde{E}_3(t)$. At time $t = t_3 + \tau$, Eq. (1) reveals the inner product $\int \mathrm{d}\nu E_1^*(\nu)E_3(\nu)$ of the reference and the readout spectral shapes. If $E_1(\nu)$ and $E_3(\nu)$ belong to the same set of orthogonal functions, the stored image is retrieved if and only if the readout code $E_3(\nu)$ coincides with the memory address code $E_1(\nu)$. More generally, when several images are stacked into the memory, the spectral shape $E_1(\nu)$ is no longer a single code but a linear combination of the orthogonal address functions. Again, any stored image can be retrieved with the help of its own code.

We follow the spectral encoding procedure developed by Weiner *et al.*[8] The spectrum of the reference and readout pulses is spectrally shaped by a liquid-crystal spatial light modulator (SLM) that is inserted within a pair of dispersion gratings. The spectrum is divided into N slices that can be selectivity affected by a 0 or a π phase shift. In this way, a set of N orthogonal spectral shapes can be built. Each element of the set is defined as an array of phase shifts that affect the N spectral slices.

0146-9592/96/010083-03$6.00/0

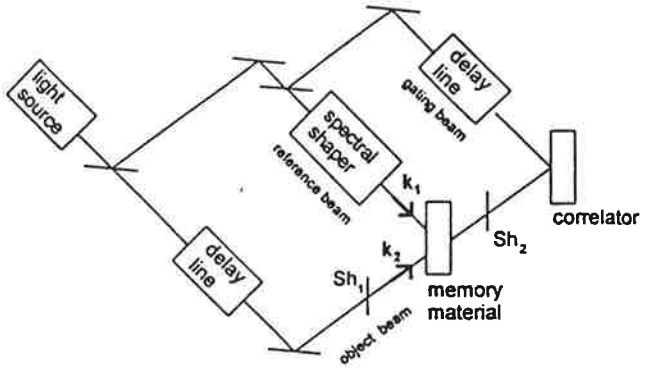

Fig. 1. Schematic of the experimental setup.

The proposed approach is free from the limitations imposed by laser frequency scanning. It takes only 10–100 μs to set the configuration of a ferroelectric liquid-crystal modulator, depending on the applied voltage. This is the access time for any stored information.

The cost of this fast retrieval technique is the excellent time resolution that is demanded from the detector. Indeed, Eq. (1) reduces to the inner product between the reference and the readout field spectral shapes during a very short time, of the order of ν_i^{-1}. Only an ultrafast optical gate is able to pickup the signal. An interference cross-correlator device[9] is well suited to achieving the needed optical gating with high repetition rate (see Fig. 1). One records the cross-correlation function $G(\mathbf{r}, T)$ of the signal field $\tilde{E}_s(\mathbf{r}, t)$ and of a gating field $\tilde{E}_G(t)$:

$$G(\mathbf{r}, T) = \int \tilde{E}_G(t - T)\tilde{E}_s^*(\mathbf{r}, t)\mathrm{d}t \Big/ \int |\tilde{E}_G(t)|^2 \mathrm{d}t . \tag{2}$$

Let the gating field time variation coincide with that of the object field. Then $\tilde{E}_G(t) = \tilde{E}_2(t - t_3)$, and the cross-correlation function reads as

$$G(\mathbf{r}, T) = P(\mathbf{r})|E_2(\nu_0)|^2 \int E_3^*(\nu)E_1(\nu) \times \exp[2i\pi\nu(\tau - T)]\mathrm{d}t \Big/ \int |E_G(\nu)|^2 \mathrm{d}\nu .$$

The T dependence of $G(\mathbf{r}, t)$ coincides with the t dependence of the signal field. At $T = \tau$ the integral over ν reduces to the inner product of the reference and the readout spectral shape, giving access to the selective retrieval of the engraved data. It should be stressed that, unlike previous cross-correlation techniques,[10,11] the present technique is operated at fixed delay. It does not require any mechanical motion of the translation stage. Indeed, the only element that has to be configured to permit access to an image is the SLM used to generate the address code.

Finally, the duration of the initial pulses has to be considered. In the above discussion, it is admitted that the duration of the stored images is not longer than ν_i^{-1}. Production of such short pulses involves sophisticated femtosecond lasers, the use of which does not seem to be pertinent in an experiment in which data are finally retrieved at video rates. Indeed, the quantity that has to be smaller than ν_i^{-1} is not the pulse length but the coherence time of the light. Broad-bandwidth light sources can deliver pulses that satisfy this condition.

We are currently experimenting with the storage of one-point images with the help of the spectral phase-encoding technique. The experimental setup is shown in Fig. 1. The light source is a broadband dye laser pumped by the second harmonic of a YAG laser. It delivers 7-ns-duration pulses at a 15-Hz repetition rate; the pulse spectrum is centered at 620 nm and spreads over approximately 1.5 THz. The sample is a 1-mm-thick piece of octaehylporphine-doped polystyrene, which is cooled to 1.4 K. The optical density of the sample at the center of the absorption band is approximately 2. The reference pulse, which propagates along $\mathbf{k}_1$, illuminates the memory element together with the object beam, directed along $\mathbf{k}_2$. The address is encoded by a spectral phase shaper that is inserted into the path of the reference pulse. The smectic C* liquid-crystal, 128-pixel, linear-array SLM used in the shaper was built at the Ecole Nationale Supérieure des Télécommunications–Bretagne. A pair of holographic gratings with 2400 grooves/mm is used to disperse the reference pulse spectrum on the SLM array and to recombine the spectral components. With a pixel period of 40 μm, the spectral window selected by the SLM spreads over a bandwidth of 2.5 THz. The dead zone between adjacent pixels is approximately 4 μm. Each active spectral pixel is 17.5 GHz wide and can be independently affected by a 0 or a π phase shift. During the recording step, shutters Sh_1 and Sh_2 are open and closed, respectively. The reverse position applies for readout. The typical exposure fluence is 10 mJ cm^{-2} min^{-1}. All the beams used in the experiment are provided by a single laser source. The cross correlation between the signal and the gating pulse is derived from the contrast of their interference fringes. The interference pattern is formed on a CCD linear array that exhibits a dynamic range of 256. A fast Fourier transform of the intensity distribution provides us with a fringe contrast that coincides with the cross-correlation function.

The present laser spectrum appears to be too narrow for performing uniform excitation of the sample over the window defined by the SLM. Hence, a slit is set on the spectral shaper to reduce its aperture by a factor of 2. With the remaining 64 pixels we experimentally test the phase-encoding technique for $N = 32$. The relevant width of each independant spectral slice is thus given by $\nu_s = 38.5$ GHz. The time delay τ between the reference and the object pulses is set to 26 ps. The product $\nu_s\tau = 1.00$ is large enough to eliminate the cross talk that could be caused by the writing pulse overlap.[4]

Each address is allocated to a binary 0 or 1. The j-labeled address is defined by the N-phase-factor array $\{\varepsilon_j\}$. We say that a binary 1 is stored in j when the sample is illuminated by the $\{\varepsilon_j\}$-encoded reference pulse, followed after a delay τ by the object pulse. When no hologram is engraved with the $\{\varepsilon_j\}$ code, the binary 0 is said to be stored at address j.

The 32 spectral shapes composed by the SLM belong to a family of Hadamard orthogonal func-

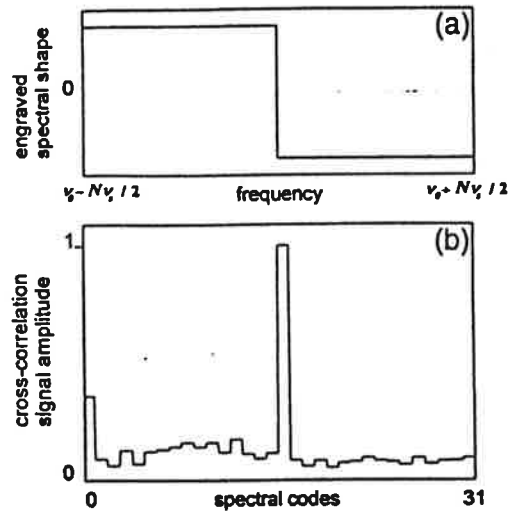

Fig. 2. Storage at a single address. (a) The shape $E_1(\nu)$, the envelope of the spectral hologram. The storage domain spreads over an $N\nu_s$-wide interval around the central frequency ν_0. Component 16 of the 32-element Hadamard family is the step function. (b) The experimental cross-correlation signal amplitude, as it is measured with the help of the 32 address codes numbered from 0 to 31.

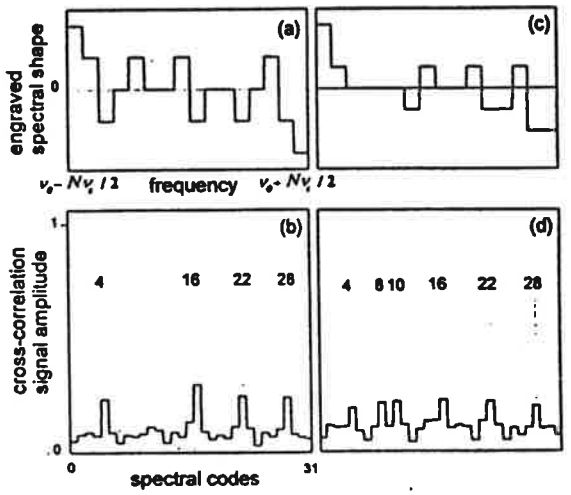

Fig. 3. Envelopes of the spectral holograms, engraved for data storage at (a) addresses 4, 16, 22, and 28 and (c) address 4, 8, 10, 16, 22, and 28. (b), (d) The corresponding cross-correlation signal amplitudes. The same y scale is used for Fig. 2(b) and Figs. 3(b) and 3(d).

tions.[4,6] Figure 2 presents the results obtained when a single binary 1 is stored. The recording step lasts for 2 min. For the readout step the delay T is set equal to τ and the correlation function is recorded while the SLM configuration is scanned through the 32 address codes at the rate of one address every 20 laser shots. The experimental data displayed in Fig. 2 results from the average of the correlation signal amplitude over 20 laser shots at each readout address. A peak is obtained when the readout code coincides with that of the stored binary 1 (address 16 in the figure). Readout with the 31 other address codes gives rise to a background that defines the binary 0 level. For storing several data, we use a cyclic procedure. During one cycle, the data are successively addressed to the memory. Each datum is exposed for 2 s per cycle, and the cycle is repeated 28 times. The readout signal after storage of four and six binary 1's is represented in Fig. 3. The incremental recording procedure yields a good balance between the engraved data. The cross-talk observed in Fig. 2 can be explained by the nonuniformity of the laser spectral distribution, in accordance with Ref. 4. The cross-talk size is consistent with the measured 1.2 ratio of the laser bandwidth to the width of the engraved spectral hologram. Other features are likely to contribute to the cross talk observed in Fig. 3. We have noticed that the exposure used to engrave the data is large enough to erase previous recordings. This means that, contrary to the assumption of Ref. 4, the recording of each datum cannot be regarded as a small perturbation of the active molecule spectral distribution. Besides, because of the large optical density of the sample, the assumption in Ref. 4 of uniform excitation throughout the sample is not valid. It is the low dynamic range of our CCD array detector that forced us to resort to large exposure and large optical density so that we could boost the diffracted signal intensity. Both result in the distortion of the engraved spectral addresses and especially affect the gray-scale spectral shapes that encode the multiplexed addresses of Fig. 3.

In summary, we have experimentally demonstrated a new method for storing data in frequency-selective materials. It should open the way to the random-access retrieval of images at video rate in spectrally selective optical memories, but the cross-talk background must be reduced.

*Permanent address, Institute of Physics, Estonian Academy of Sciences, EE2400 Tartu, Estonia.

†Permanent address, Changchun Institute of Physics, Academia Sinica, Changchun 130021, China.

References

1. B. Kohler, S. Bernet, A. Renn, and U. P. Wild, Opt. Lett. 18, 2144 (1993).
2. H. Sasaki, K. Karaki, M. Mitsunaga, and N. Uesugi, in *Spectral Hole-Burning and Related Spectroscopies: Science and Applications*, Vol. 15 of 1994 OSA Technical Digest Series (Optical Society of America, Washington, D.C., 1994), p. 384.
3. C. Wei, S. Huang, and J. Yu, J. Lumin. 43, 161 (1989).
4. H. Sonajalg, A. Débarre, J.-L. Le Gouët, I. Lorgeré, and P. Tchénio, J. Opt. Soc. Am. B 12, 1448 (1995).
5. Y. Taketomi, J. E. Ford, H. Sasaki, J. Ma, Y. Fainman, and S. H. Lee, Opt. Lett. 16, 1774 (1991).
6. C. Denz, G. Pauliat, G. Roosen, and T. Tschudi, Opt. Commun. 85, 171 (1991); Appl. Opt. 31, 5700 (1992).
7. Y. S. Bai, W. R. Babbitt, N. W. Carlson, and T. W. Mossberg, Appl. Phys. Lett. 45, 714 (1984).
8. A. M. Weiner, D. E. Leaird, J. S. Patel, and J. R. Wullert, IEEE J. Quantum Electron. 28, 908 (1992).
9. A. Débarre, J.-C. Keller, J.-L. Le Gouët, A. Richard, and P. Tchénio, Opt. Commun. 73, 309 (1989).
10. A. Rebane, J. Aaviksoo, and J. Kuhl, Appl. Phys. Lett. 54, 93 (1989).
11. A. Débarre, J.-C. Keller, J.-L. Le Gouët, P. Tchénio, and J.-P. Galaup, J. Opt. Soc. Am. B 8, 2529 (1991).

Time-encoded spatial routing in a photorefractive crystal

M. Rätsep,* M. Tian,† F. Grelet, and J.-L. Le Gouët

Laboratoire Aimé Cotton, Bâtiment 505, 91405 Orsay Cedex, France

C. Sigel and M.-L. Roblin

Groupe de Physique des Solides, Université Paris VII, Tour 23, 2, Place Jussieu, Paris Cedex 05, France

Received November 20, 1995

The spatial routing of a temporally encoded stream of optical pulses is experimentally demonstrated. The holograms that link the temporally shaped addresses to the deflection directions are engraved in a photorefractive crystal. © 1996 Optical Society of America

After the holography concept was clearly extended from the space to the time domain,[1] it appeared difficult to cope experimentally with the fast flow of short signals that represents the restored image of a temporal hologram. For instance, when such a hologram is engraved in a persistent spectral-hole-burning material embedded in an amorphous material, the retrieved temporal recording can include >1000 subpicosecond pulses, which are sequentially emitted at a rate greater than 1 Tbit/s. Fast optical gating techniques were necessary for sampling the temporal structure of the signal flow,[2,3] but they were not appropriate for simultaneously analyzing a spatial image. Only recently was a fast stream of two-dimensional spatial images successfully stored and retrieved within the frame of space and time holography.[4,5] Meanwhile, the idea also emerged of considering space and time coordinates to be on an equal footing and of designing experiments in which a steady-state spatial image is transformed into a stream of pulses and vice versa.[6–8] This is achieved at the expense of the information content of the data, because one of the spatial dimensions has to be exchanged with the temporal one. This study also aims at combining the spatial and the temporal dimensions in a holographic recording.

Recently[9] a scheme was proposed "to direct temporally structured optical signals originally propagating along a common direction into different and distinct output directions according to the precise temporal waveform encoded onto each signal." A detailed explanation of the process, making use of holograms engraved in frequency-selective materials, is given in Ref. 9. However, it has been suggested that the same routing process could be implemented in materials that possess no intrinsic frequency selectivity. Here we use a nonfrequency-selective photorefractive crystal to demonstrate experimentally the routing of data in temporally encoded spatial directions. Also, we show that, despite the subpicosecond scale of the address code, long-duration pulses can be processed in such a material, if their coherence time is short enough to match the time-scale requirements of the router.

The storage of a temporal structure in a three-dimensional holographic material relies on time–space conversion[6,10] Because a single spatial dimension is used to store the temporal information, two dimensions are left for the engraving of spatial data. Using the same notation as that in Ref. 9, we denote by $E_{1a}(\mathbf{r},t)$ and $E_{2d}(\mathbf{r},t)$ two plane waves that illuminate the material. They counterpropagate in the respective directions $\hat{k}_1$ and $\hat{k}_2$ and are defined as follows:

$$E_\epsilon(\mathbf{r},t) = \mathcal{E}_\epsilon(t - \hat{k}_\epsilon \cdot \mathbf{r}/v)\exp 2i\pi\nu(t - \hat{k}_\epsilon \cdot \mathbf{r}/v), \tag{1}$$

where v is the light's velocity within the active material. These fields are used to program the routing device. A time-encoded address is conveyed by the temporal envelope of the address pulse, E_{1a}. The direction of propagation $\hat{k}_2$ is the spatial information that is conveyed by the direction pulse E_{2d}. The address and the direction are linked together by the interference pattern, which reads as

$$\exp -(2i\pi\nu\hat{K}\cdot\mathbf{r}/v)\int dt\,\mathcal{E}_{1a}^*(t)\mathcal{E}_{2d}(t - \hat{K}\cdot\mathbf{r}/v), \tag{2}$$

where $\hat{K} = \hat{k}_2 - \hat{k}_1$. The interference pattern is engraved in the crystal as a space-dependent variation of the refractive index, which leads to a Bragg grating of vector $2\pi\nu\hat{K}/v$. In the counterpropagating configuration, the grating period is close to $\lambda/2$. Let $\mathcal{E}_{2d}(t)$ be a brief pulse that peaks at $t = 0$. The time integral expresses the sampling analysis of the temporal shape $\mathcal{E}_{1a}(t)$ through the gate $\mathcal{E}_{2d}$. The gate location, $t = \hat{K}\cdot\mathbf{r}/v$, is scanned as a function of the spatial position along direction $\hat{K}$; i.e., the temporal shape $\mathcal{E}_{1a}(t)$ is recorded as the spatial envelope $\mathcal{E}_{1a}(\hat{K}\cdot\mathbf{r}/v)$ of the Bragg grating. An entire address pulse of duration T can be recorded if its spatial extent $vT/2$ is smaller than the length of the engraved interference pattern. In an exact collinear configuration, the sample thickness L limits the address duration to $2L/v$. Storage is still possible when the waves depart from collinear propagation. Then the condition $v[\pi - (\hat{k}_1,\hat{k}_2)]T < 2d$ expresses the trade-off among the maximum object duration T, the collinear propagation angular defect $\pi - (\hat{k}_1,\hat{k}_2)$, and the beam diameter d.

After the programming, the crystal is illuminated by a plane-wave input beam of unit wave vector $\hat{k}_3 = \hat{k}_1$,

0146-9592/96/161292-03$10.00/0

which is diffracted on the Bragg grating in backward direction $\hat{k}_2$. At time t_s the input field is represented by $\mathcal{E}_3(0)$ at position $\mathbf{r} = 0$. The spatial and temporal structure of the deflected beam can be expressed as

$$\exp 2i\pi\nu(t - t_s - \hat{k}_2 \cdot \mathbf{r}/v) \int d\mathbf{r}' \int dt' \mathcal{E}_{1a}^*(t' + \hat{K} \cdot \mathbf{r}'/v)\mathcal{E}_{2d}(t')\mathcal{E}_3(t - t_s - \hat{k}_2 \cdot \mathbf{r}/v + \hat{K} \cdot \mathbf{r}'/v). \quad (3)$$

If the direction-programming pulse is brief, the signal-field temporal profile reduces to the cross correlation between the temporal envelopes of the address-programming and the input beams.

Let $\tilde{\mathcal{E}}_e(f)$ represent the time–frequency Fourier transform of the field $\mathcal{E}_e(t)$. According to expression (3) the diffracted signal amplitude in direction $\hat{k}_2$ reads as

$$\int df \tilde{\mathcal{E}}_{1a}^*(f)\tilde{\mathcal{E}}_{2d}(f)\tilde{\mathcal{E}}_3(f) \times \exp[2i\pi(\nu + f)(t - t_S - \hat{k}_2 \cdot \mathbf{r}/v)]. \quad (4)$$

Phase-only shaping of the pulses in the spectral domain gives rise to sharp correlation peaks. We assume that the envelopes $\tilde{\mathcal{E}}_{1a}(f)$ and $\tilde{\mathcal{E}}_3(f)$ result from the spectral shaping of an initial brief pulse by N-element pseudorandom binary phase codes and that the energy spectral density $|\tilde{\mathcal{E}}_e(f)|^2$ is uniformly distributed over the storage bandwidth. One code that appears suitable is the so-called maximal length sequence.[11] One can build a set of cross-correlation orthogonal codes by circular permutation of a single sequence. The total diffracted energy, as derived from expression (4), does not depend on the relative spectral phase shifts of $\tilde{\mathcal{E}}_{1a}(f)$ and $\tilde{\mathcal{E}}_3(f)$. But when $\tilde{\mathcal{E}}_{1a}(f)$ and $\tilde{\mathcal{E}}_3(f)$ belong to the same set of orthogonal functions, most of the diffracted energy is concentrated within a correlation peak if and only if $\tilde{\mathcal{E}}_{1a}(f)$ coincides with $\tilde{\mathcal{E}}_3(f)$. Then all encoding spectral phase shifts cancel one another so the correlation peak can be regarded as a replica of the initial input pulse, as it was before spectral shaping.

As explained in Ref. 9, the spatial routing of optical data is carried out as follows. During the programming process, the crystal is successively illuminated by pairs of address and direction pulses. Each address beam propagates in the common direction $\hat{k}_1$ and has a temporal shape (or address) different from that of any other address beam. The ith-direction beam propagates in a direction $\hat{k}_2^{(i)}$ different from that of any of the other programming beams and is temporally shorter than any of the temporal features encoded onto the address beam with which it is paired. By doing this, one creates multiple three-dimensional holograms. Each hologram corresponds to a specific pair of programming pulses. The ith hologram is matched to deflect a correlation peak into the direction $\hat{k}_2^{(i)}$ when an input pulse, incident along $\hat{k}_1$, has the same temporal shape as the ith address beam. In the operational phase, an optical input stream is directed to the programmed material along $\hat{k}_3 = \hat{k}_1$. Whenever a temporal segment of the input data stream matches the ith address, a pulse is deflected in the direction $\hat{k}_2^{(i)}$. Its duration is as short as the inverse storage bandwidth, and it can be detected with a fast discriminator.

Experimental demonstration is achieved in a 6-mm-thick iron-doped $LiNbO_3$ crystal. The maximum length of the address code, as imposed by the crystal thickness, is $2L/v = 100$ ps. All the different beams are split from a single initial beam (see Fig. 1). To build the temporal envelope of the address pulse we follow the spectral encoding procedure developed by Weiner *et al.*[12,13] The spectrum of the pulse can be phase shaped with a liquid-crystal spatial light modulator array that is inserted into a pair of dispersing gratings.[14] However, in this first experiment we simply detect the total energy of the diffracted signals, so we lose the spectral phase information and are able to separate only routing addresses with mutually exclusive spectra. Thus we substitute for the phase modulator a transmission mask composed of five evenly spaced transparent rectangular slits. At the output of the shaper the pulse spectrum, centered at $\lambda = 570$ nm, exhibits a grooved structure, with a 70-GHz-wide bright slice that is repeated every 0.55 THz. A stepping motor translation stage is used to vary the spectral position of the mask, with 0.7-GHz precision. Addresses are orthogonal, provided that the bright spectral slices of the ith address pulse fall onto dark regions of the other address codes.

During the programming the delay between the address and the direction pulses at the center of the crystal is adjusted to zero. The shaped address pulse, with its 70-GHz-wide spectral slices, exhibits a 9-mm-long coherent structure that, owing to the counterpropagation of the direction beam and to the 2.5 refraction index of $LiNbO_3$, shrinks to a 1.8-mm-long hologram. Two holograms are engraved in the crystal. The angle between $\hat{k}_2^{(1)}$ and $\hat{k}_2^{(2)}$ is 100 mrad. With a beam diameter of 250 μm on the crystal, this angle is small enough to allow all the temporal codes to be stored.

The bright spectral slices of address code 2 are set halfway between those of code 1. This configuration is illustrated in Fig. 2, in which the corresponding tem-

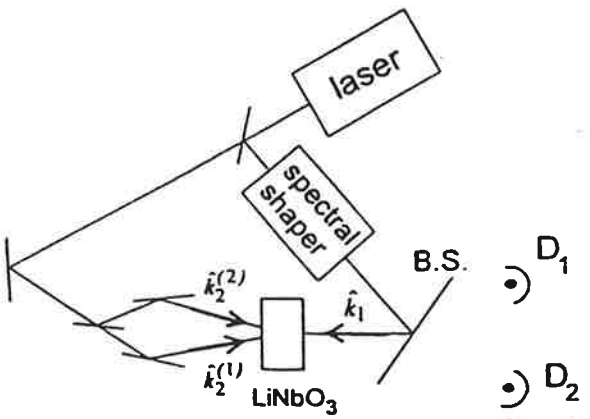

Fig. 1. Diagram of the experimental setup: Two holograms are sequentially recorded. Then beams $\hat{k}_2^{(1)}$ and $\hat{k}_2^{(2)}$ are blocked and the diffracted signals are simultaneously detected on photodiodes D_1 and D_2 through the beam splitter (B.S.).

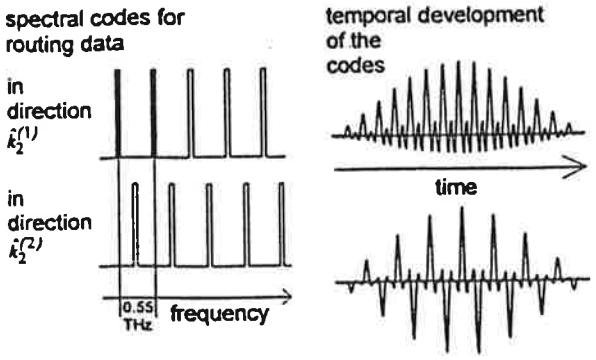

Fig. 2. Spectral slits used to encode the address beams. One obtains the corresponding temporal developments by Fourier transform of the spectral shapes. The code 1 center is set to coincide with that of the laser spectrum.

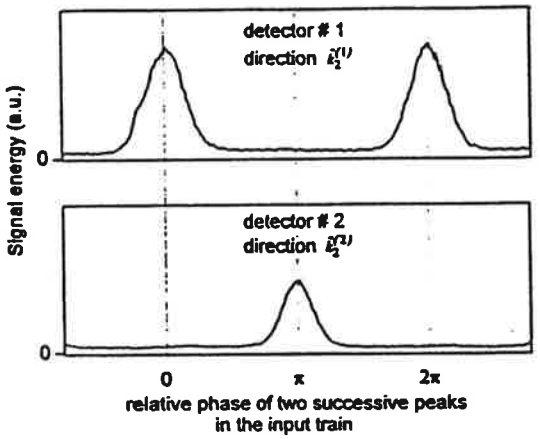

Fig. 3. Experimental data: A spectrally encoded pulse stream is directed to the programmed optical processor along $\hat{k}_1$. Diffracted energy is simultaneously detected in directions $\hat{k}_2^{(1)}$ and $\hat{k}_2^{(2)}$ as a function of the spectral position of the shaping mask. The position scan is equivalent to the scan of the relative phase of two successive peaks within the temporal profile of the input pulse. The detector zero level is represented by 0 on the vertical axis.

poral profiles are also shown. With an appropriate choice of the origin of energy, there is no phase shift between the peaks that comprise the time-domain representation of code 1, and there is a π phase shift between two successive peaks in the train that describes code 2. After the recording, the direction beams are blocked. A spectrally shaped beam is directed to the engraved hologram along $\hat{k}_1$. The diffracted energy is simultaneously detected on two avalanche photodiodes in directions $\hat{k}_2^{(1)}$ and $\hat{k}_2^{(2)}$. The experimental data are displayed in Fig. 3 as a function of the spectral position of the shaping mask. This spectral scan is regarded as the scan of the phase shift between two successive peaks in the temporal development of the input pulse. The background, which is observed outside the matched filtering regions, is caused mainly by the scattering of the input beam in the beam splitter through which the diffracted light is detected (see Fig. 1). The measured cross talk between the routing addresses is smaller than 10^{-2}. The matched temporal shapes are diffracted onto the engraved gratings with an efficiency of $\sim 10^{-5}$. It can be observed that the full width at half-maximum of the recorded profiles (Fig. 3) is larger than expected. As expressed in terms of phase shift, it amounts to $\sim 1/6$ of 2π, instead of 1/8 of 2π, which is the ratio of the spectral slit size to their period. To focus the spectrally shaped beam upon the crystal we were obliged to depart from the exact position of imaging of the mask upon the sample. As explained in Ref. 15, this results in the observed broadening of the recorded profiles.

In the above discussion, we considered temporal profiles that exhibit subpicosecond peaks. Their three-dimensional hologram recording results from their sampled analysis by use of an optical gating pulse that has to be shorter than the profiles. However, a chaotic nanosecond source (pulse width $\cong$7 ns) has been used instead of a femtosecond laser in this experiment.

To take full advantage of the time-encoding procedure, one has to detect the correlation peak that is deflected in the matched direction. Interferometric cross correlators similar to the one used in Ref. 14 could operate as discriminators in each routing direction.

*Permanent address, Institute of Physics, Estonian Academy of Sciences, EE2400 Tartu, Estonia.
†Permanent address, Changchun Institute of Physics, Academia Sinica, Changchun 130021, China.

References

1. T. W. Mossberg, Opt. Lett. 7, 77 (1982).
2. A. Rebane, J. Aaviskoo, and J. Kuhl, Appl. Phys. Lett. 54, 93 (1989).
3. A. Débarre, J.-C. Keller, J.-L. Le Gouët, P. Tchénio, and J.-P. Galaup, J. Opt. Soc. Am. B 8, 2529 (1991).
4. K. B. Hill, K. G. Purchase, and D. J. Brady, Opt. Lett. 20, 1201 (1995).
5. A. Rebane, "Storage and processing of femtosecond optical signals," presented at the Optical Society of America Annual Meeting, Portland, Ore., September 1995.
6. Yu. T. Mazurenko, Opt. Spektrosk. 57, 569 (1984); Appl. Phys. B 50, 101 (1990).
7. K. Ema, M. Kuwata-Gonokami, and F. Shimizu, Appl. Phys. Lett. 59, 2799 (1991).
8. A. M. Weiner, D. E. Leaird, D. H. Reitze, and E. Gi Paek, IEEE J. Quantum Electron. 28, 11551 (1992).
9. W. R. Babbitt and T. W. Mossberg, Opt. Lett. 20, 910 (1995).
10. C. Joubert, M.-L. Roblin, and R. Grousson, Appl. Opt. 28, 4604 (1989).
11. A. M. Weiner, J. P. Heritage, and J. A. Salehi, Opt. Lett. 13, 300 (1988).
12. A. M. Weiner, J. P. Heritage, and E. M. Kirschner, J. Opt. Soc. Am. B 5, 1563 (1988).
13. M. M. Wefers and K. A. Nelson, J. Opt. Soc. Am. B 12, 1343 (1995).
14. M. Rätsep, M. Tian, I. Lorgeré, F. Grelet, and J.-L. Le Gouët, Opt. Lett. 21, 83 (1996).
15. I. Lorgeré, M. Rätsep, J.-L. Le Gouët, F. Grelet, M. Tian, A. Débarre, and P. Tchénio, J. Phys. B 28, 565 (1995).

Mol. Cryst. Liq. Cryst., 1996, Vol. 291, pp. 295–302
Reprints available directly from the publisher
Photocopying permitted by license only

SPECTRAL HOLOGRAMS IN THE TERAHERTZ RANGE

J.-L. LE GOUËT, F. GRELET, I. LORGERE, M. RÄTSEP, M. TIAN
Laboratoire Aimé Cotton, Bâtiment 505, Campus Universitaire,
91405 Orsay Cedex, France
M.-L. ROBLIN, C. SIGEL
Groupe de Physique des Solides, Université Paris VII, 2, Place Jussieu
75251 Paris Cedex 05, France

Abstract We review recent works on temporal frequency holograms. The role of white light excitation is stressed. The interferometric data retrieval technique is emphasized. Both the photorefractive crystals and the persistent spectral hole burning amorphous materials are considered as spectral holography media.

INTRODUCTION

In the framework of optical data storage, we have been developing techniques for engraving and retrieving temporal frequency holograms, and for using them as fast optical processors[1-4]. The holographic « plates » that we consider have a spectral size of a few Terahertz. We have encountered this recording spectral width in two different classes of materials. The first class is represented by the persistent spectral hole burning (PSHB) materials that are made up of active centers embedded in an amorphous host matrix. The second class is represented by photorefractive (PR) materials in the counterpropagating-beam configuration[4]. Although their spectral coherence must be preserved over a very broad frequency domain, the holograms have not to be stored with the help of subpicosecond laser pulses. We have been using a white light source to engrave and retrieve them.

STORAGE OF A SPECTRAL PHASE FACTOR: STIMULATED PHOTON ECHO

Let a PSHB sample be illuminated by two pulses, which issue from the same source and that propagate along $\underline{k}_1$ and $\underline{k}_2$ respectively. One can vary the time separation T between the pulses by adjusting their path length difference. The spectral amplitudes of the two

fields in the sample can be represented by $E(\nu)$ and $E(\nu)\exp(-2i\pi\nu T)$ respectively. Their interference term reads as: $S(\nu)\exp(-2i\pi\nu T)$, where $S(\nu)=|E(\nu)|^2$ is the energy spectral density of the pulses. Provided T is smaller than the inverse homogeneous width Δ_h^{-1}, this interference structure is engraved over the width Δ_{in} of the absorption band $W(\nu)$. The recorded hologram is described by the expression $W(\nu)\ S(\nu)\ \exp(-2i\pi\nu T)$. The original idea of holography is to store the thorough structure (*holos*: « entire ») of an object field, given a perfectly known reference one. The present process is slightly different since the recorded spectrum $S(\nu)$ does not keep any memory of the spectral coherence properties of $E(\nu)$. The phase object $\exp(-2i\pi\nu T)$ is conveyed to the memory material by the carrier field $E(\nu)$. The phase object alone is stored while the phase structure of the carrier is lost.

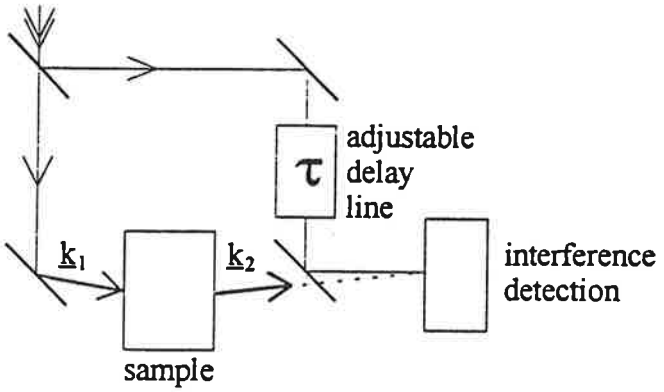

FIGURE 1 Interferometric analysis of the spectral holograms

The sample radiates a field:

$$E_s(\nu)= E_p(\nu)S(\nu)W(\nu)\exp(-2i\pi\nu T) \qquad (1)$$

in direction $\underline{k}_2$, when probed by $E_p(\nu)$ propagating along $\underline{k}_1$. The temporal structure of this signal reflects the spectral shape of the engraved hologram. However, since it coherently spreads over the THz-wide absorption band, the sample response may exhibit subpicosecond features that are not resolved by conventional detectors. In addition, the temporal behavior of the signal is affected by the probe field spectral coherence properties. Interferometric analysis offers an efficient way to recover the originally

recorded phase object[5]. The device is sketched on Fig.1. The sample is inserted in one arm of the interferometer. One detects the interference between the signal and a time-delayed replica of the probe field. As a fonction of the delay τ, the contrast of interference fringes reads as:

$$C(\tau) = \int E_s^*(\nu).E_p(\nu)\exp(-2i\pi\nu\tau)d\nu \qquad (2)$$

Substitution of Eq.1 into Eq.2 leads to:

$$C(\tau) = \int [S(\nu)]^2.W(\nu)\exp[-2i\pi\nu(\tau - T)]d\nu \qquad (3)$$

which is rid of the probe field spectral coherence structure. If the source bandwidth is larger than Δ_{in}, $C(\tau)$ exhibits a peak of width Δ_{in}^{-1} that is located at τ=T. As a function of τ, one recovers the temporal shape of the stimulated photon echo that would be generated by a sequence of femtosecond pulses. However, the validity of Eq. 3 is not conditioned by any assumption on the pulse duration. Any source that delivers broadband pulses should work, whether or not pulses are Fourier transform limited. Holograms with different T values can be multiplexed in the sample. In the framework of data storage, each hologram is regarded as a stored information[6] the address of which is represented by T. Interferometry spectroscopy proves efficient to retrieve the stored informations[1]. However, access to data is hampered by the slowness of the optical delay scan. One can improve the random access rate by taking advantage of the processing capabilities of the spectral holograms[3, 7, 8].

RETRIEVAL OF DATA THROUGH SPECTRAL PATTERN RECOGNITION

Let the pulse propagating along $\underline{k}_1$ be shaped by a phase-only filter which converts its spectral amplitude into $E(\nu)f^{(1)}(\nu)$ where $|f^{(1)}(\nu)|^2=1$. Then, the stored hologram reads as: $S(\nu)[f^{(1)}(\nu)]^*W(\nu)\exp(-2i\pi\nu T)$. The readout pulse along $\underline{k}_1$ is assumed to be shaped by the phase factor $f^{(2)}(\nu)$. Then, according to Eqs 1-3, the interferometer detected signal reads as:

$$C(\tau) = \int [S(\nu)]^2.W(\nu)[f^{(1)}(\nu)]^* f^{(2)}(\nu)\exp[-2i\pi\nu(\tau - T)]d\nu \qquad (4)$$

The spectral density $S(\nu)$ can be adjusted so that $[S(\nu)]^2\,W(\nu)$ is constant over the width

Δ_w of the shaping window. Then, at $\tau = T$, the contrast $C(\tau)$ can be expressed as:

$$C(T) \propto \int [f^{(1)}(\nu)] * f^{(2)}(\nu) d\nu \tag{5}$$

which is nothing but the scalar product of the shaping factors. This function is optically computed by the combination of the holographic memory and of the interferometer. Let the shaping factors belong to a set of orthogonal functions that satisfy the following property:

$$\int [f_i(\nu)] * f_j(\nu) d\nu = \delta_{ij} \Delta_w \tag{6}$$

A signal is detected only if the readout shape factor coincides with the recorded one. The shape factor can be regarded as a data address in the spectral memory[8]. Holograms which are built with different shape factors can be multiplexed in the memory. Each address only responds to the matched readout key. All the stored data are retrieved at the same fixed delay T of the interferometer, in contrast with temporally addressed data. In order to retrieve a data one has to compose its address phase factor. This can be accomplished within a few hundreds microsedonds with the help of a liquid crystal modulator[3]. The optical processing capability of spectral holograms is not specific to PSHB compounds. It can be adapted to PR materials[9,4], with the additional attractive property of working at room temperature.

SPECTRAL HOLOGRAMS IN PHOTOREFRACTIVE MATERIALS

Let two counterpropagating monochromatic beams, directed along $\underline{k}_1$ and $\underline{k}_2 = -\underline{k}_1$, overlap in a L-thick PR crystal (Fig.2). In this material they form a standing wave that engraves a refractive index Bragg grating of period $c/2n\nu$, where ν represents their common single frequency. The grating spreads over the entire length L of the crystal. After recording, a beam of frequency ν', that is directed to the crystal along $\underline{k}_1$, is diffracted along $\underline{k}_2$ provided $|\nu - \nu'| < c/2nL$, according to the phase matching condition. Bragg gratings engraved at different wavelengths can be multiplexed in the crystal. Data that are recorded in the shape of these gratings are thus selectively retrieved at addresses represented by their storage wavelength[10].

A wavelength multiplexed memory ignores the relative phase-shift of the different

gratings: the spectral addresses are mutually incoherent. However a coherent set of gratings is engraved when finite bandwidth pulses are substituted for the monochromatic ones. Let z be the space coordinate along $\underline{k}_1$. Let the origin located at the center of the crystal. The two pulses are split from the same beam, with a time-shift T at z= 0. Their bandwidth is denoted by Δ_p. The grating they engrave at frequency ν is proportional to $S(\nu)\exp[2i\pi\nu(-T+2nz/c)]$. The gratings associated with the different frequencies

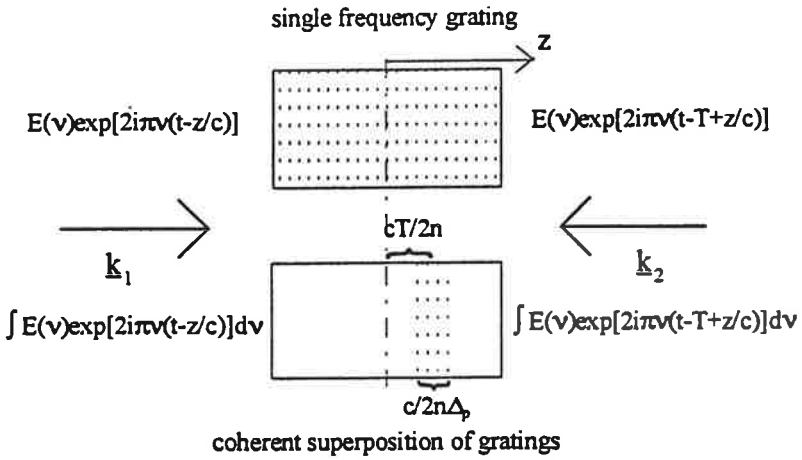

FIGURE 2 Spectral hologram in a photorefractive crystal

combine in a thin spatially modulated structure, the extension of which is $c/2n\Delta_p$. It is located around z=cT/2n. When probed along $\underline{k}_1$ the sample radiates a signal in direction $\underline{k}_2$. Interferometric analysis of the emitted field is again described by Eq. 2. The fringe contrast on the interferometer is:

$$C(\tau) = \int [S(\nu)]^2 . \exp[-2i\pi\nu(\tau - T)]d\nu \qquad (7)$$

As in a PSHB material, the parameter T can be considered as a storage address[11]. The spatial position where a data is recorded can be identified with a temporal coordinate. The number of independent addresses is about $2nL\Delta_p/c$. This is the number of non-overlapping elementary gratings that the sample can accomodate. The storage of broad bandwidth fields illustrates the spectral coherence properties that underlie the optical processing capabilities of spectral holograms. The retrieval efficiency of broad bandwidth pulses thus appears as a critical issue in the context of optical processing.

DATA RETRIEVAL EFFICIENCY

The data retrieval efficiency can be characterized by the signal-to-probe field ratio $\eta = |E_s(\nu)/E_p(\nu)|$ (Table 1). In both PR and PSHB materials we consider the recovery of a single narrowband storage as a reference to which we ultimately compare the readout of multiple broad bandwidth pulses. We first examine the local storage of a single data within the absorption band of a PSHB material. The light source bandwidth Δ_p is assumed to be much smaller than the absorption width Δ_{in}. In order to avoid causality effects we assume that the delay T of the two pulses involved in the storage satisfies the condition $\Delta_p T>1$. The data is engraved at spectral position ν_d over the spectral domain Δ_p. The maximum corresponding value of $|E_s(\nu)/E_p(\nu)|$ is denoted η_{PHB}. In order to stack different data in the material, one assigns each information to a specific address ν_d, while T is kept constant. Then the maximum η value remains equal to η_{PHB} for each recovered data, irrespective of the data number which is $<\Delta_{in}/\Delta_p$. Indeed, different data stand on different molecules. Let us now examine the storage of a single T-addressed data. The data is represented by a spectral hologram that spans the entire absorption band. The maximum η value still equals η_{PHB}. In order to record M T-addressed data within the memory, one has to multiplex M holograms. Each one, that spreads over the same spectral domain, is labeled by a specific value of the frequency period 1/T. Since the same molecules are shared between the M different data, the maximum η value drops to η_{PHB}/M. This reduction occurs when the data are sequentially recorded. A less important reduction factor of $M^{-1/2}$ can be obtained when all the data are simultaneously recorded with random relative phase-shift.

TABLE I Data retrieval. Ratio of the signal to the readout fields. The memory capacity and the number of occupied addresses are denoted N and M.

	ν-addressing	T-addressing
PSHB	η_{PSHB}	η_{PSHB}/M
PR	η_{PR}/M	$\eta_{PR}/(MN)$

As for storage in a PR material, it can be shown that data are restored with the same diffraction efficiency, whether one uses the wavelength multiplexing[10] approach or the more conventional angular multiplexing technique. Let η_{PR} represent the maximum η value when a single monochromatic data is recorded in a PR material. This value is

reduced to η_{PR}/M when M data are wavelength multiplexed in the crystal, since the maximum refractive index variation is shared between the different holograms. When data are T-addressed, each information is engraved in the shape of a $c/2n\Delta_p$-thick grating. The the number of addresses N is close to $2nL\Delta_p/c$. Thus, the spatial thickness of a monochromatic data is N times larger than that of a Δ_p-broad recording. It results that, in a PR memory where a single T-address is occupied, the maximum η value is about η_{PR}/N. This dramatic ratio between T-addressing and wavelength multiplexing persists when several data are stored. Indeed, when a data is locally recorded, it is gradually erased by the subsequent storage of additional data at different positions. When T-addressing is used to store M data in a N-address memory, the maximum η value turns out to be about $\eta_{PR}(NM)^{-1}$. Above we considered holograms that are engraved when the pulse along $\underline{k}_1$ is spectrally shaped by the phase factor $f_i(\nu)$. Comparison with wavelength multiplexing leads again to the same 1/N reduction[12]. This questions the adequacy of PR crystals to the storage of broadband spectral holograms. However operation at room temperature is a decisive advantage that can pay for the small size of the signal. In addition, one must keep in mind that η_{PSHB} and η_{PR} can reach quite dissimilar values. While a diffraction efficiency of one hundred per cent can be attained on a refractive index grating stored in a transparent PR material[13], the absorption character of the gratings engraved in a PSHB medium imposes an upper limit of about 0.37 to η_{PSHB}[14]. Further experimental investigation is required to decide between those two classes of materials.

CONCLUSION

With the help of a chaotic light source, we have been able to store and retrieve multiplexed THz-wide spectral holograms in PR and PSHB materials. When the temporal frequency address of the holograms is shaped by a liquid crystal spatial modulator, the random access to any stored page does not exceed 1 ms. In addition to their application to data storage, spectral holograms offer attractive prospects in the field of real time ultrafast optical processing where both PR and PSHB materials could play a role.

REFERENCES

1. A. Débarre, J.-C; Keller, J.-L. Le Gouët, P. Tchénio, J.-P. Galaup, J. Opt. Soc. Am. B, 8, 2529 (1991).
2. I. Lorgeré, M. Rätsep, J.-L. Le Gouët, F. Grelet, M. Tian, A. Débarre, P. Tchénio, J. Phys. B: Atom. Mol. Opt. Phys., 28 L565 (1995).
3. M. Rätsep, M. Tian, I. Lorgeré, F. Grelet, J.-L. Le Gouët, Opt. Lett., 21, 83 (1996).
4. M. Rätsep, M. Tian, F. Grelet, J.-L. Le Gouët, C. Sigel, M.-L. Roblin, Opt. Lett., 21, 1292 (1996).
5. A. Débarre, J.-C. Keller, J.-L. Le Gouët, A. Richard and P. Tchénio, Opt. Commun. 73, 309 (1989).
6. T. W. Mossberg, Opt. Lett., 7, 77 (1982).
7. Y. S. Bai, W. R. Babbitt, N. W. Carlson, T. W. Mossberg, Appl. Phys. Lett., 45, 714 (1984).
8. H. Sonajalg, A. Débarre, J.-L. Le Gouët, I. Lorgeré, and P. Tchénio, J. Opt. Soc. Am. B, 12, 2529 (1995).
9. C. Joubert, M.-L. Roblin, R. Grousson, Appl. Opt., 28, 4604 (1989).
10. S. Yin, H. Zhou, F. Zhao, M. Wen, Z. Yang, J. Zhang, Francis T.S. Yu, Opt. Commun., 101, 317 (1993).
11. K. B. Hill, K. G. Purchase, D. J. Brady, Opt. Lett., 20, 1201, (1995).
12. I. Lorgeré, F. Grelet, M. Rätsep, M. Tian, J.-L. Le Gouët, C. Sigel, M.-L. Roblin, to be published in J. Opt. Soc. Am., (october 1996).
13. H. Kogelnik, Bell. Syst. Tech. J., 48, 2909 (1969).
14. S. Bernet, B; Kohler, A. Rebane, A. Renn, and U. P. Wild, J. Lumin., 53, 215 (1992).

15 August 1997

ELSEVIER

Chemical Physics Letters 274 (1997) 518–524

CHEMICAL PHYSICS LETTERS

Four-wave hole burning spectroscopy with a broadband laser source

M. Tian, F. Grelet, D. Pavolini, J.-P. Galaup, J.-L. Le Gouët

Laboratoire Aimé Cotton (UPR 3321 CNRS), Bât. 505, Centre Universitaire d'Orsay, 91405 Orsay cedex, France

Received 20 December 1996; in final form 25 May 1997

Abstract

A spatial and frequency grating is engraved in a hole-burning material at 1.8 K by two spectrally broad pulses issued from the same incoherent laser source. A scanned monochromatic beam is diffracted by the engraved spatial-frequency grating. A theoretical approach of the analysis of the spectral distribution of the diffracted beam is presented, from which information on the electron–phonon coupling or the wavelength dependence of the hole-burning efficiency can be deduced.

1. Introduction

Spectral hole burning in a chromophore-doped host matrix opens the way to high density optical data storage by adding a fourth dimension to the 3D spatial memory volume [1]. Holographic recordings in these materials also prove attractive as fully optical data processors [2]. However, the development of applications depends on the photophysical properties of the persistent spectral hole-burning (PSHB) material. Among important characteristics to know are the linear electron phonon coupling and the quantum efficiency of the photoprocess for hole-burning, one challenge being to find out PSHB materials that work as optical memories at high above liquid helium temperature.

The individual absorption spectrum due to an electronic transition in a molecule trapped in a solid host at low temperature contains a zero phonon electronic line (ZPL) and a broad phonon side band (PSB) on its higher energy side. The ZPL is the optical analogue of the recoilless Mössbauer line of ions in solids. The linear electron–phonon coupling is measured by the Debye–Waller factor α_{DW} which is defined as the relative integrated area of the ZPL to the total homogeneous spectral area including the ZPL and the PSB. When the coupling is weak, α_{DW} is close to unity. An important parameter is the energy difference between the PSB band maximum and the ZPL. This energy difference Γ_p measures the average energy of phonon modes coupled to the electronic transition. For high temperature storage, the value of Γ_p should be as high as possible [3]. Among new materials, molecular doped zeolites [4] or inorganic sol–gel hosts with grafted organic molecules [5] have been shown to fulfill conditions for high temperature spectral hole-burning.

Another important parameter is the PSHB quantum efficiency Φ which measures the ratio between the number of selectively phototransformed molecules and the number of incoming photons. The measurement of Φ is usually based on the approach of Moerner and al. [6]. Based on this approach, Horie et al. [7] evaluated the wavelength dependence

0009-2614/97/$17.00
PII S0009-2614(97)00707-0

of Φ for different systems. At present time, there are only a few examples of similar information on other systems.

In the present work, we propose a new method which is based on the spectral analysis of a time-delayed four wave mixing signal. A space and frequency grating is engraved within the whole inhomogeneous band of a PSHB material. A read-out pulse is then diffracted on the engraved grating and the signal spectrum is analyzed. The time-delay between the recording pulses is adjusted in such a way that the diffraction signal is only radiated by the zero phonon line. As it propagates through the sample, the signal is affected by an absorption profile which includes contributions from both the ZPL and the PSB. In other words, the ZPL spectrum of the signal is intrinsically compared with the combined spectrum of ZPL and PSB. This is reminiscent of the comparison of absorption and fluorescence profiles with a view to Stokes shift measurement. However, in the present approach, an experimental profile directly reflects the spectral shift between the emission and the absorption of the signal. The combination of the information derived from the absorption profile and from the diffracted signal spectrum makes this method quite sensitive to parameters change.

This new way is useful to determine experimentally a proper value of α_{DW} if the frequency dependence of the PSHB quantum efficiency is known. In an opposite way, when α_{DW} is known from the literature, then the frequency dependence of the PSHB efficiency is measured.

The reader is reminded of the basics of spectral hole burning in Section 2, where various underlying assumptions are specified. The theory of the coherent transient process under investigation is presented in Section 3 and Section 4. In Section 5 we compare the theory with the experimental data we have obtained in a sample of octa-ethylporphyrin doped polystyrene (OEP/PS). Conclusion is given in the last Section 6.

2. Basics of spectral hole-burning

The optical properties of dye-doped polymers are determined by both the dopants and the matrix. The absorption spectra are due to electronic transitions, inter- or intra-molecular bond vibrations and also contain the interactions between guest and host molecules. At low temperature, a dopant molecule can be optically excited on the zero-phonon line (ZPL) coming from the 0–0 pure electronic transition. On account of the inhomogeneity of the host matrix, guest molecules located at different positions exhibit different ZPL transition frequencies. A ZPL frequency dependent dopant density $n_0(\nu)$ can thus be defined. It is known as the inhomogeneous distribution function. In a simple model it can be described by a Gaussian function centered at ν_0. In the following, its half width at half maximum (HWHM) is denoted by Γ_{in}. In addition to the ZPL component $k_{ZPL}(\nu-\nu')$, the absorption spectrum of each single set of molecules with the same ZPL resonance frequency ν' includes a blue-shifted broad phonon side band $k_{PSB}(\nu-\nu')$, which is caused by electron–phonon interaction. The resulting absorption spectrum reads as:

$$k(\nu-\nu') = k_{ZPL}(\nu-\nu') + k_{PSB}(\nu-\nu'). \quad (1)$$

The line shape of the ZPL can be described by a Lorentzian function:

$$k_{ZPL}(\nu) = \alpha_{DW}\frac{1}{\pi}\frac{\Gamma_0}{\nu^2+\Gamma_0^2}, \quad (2)$$

where Γ_0 is the HWHM of the ZPL, and α_{DW} the Debye–Waller factor. To simplify the mathematical description of the PSB, three assumptions, harmonic potential, low temperature and linear electron–phonon coupling were introduced in Ref. [10], which are also satisfied in the cases we are interested in. Then, the PSB line shape can be expressed as

$$k_{PSB}(\nu) = (1-\alpha_{DW})\frac{\nu}{\Gamma_p^2}e^{-\nu/\Gamma_p}, \quad (3)$$

where Γ_p equals the half Stokes shift. The profile of the whole absorption spectrum $A(\nu)$ can be described as the convolution of $n_0(\nu)$ with $k(\nu)$, i.e.

$$A(\nu) = n_0(\nu) \otimes k(\nu). \quad (4)$$

We assume that $n_0(\nu)$ is normalized in such a way that $A(\nu)$ maximum equals unity.

If a homogeneous set of molecules excited by an extremely narrow laser finally reaches a photostable product state through a photochemical reaction, a persistent spectral hole caused by the absence of the

initial molecules appears in the absorption band. In fact, the profile of such a hole can be rather complicated and strongly depends on laser line width, exposure intensity and time. First, we assume an ideal narrow laser $\delta(\nu-\nu_L)$. In addition to the molecules whose ZPL is at ν_L, those that stay on the red side to ν_L, and whose PSB's overlap the laser line, are burnt. In the linear regime, the resulting depletion of the molecular distribution is proportional to $k(\nu_L-\nu)$. Propagation through the absorbing sample reduces the intensity of the burning beam. On the other hand, the burning bleaches the sample and affects its absorption coefficient. In the following we assume that the bleaching is weak enough so that it does not affect the absorption of the burning beam. Then, at depth z from the surface of the sample, the modified distribution function reads as

$$n_0(\nu)\{1-\beta(\nu)k(\nu_L-\nu)\exp[-\alpha_0 A(\nu_L)z]\}, \tag{5}$$

where the excitation factor $\beta(\nu)$ accounts for the burning process and where α_0 represents the linear absorption coefficient at the maximal absorption frequency ν_m.

Let the laser be represented by a finite width spectrum $W_L(\nu)$, instead of a Dirac peak. According to Eq. (5), after irradiation by the laser the population distribution can be expressed as

$$n_0(\nu)\{1-\beta(\nu)[\exp(-\alpha_0 A(\nu)z)W_L(\nu)] \otimes k(-\nu)\}. \tag{6}$$

Factor $\beta(\nu)$ represents several parameters of the PSHB process:

$$\beta(\nu)=\sigma I_0 t\eta(\nu),$$

where σ is the absorption cross-section of the molecule, $\eta(\nu)$, the quantum efficiency for the photochemical transformation of the PSHB process and $I_0 t$, the burning fluence. Among these parameters, $\eta(\nu)$ is the unique quantity depending on the frequency.

3. Broadband engraving of a space-and-frequency grating

The medium with persistent spectral hole property is now illuminated by a pair of reference and object

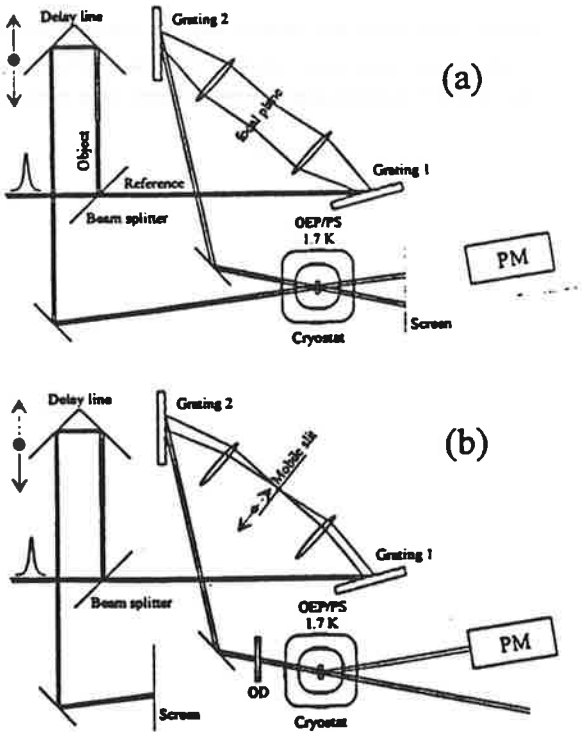

Fig. 1. The experimental set-up (a) in the configuration for engraving a spatial-frequency grating; (b) in the configuration for reading the diffracted signal of a monochromatic beam.

pulses which propagate along k_1 and k_2, respectively. Both pulses are split from a single initial beam. The object pulse is delayed by an adjustable time interval τ from the reference pulse, as shown in Fig. 1. On the input side of the sample, the spectrum of the composite field reads as

$$W_0(\nu)[1+\exp(-2i\pi\nu\tau+iK\cdot r)]+\text{c.c.}, \tag{7}$$

where $W_0(\nu)$ stands for the spectrum of the source and where $K=k_1-k_2$. Then, according to Eq. (6), the modified molecular distribution can be expressed as

$$n_0(\nu)[1-\beta(\nu)W(r,\nu)\otimes k(-\nu)], \tag{8}$$

where

$$W(r,\nu)=W_0(\nu)\exp[-\alpha_0 A(\nu)z] \times[1+\exp(-2i\pi\nu\tau+iK\cdot r)]+\text{c.c.} \tag{9}$$

The factors $\exp(iK\cdot r)$ and $\exp(-2i\pi\nu\tau)$, respectively, represent the spatial and the frequency structures of an engraved grating. In frequency domain, the grating period equals the inverse time separation between the recording pulses. However the period cannot be arbitrary small. It cannot be smaller than the width of $k(-\nu)$, which can be regarded as the grain size of a frequency domain photographic plate and which limits the resolving power of that plate. As a matter of fact, the grain structure includes two components with very different sizes. In dye-doped polymers at low temperature, Γ_{in} is several times larger than Γ_p, and Γ_p is two or three orders of magnitude larger than Γ_0. If $\Gamma_p\tau \gg 1$, the PSB component, with its Γ_p wide grain, does not contribute to the grating. The zero phonon line contribution survives alone, as long as $\Gamma_0\tau < 1$.

In the following we assume that $\Gamma_p\tau \gg 1$ and that the laser bandwidth is larger than Γ_{in}. Since the only surviving component in $k(-\nu)$ is much narrower than $A(\nu)$ and $W(\nu)$, the expression of the engraved grating can be written as

$$n(r,\nu) = \beta(\nu)n_0(\nu)W_0(\nu)\exp[-\alpha_0 A(\nu)z] \times\exp(-2i\pi\nu\tau + iK\cdot r) + \text{c.c.} \quad (10)$$

In the next paragraph we examine the diffraction of a probe beam on this grating.

4. Diffraction on the engraved grating

When a probing pulse is directed along k_1 to the engraved medium, it is diffracted in direction k_2. The probe field excites optical dipoles either on the zero phonon line or in the phonon side band. As usual in a time-delayed four wave mixing process, an interval τ elapses between the excitation of the dipoles and the moment when their relative phase shift cancel and they emit a coherent signal. Since τ is adjusted in such a way that $\Gamma_p\tau \gg 1$, the PSB dipoles decay before the emission time. In summary, PSB participate neither to the grating etching nor to the signal emission. The signal is radiated only on the zero phonon line and this is the only contribution that we have to calculate. Let $E_0(\nu)$ represent the spectral amplitude of the probe field. Then, according to Eq. (10), a dz-thick slice of the sample contributes in the following way to the signal amplitude $E_S(\nu)$:

$$dE_S(z,\nu) \propto \beta(\nu)n_0(\nu)W_0(\nu)\exp[-\alpha_0 A(\nu)z] \times\exp[-\tfrac{1}{2}\alpha_0 A(\nu)L]E_0(\nu)\,dz. \quad (11)$$

where

$$\exp[-\tfrac{1}{2}\alpha_0 A(\nu)L]$$

represents the absorption of the probe and the signal fields through the L-thick sample. The signal intensity spectral distribution $W_S(\nu)$ is calculated by squaring the field amplitude after integration over z. We assume that the spectrum of the probe beam coincides with that of the recording pulses. Finally one obtains

$$W_S(\nu) \propto \left\{\frac{n_0(\nu)}{A(\nu)}\beta(\nu)(1-e^{-\alpha_0 LA(\nu)})\right\}^2 \times e^{-\alpha_0 LA(\nu)}W_0^3(\nu). \quad (12)$$

All the quantities which are involved in this expression, except $n_0(\nu)$, can be accessed directly by standard linear spectroscopy techniques. In standard spectra $n_0(\nu)$ occurs through its convolution with $k(\nu)$. The presence of $n_0(\nu)$ alone reflects the fact that the phonon side band does not contribute to the signal which only brings the zero phonon line into play.

In order to investigate the electron–phonon coupling, one determines the three spectra $W_0(\nu)$, $W_S(\nu)$, $A(\nu)$ and the absorption parameter $\alpha_0 L$ experimentally. Then one adjusts the values of the parameters α_{DW}, Γ_p and Γ_{in} so that the experimental spectra $W_0(\nu)$ and $A(\nu)$ coincide with their theoretical profiles which are given by Eqs. (5) and (12).

5. Results and discussion

The experiment relies on the spectral analysis of a four wave mixing signal. This can be achieved in a conventional way by probing the engraved grating with a broadband pulse and by directing the signal to a spectrometer, at the expense of important energy loss. In addition, a high sensitivity detector array is required in order to simultaneously analyze all the

radiated signal and to avoid to damage the stored grating with an excessive exposure to the readout field. We have preferred to analyze the signal spectrum by probing the engraved grating with the help of a narrow band tunable laser. Then all the radiated energy is directly detected on a photomultiplier, and the signal spectrum is obtained by scanning the laser frequency.

A scheme of the set-up is plotted in Fig. 1. The laser source is a Nd:YAG (with second harmonic generation) pumped dye-laser, delivering wide band chaotic pulses centered at 620 nm with 10 ns-duration and spreading over 9 THz bandwidth approximately at 15 Hz repetition rate. The laser beam is split into reference and object beams with equal intensities.

On reference arm, pulses go through the spectral shaping device that is described in Ref. [8,9]. In the recording stage (Fig. 1a), all the spectral components are transmitted so that the reference beam holds the same broad band spectrum as the object pulse. In the readout stage (Fig. 1b), one inserts a narrow slit in the median focal plane of the spectral shaper. A 0.07 THz wide tunable source is prepared in this way (slit width = 0.16 mm), with the additional benefit that the probe pulse propagates exactly along the same direction as the reference pulse, so that the phase matching condition is automatically fulfilled. The time separation between the object and the reference pulses is adjusted with the help of an optical delay line with a 6.7 fs resolution. The delay is set to 20 ps throughout the experiment.

The tunable source is also used to obtain the absorption spectrum of the sample. Then the object beam is blocked. The reference beam, shaped by the narrow spectral slit, is directed to the sample. The transmitted light is detected on the PM (RTC XP101, with S20R photocathode). One analyses the laser spectral profile in the same way, after removing the sample.

The sample is a 0.5 mm thick slab of polystyrene doped with octa-ethylporphyrin cooled to 1.8 K. The line under investigation is the 0–0 transition of the lowest Q-band of the porphyrin dopant molecules, centered approximately at 620 nm with an optical density of about 1.8 at its maximum (Fig. 2).

By comparison between the experimental absorption profile and wavelength dependence of the diffracted signal with the theoretical shapes, one can determine the relevant parameters. The absorption profile does not depend on the value of Γ_0 as long as $\Gamma_0 \ll \Gamma_p$ and Γ_{in}. On the contrary, the parameters Γ_p, Γ_{in}, α_{DW} affect the absorption profile in such an intricate way that one cannot derive their value from the analysis of this single spectrum. Fig. 2b and 2c show the calculation from Eq. (4) with two different sets of these parameters (see figure caption) which give nearly identical profiles. The slight deviation between theoretical and experimental curves on the high energy side is assigned to the effect of high energy vibrational modes which are not taken into account in our simple model. Combining the signal spectrum with the absorption one, we can fix the parameter configuration in a more reliable way provided that $\beta(\nu)$ is known.

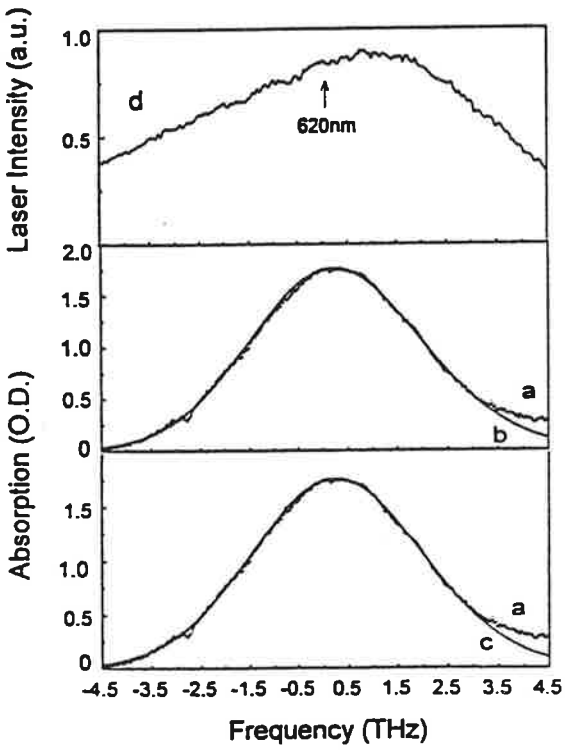

Fig. 2. Comparison of the experimental absorption profile (a), dotted line, with the theoretical simulation, solid line, using Eq. (4) with different set of parameters. (b) $\alpha_{DW} = 0.58$, $\Gamma_p = 0.45$ THz, $\Gamma_{in} = 1.93$ THz. (c) $\alpha_{DW} = 0.9$, $\Gamma_p = 0.45$ THz, $\Gamma_{in} = 2.0$ THz. On top, the curve (d) is the experimental spectral profile of the excitation laser source.

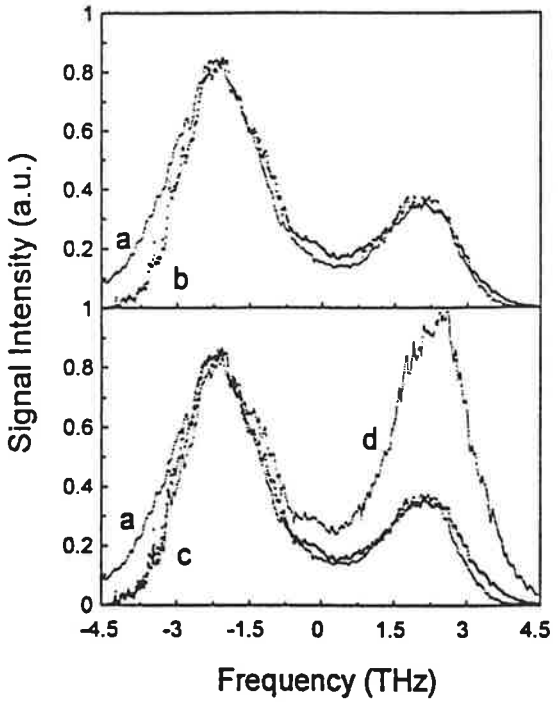

Fig. 3. Comparison of the experimental diffracted signal (a), solid line, with the theoretical simulation of the diffracted signal, open dots, using Eq. (12), (b) with $\beta(\nu)=1$ and the parameters used in Fig. 2b; (c) with $\beta(\nu)=\beta_0[1-0.112(\nu-\nu_0)]$ (ν in THz) and the parameters used in Fig. 2c; (d) with $\beta(\nu)=1$ and the parameters used in Fig. 2c, the large discrepancy proves the high sensitivity of the experiment on parameters change.

When the quantum efficiency is assumed to be uniform over the inhomogeneous width ($\beta(\nu)=1$), Fig. 3b gives the simulated signal with the following relevant parameters values (the same as determined in Fig. 2b):

$\alpha_{DW}=0.58$, $\Gamma_p=0.45\,\text{THz}$, $\Gamma_{in}=1.93\,\text{THz}$.

The resulting value for the Debye–Waller factor $\alpha_{DW}=0.58$ is now precisely determined but is rather different from that obtained by other authors in the same material. For instance, the most precise determination of α_{DW} in OEP/PS has been reported to be 0.85 at 10 K by Saikan and al. [10] using accumulated femtosecond photon echoes.

In Fig. 3d, another fit is achieved where α_{DW} is set equal to 0.9 in accordance with Saikan measurements. Notice that the set of parameters is the same as in Fig. 2c, with $\beta(\nu)=1$, but now, the same set of parameters which gave an excellent fit of the absorption profile, produces a large discrepancy shown in Fig. 3d between the simulated signal and the experimental data: This result underlines the high sensitivity of our approach on the change of parameters.

Then the assumption of a constant hole-burning efficiency over the entire inhomogeneous width appears as non-realistic and on the contrary, we have to consider its wavelength dependence. In order to eliminate the discordance, the simplest hypothesis is to assume a linear dependence of $\beta(\nu)$ with the wavelength. The best fit of the theory to the experimental data is drawn in Fig. 3c and corresponds to the following parameter values (the same as determined in Fig. 2c):

$\alpha_{DW}=0.9\,(\text{fixed})$, $\Gamma_p=0.45\,\text{THz}$, $\Gamma_{in}=2\,\text{THz}$,

with $\beta(\nu)$ defined as

$$\beta(\nu)=\beta_0[1-0.112(\nu-\nu_0)],$$

where β_0 is a proportionality factor and ν is in THz.

Horie et al. [7] reported the quantum efficiency Φ decreases by about one order of magnitude from the red side to the blue side of the inhomogeneous absorption band. These measurements were made point by point for different systems like tetraphenylporphyrin (TPP) or sulfonated TPP in PMMA and poly(vinyl)alcohol (PVA) at 20 K. The covered range was about 490 cm^{-1} (20 nm). For methylene blue in PVA at 4 K, a one order of magnitude decrease was also observed for a covered range of 1000 cm^{-1} (50 nm). From our experiment, we obtain a reasonable understanding of our data only if we introduce a continuous variation of the excitation factor $\beta(\nu)$ over the whole inhomogeneous band. The slope of the variation of $\beta(\nu)$ versus the wavelength is precisely determined and we observe that $\beta(\nu)$ changes by only a factor of 2 over 180–200 cm^{-1} in OEP/PS. Our result agrees with the general observation fact that PSHB is less efficient on the blue edge than on the red edge of the inhomogeneous band. A possible reason is that off-resonance excitation processes through phonon side bands and energy-transfer which both contribute to the diminution of the probability for a photochemical event in the

molecules excited at resonance have a higher rate at higher energies.

6. Conclusion

By adopting a spectral approach for describing a time-resolved coherent transient process, we have been able to propose a novel method to study electron–phonon coupling in a low temperature dye-doped amorphous material. Our spectral analysis of an holographic signal can also be considered in the perspective of frequency-domain storage applications. Indeed we have summarized the influence of various factors on the spectral distribution of this signal, namely the optical density of the sample, the laser spectrum, the spectral inhomogeneous distribution of the molecules, the ZPL and PSB structures. In order to decrease the cross-talk in the situation of broad band spectral phase-encoded time-holographic storage [9], a nearly uniform signal distribution is preferable. Our study gives a clue to realize it by improving the spectral uniformity of the laser source and searching for samples with a suitable concentration to balance signal emission and its re-absorption. In this work we have concentrated on the situation where the time delay between the engraving pulses is much longer than the inverse Stokes shift, and where only the ZPL's contribute to the signal emission. Small time delay will be examined in a future work.

References

[1] G. Castro, D. Haarer, R.M. Macfarlane, H.P. Trommsdorff, Frequency Selective Optical Data Storage System, US Patent No. 4,101,976 (1978).
[2] T. Mossberg, Opt. Lett. 7 (1982) 77; P. Saari, R. Kaarli, A. Rebane, J. Opt. Soc. Am. B 3 (1986) 527.
[3] U. Itoh, T. Tani, in: Polymers for Lightwave and Integrated Optics: Technology and Applications, L.A. Hornak (Ed.), Marcel Dekker, 1992, p. 707.
[4] M. Ehrl, F.W. Deeg, C. Bräuchle, O. Franke, A. Sobbi, G. Schulz-Ekloff, D. Wöhrle, J. Phys. Chem. 98 (1994) 47.
[5] A.-V. Veret-Lemarinier, J.-P. Galaup, A. Ranger, F. Chaput, J.-P. Boilot, J. Lumin. 64 (1995) 223.
[6] W.E. Moerner, M. Gehrtz, A.L. Huston, J. Phys. Chem. 88 (1984) 6459.
[7] K. Horie, M. Ikemoto, T. Suzuki, S. Machida, T. Yamashita, N. Murase, Chem. Phys. Lett. 195 (1992) 563.
[8] A.M. Weiner, D.Z. Leaird, J.S. Patel, J.R. Wullert, IEEE J. Quantum Electron. QE28 (1992) 908.
[9] I. Lorgeré, F. Grelet, M. Rätsep, M. Tian, J.-L. Le Gouët, C. Sigel, M.-L. Roblin, J. Opt. Soc. Am. B 13 (1996) 2229.
[10] Saikan, S. Nakabayashi, T. Kanematsu, Y. Tato, N. Phys. Rev. B 38 (1988) 7777; S. Saikan, A. Imaoka, Y. Kanematsu, T. Kishida, Chem. Phys. Lett. 162 (1989) 217.

Résumé

Introduction

Le « hole burning » spectral persistant (PSHB) et l'holographie sont les deux pierres angulaires de ce travail. Après en avoir retracé l'histoire parallèle au cours de ces cinquantes dernières années, nous passons en revue les travaux récents où ce processus physique et cette technique d'enregistrement optique se rejoignent dans de nouvelles applications. La présente thèse s'inscrit dans ce contexte sous un double aspect. D'une part, elle propose une nouvelle approche de l'enregistrement holographique d'information dans un matériau PSHB. D'autre part, tirant parti de l'éclairage nouveau porté sur le « hole burning » spectral par l'holographie en bande large, elle l'utilise comme moyen d'investigation des mécanismes photophysiques dont le matériau PSHB est le siège. Elle complète ainsi le modèle de la photo-tautomérisation de l'octaéthylporphine dispersée dans du polystyrene.

1. « Hole burning » spectral et holographie spectro-temporelle

A très basse température, dans un matériau solide où sont dispersés des centres absorbants, la largeur de la bande d'absorption est en général très supérieure à la largeur homogène Γ_{hom} de la transition optique mise en jeu. L'inhomogénéité de l'environnement autour des centres actifs disperse en effet la fréquence de transition sur un grand intervalle, appelé largeur inhomogène et noté Γ_{in}. L'excitation monochromatique du matériau se traduit par une diminution locale de l'absorption à la fréquence de l'excitation. Produit par saturation de la transition dans les centres actifs en résonance avec l'onde incidente, ce phénomène est appelé « hole burning » spectral. Lorsque des voies réactives s'ouvrent dans le niveau supérieur de la transition, les centres actifs, en se relaxant, ne reviennent pas tous à leur état initial. La réduction locale d'absorption subsiste alors pendant un temps qui peut n'être limité que par le maintien en froid de l'échantillon. On est alors en présence de « hole burning » spectral persistant.

Nous montrons comment ce mécanisme de gravure permet d'imprimer un hologramme spatial dans un tel matériau. Le hologramme, enregistré à l'aide d'un laser monochromatique, n'occupe qu'une étroite fenêtre spectrale de l'ordre de Γ_{hom} au sein de la bande d'absorption inhomogène. La notion même d'holographie, en tant qu'il s'agit de l'enregistrement de la distribution d'un champ électromagnétique, est ensuite étendue à la quatrième dimension que constitue les fréquences temporelles. Il ne s'agit plus seulement d'enregistrer la distribution spatiale du champ lumineux comme en holographie spatiale conventionnelle, mais de saisir en même temps la répartition spectrale de ce champ, reflet de son évolution temporelle. Cette extension de l'holographie s'appelle l'holographie spectro-temporelle.

L'application au stockage de données binaires dans un matériau PSHB est alors décrit. A l'holographie conventionnelle correspond la possibilité nouvelle d'un adressage spectral (Stockage Optique dans le Domaine Spectral ou SODS), chaque donnée étant repérée par la position qu'elle occupe dans le spectre d'absorption. A l'holographie spectro-temporelle est associée un adressage temporel (Stockage Optique dans le Domaine Temporel ou SODT). Chaque donnée se présente alors sous la forme d'une impulsion brêve, dont le retard par rapport à l'impulsion de référence dans la phase d'écriture, ou par rapport à l'impulsion sonde dans la phase de lecture, constitue l'adresse. Nous présentons également des schémas intermédiaires ou combinatoires entre ces deux approches extrêmes.

Dans une mémoire de capacité potentielle élevée, il importe de réduire le temps d'accès aux informations enregistrées. Alors que des vitesses de transfert très encourageantes ont été observées par quelques groupes, le temps d'accès aléatoire reste très long, en particulier dans les matériaux organiques où les enregistrements s'étendent sur de très grandes largeurs spectrales.

Nous proposons une méthode d'adressage originale qui devrait permettre de réduire le temps d'accès aléatoire.

2. Codage de phase spectral des adresses de la mémoire

Dans un hologramme on enregistre simultanément les champs « objet » et « référence ». C'est sur cette propriété que repose le principe du codage d'adresse. Comme le montre la figure 2.1, le faisceau référence porte un motif temporel qui se grave en même temps que l'image spatiale transportée par le faisceau objet. Lorsqu'on

dispose d'une famille de motifs orthogonaux, on peut empiler dans le matériau autant d'images différentes qu'il y a de motifs orthogonaux. Chaque motif temporel constitue l'adresse de l'image à laquelle il est associé. Pour interroger sélectivement une adresse, on charge le motif correspondant sur le faisceau de lecture. L'étendue spectrale de chaque motif temporel est limitée par la bande passante de la mémoire, c'est à dire par la largeur inhomogène du matériau mémoire.

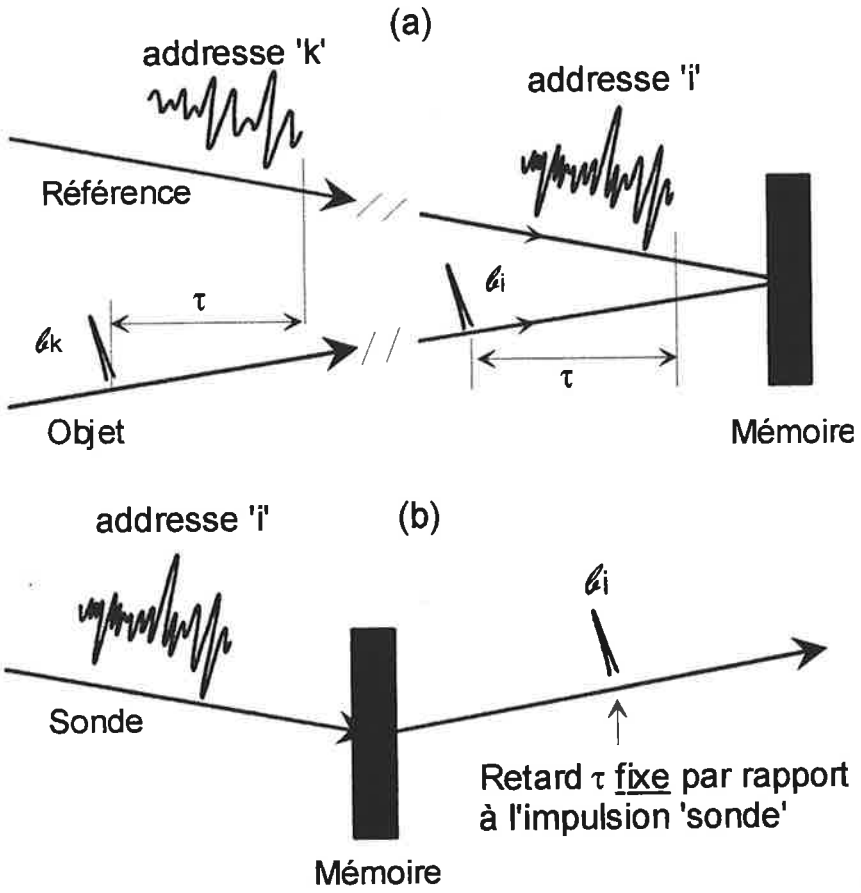

Figure 2.1: Principe de l'adressage spectro-temporel. (a) Enregistrement de deux données ℓ_i et ℓ_k représentées par des impulsions brèves aux adresses 'i' et 'k', respectivement dans le même volume 4D. (b) Lecture sélective de la donnée ℓ_i à l'adresse 'i'.

Ce principe d'adressage évite les écueils rencontrés par les approches SODS et SODT évoquées au chapitre précédent. A la différence de l'adressage spectral, cette méthode n'utilise pas de laser accordable. La source large bande couvre en permanence toute la bande spectrale d'enregistrement. On n'a donc pas à balayer sa fréquence. A la

différence de l'adressage temporel, ce codage est effectué à retard fixe et ne requiert donc pas la modification mécanique d'un chemin optique.

Ce sont des distributions de champ et non d'intensité qu'on enregistre. On tire parti des propriétés de cohérence qui en résultent en choisissant des codes d'adresse définis par des facteurs de phase. Le dispositif utilisé pour façonner les faisceaux référence et sonde est représenté sur la figure 2.2.

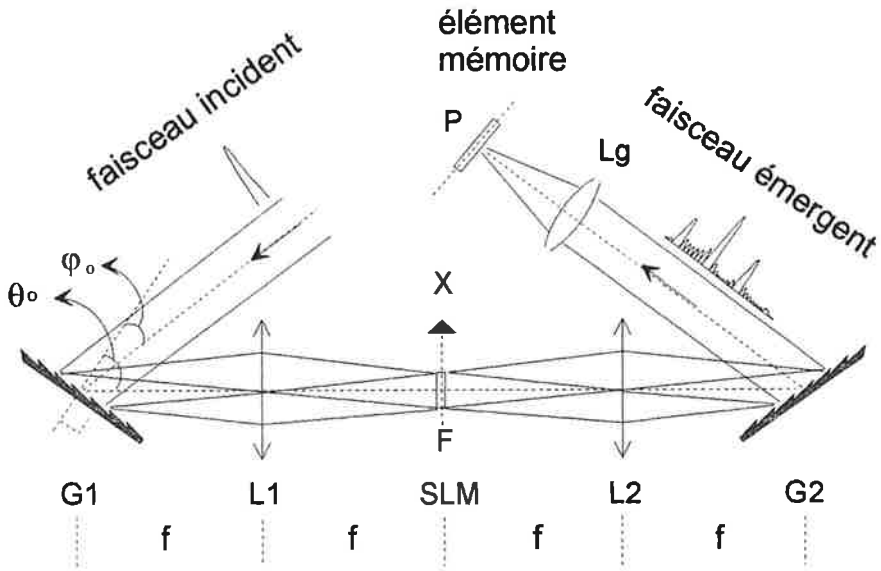

Figure 2.2: Façonnage spectral. Les composantes spectrales du faisceau faisceau incident, dispersées sur le réseau G_1, traversent le modulateur spatial de lumière (SLM) puis sont rassemblées et recollimatées par le réseau G_2. Le SLM permet de contrôler électroniquement la phase relative des composantes spectrales.

La barrette SLM constitue l'organe d'adressage. Composée de 128 pixels, elle pourrait permettre de définir 128 adresses distinctes. Nous n'en utilisons que 32 dans ce montage de démonstration. Il faut moins de 100 µsecondes pour charger un code d'adresse dans le SLM. C'est le temps d'accès aléatoire de la mémoire ainsi codée.

L'orthogonalité des adresses se maintient sur un intervalle de temps très court, défini par l'inverse de la dimension spectrale de la mémoire. Dans notre montage, où la fenêtre délimitée par le SLM s'étend sur une largeur de 1,1THz, on dispose seulement de 800 femtosecondes environ pour recueillir les données restituées. Ceci dépasse la résolution des détecteurs électroniques. On procède donc par corrélation. La figure 2.3 illustre la qualité du façonnage spectro-temporel et de la détection par corrélation. Elle représente la distribution spatiale du facteur de phase chargée sur le SLM, le profil temporel du code d'adresse ainsi construit, et le résultat de son analyse par corrélation.

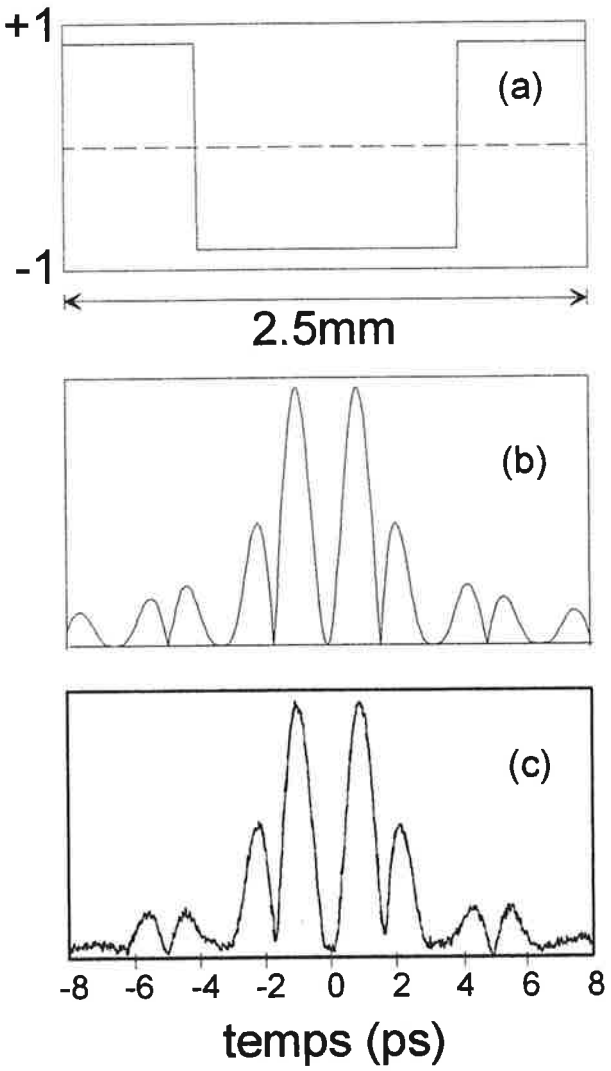

Figure 2.3: *Test du façonneur spectral et de la détection par corrélation. (a) Distribution spatiale du facteur de phase chargé sur le SLM. (b) Profil temporel théorique du champ à la sortie du façonneur. (c) Profil temporel expérimental, enregistré à l'aide du corrélateur.*

Dans ce premier montage l'objet spatial mis en mémoire se réduit à une onde plane. Dans un échantillon d'octaéthylporphine dispersé dans du polystyrène, on enregistre d'abord une seule donnée puis on relit le contenu de la mémoire en interrogeant une à une les 32 adresses disponibles. Le résultat de cette expérience est présenté sur la figure 2.4. Un signal non nul est recueilli dans chaque adresse, la réponse la plus importante étant produite par l'adresse n°16 où une donnée a été enregistrée.

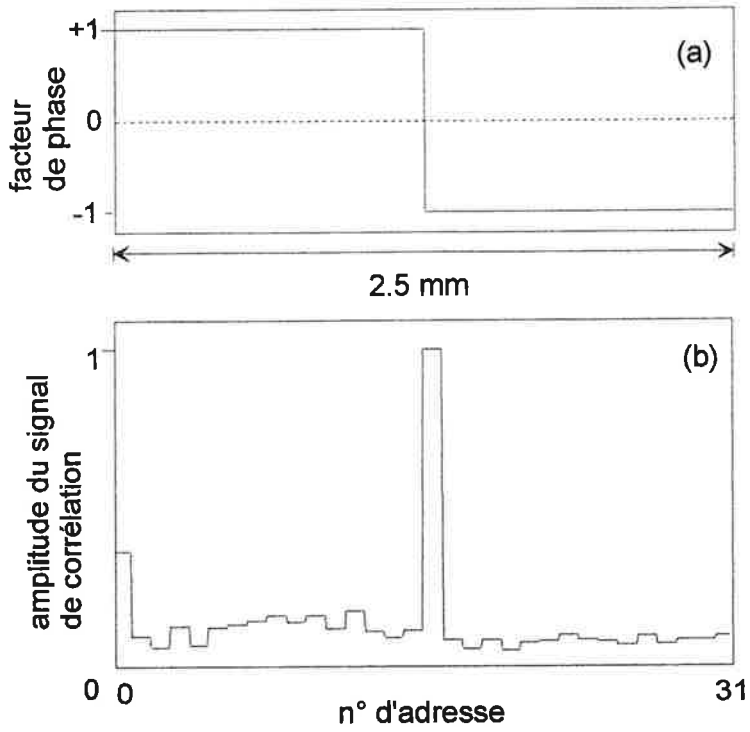

Figure 2.4: Stockage d'une donnée à l'adresse n°16. (a) Distribution spatiale du facteur de phase chargé sur le SLM. (b) Réponse des adresses interrogées.

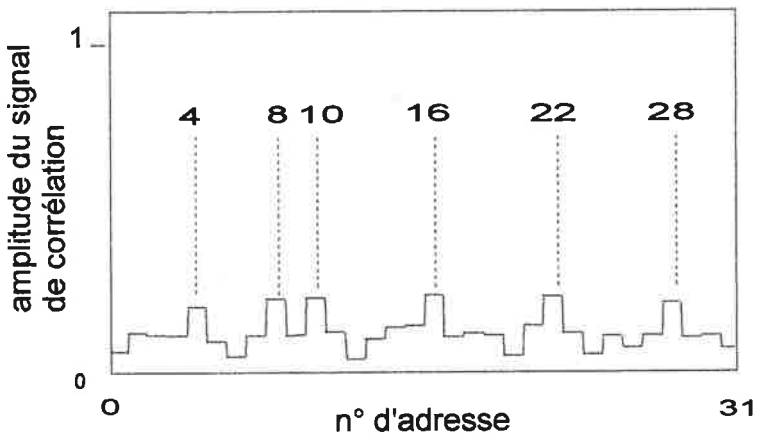

Figure 2.5: Stockage de six données aux adresses n°4, 8, 10, 16, 22, 28. Réponse des adresses interrogées.

On tente ensuite de multiplexer plusieurs données dans la mémoire (figure 2.5). Mais la diaphonie entre les adresses vides et occupées augmente rapidement. Il semble difficile d'utiliser plus de six adresses sur les trente deux disponibles. L'origine ne semble pas devoir être recherchée du côté des dispositifs de codage et de détection qui ont été testés par ailleurs (voir figure 2.3). En revanche plusieurs hypothèses ont été requises pour établir le principe de l'adressage par codage de phase et la plupart d'entre elles ne sont pas satisfaites. Il s'agit en particulier des conditions de faible dose

de gravure, de faible densité optique initiale, d'uniformité de la distribution spectrale des centres actifs et de l'intensité lumineuse sur la fenêtre de stockage. La suite de cette étude est consacrée à la recherche des conditions optimales de fonctionnement de la mémoire. Pour ce faire, nous devons préciser le mécanisme de gravure et de lecture d'un hologramme spectral dans une lame de polystyrène dopé par des molécules d'octaéthylporphine.

3. Holographie spectrale: un modèle portatif

La diaphonie importante observée dans nos expériences sur le codage de phase nous incite à clarifier notre compréhension de l'holographie spectrale dans les matériaux PSHB. Sans investigation plus approfondie, nous savons que la technique d 'adressage proposée dans le chapitre 2 requiert une distribution spectrale uniforme des molécules et de l'énergie lumineuse sur toute la largeur de la fenêtre spectrale de stockage. D'après l'analyse élémentaire du mécanisme d'enregistrement, nous savons aussi que les adresses codées en phase sont bien orthogonales dans les conditions de faible exposition et de faible épaisseur optique. Cependant, des travaux théoriques montrent qu'on devrait atteindre des efficacités de diffraction bien plus élevées en gravant fortement des hologrammes spectraux dans des échantillons de grande densité optique. Malheureusement ces prédictions théoriques ne s'appliquent pas simplement à notre problème car les impulsions de gravure mises en jeu ne transportent aucune structure spectrale. D'autre part ils supposent que les molécules « brûlées » disparaissent de la fenêtre spectrale d'enregistrement, ce qui n'est pas vrai pour l'octaéthylporphine dispersée dans le polystyrene. Dans un calcul antérieur, la structure spectrale de codage de phase avait été inclue mais on avait supposé que l'énergie lumineuse était également répartie dans l'épaisseur de l'échantillon. Cette approximation n'est pas acceptable lorsque la densité optique dépasse l'unité.

Nous entreprenons une étude en deux temps, afin d'élucider l'influence de la dose et de l'épaisseur optique sur la diaphonie. Un modèle simple est d'abord mis au point. Il a pour but de dégager quelques propriétés générales concernant la formation du signal dans un matériau de grande densité optique. Ce modèle est exposé dans le chapitre 3. Il sert de fil conducteur à la mise au point d'un modèle plus élaboré présenté au chapitre 4.

La configuration considérée est représentée sur la figure 3.1. On suppose que la répartition spatiale et spectrale de l'énergie lumineuse de gravure sur la face d'entrée de l'échantillon s'écrit sous la forme:

$$Y(0,x,\nu)=Y_0(\nu)\left\{1+\frac{1}{M}\cos(2\pi\nu\tau+Kx)\sum_{m=1}^{M}\mathscr{E}_m f_m(\nu)\right\}$$

où les fonctions $f_m(\nu)$ représentent les codes de phase spectraux utilisés comme adresses des données représentées par $\mathscr{E}_m$. La période de modulation spectrale $1/\tau$ est supposée beaucoup plus petite que le pas δ. Les impulsions lumineuses impriment dans le matériau ce réseau spectro-spatial.

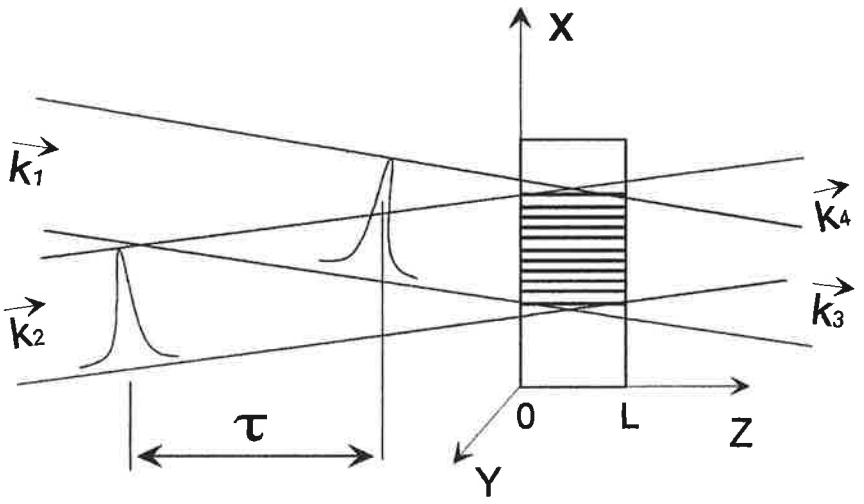

Figure 3.1: Holographie spatio-temporelle. Les impulsions référence, objet, sonde et signal se propagent suivant $\vec{k}_1$, $\vec{k}_2$, $\vec{k}_3$, et $\vec{k}_4$ *respectivement.*

Nous montrons que si le coefficient d'absorption $\alpha(z,x,\nu)$ présente, après gravure, une modulation spatiale qui s'exprime en fonction de la variable $2\pi\nu\tau+Kx$ alors les équations d'onde couplées qui décrivent la propagation et la diffraction du champ sonde sur le hologramme enregistré s'écrivent:

$$\frac{\partial}{\partial z}\underline{\tilde{E}}^{(p)}(z,\nu)+\frac{1}{2}\tilde{\alpha}^{(0)}(z,\nu)\,\underline{\tilde{E}}^{(p)}(z,\nu)+i\frac{(\vec{k}_1+p\vec{K})^2-k_0{}^2}{2k_0}\underline{\tilde{E}}^{(p)}(z,\nu)=$$

$$-\sum_{q>0}\tilde{\alpha}^{(q)}(z,\nu)\,\underline{\tilde{E}}^{(p-q)}(z,\nu)$$

où les ondes $\underline{\tilde{E}}^{(p)}(z,\nu)$ résultent d'un développement du champ sous la forme:

$$\tilde{E}(\vec{r},\nu)=\sum_{p}\underline{\tilde{E}}^{(p)}(z,\nu)\,e^{-i(\vec{k}_1\cdot\vec{r}+pKx)}$$

et où les coefficients de Fourier de $\alpha(z,x,\nu)$ sont représentés par $\tilde{\alpha}_p(z,\nu)$. Le résultat important est que chaque mode alimente exclusivement les modes d'ordre supérieur, à la différence de ce qui se produit dans le cas d'un hologramme conventionnel. Il en résulte que, lorsqu'un champ $\tilde{\mathcal{E}}_L(\nu)\,f_j(\nu)$ est dirigé sur l'échantillon suivant $\vec{k}_3=\vec{k}_1$, le champ diffracté dans la direction $\vec{k}_2$ s'écrit:

$$\underline{\tilde{E}}^{(1)}(z,\nu)=-\,\tilde{\mathcal{E}}_L(\nu)\,f_j(\nu)\,e^{-\frac{1}{2}\tilde{A}^{(0)}(\nu)}\,\tilde{A}^{(1)}(\nu)$$

où $\tilde{A}^{(p)}(\nu)$ est un coefficient de Fourier de l'absorption intégrée sur l'épaisseur de l'échantillon (celle-ci coïncide à un facteur ln(10) près avec la densité optique).

Dans l'hypothèse où les molécules « brûlées » disparaissent de la fenêtre spectrale d'enregistrement, on montre alors que les coefficients $\tilde{A}^{(0)}(\nu)$ et $\tilde{A}^{(1)}(\nu)$ s'expriment simplement comme des fonctions linéaires de la dose reçue sous la forme:

$$\tilde{A}^{(0)}(\nu)=A_0(\nu)-\beta(\nu)Y_0(\nu)$$

$$\tilde{A}^{(1)}(\nu)=-\tfrac{1}{2}\,\beta(\nu)Y_0(\nu)\,\frac{1}{M}\sum_{m=1}^{M}\mathcal{E}_m f_m(\nu)\,e^{2i\pi\nu\tau}$$

à condition que:

$$\beta Y_0(\nu) < \tfrac{1}{2}A_0(\nu)$$

A titre d'illustration de cette propriété, on a tracé sur la figure 3.2 les résultats d'un calcul exact de l'amplitude du signal et son approximation linéaire. La densité initiale est supposée égale à 1,5 et une seule donnée est enregistrée à l'adresse représentée par un code spectral rectangulaire: M=1, $\mathcal{E}_m f_m(\nu)=1$. Il faut souligner que lorsque $\tfrac{1}{2}A_0(\nu)>1$, le domaine de validité du régime linéaire s'étend bien au-delà de celui du développement perturbatif au premier ordre, pour lequel on doit vérifier: $\beta Y_0(\nu)<<1$.

Dans le cadre du régime linéaire on peut discuter simplement la diaphonie. En utilisant les expressions précédentes, on montre que dans ce régime l'orthogonalité des adresses est préservée tant que les molécules actives et l'énergie du laser sont distribuées de façon uniforme sur la fenêtre spectrale d'enregistrement. Il est

remarquable qu'on retrouve ainsi la même condition d'orthogonalité que dans la limite de faible dose et faible épaisseur optique. Ceci est dû au caractère de codage de phase des adresses.

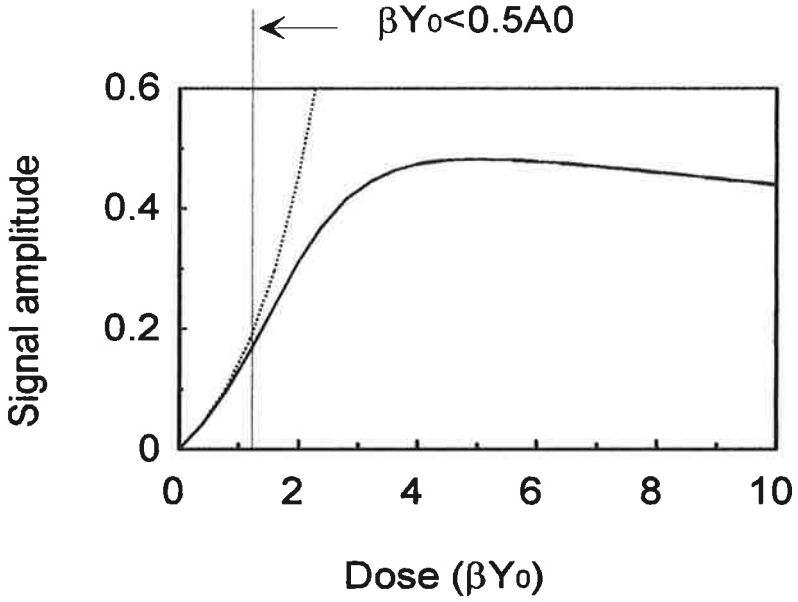

Figure 3.2: Champ diffracté en fonction de la dose. Trait plein: calcul exact. Pointillés: approximation linéaire. $\frac{1}{2}A_0(\nu) = 1{,}7$.

L'expression du signal en fonction des deux premiers coefficients de Fourier de la densité optique et l'existence d'un régime linéaire où l'orthogonalité des adresses est préservée sont les deux principaux résultats qui, obtenus dans le cadre d'un modèle simple, serviront de fil d'Ariane dans la suite du travail.

4. Photophysique et holographie en bande large

Les méthodes que nous avons élaborées pour coder les adresses spectrales ont des retombées dans l'étude du processus de « hole burning » lui-même, en proposant de nouvelles approches expérimentales. De nouvelles informations deviennent accessibles. Cela implique que la description du mécanisme doit rendre compte d'un ensemble plus large d'observations qui ne se limitent plus au creusement d'un trou dans le profil d'absorption par un laser monochromatique mais doivent inclure également le creusement par une source large bande ainsi que la diffraction par un réseau gravé sur une large fenêtre spectrale.

Afin de compléter le modèle physique, nous devons clarifier le rôle du couplage électron-phonon, connaître plus précisément la dépendance en fréquence du taux de « hole burning » $\beta(\nu)$, ainsi que la distribution spectrale des molécules qui ont subi une transformation photochimique.

De plus, nous devons construire une analyse unifiée de la propagation de la lumière dans un matériau PSHB, susceptible de relier la profondeur de trou spectral mesurée dans les expériences conventionnelles et l'efficacité de diffraction sur un hologramme spectral large bande. Cette théorie unifiée est dérivée du modèle développé au chapitre 3.

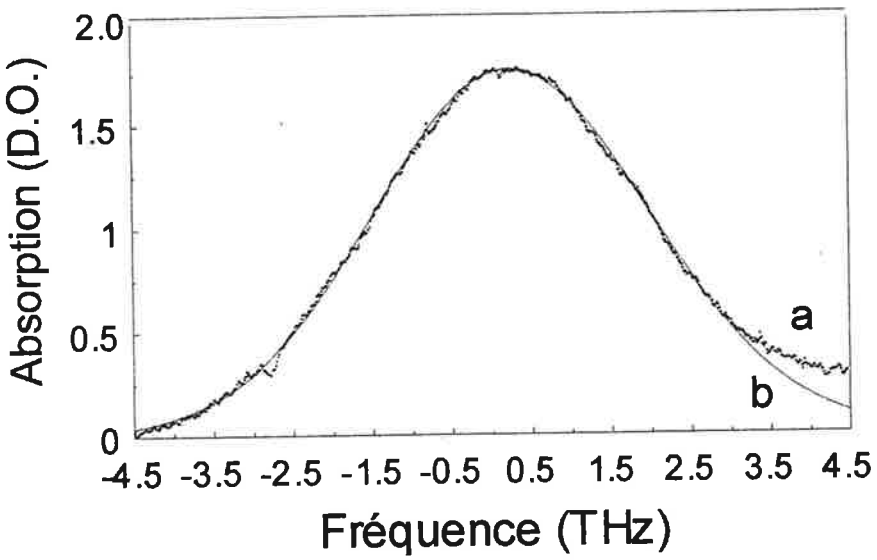

Figure 4.1. Absorption: profil expérimental (a), profil simulé (b).

Une première expérience est destinée à étudier l'évolution de $\beta(\nu)$ en fonction de la fréquence. Elle consiste à confronter le profil d'absorption de l'échantillon à la distribution spectrale de l'efficacité de diffraction sur un réseau gravé par un laser très large bande sur toute la largeur de la raie d'absorption. Une densité optique élevée est favorable dans cette expérience car elle fait apparaître plus nettement le décalage entre ces deux spectres. On enregistre le profil spectral du laser $I_L(\nu)$, le profil d'absorption de l'échantillon $A_0(\nu)$, et la distribution spectrale d'intensité $I_S(\nu)$ du signal diffracté sur le hologramme, gravé dans des conditions de faible dose.

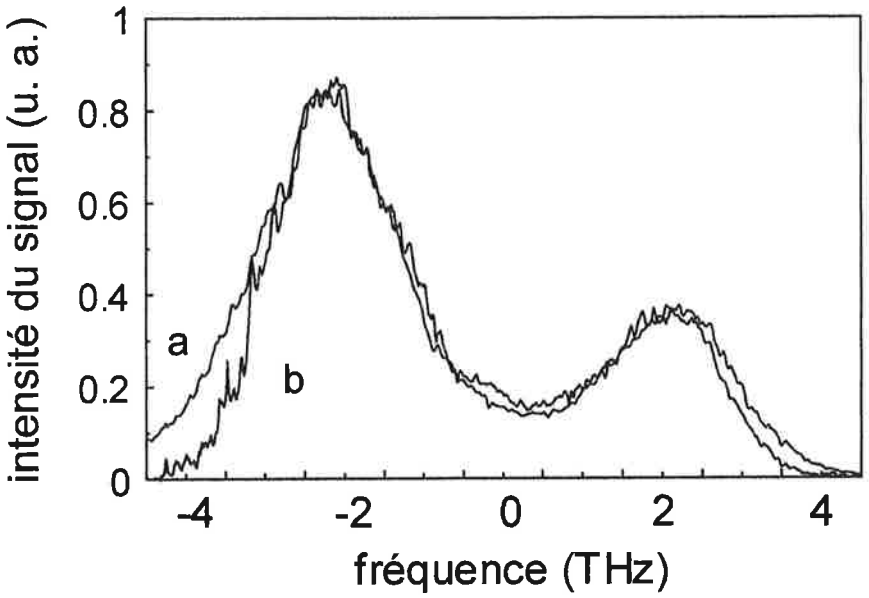

Figure 4.2 *(a) Spectre du signal diffracté.*
(b) Simulation du signal avec $\beta(\nu)=\beta_0.[1-0,112(\nu-\nu_0)]$

L'expression théorique de cette dernière quantité s'écrit:

$$I_S(\nu) \propto \left\{\frac{n_0(\nu)}{A_0(\nu)}\right\}^2 .(1-e^{-A_0(\nu)})^2 .e^{-A_0(\nu)} .\beta(\nu) I_L^3(\nu)$$

où $n_0(\nu)$ désigne la distribution spectrale des molécules en fonction de leur fréquence de transition sur la raie à zéro phonon. Les fonctions $A_0(\nu)$ et $n_0(\nu)$ sont reliée entre elles par:

$$A_0(\nu) = A_0\, n_0(\nu) \otimes k(\nu)$$

où A_0 et $k(\nu)$ représentent respectivement l'absorption au centre de la raie et le profil de raie homogène. Ce dernier étant connu par d'autres expériences, on déduit $n_0(\nu)$ de la confrontation du profil expérimental de $A_0(\nu)$, représenté sur la figure 4.1, avec son expression mathématique. Il ne reste plus alors qu'à substituer, dans l'expression théorique de $I_S(\nu)$, les fonctions $A_0(\nu)$, $n_0(\nu)$ et $I_L(\nu)$, et à ajuster la forme de $\beta(\nu)$ pour faire coïncider les profils théorique et expérimental de $I_S(\nu)$. Ceci est illustré sur la figure 4.2. Le meilleur accord est obtenu pour:

$$\beta(\nu) = \beta_0.[1-0,112(\nu-\nu_0)]$$

où β_0 est un facteur de proportionnalité et où ν est exprimé en THz

L'étape suivante du travail consiste à décrire la cinétique du mécanisme de tautomérisation. Ce dernier se traduit par un déplacement de la fréquence de résonance des molécules. Dans la configuration habituelle où la phototransformation est produite par un laser monochromatique, seules sont atteintes les molécules situées à la fréquence du laser, et chacune d'elles n'interagit qu'une fois avec lui. Dans une situation d'excitation large bande, il faut exprimer le bilan détaillé des échanges entre les différentes classes de fréquence en présence de l'excitation lumineuse, sachant que la réaction de tautomérisation se traduit à la fois par un changement de fréquence et par une rotation de 90° du dipôle optique dans le plan de la molécule. Nous sommes amenés à définir la densité $n(\phi,\theta,\psi,\vec{r},\nu,\nu')$ des molécules de fréquence de résonance ν, dont le dipôle optique est orienté dans la direction (ϕ,θ,ψ), et qui passent à la fréquence ν' lorsque leur dipôle bascule dans la direction $(\phi,\theta,\psi+\pi/2)$. Cette quantité vérifie l'équation cinétique suivante:

$$\frac{dn(\Omega,\vec{r},\nu,\nu')}{dt} = 2\kappa(\Omega',\vec{r},\nu')n_0(\nu,\nu') - [\kappa(\Omega,\vec{r},\nu)+\kappa(\Omega',\vec{r},\nu')]n(\Omega,\vec{r},\nu,\nu')$$

où $\Omega=(\phi,\theta,\psi)$ et $\Omega'=(\phi,\theta,\psi+\pi/2)$, et où les taux d'excitation sont définis par:

$$\kappa(\Omega,\vec{r},\nu)=\beta(\nu)\,I(\vec{r},\nu)\sin^2\theta\sin^2\psi,$$

$$\kappa(\Omega',\vec{r},\nu')=\beta(\nu')\,I(\vec{r},\nu')\sin^2\theta\cos^2\psi,$$

où $I(\vec{r},\nu)$ représente l'intensité lumineuse.

Le coefficient d'absorption est lié à cette densité par la relation:

$$\alpha(\vec{r},\nu)=\alpha_0\left\langle\int d\nu' n(\Omega,\vec{r},\nu,\nu')(\sin\theta.\sin\psi)^2\right\rangle_\Omega / \left\langle(\sin\theta.\sin\psi)^2\right\rangle_\Omega$$

On dispose donc d'une description microscopique de la modification du coefficient d'absorption par phototautomérisation.

L'hypothèse photophysique que nous cherchons à tester est contenue dans la distribution initiale $n_0(\nu,\nu')$. Nous supposons que chaque classe, de fréquence ν et d'orientation dipolaire Ω, est composée de molécules qui, lorsque leur moment est tourné dans la direction Ω', se retrouvent distribuées sur toute la bande d'absorption du matériau. Ceci s'exprime sous la forme suivante:

$$n_0(\nu,\nu')=\frac{2\sqrt{\ln 2}}{\sqrt{\pi}\Gamma_{in}}n_0(\nu)n_0(\nu')$$

où $n_0(\nu)$ représente la distribution d'équilibre de largeur Γ_{in}.

Dans un processus de gravure holographique, les équations du matériau sont couplées à l'équation de propagation de l'énergie lumineuse à travers le matériau. Nous supposons que le hologramme est formé par deux impulsions de largeur spectrale Δ. Aucune structure spectrale n'est imprimée sur les impulsions mises en oeuvre hormis la modulation de période τ^{-1} qui résulte du décalage temporel τ qu'on a ménagé entre elles. Nous résolvons numériquement le système d'équations couplées. Nous en déduisons la valeur des deux premiers coefficients de Fourier de la densité optique. A l'aide des résultats obtenus au chapitre 3, nous calculons alors l'efficacité de diffraction sur le hologramme.

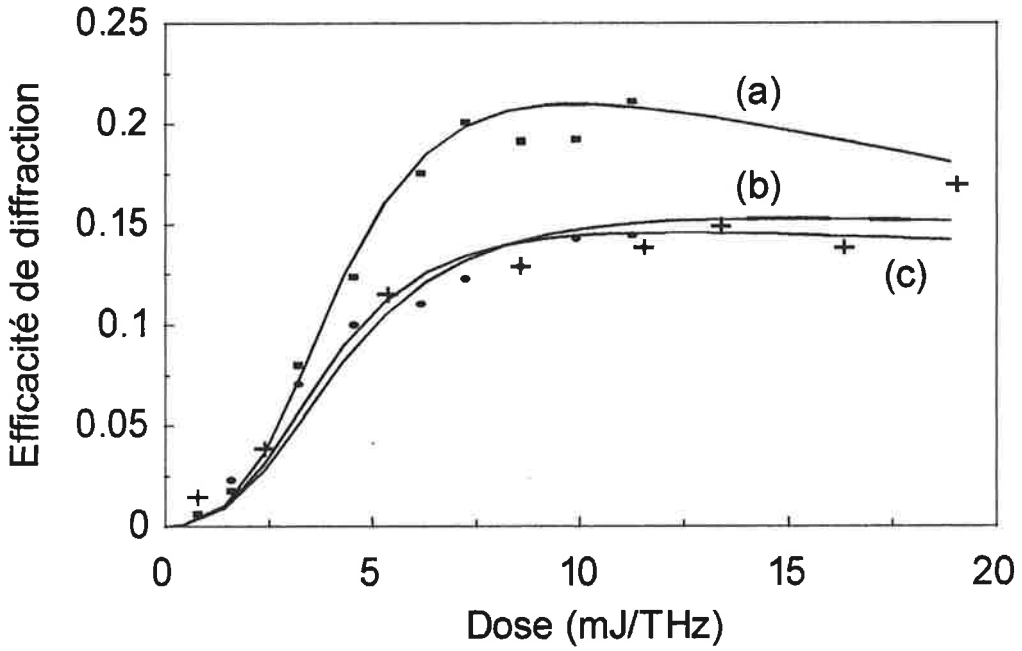

Figure 4.3: Efficacité de diffraction en fonction de la dose. En traits pleins: courbes calculées pour une largeur de fenêtre de 80GHz (a), 1,56THz (b), et dans le cas de deux gravures successives sur des bandes de 80GHz et 1,56THz (c). Résultats expérimentaux: les carrés, les cercles et les croix représentent respectivement les gravures sur une largeur de bande de 80GHz, de 1,56THz et la gravure mixte.

Le calcul est confronté à l'expérience dans un échantillon de densité optique utile de 1,5. La calibration en énergie est réalisée à l'aide d'une mesure de « hole burning » conventionnel qui permet d'établir une correspondance entre le paramètre de dose du calcul numérique et la quantité d'énergie reçue par l'échantillon dans l'expérience. Données expérimentales et courbes théoriques sont portées sur la figure

4.3 qui représente l'efficacité de diffraction en fonction de la densité spectrale d'énergie.

Les courbes théoriques reproduisent fidèlement le comportement des points expérimentaux. Cependant l'accord n'est pas bon en valeur absolue. Un facteur d'échelle a été appliqué à toutes les données expérimentales de façon à faire coïncider expérience et théorie dans le cas de l'excitation en bande étroite. Un ordre de grandeur environ sépare l'efficacité de diffraction prévue de sa valeur mesurée. Ce désaccord n'a encore trouvé aucune interprétation satisfaisante.

5. Hologrammes codés en phase dans l'octaéthylporphine/polystyrène

A l'aide du modèle mis au point dans le chapitre précédent, nous précisons le domaine d'énergie de gravure qui permet d'éviter les phénomènes de saturation sources de diaphonie. Par ailleurs nous vérifions, en nous plaçant à la limite supérieure du domaine d'énergie exempt d'effets de saturation, que la distribution spectrale du signal holographique est bien uniforme lorsque molécules et intensité laser sont elles-mêmes distribuées uniformément.

Les limites de fonctionnement de la gravure holographiques étant bien précisées désormais, nous entreprenons une nouvelle série d'expériences d'adressage par codage de phase spectral. La diaphonie entre les adresses est sensiblement améliorée. Les défauts qui subsistent semblent liés au dispositif optique, tout particulièrement aux instabilités spatiales et spectrales de la source lumineuse.

6.Conclusion

Nous avons réalisé la première expérience de stockage optique avec adressage par codage de phase spectral. L'amélioration du montage optique, menée à bien dans la thèse de François GRELET, puis l'investigation approfondie des propriétés photophysiques du matériau photosensible décrite dans le cadre du présent mémoire, ont permis d'atteindre un niveau de diaphonie qui devrait permettre une bonne exploitation de la capacité de la mémoire optique. Une meilleure source lumineuse améliorerait sans doute encore sensiblement ces résultats. De façon plus générale nous avons exploré les perspectives offertes par le traitement optique de l'information dans le domaine spectro-temporel.

Résumé

Nous proposons une nouvelle méthode d'holographie spectrale pour stocker des données dans un matériau doté de la propriété de « hole burning » spectral persistant. Dans ces matériaux, l'information est enregistrée comme une forme spectrale imprimée dans le profil d'une raie d'absorption optique. De la sorte, une quatrième dimension, celle des fréquences temporelles, est ajoutée au volume tridimensionnel de l'holographie conventionnelle. Nous proposons, et démontrons expérimentalement, une approche originale pour adresser les données dans le domaine spectral. Elle s'appuie sur un phénomène d'interférence spectrale étendu à une fenêtre de gravure qui couvre plusieurs Térahertz. Une source chaotique large bande délivre un faisceau lumineux pulsé qui est partagé entre les voies référence et objet. Les données à enregistrer sont codées sous la forme d'une modulation spatiale du faisceau objet. Chaque adresse est caractérisée par un facteur de phase dépendant de la fréquence qui est transporté par le faisceau référence et qui est gravé dans le matériau mémoire en même temps que l'information à sauvegarder. Pour lire une adresse spécifique, on utilise un faisceau sonde qui est façonné par le facteur de phase correspondant. Bien que l'adressage s'effectue dans le domaine spectral, la gravure et la lecture des données ne nécessitent ni balayage en fréquence de la source ni ajustement de ligne à retard optique. Par conséquent, le temp d'accès aléatoire aux données devrait être court. Ce mémoire est principalement consacré à un examen détaillé de la contribution du matériau à la diaphonie entre les adresses. Dans le passé, le mécanisme de photo-tautomérisation, qui est impliqué dans le processus de « hole burning », a été principalement étudié à l'aide de sources spectralement étroites. Nous étendons sa description aux conditions d'excitation en bande large. Nous développons un modèle théorique qui inclut le processus photochimique, la propagation des impulsions large bande, et le stockage holographique. Nous en déduisons la condition de dose qui permet d'éliminer la contribution du matériau à la diaphonie. La démonstration expérimentale de l'adressage par codage de phase confirme nos prédictions.

Mots cles

'HOLE BURNING' SPECTRAL
STOCKAGE OPTIQUE
TAUTOMERISATION
PORPHYRINE
HOLOGRAPHIE
MELANGE A QUATRE ONDES
INTERCORRELATION